Thermoelectric properties of TiNiSn and $Zr_{0.5}Hf_{0.5}NiSn$ thin films and superlattices with reduced thermal conductivities

Dissertation
zur Erlangung des Grades

*„Doktor
der Naturwissenschaften“*

am Fachbereich Physik
der Johannes Gutenberg-Universität Mainz

vorgelegt von

Tino Jäger

geboren in Friedrichroda

JOHANNES GUTENBERG
UNIVERSITÄT MAINZ

Fachbereich 08 - Physik, Mathematik und Informatik

Institut für Physik

Mainz, den 21. August 2013

Abstract

Rising energy costs and enhanced CO_2 emission have moved research about thermoelectric (TE) materials into focus. The suitability of a material for usage in TE devices depends on the figure of merit ZT and is equal to $\alpha^2\sigma T\kappa^{-1}$ including Seebeck coefficient α, conductivity σ, temperature T and thermal conductivity κ. Without affecting the power factor $\alpha^2\sigma$, using nanostructuring, ZT should here be increased by a depressed thermal conductivity.

As half-Heusler (HH) bulk materials, the TE properties of TiNiSn and $Zr_{0.5}Hf_{0.5}NiSn$ have been extensively studied. Here, semiconducting TiNiSn and $Zr_{0.5}Hf_{0.5}NiSn$ thin films were fabricated for the first time by dc magnetron sputtering. On MgO (100) substrates, strongly textured polycrystalline films were obtained at substrate temperatures of about 450°C. The film consisted of grains with an elongation perpendicular to the surface of 55 nm. These generated rocking curves with FWHMs of less than 1°. Structural analyses were performed by X-ray diffraction (XRD). Having deposition rates of about 1 nms^{-1} within shortest time also films in the order of microns were fabricated. For TiNiSn the highest in-plane power factor of about 0.4 $mWK^{-2}m^{-1}$ was measured at about 550 K. In addition, at room temperature (RT) a cross-plane thermal conductivity of 2.8 $Wm^{-1}K^{-1}$ was observed by the differential 3ω method. Because the reduction of thermal conductivity by mass fluctuation is well-known and interface scattering of phonons is expected, superlattices (SL) were fabricated. Therefore, TiNiSn and $Zr_{0.5}Hf_{0.5}NiSn$ were successively deposited. While the sputter cathodes were continuously running, for fabrication of SLs the substrates were moved from one to another. The high crystal quality of the SLs and the sharp interfaces were proven by satellite peaks (XRD) and Scanning Transmission Electron Microscopy (STEM). For a SL with a periodicity of 21 nm (TiNiSn and $Zr_{0.5}Hf_{0.5}NiSn$ each 15 nm) at a temperature of 550 K an in-plane power factor of 0.77 $mWK^{-2}m^{-1}$ was calculated by a Seebeck coefficient of -80 μVK^{-1} and a resistivity of 8.2 $\mu\Omega m$. In addition to the enhanced power factor a tremendous reduction of the cross-plane thermal conductivity was obtained for SLs with periodicities of about 8 nm. Here, a thermal conductivity of 1 $Wm^{-1}K^{-1}$ was measured by the differential 3ω method. In principle, the concept of reduced cross-plane thermal conductivity in HH SLs was proven. At the HH interfaces, titanium, zirconium and hafnium that have significant differences in mass but are isoelectronic are assumed to have a negligible influence on the electronic band structure and thus on the power factor.

Kurzdarstellung

Durch steigende Energiekosten und erhöhte CO_2 Emission ist die Forschung an thermoelektrischen (TE) Materialien in den Fokus gerückt. Die Eignung eines Materials für die Verwendung in einem TE Modul ist verknüpft mit der Gütezahl *ZT* und entspricht $\alpha^2\sigma T\kappa^{-1}$ (Seebeck Koeffizient α, Leitfähigkeit σ, Temperatur T und thermische Leitfähigkeit κ). Ohne den Leistungsfaktor $\alpha^2\sigma$ zu verändern, soll *ZT* durch Senkung der thermischen Leitfähigkeit mittels Nanostrukturierung angehoben werden.

Bis heute sind die TE Eigenschaften von den makroskopischen halb-Heusler Materialen TiNiSn und $Zr_{0.5}Hf_{0.5}NiSn$ ausgiebig erforscht worden. Mit Hilfe von dc Magnetron-Sputterdeposition wurden nun erstmals halbleitende TiNiSn und $Zr_{0.5}Hf_{0.5}NiSn$ Schichten hergestellt. Auf MgO (100) Substraten sind stark texturierte polykristalline Schichten bei Substrattemperaturen von 450°C abgeschieden worden. Senkrecht zur Oberfläche haben sich Korngrößen von 55 nm feststellen lassen. Diese haben Halbwertsbreiten bei Rockingkurven von unter 1° aufgewiesen. Strukturanalysen sind mit Hilfe von Röntgenbeugungsexperimenten (XRD) durchgeführt worden. Durch Wachstumsraten von 1 nms^{-1} konnten in kürzester Zeit Filmdicken von mehr als einem µm hergestellt werden. TiNiSn zeigte den höchsten Leistungsfaktor von 0.4 $mWK^{-2}m^{-1}$ (550 K). Zusätzlich wurde bei Raumtemperatur mit Hilfe der differentiellen 3ω Methode eine thermische Leitfähigkeit von 2.8 $Wm^{-1}K^{-1}$ bestimmt. Es ist bekannt, dass die thermische Leitfähigkeit mit der Variation von Massen abnimmt. Weil zudem angenommen wird, dass sie durch Grenzflächenstreuung von Phononen ebenfalls reduziert wird, wurden Übergitter hergestellt. Dabei wurden TiNiSn und $Zr_{0.5}Hf_{0.5}NiSn$ nacheinander abgeschieden. Die sehr hohe Kristallqualität der Übergitter mit ihren scharfen Grenzflächen konnte durch Satellitenpeaks und Transmissionsmikroskopie (STEM) nachgewiesen werden. Für ein Übergitter mit einer Periodizität von 21 nm (TiNiSn und $Zr_{0.5}Hf_{0.5}NiSn$ jeweils 10.5 nm) ist bei einer Temperatur von 550 K ein Leistungsfaktor von 0.77 $mWK^{-2}m^{-1}$ nachgewiesen worden ($\alpha = -80\ \mu VK^{-1}$; $\sigma = 8.2\ \mu\Omega m$). Ein Übergitter mit der Periodizität von 8 nm hat senkrecht zu den Grenzflächen eine thermische Leitfähigkeit von 1 $Wm^{-1}K^{-1}$ aufgewiesen. Damit hat sich die Reduzierung der thermischen Leitfähigkeit durch die halb-Heusler Übergitter bestätigt. Durch die isoelektronischen Eigenschaften von Titan, Zirkonium und Hafnium wird angenommen, dass die elektrische Bandstruktur und damit der Leistungsfaktor senkrecht zu den Grenzflächen nur schwach beeinflusst wird.

Table of contents

Table of contents III

Declaration VI

List of publications VII

List of figures VIII

List of tables XI

Abbreviations XII

1 Introduction 1

2 Half-Heusler materials in thermoelectrics 7

2.1 Thermoelectric effects and applications – a brief introduction 7

2.2 *ZT* – the figure of merit in the field of thermoelectrics 10

2.3 Formation of half-Heusler materials 13

2.4 TiNiSn and $Zr_{0.5}Hf_{0.5}NiSn$ in thermoelectrics 15

3 Theoretical and experimental background 20

3.1 Thermal conductivity 20

3.1.1 Fundamental treatment of lattice vibrations 20

3.1.2 Thermal conductivity 24

3.1.3 Disorder in solid solutions 28

3.1.4 The effect of superlattices on thermal conductivity 31

3.2 Electronic behavior 36

3.2.1 Electrons in a metal – Drude model 36

3.2.2 Semi-classical treatment – Onsager reciprocal relations 39

3.2.3 Mott's formula based on the Boltzmann transport equation 44

3.2.4 Final considerations about TE material properties 47

4 Structural quality, chemical analysis and surface morphology of thin film TiNiSn and $Zr_{0.5}Hf_{0.5}NiSn$ 51

4.1 Fabrication process – dc magnetron sputter deposition 51
4.2 Epitaxial film quality defined by X-ray diffraction 52
4.3 Stoichiometric composition of TiNiSn and $Zr_{0.5}Hf_{0.5}NiSn$ films 58
4.4 Surface morphology of TiNiSn and $Zr_{0.5}Hf_{0.5}NiSn$ films 63

5 Vanadium buffer layer – quality enhancement of the half-Heusler thin films 66

5.1 Introduction 66
5.2 Thin film vanadium sputtered on MgO (100) 68
5.3 Half-Heusler film growth on a vanadium buffer layer 76
5.4 Half-Heusler film growth on native SiO_x 79

6 Superlattices - TiNiSn and $Zr_{0.5}Hf_{0.5}NiSn$ subsequently deposited at elevated substrate temperatures 82

6.1 Introduction 82
6.2 Interface roughness affected by substrate temperatures 83
6.3 Further enhancement in interface roughness 89
6.4 Thin films and superlattices investigated by photoelectron spectroscopy 92
6.4.1 Introduction 92
6.4.2 Core level analysis performed with HAXPES 94
6.4.2 Valence band spectra measured with HAXPES 97

7 Seebeck coefficients and conductivity measured at varied temperatures **102**

7.1 Introduction 102
7.2 TE properties measured at low temperatures 104
7.3 Origin of enhanced conductivity 107
7.4 Thermoelectric measurements and thin film stability at elevated temperatures 112
7.4.1 TiNiSn 112
7.4.2 $Zr_{0.5}Hf_{0.5}NiSn$/TiNiSn bilayer 115
7.4.3 Superlattices 119

8 Reduced thermal conductivity for superlattices measured by 3ω method **123**

8.1 Introduction 123
8.2 Thermal conductivity measured by the differential 3ω method 125
8.2.1 Temperature oscillations obtained by 3ω voltage 125
8.2.2 Measurement setup 128
8.2.3 The calculation of thermal conductivities 130
8.2.4 Layer stack for differential 3ω method 135
8.3 Thermal conductivities of TiNiSn, $Zr_{0.5}Hf_{0.5}NiSn$ and superlattices 140

9 Summary and Outlook **149**

Bibliography **153**

Declaration

Hiermit erkläre ich, dass ich die vorliegende Doktorarbeit selbstständig angefertigt habe. Es wurden nur die in der Arbeit ausdrücklich benannten Quellen und Hilfsmittel benutzt. Wörtlich oder sinngemäß übernommenes Gedankengut habe ich als solches kenntlich gemacht.

I hereby affirm that I wrote this work independently. Just specifically marked references and sources have been used for the thesis. Literally or analogously transferred ideas have been indicated as well.

Unterschrift:

TINO JÄGER

List of publications

Tino Jaeger, Christian Mix, Michael Schwall, Xeniya Kozina, Joachim Barth, Benjamin Balke, Martin Finsterbusch, Yves U. Idzerda, Claudia Felser and Gerhard Jakob; **Epitaxial growth and thermoelectric properties of TiNiSn and $Zr_{0.5}Hf_{0.5}NiSn$ thin films;** *Thin Solid Films 520; 1010–1014; (2011)*

Xeniya Kozina, Tino Jaeger, Siham Ouardi, Andrei Gloskowski, Gregory Stryganyuk, Gerhard Jakob, Takeharu Sugiyama, Eiji Ikenaga, Gerhard H. Fecher and Claudia Felser; **Electronic structure and symmetry of valence states of epitaxial NiTiSn and $NiZr_{0.5}Hf_{0.5}Sn$ thin films by hard x-ray photoelectron spectroscopy**; *Applied Physics Letters 99, 221908; (2011)*

Nina Vogel-Schäuble, Tino Jaeger, Yaroslav E. Romanyuk, Sascha Populoh, Christian Mix, Gerhard Jakob and Anke Weidenkaff; **Thermal conductivity of thermoelectric Al-substituted ZnO thin films**; *Phys. Status Solidi RRL 7; No. 5; 364–367; (2013)*

List of figures

Figure 1 2D figure of merit as a function of layer thickness of Bi_2Te_3 **1**

Figure 2 TE generator embedded into a BMW **2**

Figure 3 Record *ZT* value of 2.4 **4**

Figure 5 TE module **8**

Figure 6 TE generator based on a thin film **9**

Figure 7 TE generator based on thin film VFe_2Al (in-plane) **10**

Figure 8 Seebeck coefficient, conductivity, thermal conductivity, power factor and figure of merit as a function of carrier concentration **11**

Figure 9 Efficiency for varied *ZT* values as a function of temperature difference **12**

Figure 10 HH crystal structure, atomic positions and the origin in PSE **14**

Figure 11 Calculated band structure and density of states of TiNiSn **16**

Figure 12 *ZT* as a function of temperature for $Zr_{0.5}Hf_{0.5}NiSn$ and TiNiSn **17**

Figure 13 Dispersion relation for acoustic phonons **22**

Figure 14 Dispersion relation for two atoms **23**

Figure 15 Calculated influence of semiconducting behavior on thermal conductivity of ZrNiSn **25**

Figure 16 N- and U-processes as possible scattering events for phonons **26**

Figure 17 Thermal conductivities for TiNiSn and $Zr_{0.5}Hf_{0.5}NiSn$ **27**

Figure 18 Thermal resistivity as a function of disorder **28**

Figure 19 Electron mobility and phonon MFP due to grain sizes in $Zr_{0.5}Hf_{0.5}NiSn$ **30**

Figure 20 Heat conductivity calculated as a function of SL periodicity **32**

Figure 21 Thermal conductivity, phonon MFP and cut-off frequency for Bi_2Te_3/Sb_2Te_3 SLs as a function of SL period thickness **33**

Figure 22 Thermal conductivity of $Si/Si_{0.7}Ge_{0.3}$ and ZrN/ScN SLs as a function of periodicity **34**

Figure 23 Favored shape of electron states in a TE material **46**

Figure 24 Broadening of the Fermi-Dirac distribution due to ΔT **47**

Figure 25 Favorable DOS for a material suitable for TE application **48**

Figure 26 Degeneracy of $PbTe_{0.85}Se_{0.15}$ **49**

Figure 27 XRD $\theta/2\theta$ and XRR scans of TiNiSn layers **53**

Figure 28 Φ-scan of TiNiSn layers on MgO and Al_2O_3 substrates **55**

Figure 29 XRD $\theta/2\theta$ and XRR scans of $Zr_{0.5}Hf_{0.5}NiSn$ layers **56**

Figure 30 XRD $\theta/2\theta$ scan of a $Zr_{0.5}Hf_{0.5}NiSn$/TiNiSn bilayer **57**

Figure 31 RBS spectra and fit of a $Zr_{0.5}Hf_{0.5}NiSn$/TiNiSn bilayer **59**

Figure 32 MgO/TiNiSn interface measured by an EDX line scan **61**

Figure 33 AFM images taken from two $Zr_{0.5}Hf_{0.5}NiSn$/TiNiSn bilayers **64**

Figure 34 Schematic illustration of a potential cross-plane measurement **66**

Figure 35 Alignment of thin film vanadium on MgO (100) **67**

Figure 36 XRD $\theta/2\theta$ scan of 300 nm vanadium sputtered on MgO (100) **70**

Figure 37 AFM images from thin film vanadium deposited on MgO (100) **71**

Figure 38 XRD $\theta/2\theta$ and XRR scans of vanadium with a thickness of 10 nm **73**

Figure 39 Rocking curve thin film vanadium **75**

Figure 40 XRD $\theta/2\theta$ scan and rocking curve of a TiNiSn layer deposited on a thin vanadium buffer layer **77**

Figure 41 XRD $\theta/2\theta$ scan of a TiNiSn/ $Zr_{0.5}Hf_{0.5}NiSn$/vanadium layer stack **78**

Figure 42 XRD $\theta/2\theta$ scan of polycrystalline $Zr_{0.5}Hf_{0.5}NiSn$ grown on Si (100) by using a 10 nm vanadium buffer layer **80**

Figure 43 EDX line scan and HAADF-STEM image taken from a SL **83**

Figure 44 XRD $\theta/2\theta$ scans of SLs grown different substrate temperatures **85**

Figure 45 HAADF-STEM images of SLs with periodicities of 21 nm and 3 nm **88**

Figure 46 XRD $\theta/2\theta$ scan and simulation of a SL **89**

Figure 47 AFM image and XRD $\theta/2\theta$ scan of a SL **90**

Figure 48 SLs with and without a vanadium buffer layer **91**

Figure 49 Calculated MFP for electrons **92**

Figure 50 XPS spectrum taken of a natively oxidized aluminum capping layer **94**

Figure 51 HAXPES survey spectra taken with a photon energy of 6 keV **95**

Figure 52 Enlarged HAXPES spectra focused on E_B up to 480 eV **97**

Figure 53 VB spectra for TiNiSn and $Zr_{0.5}Hf_{0.5}NiSn$ prepared as bulk materials **98**

Figure 54 VB spectra of thin film TiNiSn and $Zr_{0.5}Hf_{0.5}NiSn$ **99**

Figure 55 Comparison between VB spectra of TiNiSn and a multilayer system containing TiNiSn/$Zr_{0.5}Hf_{0.5}NiSn$/TiNiSn **100**

Figure 56 VB spectra of a SL measured with s- and p-polarized X-rays **101**

Figure 57 Seebeck coefficient, specific resistivity and power factor of TiNiSn and $Zr_{0.5}Hf_{0.5}NiSn$ thin films **106**

Figure 58 Hall measurements taken from TiNiSn and $Zr_{0.5}Hf_{0.5}NiSn$ **108**

Figure 59	Specific resistivities and Seebeck coefficients for TiNiSn at HT	**112**
Figure 60	XRD $\theta/2\theta$ scans and a picture taken from the TiNiSn sample surface after HT Seebeck treatment	**113**
Figure 61	Seebeck coefficient, specific resistivity, power factor and *ZT* of TiNiSn bulk samples (Birkel et. al.; Ref. 206)	**114**
Figure 62	Up to different temperatures, three cycles of HT TE measurements conducted with a $Zr_{0.5}Hf_{0.5}NiSn$/TiNiSn bilayer	**116**
Figure 63	XRD $\theta/2\theta$ scans of a $Zr_{0.5}Hf_{0.5}NiSn$/TiNiSn bilayer measured before and after HT TE measurements	**117**
Figure 64	HT Seebeck measurements of SLs measured up to 550 K and 850 K	**119**
Figure 65	XRD $\theta/2\theta$ scan of a SL measured before and after a HT TE measurement with a maximum temperature of 550 K	**120**
Figure 66	XRD $\theta/2\theta$ scans of a SL measured before and after a HT TE measurement with a maximum temperature of 850 K	**121**
Figure 67	XRD $\theta/2\theta$ scan of a TiNiSn layer, a SL and a $Zr_{0.5}Hf_{0.5}NiSn$/TiNiSn bilayer done after the HT TE measurements (enlarged)	**122**
Figure 68	Heater structure for measuring thermal conductivity with 3ω method	**126**
Figure 69	Schematic assembly of the 3ω measurement setup (bridge circuit)	**129**
Figure 70	Applied power calculated by voltage and current oscillations	**131**
Figure 71	Real and imaginary part of the $U_{3\omega}$ voltage and temperature oscillation as a function of applied frequency (Calculation of $\mathrm{d}R\mathrm{d}T^{-1}$)	**133**
Figure 72	The color of alumina as a function of layer thickness	**135**
Figure 73	AFM image of a layer stack intended for 3ω measurement	**136**
Figure 74	Temperature oscillations simulated for different heater structures	**137**
Figure 75	Variation of film thicknesses in two $Zr_{0.5}Hf_{0.5}NiSn$ films	**138**
Figure 76	XRR scan to determine the layer thickness of alumina	**139**
Figure 77	As measured, $\Delta T' = f(\ln(2\omega)$ for TiNiSn, $Zr_{0.5}Hf_{0.5}NiSn$ and SLs	**142**
Figure 78	Calibrated, $\Delta T = f(\ln(2\omega)$ for TiNiSn, $Zr_{0.5}Hf_{0.5}NiSn$ and SLs	**143**
Figure 79	Thermal conductivity of TiNiSn, $Zr_{0.5}Hf_{0.5}NiSn$ and a variety of SLs with periodicities from 6.6 nm to 55 nm	**146**

List of tables

Table 1 TiNiSn bulk samples and *ZT* values at given temperatures **18**

Table 2 Transport parameters included in Onsager reciprocal relations **43**

Table 3 Summarized atomic compositions of TiNiSn and $Zr_{0.5}Hf_{0.5}NiSn$ films **63**

Table 4 Electron mobilities / electron densities for TiNiSn and $Zr_{0.5}Hf_{0.5}NiSn$ **109**

Table 5 Thicknesses of various deposited films measured at different substrate positions **138**

Abbreviations

AFM	Atomic Force Microscopy
BZ	Brillouin zone
CB	conduction band
DOS	density of states
EDX	Energy-Dispersive X-ray
EMPA	Eidgenössische Materialprüfanstalt
fcc	face centered cubic
FWHM	full width half maximum
HAADF	High-Angular Annular Dark Field
HAXPES	Hard X-ray Photoelectron Spectroscopy
hcp	hexagonal close-packed
HH	half-Heusler
HT	high temperature
LASER	Light Amplification by Stimulated Emission of Radiation
LED	Light-Emitting Diodes
MBE	Molecular Beam Epitaxy
MFP	mean free path
ML	monolayer
PES	Photoelectron Spectroscopy
PPMS	physical property measurement system
PTE	periodic table of elements
RBS	Rutherford Backscattering
RT	room temperature
SC	semiconductor
SPS	Spark Plasma Sintering
STEM	Scanning Transmission Electron Microscopy
TE	thermoelectric
UHV	ultra-high vacuum
VB	valance band
XPS	X-ray Photoelectron Spectroscopy
XRD	X-ray Diffraction
XRR	X-ray Reflectometry

Chapter 1

Introduction

Since 1993, when L. D. Hicks and M. S. Dresselhaus published a theory about confined systems and their effect on the thermoelectric (TE) figure of merit *ZT*,[1] nano-engineering of TE materials has moved into focus. With about 600 citing articles it is representing one of the most famous articles in the field of TE.

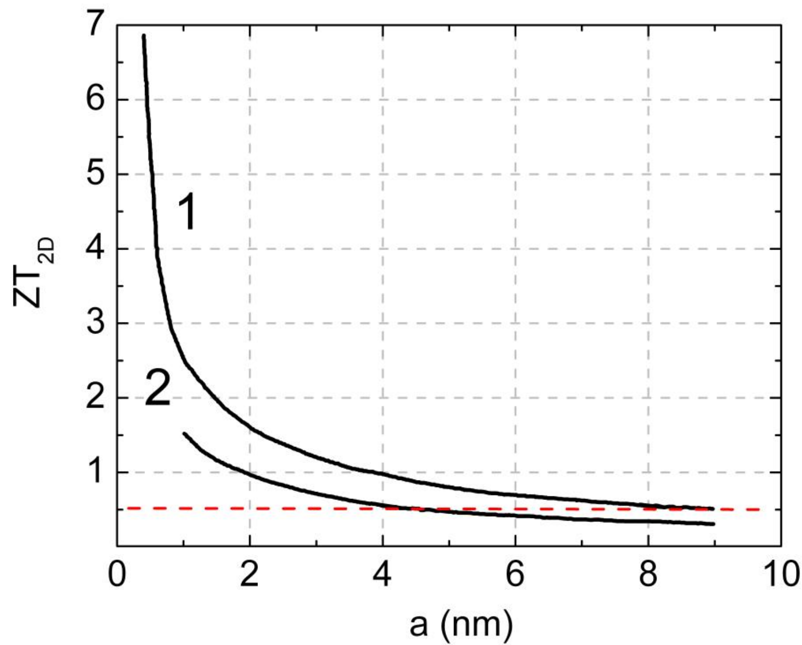

Figure 1 2D figure of merit $Z_{2D}T$ calculated along a_0 as a function of layer thickness *a* of Bi_2Te_3 having a 2D a_0-b_0 (1) and a_0-c_0 (2) plane; The dashed line represents *ZT* of Bi_2Te_3 bulk material. (Adapted from Ref. 1)

Calculations revealed an opportunity of increasing *ZT* of Bi_2Te_3 by a factor of 13 if the electrons are confined in a 2D system. Therefore, Bi_2Te_3 as a narrow band semiconductor (SC) must be grown in a multilayer system with an appropriate material that prevents electrons from the Bi_2Te_3 layer to enter. Without considering tunneling effects, the 2D electron confinement in the Bi_2Te_3 layer causes the extraordinary enhancement of *ZT* that illustrates suitability of a material for TE applications. Bi_2Te_3 exhibits the highest electron mass and mobility along c_0- and a_0-axis, respectively. Due to the anisotropy much higher *ZT* values are calculated if the a_0-b_0 plane is confined (Figure 1).

But material research about TE materials is much older than this rather recent trend in downsizing and was manly done in the former Soviet Union and in the United States of America. Here, applications in military, astronautics (cosmonautics) and other heavy machinery as tractors or locomotives were in focus. Today, research in TE generators undergoes a renaissance. Due to the European Parliament and their resolution in 2007 about threshold values for the average vehicle fleet CO_2-emission of single companies (130 gkm^{-1} by 2015 and 95 gkm^{-1} by 2020), enhanced efforts have been done to reduce the fuel consumption of their cars.

Figure 2 TE generator embedded into a BMW[I]

The energy in terms of gas burned in a vehicle can be divided into three parts:

Actual driving (including all devices)	30 %
Parasitic losses (friction, distributed heat)	30 %
Exhaust-gas heat	40 %

To recover the huge amount of energy leaving the exhaust pipe has been a big challenge for car industry. So close to the engine a TE generator has been adapted into the exhaust pipe (Figure 2). In the case of upper class cars equipped by a huge engine sufficient energy has been generated at high speed.[II] Aspired 800 W were not reached for smaller cars with less fuel consumption. Additionally, worldwide the majority of driving is done at reduced speed within towns. There exhaust fumes are colder and the aspired power has

[I] Talk given by Harald Böttner at the Johannes Gutenberg Universität (02/2009) about 'Survey on High Temperature Thermoelectric Materials, Modules, and Applications'
[II] Results presented in the talk 'Heat Recovery in the vehicle' from J. Kitte at the Thermoelectric Spring School, April 1st 2011

been missed by far. So, TE generators are still not ready for the market and electric generators are providing the electric power in vehicles.

Among others, improved material properties of the TE materials enable one opportunity to increase the efficiency. So, more applications become feasible. For sake of completeness, biggest advantages and crucial difficulties of TE generators are addressed at this point. Rather than in thermal engines, no moving parts are included in TE generators. So, its low-maintenance makes a TE generator sometimes to be the method of choice. But going to higher temperatures for obtaining also higher temperature differences reveals the difficulty. Often the electrical contacts between TE material and metal but also the thermal connection to heat and cooling sources can become brittle with time. Especially, TE generators that have to last cycles with high temperature (HT) differences suffer the most and the fabrication for sustainable TE generators becomes challenging.[I]

To overcome challenges about stability and efficiency of the TE materials research is going on for a while. So new materials as nano-structured oxides,[2] but also half-Heusler (HH) materials,[3] appear frequently until now. The latter one in the forms of TiNiSn and $Zr_{0.5}Hf_{0.5}NiSn$ are studied in this work. Recently, Poon et. al. have started to build devices utilizing HH materials.[4] Based on doped $Zr_{1-x}Hf_xNiSn_{1-x}Sb_x$ they were capable to fabricate a heat-to-electric power generator with an overall efficiency of 8.7 %. Power output, hot side temperature and temperature difference were 380 mW, 697°C and 657°C, respectively. For this reason, Poon et. al. claimed to have a better performance than obtained by conventional PbTe devices.

By utilizing InSb nanoinclusions, Xie et. al. have reduced the thermal conductivity of $Ti_{0.5}Zr_{0.25}Hf_{0.25}Co_{0.95}Ni_{0.05}Sb$ by almost 25 %.[5] Interestingly, smallest grain sizes of about 30 nm showed the highest reduction in thermal conductivity without destroying the excellent electrical behavior of the HH materials. For Ti_2O particles embedded in $TiFe_xCo_{1-x}Sb$ similar results have been obtained.[6] Simultaneously, the material system represents a further advantage of HH materials that is needed for TE devices. Among others, $TiFe_xCo_{1-x}Sb$ shows n-type as well as p-type behavior for $x = 0$ and $x = 0.15$, respectively. Therefore n- and p-type materials with similar thermal expansion

[I] Paul van der Sluis (Philips Research Eindhoven) presented 'Thermoelectric generators in woodstoves and their reliability' at the 'TE winter school 2010' (Bremen). The efficiency of a woodstove is significantly enhanced if air is blown into the combustion chamber. This process was planned to be powered by a TE generator.

coefficients can be assembled. By exchanging small amounts of titanium by scandium, a p-type compound, similar to TiNiSn, can also be obtained. [7] To get sufficient performance, TE devices have to be assembled by p- and n-type TE materials. Because both types are connected parallel between the hot and the cold end, a similar thermal expansion is of absolute importance to prevent cracks in the device. These cracks contribute to the lifetime of TE devices. Beside high efficiencies, this leads to a further advantage of HH materials. By exchanging only a few atoms, HH compounds can be p- and n-doped.

In 2001 a further publication in the field of TE has attracted attention far above-average. [8] By now, more than 1600 citations have been created by the highest ever published efficiency for a TE material system. The efficiency of a TE material depends on the dimensionless *ZT* that is given by a material dependent parameter *Z* and the temperature *T*. A more detailed explanation will be given in chapter 2.2.

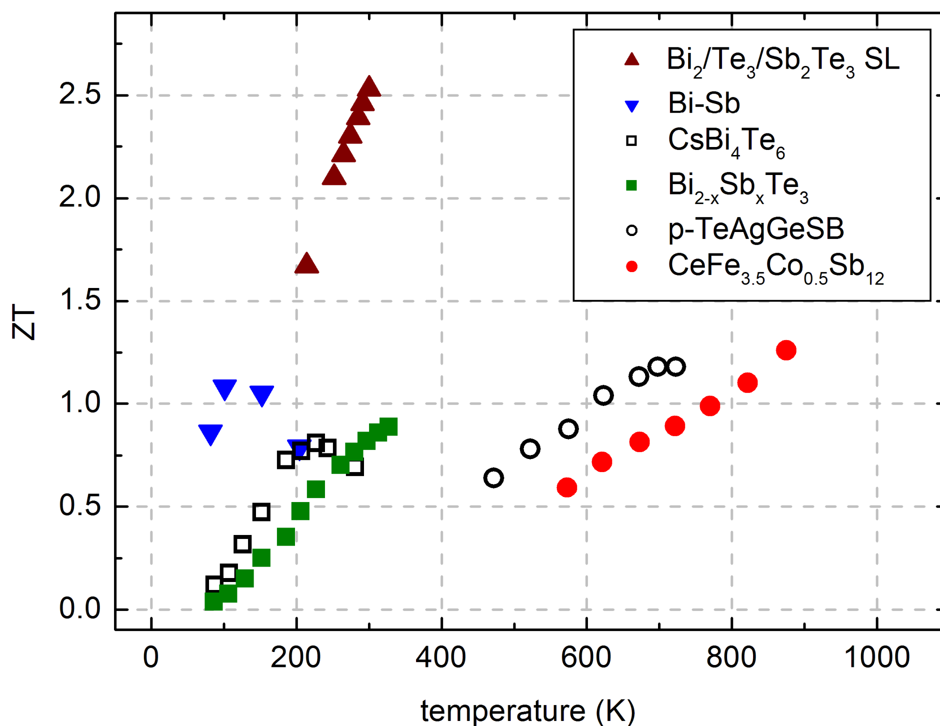

Figure 3 Record *ZT* value of 2.4 measured for p-type Bi_2Te_3/Sb_3Te_3 superlattices . (Adapted from Ref. 8)

To obtain the room temperature (RT) record *ZT* value that exceeds other material systems by far (Figure 3), Venkatasubramanian et. al. have grown p-type superlattices containing Bi_2Te_3 and Sb_2Te_3. For optimizing the superlattice (SL) concerning phonon-blocking and electron-transmission, measurements have been performed perpendicular to

the interface (cross-plane). Due to interaction between mean free path (MFP) for phonons and electrons that need to be depressed and kept rather unchanged by the interfaces, respectively, for the Bi_2Te_3 and Sb_2Te_3 layers thicknesses of 10 Å and 50 Å have been found ideal.

For the thermal management of an infrared detector, Bulman et. al. have fabricated TE microcoolers.[9] Beside p-type SLs mentioned above, n-type SLs containing Bi_2Te_3 and $Bi_2Te_{2.7}Sb_{0.3}$ have been integrated into a three cascade stage with a TE leg length and an overall thickness of ~10 µm and 2.5 mm, respectively. One three stage cascade consists of three couples in the first row. To enhance the efficiency, amount and size of TE couples varies in different stages. Here, the quantity decreases in the direction of cooling. Finally, with a total current of 4 A a plate with a size of 19 mm x 38 mm has been cooled from RT down to minus 75°C. A maximum heat pumping and input power of 0.54 W and 29.3 W have been calculated. It results in an efficiency of 1.84 %. Compared to former bulk devices, an equal performance has been reached by using less TE material.

As it is true for bulk applications, it is also right for thin film applications: increasing their efficiency or/and lowering their price increases the fields of application. To do so, in this work nanostructured HH material are under investigation. Therefore, SLs containing TiNiSn and $Zr_{0.5}Hf_{0.5}NiSn$ have been made. As a bottom up approach, the SLs have been grown by magnetron sputter deposition. For fabrication the substrate has been driven back and forth between simultaneously burning magnetron sputter cathodes. As it has been demonstrated above, for the Bi_2Te_3/Sb_2Te_3 SLs a reduced thermal conductivity shall be reached for cross-plane application. So, besides introducing HH materials, an introduction into TE effects will be given in the next chapter that for example clarifies the correlation between ZT and the thermal conductivity. Here atomic masses from titanium, zirconium and hafnium of 47.88 u, 91.22 u and 178.49 u,[10] respectively, play the key role in the reduction of cross-plane thermal conductivity. Starting from a simple model, a state-of-the-art discussion about scattering in bulk materials as well as in SLs is given in chapter 3. Besides thermal conductivity, electronic properties are of importance. Based on several models, linkage and origin of the electronic properties in TE materials will be explained in the following. The main part of this thesis starts with chapter 4. Here, results about structural properties as composition and surface morphology will be given for single TiNiSn and $Zr_{0.5}Hf_{0.5}NiSn$ films. In chapter 5, results obtained for thin films grown on an additional vanadium buffer layer are shown. Besides an increased HH film quality, the vanadium buffer layer is a potential candidate as back electrode for cross-plane

applications. The opportunity of fabricating SLs containing TiNiSn and $Zr_{0.5}Hf_{0.5}NiSn$ is presented in chapter 6. Next to X-ray Diffraction (XRD) pattern, X-ray Absorption Spectroscopy (XAS) is used to demonstrate the sustainment of film quality for the HH SLs. For showing semiconducting and TE behavior of the single films and SLs, Seebeck and conductivity measurements are performed and illustrated in chapter 7. The measurements have been done in a temperature range between 50 K and 900 K. After giving a brief introduction in the principles of the 3ω method and its challenges, thermal conductivities of thin films and SLs are presented in chapter 8. Since the differential 3ω technique measures a thermal resistance (thin film) between a heater and infinity (substrate), due to its varied thermal conductivities, the measured material system containing HH thin films (low thermal conductivity) on MgO substrates (high thermal conductivity) is suitable. For the differential method two thin gold strips, fabricated on two samples that differ in film thickness, and their temperature oscillations are used to calculate the thermal conductivity of the varied films. Finally, summary and outlook are given in chapter 9.

Chapter 2

Half-Heusler materials in thermoelectrics

2.1 Thermoelectric effects and applications – a brief introduction

Since 1960, the human race conducts experiments at the edge of the universe. Because of insufficient sun radiation, photovoltaics cannot be used for energy supply. So, spacecrafts are utilizing radioactive materials whose decay heat lasts over decades. The temperature gradients between outer space and core of the spacecraft are exploited by TE effects.

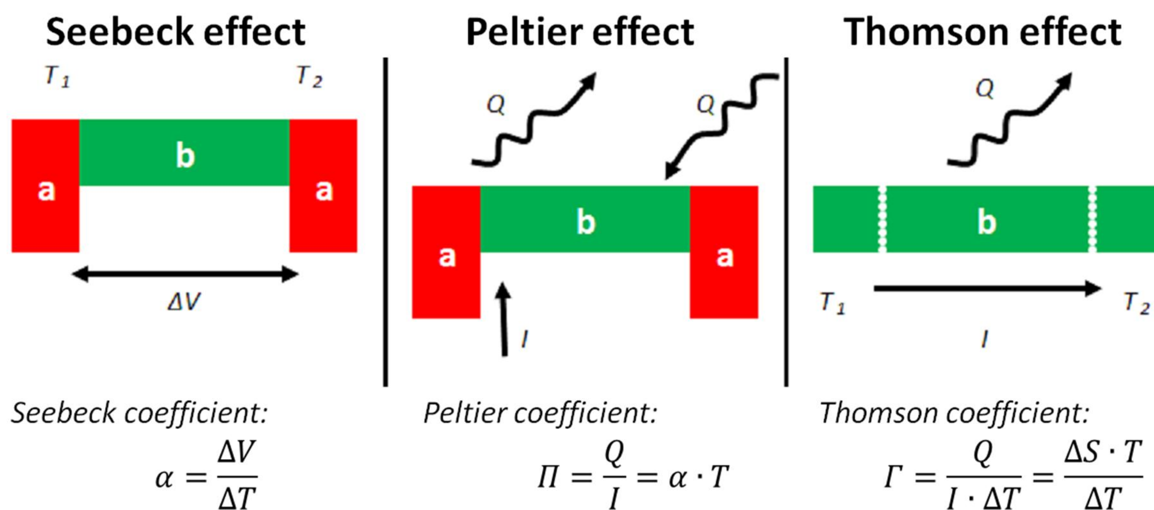

Figure 4 Illustration of Seebeck, Peltier and Thomson effect (Adapted from Ref. 11)

In 1821,[12] Thomas Johann Seebeck discovered that an applied temperature gradient ΔT along a proper material system a-b-a (Figure 4) causes an electric voltage ΔV or ΔU. Two metals (red) are kept at two different constant temperatures T_1 and T_2. The Seebeck coefficient α depends on the TE material b (green) and is used to connect temperature ΔT with voltage difference ΔV.

The reverse effect is called Peltier effect. Here, the Peltier coefficient Π is defined by the transported heat Q divided by the applied electric current I. Absorption and emission of heat take place at the interface towards the metal.[13] The specific area depends on the electron energy relaxation length that is typically between 200 nm and 400 nm.

Finally, the Thomson effect can be observed if an electrical current I flows along a temperature gradient ΔT. Then the Thomson coefficient Γ specifies the change in heat transported by I along ΔT. This effect plays a minor role, but as well as Joule heating, it influences the overall efficiency of a TE device.[14,15]

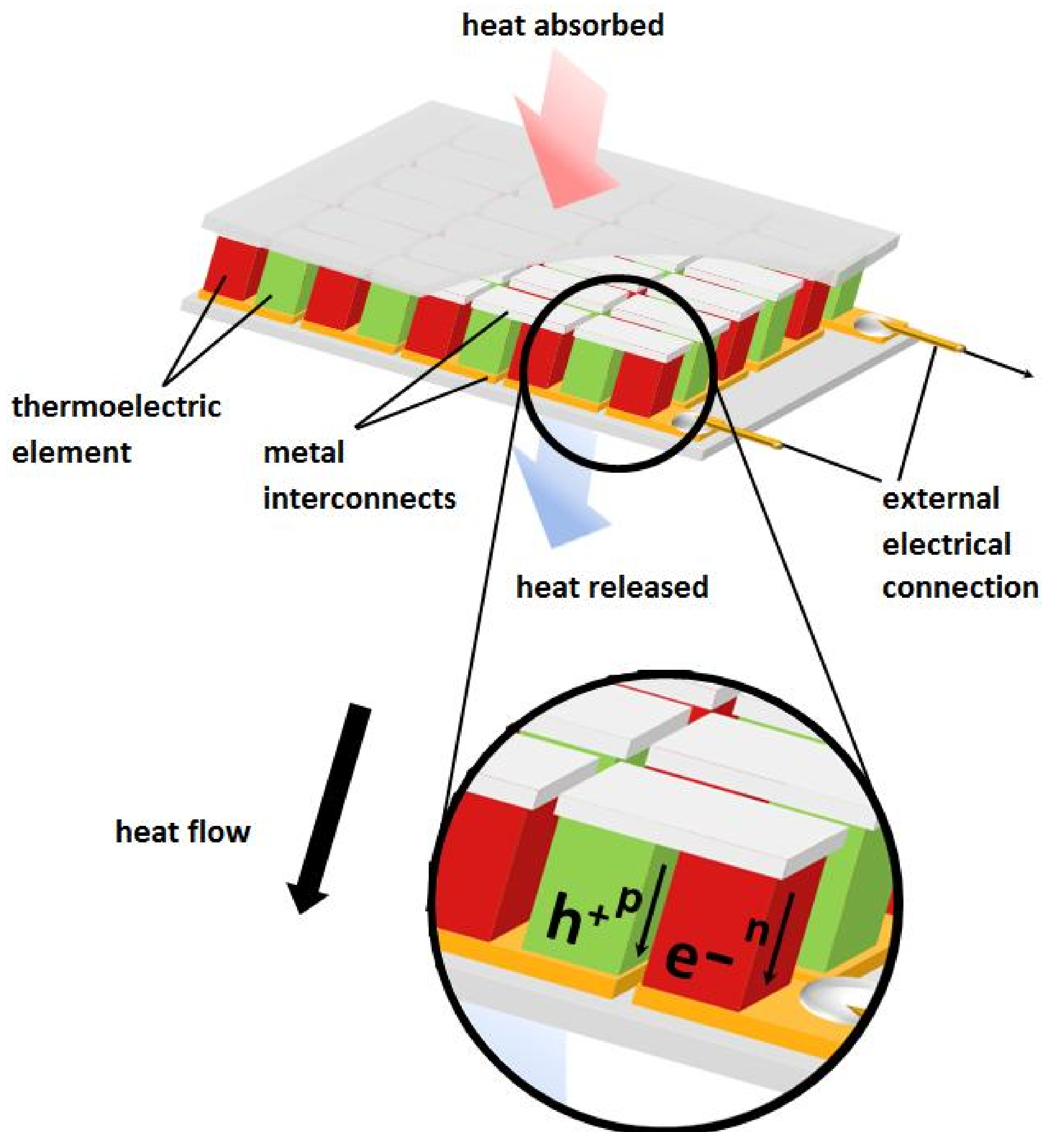

Figure 5 TE module (Adapted from Ref. 16)

The assembly of the TE module is shown in Figure 5. It contains a top and a bottom side made of electrically isolating but highly thermal conducting materials to ensure the thermal connection to the surrounding. In-between, metal contacts are attached so that n- and p- conducting TE materials are connected (see magnification). As it is illustrated, the existences of p-doped SCs enable a net current flow of electrons though several TE legs in series. Electrons having the properties of holes move through an almost filled valence band (VB). So, either individually generated voltages can be summed up if an

temperature gradient is applied (Seebeck effect) or in each leg heat is carried from one side to the other if an electric current is applied (Peltier effect).

Of course, nanostructured thin films are not suitable for macroscopic TE generators as schematically shown in Figure 5. Those have dimensions in the order of centimeter and are driven by a few watts. But where the technology goes to, can be seen in Figure 6. Micropelt GmbH Freiburg has started the commercial usage of their 'two-wafer-concept'.[17] On top of metallic contact structures, Bi_2Te_3 related p- or n-type materials and solder is sputtered on a Si/SiO_2 wafer. After the final structures are obtained by dry etching (Figure 6) both wafers are bonded together. By applying this technique, TE pairs with a density of 7200 cm^{-2} can be realized. Despite smallest dimensions of 1666 µm x 832 µm and a total thickness of 1090 µm, temperature differences of about 40 K can be generated by 0.3 W.

Using a single barrier heterostructure consisting of InGaAsP, A. Shakouri et. al. obtained a temperature difference of 1 K for an area of 90 µm x 180 µm and heights of 1µm.[18]

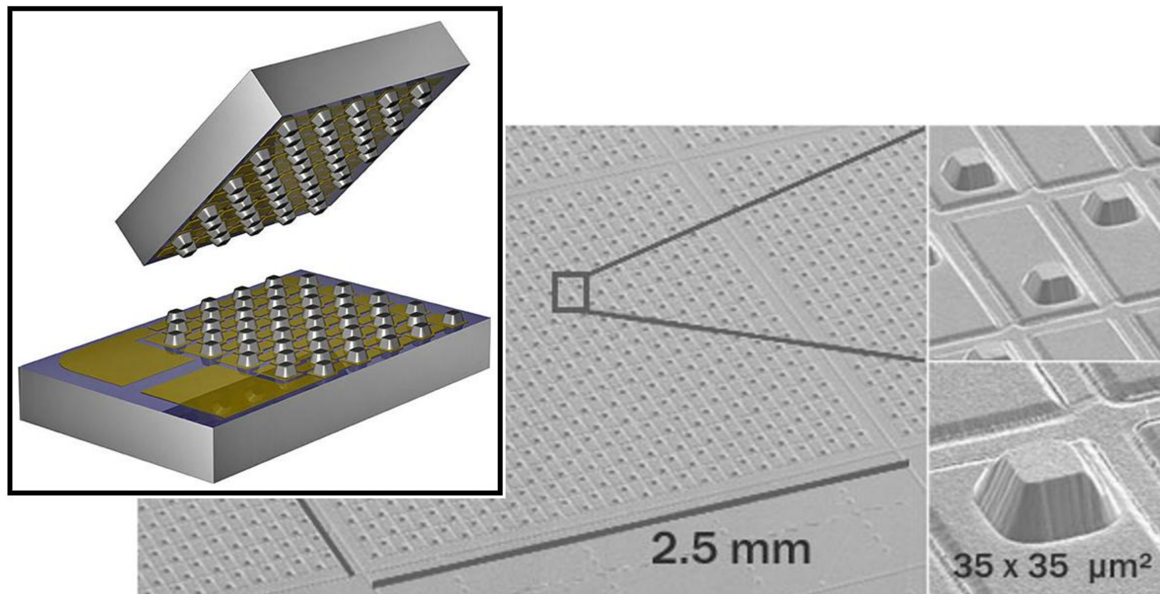

Figure 6 Schematic assembly and Scanning Electron Microscope (SEM) image of a TE generator[I]

For in-plane usage, thin legs containing p-type $Bi_{0.4}Sb_{1.6}Te_3$ and n-type Bi_2Te_3 have been fabricated by Metal Organic Vapor Deposition (MOCVD).[19] Instead of $Bi_{0.4}Sb_{1.6}Te_3$, electrodeposited Sb_2Te_3 has been used by others.[20] So in-plane, temperature

[I] Copyright Micropelt GmbH

differences separated by the length of the parallel aligned p- and n-type legs can be generated. Vice versa, just small amounts of TE material must be deposited to obtain powers in the order of µW.[21] Similar structures have been deposited on flexible polyimide Kapton® substrates with a thickness of 12 µm.[22] Others have fabricated one pair of TE legs that is sufficient for a precise temperature measurement.[23]

Less sophisticated but using Heusler materials,[24] in 2007 Masumoto et. al. have published a TE module showing the potential application of the material class. The assembly of n- and p-type material containing pure and Si-doped VFe_2Al, respectively, can be extracted in Figure 7. With a film thickness of about 4 µm and applying a temperature difference from 343 K to 313 K resulted in an electric voltage of 31 mV. Divided by 30 K and 16 legs, it results in an average Seebeck coefficient of about 65 μVK^{-1}.

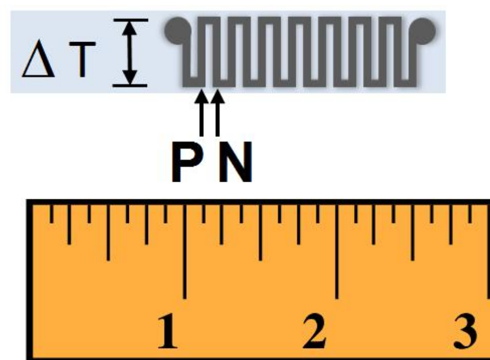

Figure 7 Eight pairs of n-type VFe_2Al and Si-doped p-type VFe_2Al
(Adapted from Ref. 24)

Beside well known bulk application that still fill niche applications, the miniaturization opens new fields for TE devices using thin film technology. Next to self-sufficient sensors that are using a surrounding temperature gradient for measuring and sending a physical property,[17] thermal on-chip temperature controlling moves into focus.[25] The increasing number of heat density in processors could be actively cooled right at the hot spots.[26,27] Additionally, temperature stabilization for solid state LASERs and their emitting frequency can be done.[28]

2.2 *ZT* – the figure of merit in the field of thermoelectrics

Although changing the shape of the TE material in a TE generator can also influence the efficiency,[29] the current focus is set on material parameters as Seebeck coefficient α, conductivity σ and thermal conductivity κ. Because heat can be transferred either by the

lattice κ_{ph} or by free electrons κ_{el}, the thermal conductivity can be split into parts. Taking into account the temperature T, these material properties are combined by the figure-of-merit ZT to assign material to be suitable for TE applications:[30]

$$Z \cdot T = \frac{\alpha^2 \sigma}{\kappa} \cdot T = \frac{\alpha^2 \sigma}{\kappa_{ph} + \kappa_{el}} \cdot T \qquad 2.1$$

For measuring Seebeck coefficients (see Figure 4) as well as thermal conductivities a temperature gradient must be applied. Here, measured values are assigned to an average temperature of a sample. $\alpha = f(T)$ and $\kappa = f(T)$ are obtained by driving a temperature gradient though a certain temperature range.

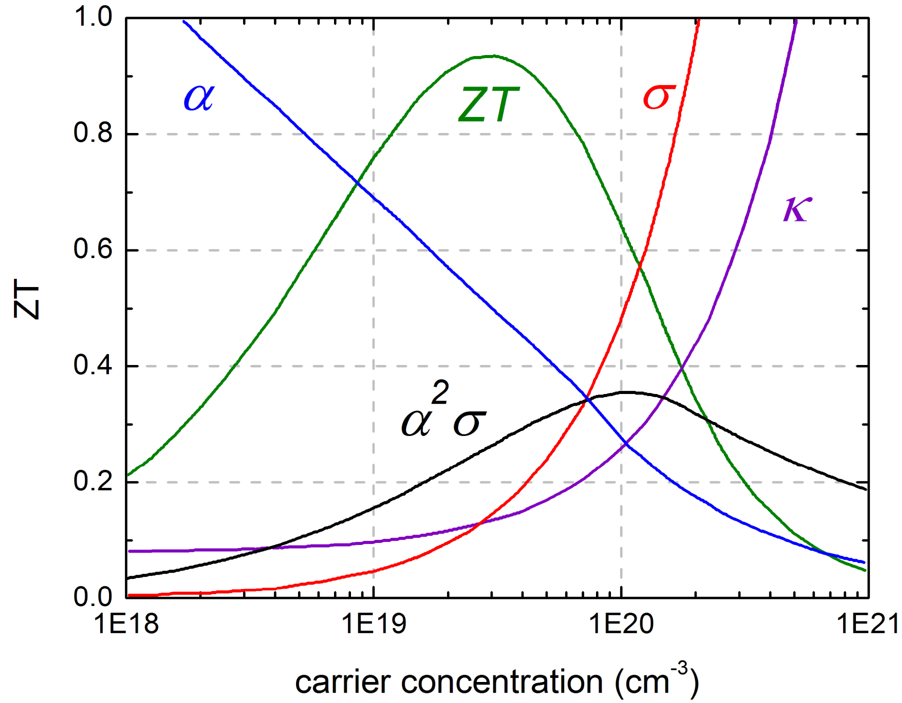

Figure 8 Seebeck coefficient α, conductivity σ, thermal conductivity κ, power factor $\alpha^2\sigma$ and figure of merit ZT as a function of carrier concentration (Adapted from Ref. 16)

Based on variously doped Bi_2Te_3, in Figure 8, TE properties α (blue), σ (red) and κ (purple) are calculated. So, quantitatively the ordinate goes from zero to 500 μVK^{-1}, 5000 $\Omega^{-1}cm^{-1}$ and 10 $Wm^{-1}K^{-1}$, respectively. While the conductivity increases at higher electron concentrations, the Seebeck coefficient decreases simultaneously. Calculating $\alpha^2\sigma$ combines the electrical coefficients and is called power factor (black). Due to the thermal conductivity that rises at enhanced electron densities, the maximum of the ZT (green) shifts to smaller electron densities. Beside Figure 8, a semi-classical treatment that will be shown in chapter 3.2.2 can be used to demonstrate the connection of the TE

parameters. It demonstrates the challenge of optimizing one parameter without degrading another one. But theoretically, an upper limit for *ZT* has not been found.[31]

In the case of anisotropic materials, material properties have to be measured along identical directions. If an identical sample is used for subsequent measurements, remained sample quality before and after single measurements should be assured. If different samples are used for measuring several properties, sample fabrication and quality must be as similar as possible. Ignoring these principles can distort *ZT* tremendously.

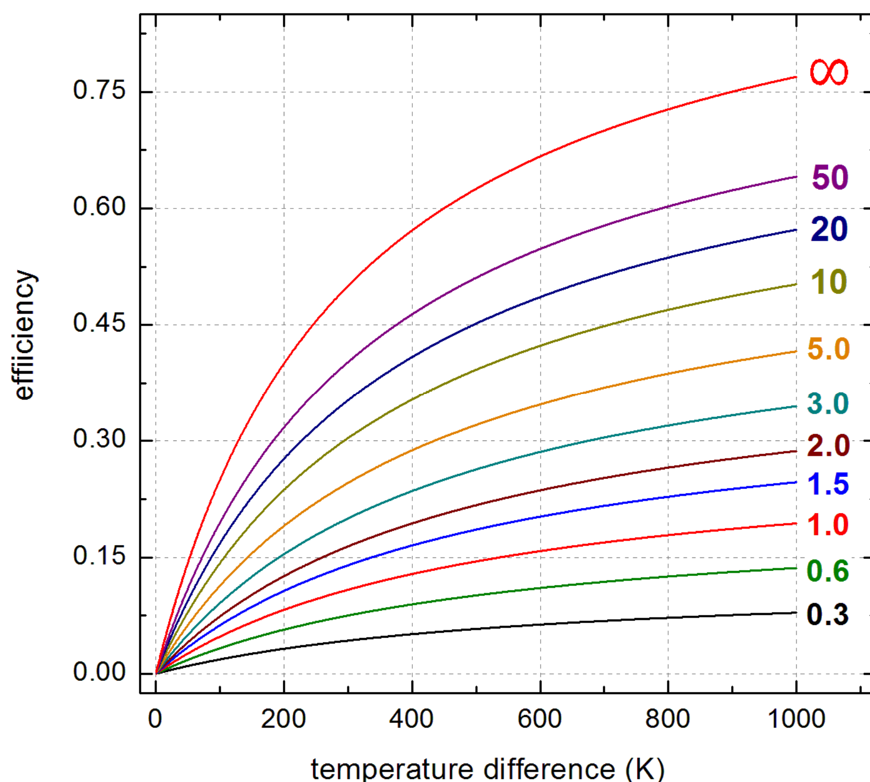

Figure 9 Equivalent to Eq. 2.2, for varied *ZT* values (colored numbers) the efficiency is plotted as a function of temperature difference. The cold side temperature is set to 300 K.

Using *ZT* and the temperatures at the hot T_h and the cold side T_c of TE material, for the efficiency η it can be written:[16]

$$\eta = \frac{T_h - T_c}{T_h} \cdot \frac{\sqrt{1+ZT}-1}{\sqrt{1+ZT}+\frac{T_c}{T_h}} \qquad 2.2$$

As one easily can see, the efficiency of a TE material is composed of two products. The former is equal to the Carnot efficiency and the latter incorporates the material specific behavior including the dimensionless *ZT*. Having a fixed cold side temperature of 300 K, the efficiency as a function of temperature difference $(T_h - T_c)$ is shown in Figure 9.

Different curves correspond to different *ZT* values (colored numbers). The efficiency goes up if either higher temperature differences or higher *ZT* values are applied. For $ZT = \infty$ the Carnot efficiency is reached. Currently, *ZT* values of about 1 are obtained by p- and n-type materials.[32,33] It can be taken from Figure 9 that further developments in efficiency become more difficult. But as already mentioned in the introduction, not only high *ZT* values are essential for implementing new TE materials into modules.[34] To replace established energy conversion systems, $ZT > 4$ must be obtained.[13] Additional losses in TE generators are not considered.

2.3 Formation of half-Heusler materials

In 1970, W. Jeitschko was one of the earliest scientists publishing about TiNiSn.[35] Without mentioning TE application, he fabricated TiNiSn by arc melting. Due to XRD analyses, TiNiSn was assigned to MgAgAs structure with a lattice constant of 5.941 Å.

Figure 10 illustrates the crystallization of HH compounds in the space group of zinc blende ($F\bar{4}3m$). Four interpenetrating face centered cubic (fcc) unit cells, each shifted one fourth of the unit cell along the diagonal is probably the most demonstrative structural description. Similar to the rock salt structure, least and most electronegative elements are generally forming X (1/2;1/2;1/2) and Z (0;0;0) position, respectively. In the center of the rock salt structure, forming tetrahedral zinc blende structure with Z position, Y can be found at (1/4;1/4;1/4) position.[I] For TiNiSn ($Zr_{0.5}Hf_{0.5}NiSn$), titanium (zirconium and hafnium), nickel and tin can be addressed to X, Y and Z. Concerning the corresponding full-Heulser Ni_2TiSn, it would be more consistently (Figure 10) to label Y_2 as the vacant fcc lattice or to name it NiTiSn, as is has been done by others.[36] Early calculations have shown that the missing nickel atom is essential in changing the compound from a metal to a SC.[37]

As it is known from classical SC physics, the valence electrons have to fill the last occupied electron band (valence band) to make a material semiconducting or isolating depending on the energetic gap to the next unoccupied energy band (conduction band). Similar to GaAs that is a III-VI SC, there are HH compounds formed by main group

[I] Giving the atomic positions of TiNiSn, ZrNiSn and HfNiSn, *Pearson's handbook of crystallographic data for intermetallic phases* refers to Jeitschko et. al..[35] While Jeitschko et. al. defines identical positions as given here, *Pearson's handbook of crystallographic data for intermetallic phases* has done a mistake while copying the data.

elements that have to have eight valence electrons to fill the VB.[38] For LiMgAs, one can sum up one, two and five electrons for lithium, magnesium and arsenic, respectively. It can be assumed that there is a sp^3-hybridisation between magnesium and arsenic that are forming the zinc blende structure. Since valence states from lithium lie above the bonding sp^3-states, there is an electron transfer leading to $Li^+[MgAs]^-$. The difference in bonding and anti-bonding states determines the energy gap between the filled VB and the empty conduction band (CB).

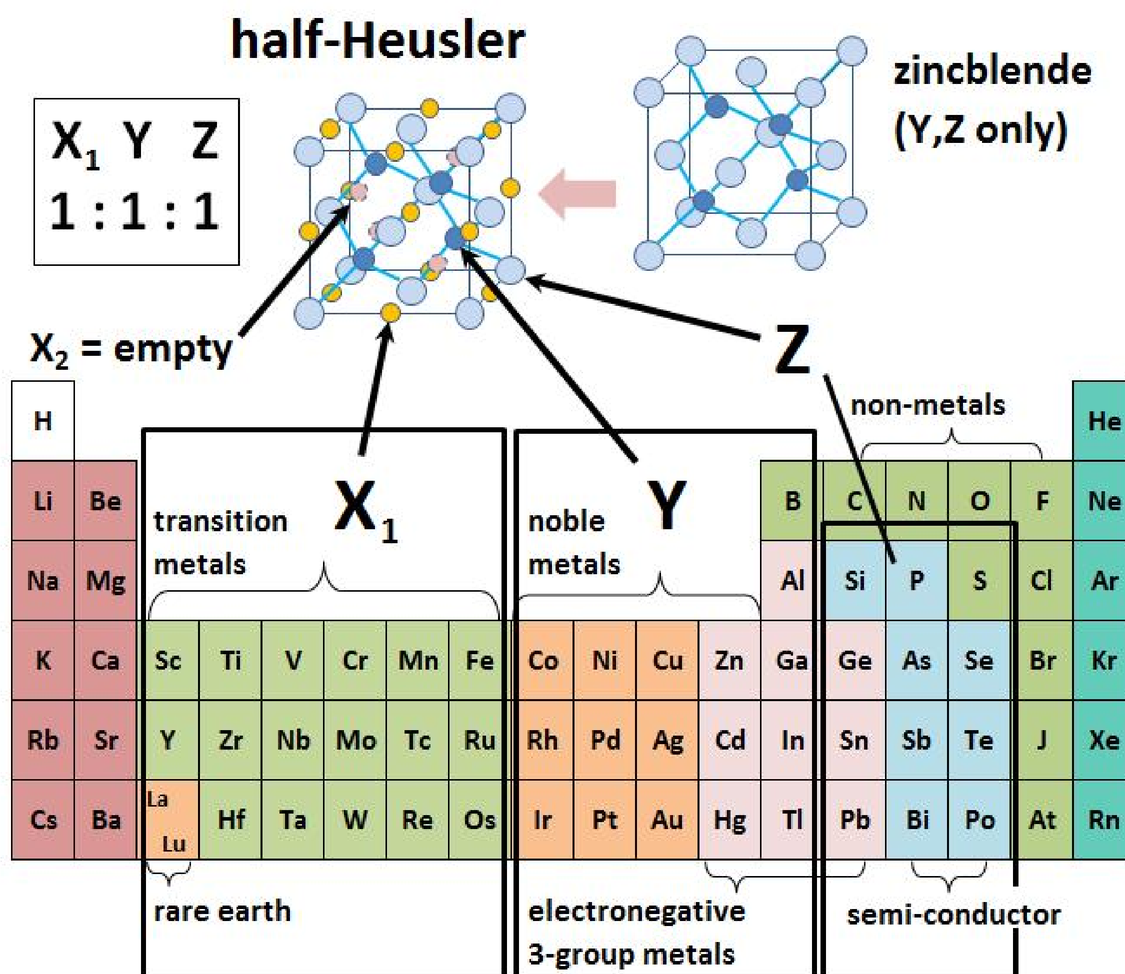

Figure 10 HH crystal structure, atomic positions and the origin in the periodic table of elements (PTE) (adapted from Ref. 39)

Due to d-band valence states for titanium and nickel the issue becomes more difficult for TiNiSn.[40] Because of their similarity in electronegativity, nickel (1.91) and tin (1.96) are forming covalent bonds within a zinc blende structure. Other than for LiMgAs, the 5s and 5p states that are empty for nickel and partially filled for tin are forming bonding a_1 and triple-degenerated t_2 orbitals that are crucial for the stability of HH compounds.[41]

These bonding states as well as empty nickel d-orbitals are filled by four titanium valence electrons leading $Ti^{4+}[NiSn]^{4-}$. The ionic character arises from the lower electronegativity of titanium (1.54). The d-orbitals from nickel (fully occupied) and titanium (empty) generate bonding and anti-bonding states of double degenerated e and triple degenerated t_2 orbitals. These bonding orbitals and their anti-bonding counterparts form the energy gap in most HH alloys. Although the localization of the orbitals plays a role as well,[42] one can say that as bigger the difference in electronegativities, as stronger the bonding and as bigger the energy gap becomes. For semiconducting behavior, all states below the energy gap must be occupied. According to the explanation above, one a_1, one double-degenerated e and two triple-degenerated t_2 orbitals must be completely filled by spin up and spin down electrons. So for TiNiSn, 18 VB electrons are provided by Ti $3d^2 4s^2$, Ni $3d^8 4s^2$ and Sn $5s^2 5p^2$. An identical calculation can be made for $Zr_{0.5}Hf_{0.5}NiSn$. Here, two VB electrons each from Zr $4d^2 5s^2$ and Hf $5d^2 6s^2$ substitute Ti $3d^2 4s^2$.

A more simplified consideration can also be done to explain that the sum of participating VB electrons must be 18. Compared to conventional SCs as GaAs or ZnSn that need to have two and six electrons occupying the s and p orbitals, respectively, for HH compounds ten additional valence electrons are required to fully occupy the existing d orbitals.

2.4 TiNiSn and $Zr_{0.5}Hf_{0.5}NiSn$ in thermoelectrics

In general, the Fermi energy lies within the VB or CB, if the sum of valence electrons is 17 or 19, respectively.[43] If 40 % of scandium is exchanged for titanium in $Ti_{1-x}Sc_xNiSn$, the Fermi energy moves significantly into the VB.[44] Does a HH compound have more than 19 VB electrons, too many electrons are located in the anti-bonding states and most of the HH compounds become unstable.[45]

As it is schematically shown in Figure 10, HH compounds can be formed by several combinations of elements. So, by changing elements and their electronegativity, a broad variety of energy gaps can be fabricated. For TiNiSn, a band gap of 0.45 eV has been calculated by several groups.[43,46,47] As it can be seen from the band structure (Figure 11), the gap occurs from the center (Γ) to an edge (X) of the Brillouin zone BZ. Therefore, that is an indirect band gap and a phonon is needed for the electron transition between highest VB edge and lowest CB edge. The direct gap at Γ –point has been calculated to be 1.20 eV.[37] In contrast, Chaput et al. calculated a direct energy gap of 0.46 eV for

$Ti_{0.5}Hf_{0.5}NiSn$.[42] Importantly, the size of the energy gap E_G creates the appropriate number of charge carriers that is crucial for TE materials (see Figure 8). For SCs as TiNiSn and $Zr_{0.5}Hf_{0.5}NiSn$, the amount of electrons is increased at elevated temperatures.

In general, the temperature exhibiting the highest *ZT* values strongly depends on the energy gap of a material (see Figure 8). At RT, materials as Bi_2Se_3, Bi_2Te_3 and Sb_2Te_3 with E_G of less than 0.35 eV,[48] are suitable TE materials. Has energy conversion to be done at much higher temperatures (~1000°C), $Si_{0.8}Ge_{0.2}$ alloys play an essential role. With E_G of about 1 eV, also *ZT* values above 1 are reached.[49,50] In 1994, J. O. Sofo and G. D. Mahan derived a general model for direct and indirect SCs saying that the application temperature of a TE material is about six times lower than its energy gap.[51] If one looks for TE materials having highest performance at intermediate temperatures, due to its intermediate E_G, TiNiSn and $Zr_{0.5}Hf_{0.5}NiSn$ are appropriate candidates. Their *ZT* as a function of temperature is shown in Figure 12.

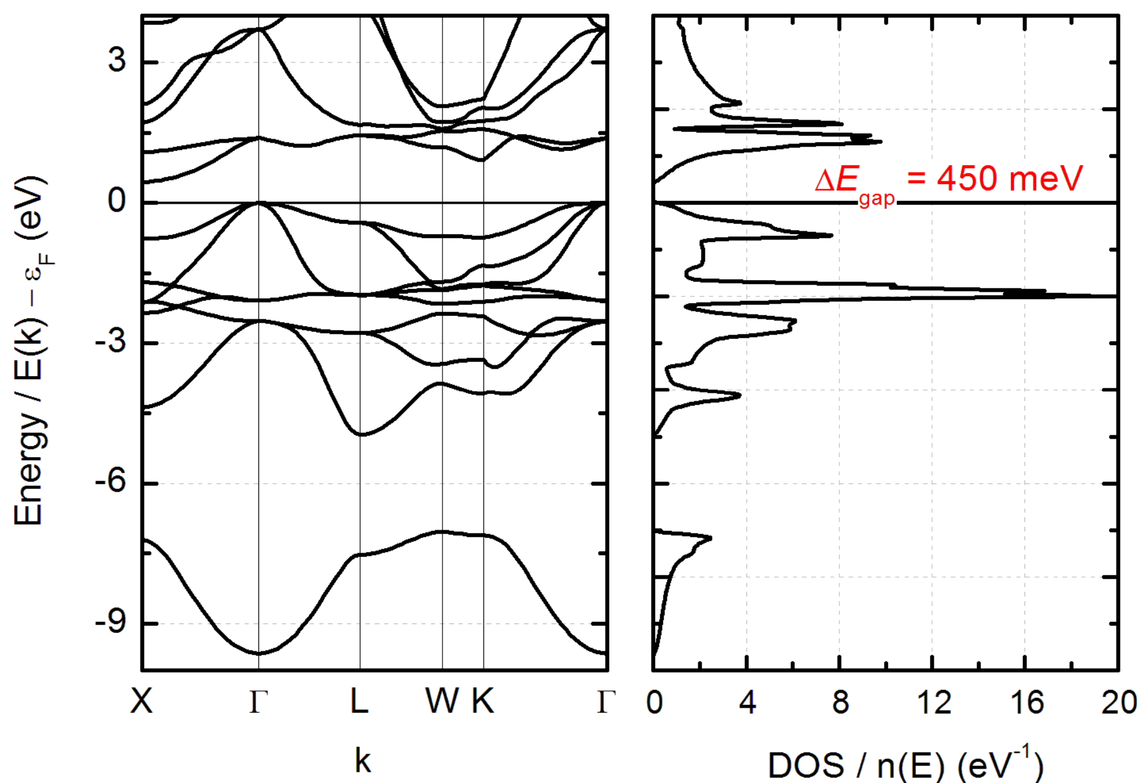

Figure 11 Calculated band structure (left) and density of states (right) of TiNiSn (Adapted from Ref. 47)

In Figure 12a, *ZT* values for several HH compounds that have been fabricated by directional solidification are shown.[52] For comparison, *ZT* for ZrNiSn (red) and HfNiSn (black) are represented by crosses. Compounds with two different elements at the X_1

position are illustrated by connected open symbols. In average, higher *ZT* values are obtained. Highest *ZT* values are measured for $Zr_{0.5}Hf_{0.5}NiSn$ (circles). Because the fabrication process influences the *ZT* values by the sample quality, the definite origin of an extraordinary performance cannot be concluded by a single publication. Here, in contrast to compared HH compounds, a higher Seebeck coefficient causes this outstanding result for $Zr_{0.5}Hf_{0.5}NiSn$.

The influence of sample preparation can be seen in Figure 12b. After Spark Plasma Sintering (SPS, black), TiNiSn bulk samples have been treated by post-annealing.[55] A short annealing time already causes an enhanced power factor (blue). But with increased annealing time (red), ongoing grain size growth also increases the thermal conductivity. Of course deviating *ZT* numbers can also be found in different publications (Table 1). Besides varying fabrication processes, the measurement techniques and their measurement error generate deviations. Nevertheless, with *ZT* numbers of about 0.5, TiNiSn and $Zr_{0.5}Hf_{0.5}NiSn$ belong to a closer circle of relevant TE materials.

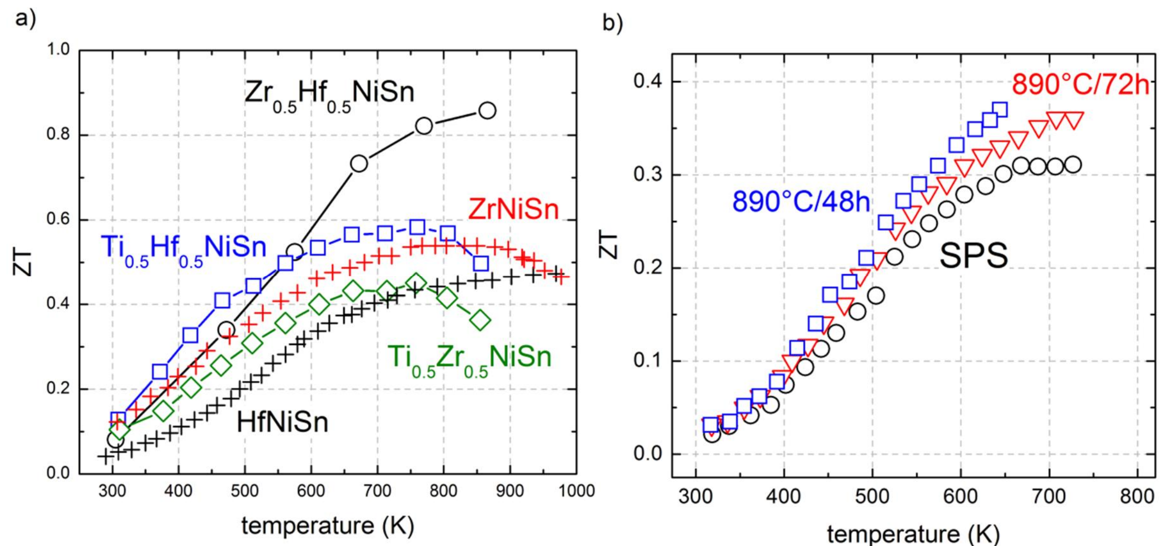

Figure 12 *ZT* as a function of temperature for $Zr_{0.5}Hf_{0.5}NiSn$ (a) and TiNiSn (b) (Adapted from Ref. 52 and Ref. 55)

It was intended to include also TiNiSn into Figure 12a.[52] But other than shown combinations of XNiSn (X = Ti, Zr, Hf), the fabrication of stable TiNiSn bulk samples was not doable by directional solidification. For spark plasma sintered bulk samples with purposely changed nickel composition, Ti_6Ni_5 and $TiNi_2Sn$ were observed.[53] Next to the formation of pure tin, a significant reduction of Ti_6Ni_5 and $TiNi_2Sn$ phases with increased annealing temperature has been observed by others.[54,55] So, TiNiSn is known to form several phases within the alloy. Inconsistently, to most other publications, ball milled and

arc-melted bulk samples that were additionally annealed up to 1023 K decomposed in Ni_3Sn_4 and pure Ti.[39] But also Ti_5Sn_3 has been found in TiNiSn.[55] Additionally, in Ti-Co-Sn ternary systems, Ti_2Sn and Ti_3Sn have been found as stable phases.[56]

In 1970, when Jeitschko published about TiNiSn, analyses about ZrNiSn had been already done.[35] Arc melting as well as the high frequency induction furnace were used for fabrication. Beside ZrNiSn stable phases as $ZrSn_2$, Zr_5Sn_3, Zr_3Sn, Zr_2Ni, ZrNi, Zr_7Ni_{10}, $ZrNi_5$, Ni_3Sn, $Ni_{14}Sn_{10}$, Ni_3Sn_4 and $ZrNi_2Sn$ have been found. Single phase $Zr_{0.5}Hf_{0.5}NiSn$ was fabricated by directional solidification.[52] For niobium doped $Zr_{0.5}Hf_{0.5}NiSn$, XRD measurements have revealed small amount of secondary phases ($Ni_2Zr_{0.5}Hf_{0.5}Sn$, $Ni_{1.35}Sn$ and Hf_5Sn_4).[57]

ZT	**Temperature**	**Fabrication**	**Reference**
0.3	700 K	arc melted; ball milled; annealed	54
0.4	770 K	arc melted; ball milled; SPS	58
0.45	740 K	microwave, ball milled, hot pressed	55

Table 1 Differently fabricated TiNiSn bulk samples and their maximum *ZT* values obtained at given temperatures

In literature, several experimentally obtained lattice constants for TiNiSn can be found reaching from 0.5919 nm to 0.5964 nm (0.5919 nm,[39] 0.5927 nm,[59,60] 0,5930,[55] 0.5934 nm,[53] 0.5940 nm,[61] 0.5941 nm,[35] 0.5964 nm[62]). Similar to the documentation of secondary phases only a few reports about lattice constants of un-doped $Zr_{0.5}Hf_{0.5}NiSn$ can be found. Measured bulk samples fabricated by arc-melting and post annealing have given a lattice constant of 0.61082 nm.[57]

As it has been shown above, enhanced efficiency can be obtained by increasing *ZT* that is directly related to the power factor. For n-type or p-type TE materials,[47] the power factor can be enhanced if a few atoms are exchanged by atoms with plus or minus one valence electron, respectively. But also a reduction in thermal conductivity increases the efficiency of HH materials. In general, compounds including bigger atoms exhibit weaker interactions between the atoms and the thermal conductivity falls with atomic number. So at RT, the thermal conductivities for TiNiSn, ZrNiSn and HfNiSn have been measured to be 9.3 W/mK, 8.8 W/mK and 6.7 W/mK, respectively.[63] Furthermore, using the same measurement setup for $Zr_{0.5}Hf_{0.5}NiSn$, $Ti_{0.5}Zr_{0.5}NiSn$ and $Ti_{0.5}Hf_{0.5}NiSn$ thermal conductivities of 4.4 W/mK, 4.9 W/mK and 3.6 W/mK have been obtained. Here,

additional mass fluctuation causes a reduction in thermal conductivity – the bigger the mass difference the lower the thermal conductivity. Since phonon scattering depends on grain size and crystal quality, thermal conductivity is strongly influenced by the fabrication process. At RT, thermal conductivity of bulk TiNiSn has been measured to be 7.4 $Wm^{-1}K^{-1}$.[64]

So far, n-type HH materials and their research dominate the class of p-type materials by far. Bit by bit p-type HH materials with similar performance are discovered. Recently, $Hf_{0.3}Zr_{0.7}CoSn_{0.3}Sb_{0.7}$ with a *ZT* of 0.8 has been fabricated.[4] 2 % ZnO as additive has been used to decrease thermal conductivity. After arc-melting and ball milling, the samples have been fabricated by SPS that is the state of the art technique in TE bulk sample fabrication.

In the field of TEs, TiNiSn and $Zr_{0.5}Hf_{0.5}NiSn$ have been extensively studied. Power factors as well as thermal conductivities have been increased. The ongoing miniaturization opens new fields of application. In this work, a reduced thermal conductivity perpendicular to a multilayer structure containing TiNiSn and $Zr_{0.5}Hf_{0.5}NiSn$ shall be obtained for thin films.

Chapter 3

Theoretical and experimental background

3.1 Thermal conductivity

In a solid, heat is transported by atomic oscillations that are transferred from one atom to another. Finally, created waves that are also named as phonons are responsible for the heat transport. This chapter explains varied kinds of waves that are generated in different material systems. According to the dispersion relation, it is shown that acoustic waves move the fastest through a solid. Typically, dispersion relations for acoustic phonons are measured by inelastic neutron scattering.[65] Optical phonons can be measured by infrared absorption. Appling LASER light with higher photon energies enables the observation of energy shifts due to the absorption or the creation of phonons at the surface. The momentum of the photons that are interacting with phonons is small and therefore only phonons close to the Γ-point can be excited. It is distinguished between Brillouin-scattering and Raman-scattering if photons interact with acoustic or optical phonons, respectively. The excitation of single phonon states can be done by Mössbauer spectroscopy. Here, the nucleus absorbs and re-emits γ-radiation. So, also quantum-mechanic behavior of phonons becomes obvious.

The discussion about different kinds of lattice vibrations and their influence on thermal conductivity is followed by presenting phonon scattering events that prevent the unresisted propagation of heat. An introduction in bulk scattering is followed by a final discussion about emerging effects on thermal conductivity in SL. Here, the focus is set on the heat propagation perpendicular to the interfaces.

In the following, electron-phonon interaction is not considered.[66]

3.1.1 Fundamental treatment of lattice vibrations

In a most simple model,[67] atoms in a lattice are considered as a linear chain of point masses M having equal distances a in-between. Each mass has a position of zero excitation. Due to elastic forces between several atoms, an atom can be miss-aligned u

from its equilibrium position by its neighbor atom. By transferring the excitation from atom to atom a so called wave moves through a solid. Upon the orientation of the excitation and the propagation, the waves can be classified in longitudinal or transversal waves. Similar to sound or water waves, the excitation can be parallel or perpendicular to the propagation, respectively. By considering a linear force similar to the Hooke's law (constant *C*) and only the interaction between neighboring atoms and their distance away from equilibrium (u_{s+1}, u_{s-1}), one can determine the force *F* affecting the atom *s* and its position u_s in-between:

$$F_s = C(u_{s+1} - u_s) + C(u_{s-1} - u_s) \quad 3.1$$

The equation of motion for the atom can be written:

$$M\frac{\mathrm{d}^2 u_s}{\mathrm{d}t^2} = C(u_{s+1} + u_{s-1} - 2u_s) \quad 3.2$$

The differential equation can be solved by a propagating wave equation

$$u_{s\pm1} = u \cdot \exp(i\omega t) \cdot \exp(isKa) \cdot \exp(\pm iKa) \quad 3.3$$

and leads to

$$\begin{aligned} &-Mu\omega^2 \cdot \exp(i\omega t) \cdot \exp(isKa) \\ &= C \cdot u \cdot \exp(i\omega t) \cdot \left(\exp(i(s+1)Ka) + \exp(i(s-1)Ka) - 2\exp(isKa)\right). \end{aligned} \quad 3.4$$

Finally

$$M\omega^2 = -C \cdot (\exp(iKa) + \exp(-iKa) - 2) \quad 3.5$$

can be exchanged by $2\cos(Ka) = \exp(iKa) + \exp(-iKa)$ and results in the dispersion relation that combines the angular frequency ω with the wave vector *K* of the propagating wave. It can be written

$$\omega^2 = \frac{2C}{M}\left(1 - \cos(Ka)\right) \qquad \text{or} \quad 3.6$$

$$\omega = \sqrt{\frac{4C}{M}}\left|\sin\left(\frac{1}{2}Ka\right)\right|. \quad 3.7$$

A plot of the dispersion relation is shown in Figure 13. Dashed lines represent the first Brillouin zone (BZ). Due to symmetry within a crystal, all waves can be described by

$K \leq \frac{\pi}{a}$. Usually, transversal and longitudinal acoustic modes differ in C and therefore two branches can be observed. A stronger longitudinal interaction of the atoms leads to a higher C and a higher energy dispersion branch. So having identical wave vectors, transversal acoustic waves appear with a lower phonon frequency.

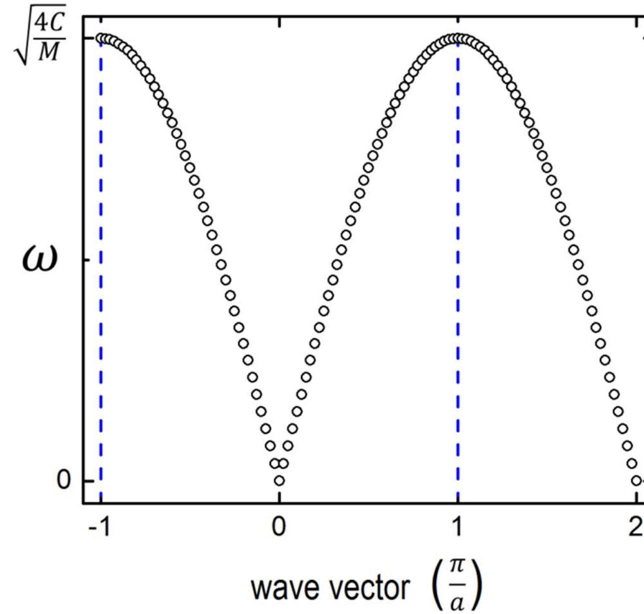

Figure 13 Dispersion relation (ω = f (K)) for acoustic phonons

The energy transport of a wave is described by the group velocity of a wave packet and given by:

$$v_G = \frac{\mathrm{d}\omega}{\mathrm{d}K} = \sqrt{\frac{Ca^2}{M}}\cos\left(\frac{1}{2}Ka\right) \qquad 3.8$$

Hence, phonons that transport energy have to have small wave vectors. As it can be seen by the nearly linear slope of the dispersion branch (Figure 13), the propagation is almost independent from the wave vector and corresponds to the speed of sound in a solid. For smaller wave lengths (higher angular frequency), the dispersion relation flattens out and phonons do not contribute to the energy transport.

More sophisticated it becomes, if more than one atom is located within the first BZ. Due to charge transfers, optical oscillations can be excited. In contrast to acoustic phonons, for optical phonons two neighbor atoms oscillate reversely. A similar derivation but with two different masses (M_1 > M_2) can be done. Compared to Figure 13, an additional optical phonon branch occurs (Figure 14). As valid for the acoustic phonons that have a short wave length, the weak curvature of the whole optical phonon branch

indicates only a little energy transport. Notably, a gap arises between acoustic and optical phonon branches. Here, imaginary solutions can be found. Phonons having these frequencies are damped.

For optical phonons it can also be distinguished between longitudinal and transversal waves. Having p atoms in the first BZ leads to $3p$ dispersion branches: 3 acoustic and $3p - 3$ optical. Acoustic phonons that are independent of the number of atoms in the first BZ are assembled by one longitudinal and two transversal branches. The amount of optical phonons is enhanced by additional atoms. $(p - 1)$ longitudinal and 2 x $(p - 1)$ transversal optical branches are generated by p atoms in the first BZ.[68]

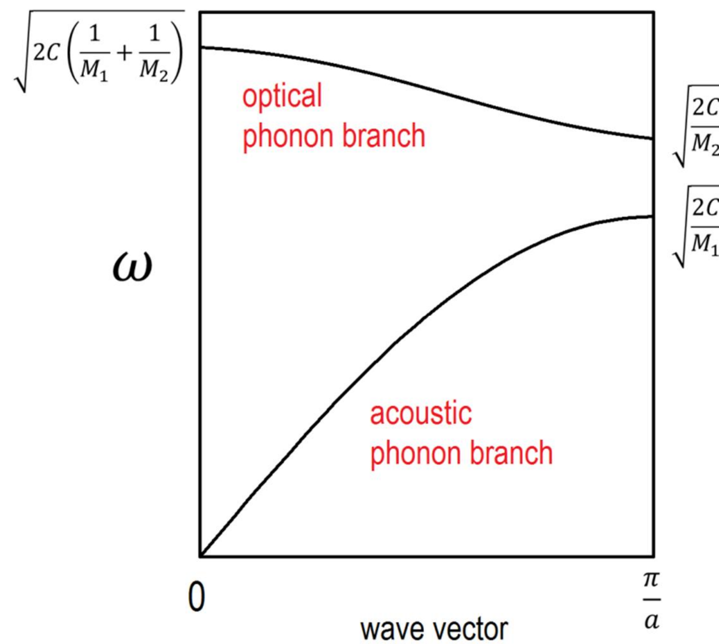

Figure 14 Dispersion relation for two atoms with $M_1 > M_2$

Although a variety of properties can be explained by a classical treatment, phonons are quasi-particles that have to be treated quantum mechanically with an integer spin. By taking into account the Boltzmann constant k_B, the reduced Planck constant $\hbar$ and the total energy of all phonons k_BT, the probability of a single phonon state to be occupied $\langle n \rangle$ is given by the Bose-Einstein statistics:

$$\langle n \rangle = \frac{1}{\exp\left(\frac{\hbar\omega}{k_B T}\right) - 1} \quad 3.9$$

With an integer number n, for single phonons the energy can be assigned to be:

$$E = \left(n + \frac{1}{2}\right) \cdot \hbar\omega \quad 3.10$$

Similar to the harmonic oscillator, $\mathbf{1/2}\,\hbar\omega$ belongs to a zero-point energy. For phonons, the physical momentum **p** must be taken into account as

$$\mathbf{p} = \hbar\mathbf{K} \tag{3.11}$$

if phonons interact with other particles as photons, neutrons or electrons.

3.1.2 Thermal conductivity

The heat flow $\dot{Q}$ that is conducted through an area per time is given by:

$$\dot{Q} = -\kappa\frac{\mathrm{d}T}{\mathrm{d}x} \tag{3.12}$$

Therefore, it depends on the thermal gradient dT/dx and the thermal conductivity κ.[69,70] Naturally, the minus makes the heat flowing from a warmer to a colder region. With TE devices one either wants to generate electric power or a thermal gradient by a hot and a cold side or an applied current, respectively. In both cases it is of importance that the heat flow between hot and cold end is minimized. So, an appropriate TE material must have a low thermal conductivity.

Besides phonons, heat can be transferred by electrons as well. Therefore the thermal conductivity is composed of an electronic κ_{el} and a lattice κ_{ph} part:

$$\kappa = \kappa_{el} + \kappa_{ph} \tag{3.13}$$

Of course, only free electrons are suitable to carry energy through the solid. For metals,[71] conductivity and the electronic part of the thermal conductivity can be linked by the Wiedemann-Franz Law including Lorenz number L and elementary charge e:

$$\frac{\kappa_{el}}{\sigma} = \frac{\pi^2}{3}\left(\frac{k_B}{e}\right)^2 T \equiv L \cdot T \sim \mathbf{2.44} \cdot \mathbf{10}^{-8}\,\frac{\mathrm{W\Omega}}{\mathrm{K}^2} \cdot T \tag{3.14}$$

In general, TE materials are semi-metals where phonons dominate the thermal conductivity. For thin films deposited for this work, at 300 K, conductivities in the order of $\mathbf{10}^5\ \Omega^{-1}\mathbf{m}^{-1}$ have been measured. Hence, the contribution of the electrons to thermal conductivity is about 0.75 $\mathbf{Wm}^{-1}\mathbf{K}^{-1}$ and cannot be neglected.

Based on Hall measurements and a more sophisticated model,[72] the thermal conductivity of ZrNiSn including the influence of free electrons and holes is shown as a function of temperature in Figure 15. Considering different properties for electrons and

holes and the temperature dependence due to semiconducting behavior, allowed simulating the thermal conductivity at elevated temperatures. An additional measurement of the thermal conductivity was performed (black squares). While further considerations in this chapter will explain decreasing thermal conductivities, here is shown an example that for SCs the thermal conductivity can rise at elevated temperatures due to emerging charge carriers. But the dashed line shows that only a correction of the lattice contribution of the thermal conductivity due to Lorenz number L_0 and conductivity σ is insufficient. A further correction needs to be done that includes partial electron-hole generation and recombination L_{am} (ambipolar diffusion effect).[73] Because electron-hole interaction is enhanced for intrinsic SCs, for ZrNiSn, having many in-gap states, the effect increases with temperature.

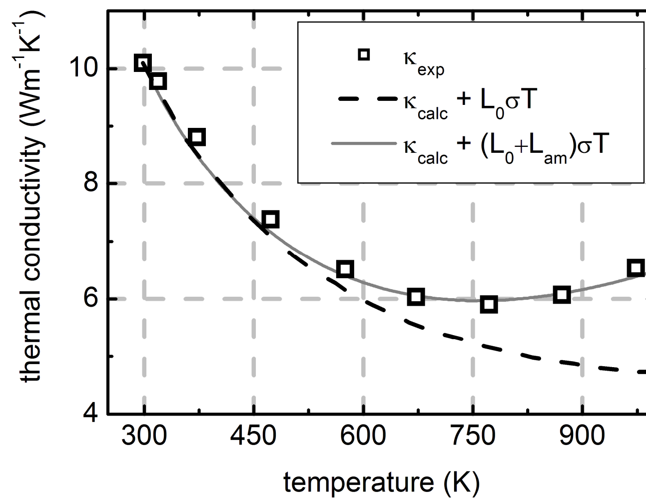

Figure 15 Calculated influence of semiconducting behavior on thermal conductivity of ZrNiSn (Adapted from Ref. 72)

In kinetic gas theory, the thermal conductivity that is generated by the lattice of a solid can be estimated to be:

$$\kappa_{ph} = \frac{1}{3} C_V v_s l_{ph} \qquad 3.15$$

Beside specific heat capacity per unit volume C_V and phonon velocity v_s, the MFP of phonons l_{Ph} plays an essential role. Therefore the equation expresses how much heat is carried how fast and how far until the next phonon-phonon collision appears. Due to symmetry only one third of the energy is carried along a specified direction. By exchanging:

$$l_{ph} = v_s \cdot \tau \qquad 3.16$$

with time (τ) between two collisions, the thermal conductivity can be written as:

$$\kappa_{ph} = \frac{1}{3} C_V v_s^2 \tau \quad 3.17$$

In combination with Figure 14, it becomes obvious why the thermal conductivity is dominated by the acoustic phonons having long wave lengths. Based on different considerations, the group velocity of a wave packet ($v_G = d\omega/dK$) and phonon velocity v_s have finally the same meaning. As faster phonons move, as higher the thermal conductivity becomes.

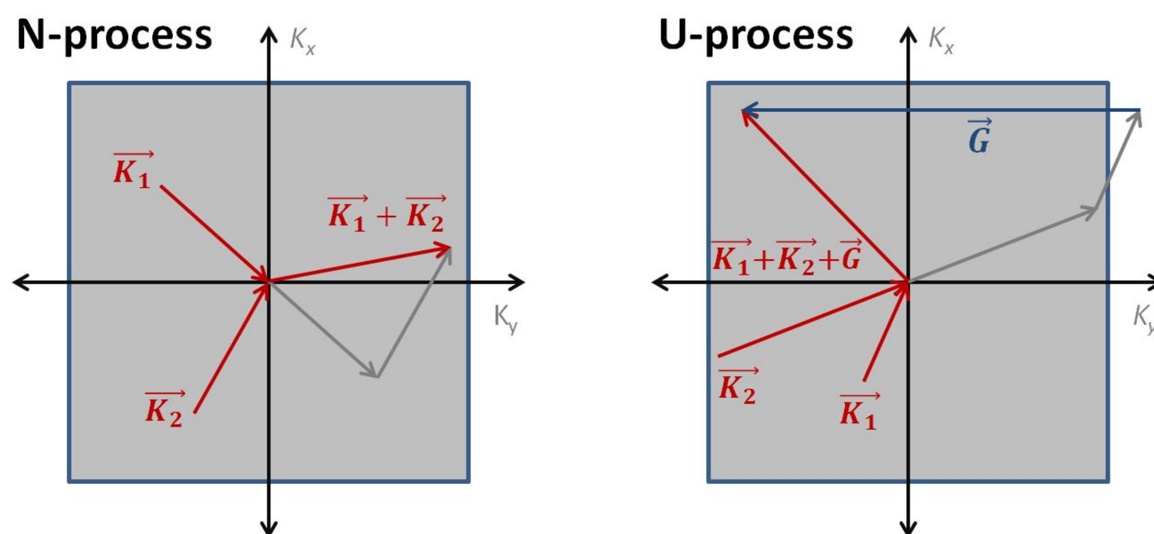

Figure 16 N- and U-processes as possible scattering events for phonons

Furthermore, different effects at different temperatures must be taken into account. According to the specific heat, at low temperatures, the thermal conductivity increases proportional to T^3. More and more phonons are excited and take part in carrying heat. The phonons barely interact and their MFP is limited by the size of the sample and its impurities. Depending on the material, the thermal conductivity increases to a maximum at ~20 K. So, single crystals as sapphire even exceed thermal conductivity of metals.[74] But with rising temperature, phonon-phonon interaction starts. As it is illustrated in Figure 16, two scattering phonons create a third phonon. For the wave vector of the generated phonon, the wave vectors of the scattering phonons must be summed up. While so called Normal (N-) processes have an insignificant effect on thermal conductivity, so called Umklapp (U-) processes generate a noticeable reduction of the thermal conductivity. As it illustrated in Figure 16, the participating lattice vector $G = 2\pi a^{-1}$ can

generate a phonon with an opposite direction to the incoming ones. The change in total phonon momentum is taken by complete crystal.

Related to the Bose-Einstein statistics, the amount of phonons that can participate on U-processes due to a sufficient energy is given by:

$$\langle n \rangle = \frac{1}{\exp\frac{\hbar\omega}{k_B T}-1} \approx \frac{1}{\exp\frac{\theta_D}{T}-1} \approx \mathbf{exp}\left(-\frac{\theta_D}{T}\right) \qquad 3.18$$

The Debye-Temperature θ_D indicates the temperature where all phonon modes are excited. It can be applied to calculate U-processes for $T < \theta_D$. The amount of phonons that generate U-processes can directly be converted into the time between two scattering events:

$$\tau^{-1} \sim \mathbf{exp}\left(-\frac{T_0}{T}\right) \qquad 3.19$$

Calculations and experimental data have shown that θ_D and T_0 are almost equal. For $T > \theta_D$, the amount of phonons is proportional to T and for the thermal conductivity it can be written:

$$\kappa_{ph} \sim \frac{1}{T} \qquad 3.20$$

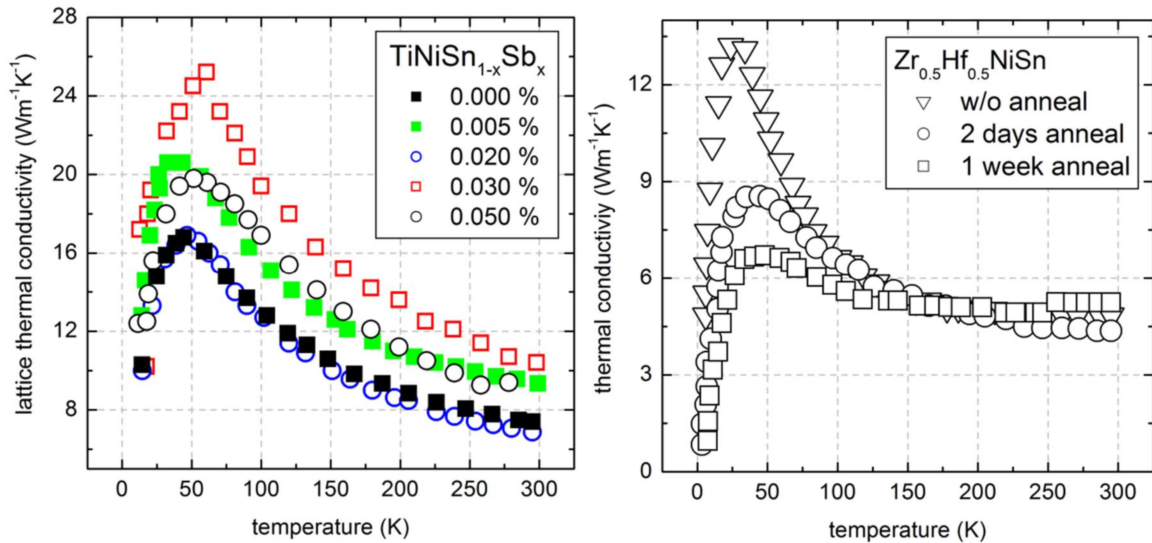

Figure 17 Thermal conductivities for TiNiSn and $Zr_{0.5}Hf_{0.5}NiSn$
(Adapted from Ref. 75 and Ref. 76)

For TiNiSn and $Zr_{0.5}Hf_{0.5}NiSn$ thermal conductivities from 0 to 300 K are shown in Figure 17. Due to the large number of atoms in the unit cell, many phonon modes appear

and Debye temperature is above RT. For some HH materials, it has been calculated upon the velocity of sound that was measured to be ~3000 ms^{-1}.[72] So, following the $\kappa_{ph} \sim T^3$ dependency, only $\kappa_{ph} \sim \mathbf{exp}(T_0/T)$ behavior can be seen in Figure 17. Due to doping and crystal quality, varied $\kappa_{ph} = \mathbf{f}\,(T)$ can be observed. Nevertheless, $\kappa_{ph} \sim T^{-1}$ behavior of the lattice thermal conductivity has also been measured for $Ti_{0.5}Zr_{0.25}Hf_{0.25}Co_{0.95}Ni_{0.05}Sb$ with InSb nanoinclusions between RT and 800 K.[5] Theoretically, in the case of strong defect scattering, $T^{-1/2}$-behavior can be observed as well.[79]

3.1.3 Disorder in solid solutions

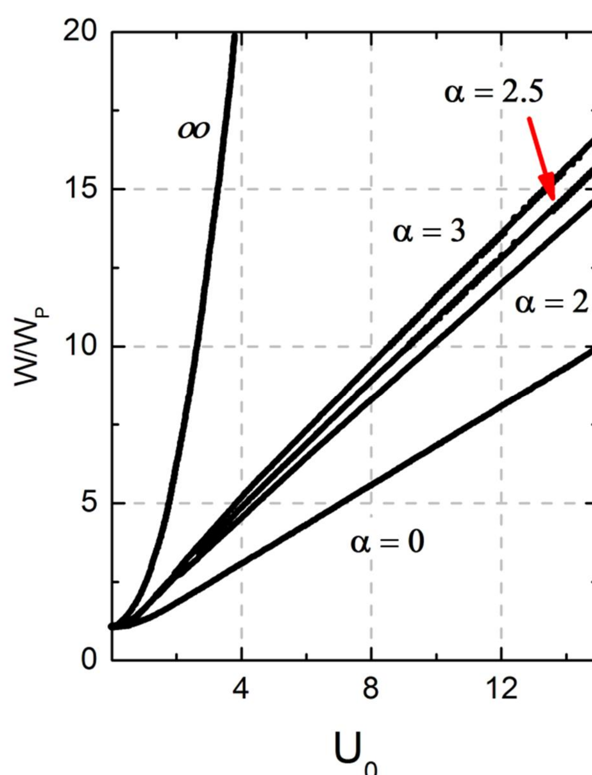

Figure 18 Thermal resistivity (W/W_P) as a function of disorder parameter U_0 and ratio α between three phonon N- and U-processes (Adapted from Ref. 77)

Besides phonon-phonon interaction, mass fluctuation in a crystal can influence the thermal conductivity tremendously. In 1963, upon Klemens-Callaway-Theory,[78,79] Abeles calculated a model including phonon-phonon and impurity scattering.[77] In an isotropic elastic continuum model, the disorder results in point-defect-scattering and is included in a disorder parameter U_0. As more disorder, given by strain and mass point defects, is considered as bigger U_0 becomes. In the calculation, reciprocal phonon scattering times caused by the defects depend on phonon frequency as ω^4. The reciprocal phonon

scattering time of phonon-phonon-interaction of N- and U-processes depend on the frequency as ω^2. Upon described parameters thermal resistivity divided by thermal resistivity at zero disorder (W/W_P) can be seen in Figure 18. At low ($\alpha = \infty$) and at high ($\alpha = 0$) temperatures, thermal resistivity (conductivity) increases (decreases) with disorder (U_0). Since phonon-phonon-interaction rises with temperature and increased U-scattering takes place at high temperatures, disorder affects thermal conductivity even more at low temperatures.

Based on a similar theory,[79] in 2004 Yang et.al. calculated the RT lattice thermal conductivity of ZrNiSn, $Zr_{0.5}Hf_{0.5}NiSn_{0.99}Sb_{0.01}$ and $Zr_{0.5}Hf_{0.5}Ni_{0.5}Pd_{0.5}Sn_{0.99}Sb_{0.01}$ to be 11.14 $Wm^{-1}K^{-1}$, 5.14 $Wm^{-1}K^{-1}$ and 1.15 $Wm^{-1}K^{-1}$, respectively.[80] Similar to zirconium and hafnium that are enhancing mass and strain field fluctuations at the X_1-position (see Figure 10), palladium shares the Y-position with nickel. Impressively, the calculation shows the capability of mass point and strain field defect scattering generated by varied elements at the same position in a crystal structure.

A more specified calculation on defects in a crystal has been done by Klemens.[81] A phonon lifetime that is similar to $\tau^{-1} \sim \omega$ was found for dislocation defects and static imperfections. Exchanged atoms that cause differences in mass and binding force resulted separately in $\tau^{-1} \sim \omega^4$ behavior. Notably, the relative changes in mass and bonding strength affect the reciprocal phonon lifetime as $\tau^{-1} \sim (\Delta M/M)^2$ and $\tau^{-1} \sim (\Delta \nu/\nu)^2$, respectively. Finally, several scattering events and their single phonon lifetimes can be summed as:[82]

$$\frac{1}{\tau} = \sum \frac{1}{\tau_i} \tag{3.21}$$

For TiNiSn, atomic disorder plays an important role concerning TE properties. Besides electronic in-gap states that are valuable for a low resistivity of the compound, enhanced phonon scattering has its origin in atomic disorder. By the existence of the full Heusler $TiNi_2Sn$,[83] it can easily be seen and has been proven by core level photoelectron spectroscopy that nickel atoms are located at the vacant side as well.[84] But also titanium atoms swap to the vacant side.[47] Due to their atomic size, swapping of zirconium or hafnium in $Zr_{0.5}Hf_{0.5}NiSn$ is less probable. Therefore, TiNiSn shows an intrinsic behavior in reducing thermal conductivity.

Already in 1980, it has been shown for hot-pressed $Si_{30}Ge_{70}$ bulk samples that already grain sizes much larger than the MFP of phonons affect the thermal conductivity.[85] As the

grain diameter is reduced from infinity to 2 µm, the RT thermal conductivity decreases from 5.8 $Wm^{-1}K^{-1}$ to 3.7 $Wm^{-1}K^{-1}$. Due to smaller grains, depressed thermal conductivity has also been found for $TiNiSn_{1-x}Sb_x$.[75] If the grain size is reduced in $TiNiSn_{0.97}Sb_{0.03}$, as published by Battacharya et. al.,[86] the lattice thermal conductivity can be further depressed. Applying ball milling and shock compaction has generated grain size diameters of less than 1 µm. So, the thermal conductivity has been decreased from ~10.5 $Wm^{-1}K^{-1}$ for grain size diameters of 9.5 µm to 3.7 $Wm^{-1}K^{-1}$. Consequences upon electrical properties are not mentioned.

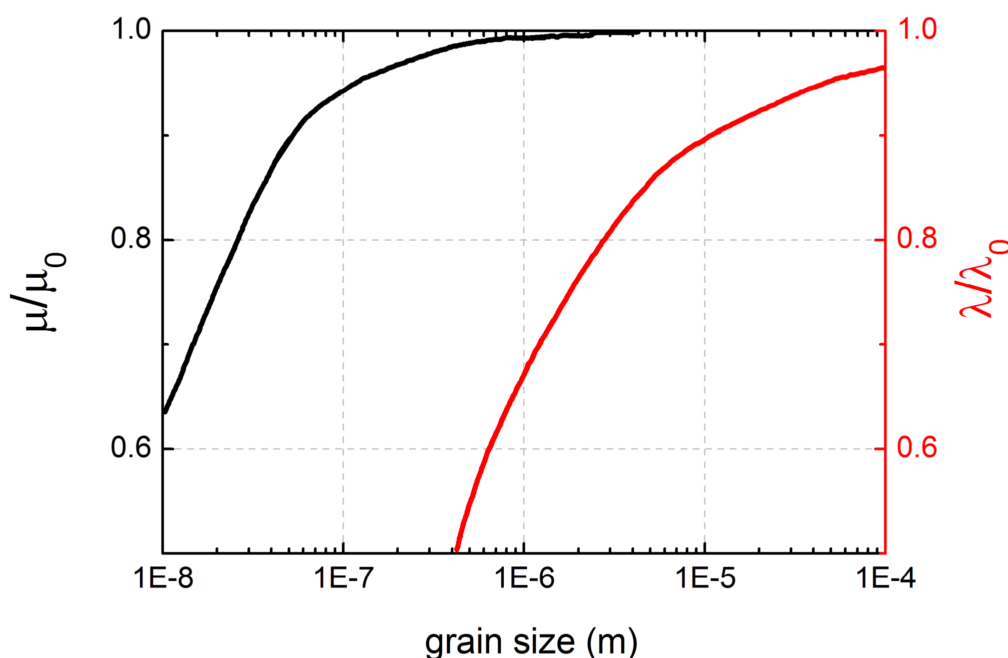

Figure 19 Reduced electron mobility μ/μ_0 and phonon mean free path λ/λ_L due to grain sizes in $Zr_{0.5}Hf_{0.5}NiSn$ (Adapted from Ref. 87)

In 2001, upon experimental data taken from Uher el. al.,[76] Sharp et. al. calculated grain size dependent phonon scattering in bulk $Zr_{0.5}Hf_{0.5}NiSn$ at elevated temperatures (Figure 19).[87] Their calculation revealed a tremendous reduction of the thermal conductivity if the grain sizes becomes smaller than 10 µm. This trend goes further on, but a beginning reduction in electron mobility at about 1 µm must be considered in the overall efficiency of a TE material.

Beside an increased electron mobility, Uher et. al. observed enhanced thermal conductivity for $Zr_{0.5}Hf_{0.5}NiSn$ (Figure 17) due to two weeks of post annealing.[76] Since TE materials are mostly used at elevated temperatures, it points out one of the major challenges in TE research: TE materials must be stable over time to be utilized at a constant efficiency in TE devices.

3.1.4 The effect of superlattices on thermal conductivity

Although a reduction of in-plane thermal conductivity has been also measured,[88] in the following section, theoretical and experimental results of thermal conductivity perpendicular to the interfaces of SLs are discussed. Several approaches are presented that describe emerging effects if material A and B are subsequently deposited on top of each other.

By generating a polariton at the interface, it is shown that LO phonons can theoretically tunnel through a barrier.[89] Mode conversion has been suggested that transforms acoustic into optical modes right at the interface.[90] So, the thermal conductivity is decreased by the reduced group velocity. For layer thickness between 4 and 12 monolayer (ML) this effect has been calculated to be constant for Si/Ge SLs. Furthermore, a reduced group velocity due to flatting of the optical dispersion branches for Si/Ge and GaAs/AlAs SLs has been calculated by others.[91] It has been calculated that it is mostly affected by periods of about 10 ML.

Based on non-equilibrium molecular dynamics calculation, Termentzidis et. al. have shown that the thermal conductivity of GaAs/AlAs SLs cannot be reduced below the thermal conductivity of the alloy.[92] Additionally, their modeled GaAs/AlAs SLs show only a minimum in thermal conductivity as a function of SL period for smooth interfaces.

Similar calculations have been done for Si/Ge SLs.[93] Here, going from larger to smaller SL periods, for the thermal conductivity a plateau region has been calculated. Only for very small SL periods, the thermal conductivity starts increasing. Based on density-functional perturbation theory, including harmonic and an-harmonic force constants, a dramatic reduction in the scattering of acoustic phonons has been simulated. For SLs with less than 4 ML, the acoustic-acoustic-optical scattering channel vanishes. Usually, TA phonons scatter with LA phonons by generating LO phonons. Due to a rising energy gap between the sum of both acoustic phonons and the optical one, for smallest SL periods this scatter event disappears. By flattening the optical dispersion branch, a further acoustic-optical-optical scattering event becomes unfeasible as well. For that event TA phonons scatter by absorbing LO phonons and generating TO phonons. Due to the disappearance of both scatting events at very small SL periods, lifetimes of acoustic phonons and thermal conductivity are enhanced.

In 1982, Ren et. al. calculated the formation of phonon mini-bands due to an artificial BZ formed by the additional SL structure perpendicular to the heat transfer.[94] A reduction

of thermal conductivity was predicted due to enhanced U-scattering at around 20 K. Here, depressed thermal conductivity has been found for smaller periods. In 2000, M.V. Simkin and G. D. Mahan published an advanced model that assumes the formation of mini-bands as well.[95] But additionally, a transition from particle to wave behavior has been shown if the SL period becomes smaller than the MFP of the phonons. As it is illustrated in Figure 20, for shorter phonon MFP, the minima of the heat conductivities shift to smaller SL periods. The minimum in thermal conductivity becomes even more pronounced if additionally diffuse scattering is considered at larger SL periods.[96] Based on a molecular dynamics simulation a minimum at about 10 ML has been calculated at RT.[97] By simulating emerging interface roughness, the thermal conductivity could be further reduced by diffuse scattering at the interfaces. Based on the Bolzmann transport equation and on the relaxation time approximation, a further calculation has revealed the same effect of diffuse phonon scattering at the interfaces.[98] Specular scattering is calculated to be less affecting. But it strongly depends on the mismatch in acoustic impedance and phonon group velocity of the participating layers.

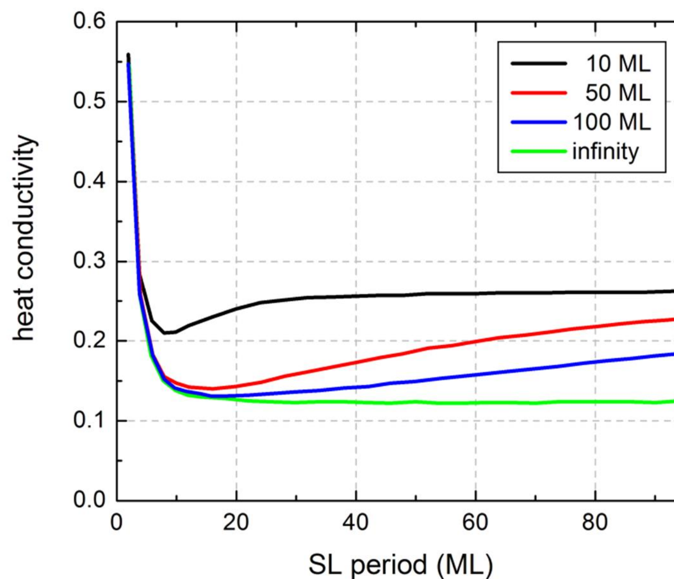

Figure 20 Based on a three dimensional model, for several phonon MFPs (caption), at RT the heat conductivity is calculated as a function of SL period. (Adapted from Ref. 95)

What has been shown for enhanced impurity scattering in bulk samples can also be transferred to phonon scattering interfaces. For GaAs/AlAs SLs, $\kappa_{ph} \sim T^{-0.8}$ has been measured for the thermal conductivity at elevated temperatures.[99] The temperature behavior deviates from $\kappa_{ph} \sim T^{-1}$ if it is not only phonon-phonon scattering that defines the thermal conductivity.[100]

For obtaining the record *ZT* value of 2.4,[8] Venkatasubramanian experimentally demonstrated the minimum in thermal conductivity for Bi_2Te_3/Sb_2Te_3 SLs.[101] By 3ω measurements, a minimum has been found at a period of about 5 nm. By utilizing Eq. 3.15 obtained by kinetic theory, phonon MFP is calculated from thermal conductivity measurements. Both are shown in Figure 21a. The reduction in phonon MFP allowed the calculation of cut-off frequencies (Figure 21b). Waves with frequencies lower than the cut-off frequency are blocked by the SL. So, phonons with a higher (lower) frequency (wave length) contribute to the heat transfer. For SL periods smaller than 5 nm, the cut-off frequencies decrease again due to a coupling of both individual layers.[I]

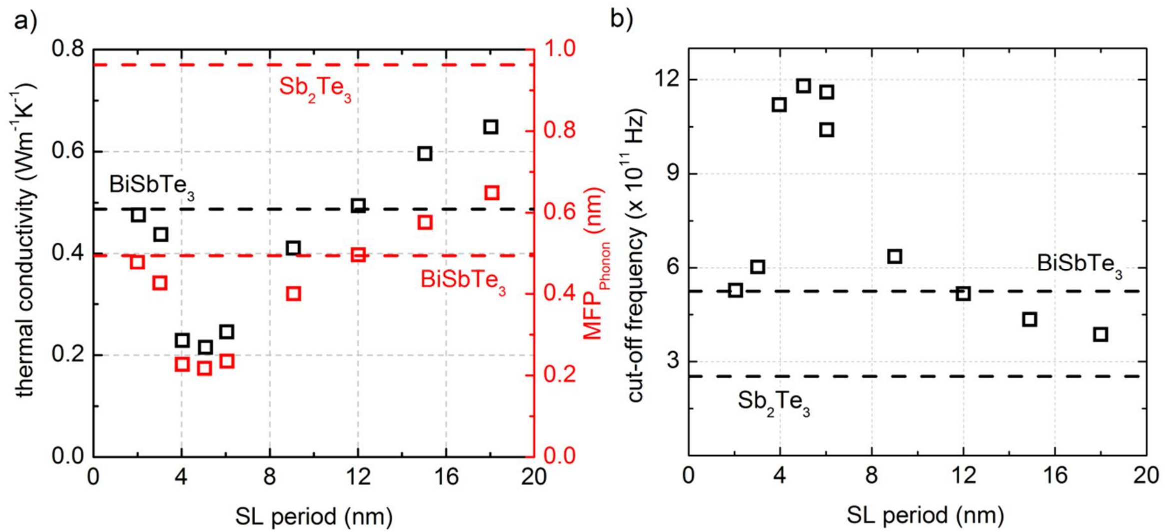

Figure 21 Thermal conductivity (black, a), phonon MFP (red, a) and cut-off frequency (b) for Bi_2Te_3/Sb_2Te_3 SLs as a function of SL period thicknesses (Adapted from Ref. 101)

Similar to the kinetic theory, the wave model can be applied. Analogical to optical dielectric filters with different indices of refraction,[102] by alternating masses in SL, LA phonons can be blocked by Bragg reflection at the interfaces.[103] The Bragg condition for a SL with the period thickness *D* and the angle of incidence θ is:

$$\mathrm{m} \cdot \lambda = 2D \cdot \sin\theta \qquad 3.22$$

With normal incidence, $\theta = 90°$ it can be simplified to:

$$\lambda = \frac{2}{\mathrm{m}} D \qquad 3.23$$

[I] Because optical phonons barely contribute to the thermal conductivity but heavily to the heat capacity, phonon MFPs calculated with Eq. 3.15 and illustrated in Figure 21a become too small. Thus, obtained cut-off frequencies are too high (Figure 21b).

By using $k = \frac{2\pi}{\lambda}$, it can be written as:

$$k = \mathbf{m}\frac{\pi}{D} \qquad 3.24$$

For a periodicity of 5 nm and a speed of sound of 3000 ms^{-1}, the longest wave length and the lowest phonon frequency can be calculated to be 10 nm and 3 x 10^{11} Hz, respectively.

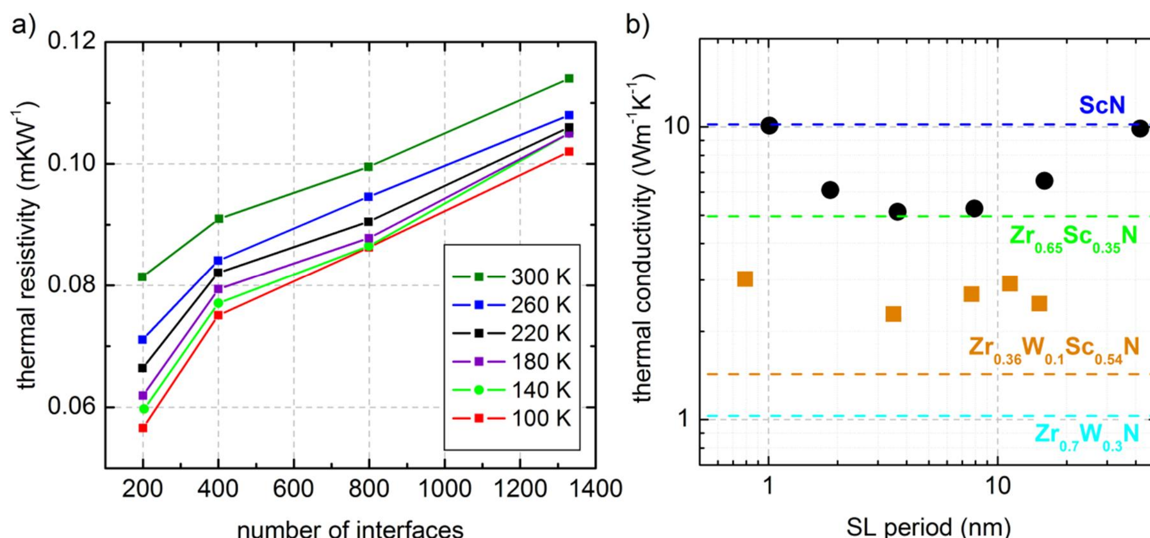

Figure 22 Thermal resistivity of $Si/Si_{0.7}Ge_{0.3}$ SLs for a changed number of interfaces measured at varied temperatures (a); Thermal conductivity of ZrN/ScN (black dots) and $Zr_{0.64}W_{0.36}$/ScN (orange squares) multilayers as a function of period (b) (Adapted from Ref. 106 and Ref. 109)

Below a SL period of 7 nm an increase of thermal conductivity has also been measured for Si/Ge superlattices.[104] Borca-Tasciuc et. al. have measured a minimal thermal conductivity of 3 $Wm^{-1}K^{-1}$ for a Si/Ge SL periodicity of 14 nm.[105] For period thicknesses of 9 nm and 4.4 nm the thermal conductivity has been determined to be almost identical and significantly higher, respectively. To demonstrate the sensibility of material systems as well as measurement techniques, by others,[106] a monotonically decreased thermal conductivity has been also measured for $Si/Si_{0.7}Ge_{0.3}$ SLs down to shortest periods of 4.5 nm. So, only increasing thermal resistivity has been observed for an increasing number of $Si/Si_{0.7}Ge_{0.3}$ interfaces (Figure 22a). In this context, Lee et. al. have refered the change in thermal conductivity in Si/Ge SLs to a varied crystal structure for different periodicities.[107] Therefore, germanium nanodots with different silicon spacer layer thicknesses have been grown by Pernot et. al..[108] So, the crystallographic quality of the thin film that also influences thermal conductivity has not changed with periodicity.

Among other techniques, increased thermal conductivities for smallest periods (4 nm) have not been observed by 3ω measurements. Thereby, for almost identical material systems different results have been published. But it can be highlighted at this point that due to the structural similarity between TiNiSn and $Zr_{0.5}Hf_{0.5}NiSn$ different period thickness are supposed to have similar crystallographic quality.

Rawat et. al. have analyzed ZrN/ScN and $Zr_{0.64}W_{0.36}$/ScN SLs (Figure 22b).[109] With a period thickness of 5 nm for a ZrN/ScN SL (black dot), a minimum in thermal conductivity has been measured that is similar to the lattice contribution of the thermal conductivity calculated by subtraction of the electronic contribution (Eq. 3.13) according to the Wiedeman-Franz law (Eq. 3.14) for $Zr_{0.65}Sc_{0.35}N$. Referred to Simkin and Mahan,[95] phonons can be treated as particles if their MFP is shorter than the SL period. Here, it is doable for periods above 5 nm. For the thermal resistance per unit area given by thickness d_x divided by thermal conductivity κ_x it can be written:

$$\frac{d_{SL}}{\kappa_{SL}} = \frac{d_1}{\kappa_1} + \frac{d_2}{\kappa_2} + \frac{2}{G_{int}}. \quad 3.25$$

The overall thermal resistance for one SL period is therefore generated by four resistances in a row.[I] It is assembled by the resistance of both participating materials and twice the boundary resistance between the attending materials G_{int}^{-1}. Assuming the same boundary resistance for a phonon to cross a ZnN and ScN interface and vice versa, Rawat et. al. have calculated a thermal conductance for the ZnN/ScN interface of 200×10^6 $Wm^{-2}K^{-1}$. It is comparable to 667×10^6 $Wm^{-2}K^{-1}$ that has been measured for a Mo/Al_2O_3 interface.[110] For AlN/GaN SLs, similar considerations have been done by Koh et. al..[111] For larger period thicknesses a constant interface conductance of 600×10^6 $Wm^{-2}K^{-1}$ has been calculated. But it increases due to the formation of minibands up to 1500×10^6 $Wm^{-2}K^{-1}$ at smallest SLs periods.

If such an interface resistance exists in a remarkable manner in the SLs containing TiNiSn and $Zr_{0.5}Hf_{0.5}NiSn$, its demonstration is one of the most challenging tasks in this work. Measuring the thermal conductivity of different period thicknesses, but calculating only one interface resistance would be outstanding. Thus, the accuracy of the measurement technique must be better than the effect of the different SL periodicities on the thermal conductivity. Furthermore, it is of interest, if an increased thermal conductivity will be observed at shortest SL periods also for this HH material system.

[I] Rawat et. al. refer to three resistances in a row but conclude with the identical equation.

3.2 Electronic behavior

Beside thermal conductivity, a further influence on ZT is given by the electric constants Seebeck coefficient α and electrical conductivity σ. Several models can be used for calculation. Already the Drude model that is intended for metals allows an estimation of the Seebeck coefficient. Even though some assumptions turned out to be off-target, a simple approach demonstrates the occurrence of an electric field along a temperature gradient. But concerning TE coefficients, a more sophisticated model needs to be applied for the simulation of TE behavior. Based on the first law of thermodynamics, Onsagers reciprocal relations offer a semi-classical approach to combine S, σ and the electronic part of the thermal conductivity κ_{el}. Already in 1960, the semi-classical treatment has been experimentally verified by Miller.[112] Afterwards, upon Boltzmann transport equation in connection with relaxation time approximation, the Mott equation is derived. By utilizing the density of states (DOS) of the electrons in a material, the Seebeck coefficient can be calculated by the Mott equation. Therefore, the deviation of the Fermi-Dirac distribution and their relaxation into equilibrium are considered. Finally, some examples are shown that are suitable for TE applications. For intrinsic SCs, an approximation using the position of the bands to calculate the Seebeck coefficient is given.

3.2.1 Electrons in a metal – Drude model

The Drude model can be used to describe the transport properties of a metal well. By transferring the kinetic gas theory to the valence electrons of a metal, their behavior concerning electrical and thermal conductivity as well as TE properties can be explained. Due to partially filled CBs, a significant amount of electrons in a metal (10^{22}-10^{23} cm^{-3}) can move quasi-free in a so called electron gas. So, the valence electrons differ from the core electrons that are locally linked to single atoms tremendously. For the calculation in the Drude model several assumptions have been made:

a) In-between two subsequent collisions of an electron with atomic cores, the interactions with other electrons or atomic cores can be neglected. So, Newton's equations of motions can be applied.
b) Collisions of electrons with impenetrable atomic cores are instantaneously.
c) The relaxation time τ defines the average time between two collisions. The probability of an electron to undergo a collision within $\mathbf{d}t$ is given by $\mathbf{d}t/\tau$.

d) Thermal equilibrium of the system is reached only by collisions.

With these assumptions included in the Drude model the empirically observed Wiedemann-Franz law that has already been introduced in 3.2.1 can be derived. By neglecting the phonons, the overall thermal conductivity κ_{el} is only generated by the valence electrons. Similar to phonons described as particles (Eq. 3.17), it can be written for electrons with velocity v_S and specific energy C_v:

$$\kappa_{el} = \frac{1}{3} C_V v_S^2 \tau \qquad 3.26$$

Taking into account elementary charge e, electron density n and electron mass m_e, the conductivity σ can be written as:

$$\sigma = \frac{ne^2\tau}{m_e} \qquad 3.27$$

So, by dividing Eq. 3.26 by Eq. 3.27, an expression for the Wiedemann-Franz law can be found:

$$\frac{\kappa_{el}}{\sigma} = \frac{\frac{1}{3} C_V m_e v_S^2}{ne^2} \qquad 3.28$$

Exchanging $C_V = \frac{3}{2} n k_B$ and $\frac{1}{3} m_e v_S^2 = \frac{3}{2} k_B T$ leads to:

$$\frac{\kappa_{el}}{\sigma} = \frac{3}{2}\left(\frac{k_B}{e}\right)^2 T = \mathbf{1.11} \cdot \mathbf{10}^{-8} \frac{\mathrm{W\Omega}}{\mathrm{K}^2} T = L \cdot T \qquad 3.29$$

In 1933 the Wiedemann-Franz law was improved by the Drude-Sommerfeld theory taking into account that only the electrons at the Fermi-surface contribute to the heat capacity. It turned out that compared to the assumption made by the Drude-model the electronic contribution to the heat capacity and the average square of the velocity is about 100 times smaller and 100 times bigger, respectively. Based on the Drude-Sommerfeld theory the Wiedemann-Franz law (Eq. 3.14) that was previously used to estimate the electronic part of the thermal conductivity can be derived. There Lorenz-factor has been calculated to be $L \approx \mathbf{2.44} \cdot \mathbf{10}^{-8}\ \mathrm{W\Omega}\mathbf{K}^{-1}$. Values similar to the latter Lorentz number have also experimentally observed.[71]

However,[113] the Drude model allows a first approximation about the Seebeck coefficient α that is responsible for the generation of an electric field $\mathbf{E}$ along a temperature gradient ∇T:

$$\mathbf{E} = \alpha \cdot \nabla T. \qquad 3.30$$

In the simplest case a temperature gradient is applied along one dimension. Since the thermal equilibrium is generated by the collisions of the electrons, an electron coming from a hot region $v(x - v\tau)$ carries more energy than one coming from a cold region $v(x + v\tau)$. The average velocity v_Q at a specified location x is given by both:

$$v_Q = \frac{1}{2}[v(x - v\tau) - v(x + v\tau)] \qquad 3.31$$

The MFP $(l = v\tau)$ can also be taken into account for electrons. It can be written as:

$$v_Q = -\tau v \frac{dv}{dx} = -\tau \frac{\mathrm{d}}{\mathrm{d}x} \frac{v^2}{2} \qquad 3.32$$

Transferred to three dimensions and introducing a temperature gradient leads to:

$$\mathbf{v}_Q = -\frac{\tau}{6} \frac{\mathrm{d}v^2}{\mathrm{d}T} \nabla T \qquad 3.33$$

An emerging electric field causes a counter movement of the electrons v_E given by

$$\mathbf{v}_E = -\frac{e\tau}{m} \mathbf{E}. \qquad 3.34$$

In in the equilibrium state, the net current is zero and therefore:

$$\mathbf{v}_Q + \mathbf{v}_E = \mathbf{0} \qquad 3.35$$

Appling Eq. 3.33 and Eq. 3.34 to Eq. 3.35, the TE force can be written as:

$$\alpha = -\left(\frac{1}{3e}\right) \frac{\mathrm{d}}{\mathrm{d}T} \frac{mv^2}{2} = -\frac{C_v}{3ne} \qquad 3.36$$

Known from classic statistic mechanics, C_V can be replaced by $3/2\, nk_B$:

$$\alpha = -\frac{k_B}{2e} = -43\ \frac{\mu\mathrm{V}}{\mathrm{K}} \qquad 3.37$$

Since $\mathbf{C}_V$ must be considered to be smaller than assumed in the Drude model, the absolute value of the Seebeck coefficient in metals is more than a magnitude lower. $\alpha < 0$ can be

observed for metals as well. But in principle already the Drude models shows that moving electrons, having different velocities due to a temperature gradient, are the reason for the generation of an electric voltage.

3.2.2. Semi-classical treatment – Onsager reciprocal relations

Another approach for calculating TE coefficients is provided by the entropy S that is enhanced in each TE device. Eliminating these enhancement would lead to an efficiency identical to the Carnot efficiency. In 1930, Onsager developed a theoretical description of linear non-equilibrium thermodynamic processes.[114] In a general form the thermodynamic forces and fluxes are described. Later on, Callen developed the thermodynamic theory of the TE phenomena in isotropic media.[115]

Although a thermodynamic system contains an assembly of subsystems that cannot be considered to be in equilibrium, the entire one is assumed to be ergodic. Because the microscopic relaxation times are much smaller than the macroscopic one, the system heads back to local equilibrium at each time. Therefore, the classical quasi-static relation can be applied: (The following discussion is based on Ref. 116, a review by C. Goupil et. al.)

$$\mathbf{d}S = \frac{\mathrm{d}Q}{T} \tag{3.38}$$

It can also be extended to the following form that includes $\mathbf{J}^S$ and $\mathbf{J}^Q$ as entropy and heat flux densities, respectively:

$$\mathbf{J}^S = \frac{\mathbf{J}^Q}{T} \tag{3.39}$$

However,[117] the crucial point in Onsager's derivation is the transformation of the first law of thermodynamics including total energy density E, chemical potential μ_e and particle density N

$$\mathbf{d}E = T\mathbf{d}S + \mu_e\mathbf{d}N \tag{3.40}$$

with the conservation of energy and flux given by total energy $\mathbf{J}^E$, heat $\mathbf{J}^Q$ and particle $\mathbf{J}^N$ flux densities into:

$$\mathbf{J}^E = \mathbf{J}^Q + \mu_e\mathbf{J}^N \tag{3.41}$$

Potentials for energy and particle densities are $\mathbf{1}/T$ and μ_e/T, respectively. The corresponding derivatives of the potentials generate the driving forces for the flux densities:

$$\mathbf{F}^N = \nabla\left(-\frac{\mu_e}{T}\right) \tag{3.42}$$

$$\mathbf{F}^E = \nabla\frac{1}{T} \tag{3.43}$$

Following the principle of superposition, flux densities and forces can be derived by a linear set of coupled equations:

$$\begin{bmatrix} \mathbf{J}^N \\ \mathbf{J}^E \end{bmatrix} = \begin{bmatrix} L_{NN} & L_{NE} \\ L_{EN} & L_{EE} \end{bmatrix} \begin{bmatrix} \nabla\left(-\frac{\mu_e}{T}\right) \\ \nabla\frac{1}{T} \end{bmatrix} \tag{3.44}$$

To describe TE coefficients it is useful to rewrite Eq. 3.41 into:

$$\mathbf{J}^Q = \mathbf{J}^E - \mu_e \mathbf{J}^N \tag{3.45}$$

Using

$$\nabla\left(-\frac{\mu_e}{T}\right) = -\frac{1}{T}\nabla(\mu_e) - \mu_e\nabla\left(-\frac{1}{T}\right), \tag{3.46}$$

Eq. 3.44 and Eq. 3.45, an equation for $\mathbf{J}^Q$ can be obtained and similar to Eq. 3.44 it can be written:

$$\begin{bmatrix} \mathbf{J}^N \\ \mathbf{J}^Q \end{bmatrix} = \begin{bmatrix} L_{11} & L_{12} \\ L_{21} & L_{22} \end{bmatrix} \begin{bmatrix} -\frac{1}{T}\nabla\mu_e \\ \nabla\frac{1}{T} \end{bmatrix} \tag{3.47}$$

Upon these set of coefficients (L_{xy}) arising from Onsager's reciprocal relations (Eq. 3.47), conductivity, Seebeck coefficient and electronic part of the thermal conductivity can be derived. Applying isothermal conditions $(\nabla T^{-1} = 0)$ in Eq. 3.47, the electrical current density can be derived:

$$\mathbf{J} = e \cdot \mathbf{J}^N = \frac{-e \cdot L_{11}}{T}\nabla\mu_e \tag{3.48}$$

Due to the electric field $\mathbf{E}$ given by $\mathbf{E} = -\nabla\mu_e/e$, for the isothermal conductivity σ_T it can be written:

$$\sigma_T(\nabla T^{-1} = 0) = -\frac{e \cdot \mathbf{J}}{\nabla\mu_e} = \frac{e^2 \cdot L_{11}}{T} \quad 3.49$$

In absence of any particle transport,

$$\mathbf{J}^N = 0 = -L_{11}\frac{1}{T}\nabla\mu_e - L_{12}\frac{1}{T^2}\nabla T \quad 3.50$$

the derivative of the electrochemical potential can be calculated

$$\nabla\mu_e = -\frac{L_{12}}{L_{11}}\frac{1}{T}\nabla T \quad 3.51$$

and the heat flux density becomes:

$$\mathbf{J}^Q = -L_{21}\frac{1}{T}\nabla\mu_e - L_{22}\frac{1}{T^2}\nabla T \quad 3.52$$

Applying Eq. 3.51 with Eq. 3.52 leads to:

$$\mathbf{J}^Q = \frac{1}{T^2}\left(\frac{L_{21}L_{12}}{L_{11}} - L_{22}\right)\nabla T \quad 3.53$$

Therefore, the electronic part of thermal conductivity at zero electrical current (open circuit) can be assigned to:

$$\kappa_J(\mathbf{J}^N = 0) = -\frac{\mathbf{J}^Q}{\nabla T} = \frac{1}{T^2}\left(\frac{L_{11}L_{22} - L_{21}L_{12}}{L_{11}}\right) \quad 3.54$$

Considering the opposite, thermal conductivity due to the electrons under zero electrochemical gradients (closed circuit), leads to:

$$\kappa_E(\nabla\mu_e = 0) = -\frac{\mathbf{J}^Q}{\nabla T} = \frac{L_{22}}{T^2} \quad 3.55$$

The Seebeck coefficient (α) is defined as the ratio between electrochemical gradient and temperature gradient

$$-\frac{1}{e}\nabla\mu_e = \alpha\nabla T \quad 3.56$$

at zero particle transport (open circuit). Hence, Eq. 3.50 can be applied:

$$\alpha(\mathbf{J}^N = 0) = -\frac{1}{e}\frac{\nabla\mu_e}{\nabla T} = \frac{1}{eT}\frac{L_{12}}{L_{11}} \tag{3.57}$$

Using Eq. 3.39 and 3.52, an expression for the entropy flux density can be found:

$$\mathbf{J}^S = \frac{\mathbf{J}^Q}{T} = \frac{1}{T}\left(-L_{21}\frac{1}{T}\nabla\mu_e + L_{22}\nabla\frac{1}{T}\right) \tag{3.58}$$

With Ohm's law (Eq. 3.48) it can be written:

$$\frac{1}{T}\nabla\mu_e = -\frac{1}{L_{11}e}\mathbf{J} \tag{3.59}$$

So, Eq. 3.58 becomes:

$$\mathbf{J}^S = \frac{L_{21}}{eTL_{11}}\mathbf{J} + \frac{L_{22}}{T}\nabla\frac{1}{T} \tag{3.60}$$

It can be seen that the entropy density flux contains two parts. Because the first summand describes the entropy flux density due to the current density, the average entropy per particle can be defined:

$$S_N = \frac{L_{21}}{TL_{11}} \tag{3.61}$$

Compared to Eq. 3.57, the direct proportionality between Seebeck coefficient and the entropy of a single carrier can be seen:

$$S_N = e\alpha \tag{3.62}$$

Including Eq. 3.57, a comparison between the thermal conductivity at zero electrochemical gradients (Eq. 3.55, κ_E) and at zero particle transport (Eq. 3.54, κ_J) leads to:

$$\kappa_E = T\alpha^2\sigma_T + \kappa_J \tag{3.63}$$

Impressively, Eq. 3.63 exhibits the rise in thermal conductivity, if an electrical current is flowing through a TE material.

In the absence of a magnetic field one obtains:[115]

$$L_{12} = L_{21} \tag{3.64}$$

By utilizing Eq. 3.49, Eq. 3.54 and Eq. 3.57, the transport parameters can also be expressed by TE coefficients (Table 2).

TRANSPORT PARAMETERS	***THERMOELECTRIC COEFFICIENTS***
L_{11}	$\frac{T}{e^2}\sigma_T$
$L_{12} = L_{21}$	$\frac{T^2}{e}\sigma_T\alpha$
L_{22}	$T^3\sigma_T\alpha^2 + T^2\kappa_J$

Table 2 Transport parameters included in Onsager reciprocal relations expressed with TE coefficients

Of course, Table 2 enables the compilation of the Onsager reciprocal relations (Eq. 3.47):

$$\begin{bmatrix} \mathbf{J}^N \\ \mathbf{J}^Q \end{bmatrix} = \begin{bmatrix} \frac{T}{e^2}\sigma_T & \frac{T^2}{e}\sigma_T\alpha \\ \frac{T^2}{e}\sigma_T\alpha & T^3\sigma_T\alpha^2 + T^2\kappa_J \end{bmatrix} \begin{bmatrix} -\frac{1}{T}\nabla\mu_e \\ -\frac{1}{T^2}\nabla T \end{bmatrix} \quad 3.65$$

Eq. 3.65 results in, if $\mathbf{J}^N$ is set into $\mathbf{J}^Q$:

$$\mathbf{J}^N = -\frac{\sigma_T}{e^2}\nabla\mu_e - \frac{\sigma_T\alpha}{e}\nabla T \text{ and} \quad 3.66$$

$$\mathbf{J}^Q = e\alpha T\,\mathbf{J}^N - \kappa_J\nabla T \quad 3.67$$

Exchanging $\nabla\mu_e = -e\mathbf{E}$ and $\mathbf{J}^N = \mathbf{J}/e$ leads to

$$\mathbf{J} = \sigma_T\mathbf{E} - \sigma_T\alpha\nabla T \qquad \text{and} \quad 3.68$$

$$\mathbf{J}^Q = \alpha T\,\vec{\mathbf{J}} - \kappa_J\nabla T. \quad 3.69$$

Finally, by including the electrical resistivity $(\rho = 1/\sigma_T)$, a familiar equation can be derived from Eq. 3.68:

$$\mathbf{E} = \alpha\nabla T + \rho\mathbf{J} \quad 3.70$$

Based on the first law of thermodynamics and the conservation of total energy, heat and particle flux densities have been introduced. A set of transport parameters has been used to connect driving forces and flux densities. Running through some examples has allowed the connection between transport parameters and TE parameters (Table 2). The linkage between Seebeck coefficient, conductivity and electrical part of the thermal conductivity has been shown. Using Onsager's reciprocal relations, simulations can be performed to predict performances in the field of TE.

3.2.3 Mott's formula based on the Boltzmann transport equation

In equilibrium, the distribution of electrons in a solid is given by the Fermi-Dirac distribution:

$$f_0 = \frac{1}{\exp\frac{E-\mu}{k_B T}+1} \qquad 3.71$$

The probability f_0 if an electron state at a given energy E is occupied depends on the chemical potential μ that is similar and identical to the Fermi energy at $T > 0\,\mathrm{K}$ and $T = 0\,\mathrm{K}$, respectively. At $T = 0\,\mathrm{K}$, the Fermi energy is given by the energy of the highest occupied electron state. All lower and higher energies states are completely occupied and empty, respectively. With increasing temperatures, Eq. 3.71 describes a broadening and electron states can be empty and occupied below and above the Fermi-energy. Besides temperature, the probability of an electron state to be occupied can be influenced by external effects. Here, the electron distribution function f is described by electron position **r**, electron wave vector **k** and time t. For the total differential can be written:[118]

$$\mathrm{d}f(\mathbf{r},\mathbf{k},t) = \frac{\partial f}{\partial \mathbf{r}}\mathrm{d}\mathbf{r} + \frac{\partial f}{\partial \mathbf{k}}\mathrm{d}\mathbf{k} + \frac{\partial f}{\partial t}\mathrm{d}t \quad \text{or} \qquad 3.72$$

$$\frac{\mathrm{d}f(\mathbf{r},\mathbf{k},t)}{\mathrm{d}t} = \frac{\partial f}{\partial \mathbf{r}}\frac{\mathrm{d}\mathbf{r}}{\mathrm{d}t} + \frac{\partial f}{\partial \mathbf{k}}\frac{\mathrm{d}\mathbf{k}}{\mathrm{d}t} + \frac{\partial f}{\partial t} \qquad 3.73$$

Exchanging

$$\frac{\mathrm{d}\mathbf{r}}{\mathrm{d}t} = \mathbf{v} \quad \text{and} \qquad 3.74$$

$$\frac{\mathrm{d}\mathbf{k}}{\mathrm{d}t} = \frac{1}{\hbar}\frac{\mathrm{d}\mathbf{p}}{\mathrm{d}t} = \frac{1}{\hbar}\mathbf{F} \qquad 3.75$$

leads to the Boltzmann transport equation:[I]

$$\frac{\mathrm{d}f(\mathbf{r},\mathbf{k},t)}{\mathrm{d}t} = \mathbf{v}\cdot\nabla_{\mathbf{r}}f + \frac{1}{\hbar}\mathbf{F}\cdot\nabla_{\mathbf{k}}f + \frac{\partial f}{\partial t} \qquad 3.76$$

In the case of steady state $(\mathrm{d}f(\mathbf{r},\mathbf{k},t)/\mathrm{d}t = 0)$, Eq. 3.76 becomes:[119]

$$-\left(\frac{\partial f}{\partial t}\right)_{\mathrm{coll}} = (\mathbf{v}\cdot\nabla_{\mathbf{r}}f)_{\mathrm{diffusion}} + \left(\frac{1}{\hbar}\mathbf{F}\cdot\nabla_{\mathbf{k}}f\right)_{\mathrm{field}} \qquad 3.77$$

A scattering mechanism is responsible $(\partial f/\partial t)_{\mathrm{coll}}$ for slowing down electrons if they are driven by an external force. For small deviations f_1 away from the Fermi-Dirac distribution the relaxation time approximation (RTA) can be utilized:

$$f_1 = f - f_0 \qquad 3.78$$

Among others,[120] relaxation time approximation is a widely used approach to solve the Boltzmann transport equation.[118,121] Therefore, the driving mechanism for holding the system in equilibrium or causing a relaxation to f_0 is described by relaxation time $(\tau(\mathbf{k}))$:

$$\left(\frac{\partial f}{\partial t}\right)_{\mathrm{coll}} = -\frac{f_1}{\tau(\mathbf{k})} \qquad 3.79$$

The average relaxation time $\langle\tau(E)\rangle$ for a non-degenerated SCs can be calculated with

$$\langle\tau(E)\rangle = \frac{\int_0^\infty \tau(E)E^{3/2}\left(\frac{\partial f_{eq}}{\partial E}\right)\mathrm{d}E}{\int_0^\infty E^{3/2}\left(\frac{\partial f_{eq}}{\partial E}\right)\mathrm{d}E} \qquad 3.80$$

by including the equilibrium distribution function (f_{eq}):[II]

$$f_{eq} = \frac{1}{\exp(\eta-\xi)+1}. \qquad 3.81$$

$\eta = E/k_BT$ and $\xi = E_F/k_BT$ are used as reduced carrier energy and reduced Fermi-energy, respectively. So, the equilibrium distribution function is almost identical to the Fermi-Dirac-distribution.

Utilizing unit charge q and momentum **k** the spectral conductivity $\sigma(E)$,[13]

$$\sigma(E) = q^2\tau(E)\iint v_x^2(E,k_y,k_z)\,\mathrm{d}k_y\mathrm{d}k_z \qquad 3.82$$

[I] Eq. 3.77, can be also found with $(\mathrm{d}f/\mathrm{d}t)_{\mathrm{coll}}$[118]

[II] Named as A. Shakouri (1996): http://users.soe.ucsc.edu/~ali/ConvTE.html

can be converted into:

$$\sigma(E) \cong q^2\tau(E)\bar{v}^2(E)D(E) \qquad 3.83$$

By integrating over the spectral conductivity, an equation for conductivity and Seebeck coefficient can be obtained:

$$\sigma = \int \sigma(E)\left(-\frac{\partial f_{eq}}{\partial E}\right)\mathbf{d}E \qquad 3.84$$

$$\alpha = \frac{k_B}{q}\frac{\int \sigma(E)\left(\frac{E-E_F}{k_BT}\right)\left(-\frac{\partial f_{eq}}{\partial E}\right)\mathbf{d}E}{\int \sigma(E)\left(-\frac{\partial f_{eq}}{\partial E}\right)\mathbf{d}E} \qquad 3.85$$

Hence, the Seebeck coefficient is proportional to $\langle E - E_F \rangle$. Because the equilibrium distribution function affects Eq. 3.84 and Eq. 3.85, it is also of importance for TE performance. $\partial f_{eq}/\partial E$ is bell shaped, has a width of about k_BT and is centered at E_F. To enhance the power factor $(PF = \alpha^2\sigma)$, most electrons should be at E_F for a high electrical conductivity.[13] Simultaneously, the Seebeck coefficient requires an asymmetric shape of the DOS around E_F. In the case of a parabolic CB, an appropriate example is illustrated in Figure 23. With respect to the Fermi energy, the Peltier coefficient $(\Pi = \alpha T)$ corresponds to the average energy (divided by charge) transported by the majority of carriers.

Thus, also simulations about lower dimensionalities and therefore adapted DOS have been done.[122] But so far, only theoretical progress has been made.

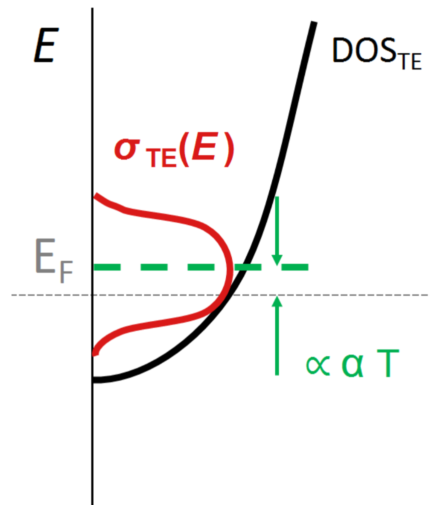

Figure 23 Favored shape of the electron states in a TE material in a parabolic CB (Adapted from Ref. 13)

In the case of degenerated SCs or metals (the Fermi-level lies well above the CB edge), Eq. 3.85 can be transformed into:[123]

$$\alpha = \frac{\pi^2}{3}\frac{k_B^2 T}{q}\frac{\mathbf{d}\ln[\sigma(E)]}{\mathbf{d}E}\bigg|_{E=E_F} \qquad 3.86$$

In the well-known Mott formula, derived in 1969,[124] the derivative of the differential conductivity can be used to calculate the Seebeck coefficient.

3.2.4 Final considerations about TE material properties

In metals, free electrons are only separated by a few Å. But the Pauli Exclusion Principle causes only a small cross section for electron-electron scattering. Thereby at moderate temperatures, electron scattering is dominated by electron-phonon-scattering.[125] In this range Eq. 3.86 can be further simplified:[126]

$$\alpha = \pm\frac{1}{3}\pi^2\left(\frac{k_B}{e}\right)\frac{k_B T}{E_F} \qquad 3.87$$

So, the derivative $\mathbf{d}\ln[E(\sigma)]/\mathbf{d}E$ can be exchanged and it remains a dependency on temperature and Fermi energy. A schematic illustration for electron systems is shown in Figure 24.

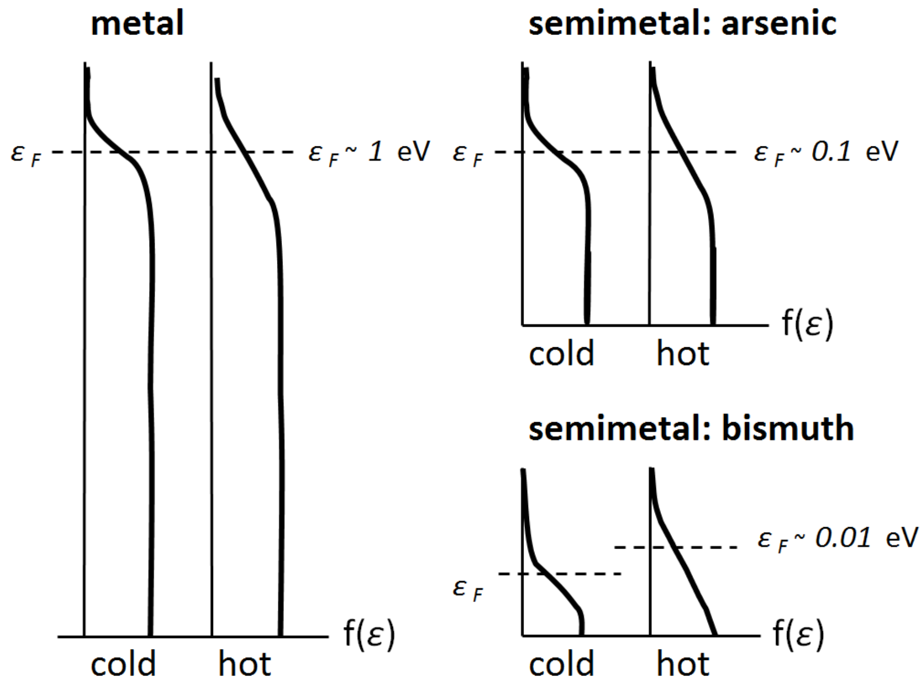

Figure 24 Broadening of the Fermi-Dirac distribution due to a temperature difference (Adapted from Ref. 123 and Ref. 127)

The further the Fermi energy lies within the parabolic CB (metals and degenerated SCs), the flatter the slope of the $DOS = f(E) \propto \sqrt{E}$ becomes.[71] Therefore, chemical potential (labeled as ε_F in Figure 24) shifts less with temperature when electrons move from an occupied into an unoccupied state. If one compares two elements from the fifth main group of the PTE, the less free electron density is obtained by the elements having larger atoms. Compared to arsenic ($n_e = 2.12 \times 10^{20}$ cm^{-3}), assuming a single parabolic CB, the Fermi energy of bismuth ($n_e = 1.88 \times 10^{20}$ cm^{-3}) is closer to the CB edge where the DOS changes the most with energy. So, the difference in chemical potential and total energy of the system between a hot and a cold side differs more than in a metal where the Fermi energy is located in the middle of the CB.

Next to parabolic bands, more complex band structures exist. Often the complexity is increased if elements participate in the crystal structure with valence electrons that are located in additional d- or f-orbitals.

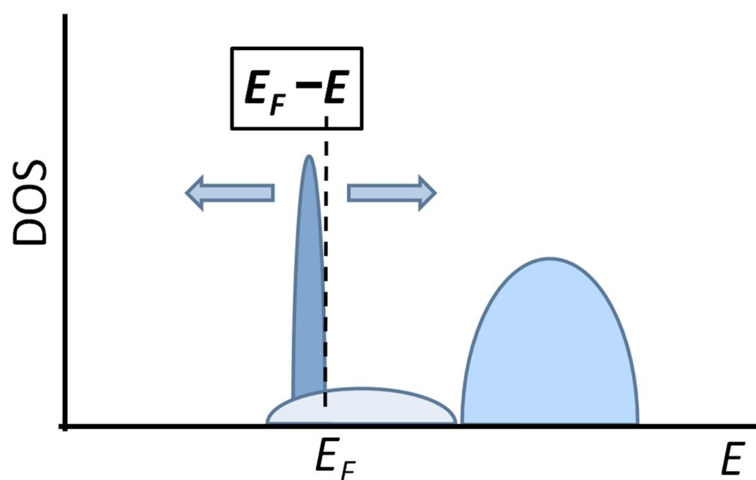

Figure 25 Favorable DOS for a material suitable for TE application (Adapted from Ref. 128)

A suitable band structure for a TE material is shown in Figure 25. Electron states right at the Fermi energy enable a desired electron flow. The sharp feature located at VB edge can be seen as an electron reservoir. Due to changes in the DOS, electrons exhibit a low mobility. Importantly, the steep slope of the VB at E_F causes that many thermally excited electrons have to occupy electron states far above the E_F. So, there is a huge change in the chemical potential between the hot and the cold end of a TE material which then causes high Seebeck voltages. Additionally, the electron mobility is much higher in the band above E_F.

High Seebeck coefficients as well as sufficient conductivities can also be observed by materials with high degeneracy at the VB edge.[129] As illustrated in Figure 26a, it can be observed if the Fermi pockets are generated at low symmetry points. For PbTe, fourfold symmetry is obtained for the L-points of the BZ (orange). Additionally, with a shift of 0.2 eV, 12 bands are located along the Σ-line (blue). By ignoring at this point that the energetic position can also be shifted by the composition of the alloy ($PeTe_xSb_{1-x}$), Figure 26b indicates a shift due to the temperature. While the Σ-band remains unchanged the L-band decreases with temperature. At about 450 K, all 16 pockets have the same energetic position and hence generate the highest degeneracy. Similar to Figure 25, many thermally excited electrons have to find unoccupied electron states far above their VB states. This highly degenerated VB makes PbTe to one of the best TE material at intermediate temperatures.

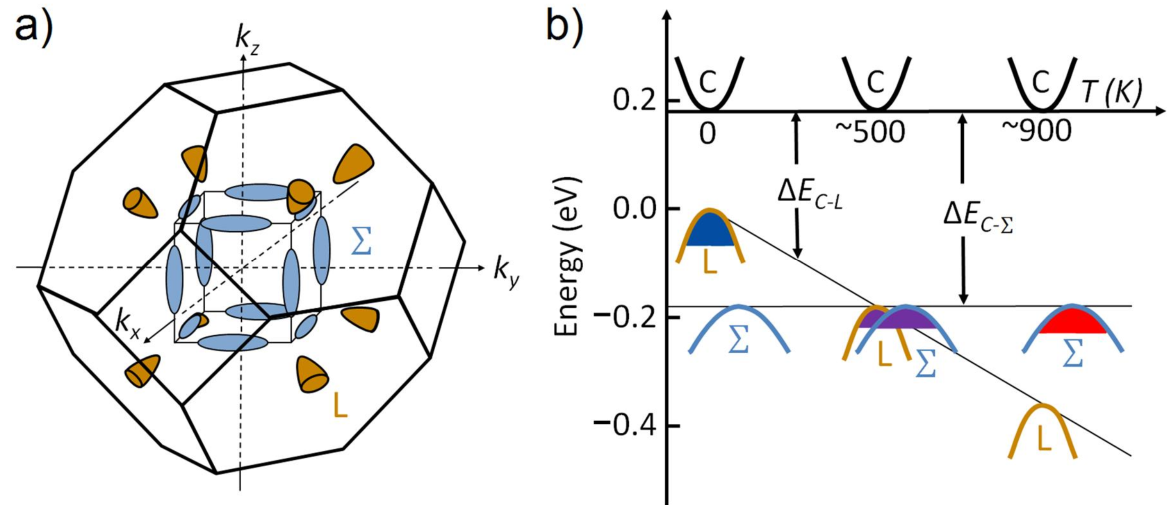

Figure 26 a) BZ of $PbTe_{0.85}Se_{0.15}$ having a low degeneracy at L-point (orange) but a high degeneracy along the Σ-line (blue); b) At different temperatures pockets from the L-point are located at different energies. (Adapted from Ref. 129)

Based on simple consideration, a final reasonable estimation will be done.[130] The Peltier-coefficient Π can be defined as carried energy per unit charge. Applying current densities, it can be written:

$$\Pi = \frac{|\mathbf{j}_q|}{|\mathbf{j}_e|} \tag{3.88}$$

Following equations for energy current density $\mathbf{j}_q$ and charge current density $\mathbf{j}_e$ including electron mobility μ_e can be used:

$$\mathbf{j}_q = n\left(E_C - \mu + \frac{3}{2}k_BT\right)(-\mu_e)\mathbf{E} \qquad 3.89$$

$$\mathbf{j}_e = n(-e)(-\mu_e)\mathbf{E} \qquad 3.90$$

It can easily be seen that instead of the charge -*e*, for the energy current density a factor for the average energy carried by an electron $\left(E_C - \mu + \frac{3}{2}k_BT\right)$ has been exchanged. It is assembled by the difference in CB edge E_C and chemical potential μ plus the thermal energy. Eq. 3.89 and Eq. 3.90 can be inserted into Eq. 3.88:

$$\Pi = -\left(\frac{E_C - \mu}{e} + \frac{3k_BT}{2e}\right) \qquad 3.91$$

By the Kelvin Relation ($\Pi = \alpha \cdot T$), an equation for the Seebeck coefficient can be found:

$$\alpha = -\frac{E_C - \mu}{eT} - \frac{3k_B}{2e} \qquad 3.92$$

Assuming an intrinsic semiconductor (SC) with a gap of **0.44 eV** ($E_C - \mu$ = **0.22 eV**) , at room temperature (RT) a Seebeck coefficient of –**460** µ**V** can be calculated. Notably, for SCs with dominated hole conduction, positive Seebeck coefficients can be obtained by adapting charge and VB edge.

Chapter 4

Structural quality, chemical analysis and surface morphology of thin film TiNiSn and $Zr_{0.5}Hf_{0.5}NiSn$

4.1 Fabrication process – dc magnetron sputter deposition

Beside conventional techniques as Molecular Beam Epitaxy (MBE), Metal-Organic Chemical Vapor Deposition (MOCVD) and Pulsed LASER Deposition (PLD) that base on thermal evaporation, a material carrying stream and LASER ablation, respectively, dc magnetron sputter deposition is a widely used technique for thin film deposition. Here, usually purified argon as an inert gas is let into an ultra-high vacuum (UHV) chamber to obtain ambient pressures of about 10^{-2} mbar. At this pressure, for atoms and molecules MFPs of about 1 cm are present. By applying a few hundred volts to a target, composed of the material intended to be deposited on a substrate, ionized argon ions are accelerated. The diameter of the disk-shaped target material depends on the technical equipment and has been about 50 mm. Heights up to a few millimeters can be varied. Two ring magnets that differ in diameter are connected oppositely poled on the backside of the target to generate a line symmetric magnetic field along the central axis perpendicular to the target surface. Considering the electric field generated by the applied voltage, there is a ring-shaped area away from target where magnetic and electric fields are perpendicular to each other. So electrons, struck out of ionized argon atoms, are accelerated on a spiral away from the target material. Therefore the distance for an electron to leave the electric field originating from the target and the probability to ionize further argon atoms is increased. Due to its increased mass, ionized argon atoms are barely influenced by the magnetic field. Therefore, ions are accelerated almost perpendicular to the target surface. Importantly, with magnets the plasma can be operated at lower argon ambient pressures. So, atoms or clusters that are struck out of the target can reach the substrate that is located a few centimeters away from target. By changing argon ambient pressure, sputtering power and target-to-substrate distance, the amount of material reaching the substrate, its ratio between heavy and light atoms and its kinetic energy can be influenced. With dc

magnetron sputter deposition growth rates of about 1 nms^{-1} can be obtained. To obtain epitaxial film growth, often the substrate temperature is kept at an elevated temperature during growth. Increased substrate temperatures cause enhanced mobility of the surface atoms that allows them to reach the energetically favorable position before arriving atoms complicate further rearrangement. Additionally, surface roughness as well as the formation of several phases can be influenced by the substrate temperature. Thus, for the sputter process there are several and partially interfering growth parameters and their consequences that have to be analyzed for achieving successful epitaxial film growth.

4.2 Epitaxial film quality defined by X-ray diffraction

Initially, TiNiSn thin films have been grown by dc magnetron sputter deposition. To determine deposition rates, film thicknesses have been obtained by X-ray Reflectometry (XRR) measurements. XRR measurements base on the superposition of an X-ray beam that is partially reflected at the film surface and at the film-to-substrate interface. For TiNiSn, surfaces that are sufficiently smooth to detect optical path length differences for constructive and deconstructive interference of both reflected beams, film deposition had to be performed without any additional substrate heating. Even for thicknesses less than 10 nm, metallic films have been known to form island on MgO substrates at enhanced substrate temperatures.[131,132] The deviation in thickness between an amorphous film and an epitaxial film generated by an equal amount of material is neglected. Furthermore, at elevated substrate temperatures no re-evaporation is expected due to the high vapor pressures of titanium, nickel and tin.[I]

In the inset of Figure 27, a XRR scan that is identical to XRD $\theta/2\theta$ scans at grazing incidence has been shown. Instead of 2θ**,** the reciprocal lattice vector has been given on the x-axis and the y-axis is logarithmically scaled. With a sputtering power of 26.5 W and an argon ambient pressure of 4.0×10^{-2} mbar, beside the plateau of total reflection, interference effects have been observed (black). By calculating the index of refraction for TiNiSn and the semi-infinite MgO substrate,[II] the film thickness has been simulated (red). Here 26 nm have been deposited in 26 s that leads to a growth rate for TiNiSn of

[I] Vapor pressures for a variety of elements are given at MBE-Komponenten – Dr. Karl Eberl: http://www.mbe-components.com/applications/vap_data.html
[II] The Scattering Length Density Calculator provided by the National Institute for Standard and Technology (NIST) has been used to determine the index of refraction: http://www.ncnr.nist.gov/resources/sldcalc.html

1.0 nms^{-1}.[I] For further film analysis, growth parameters could have been changed. Thus growth rates have been slightly varied and are not explicitly given if results are not influenced thereby.

Analog to Bragg's law (Eq. 4.2) that describes the diffraction on crystal planes, instead of 2θ, q has been used for illustration of the XRR measurements:

$$q = 2\left(\frac{2\pi}{\lambda}\right)\sin\theta \quad (4.1)$$

Using the index of refraction of a thin film, its thickness can be calculated by the distances of the equidistant maxima or minima. As mentioned above, XRR scans have been simulated and fitted by Parrat32.

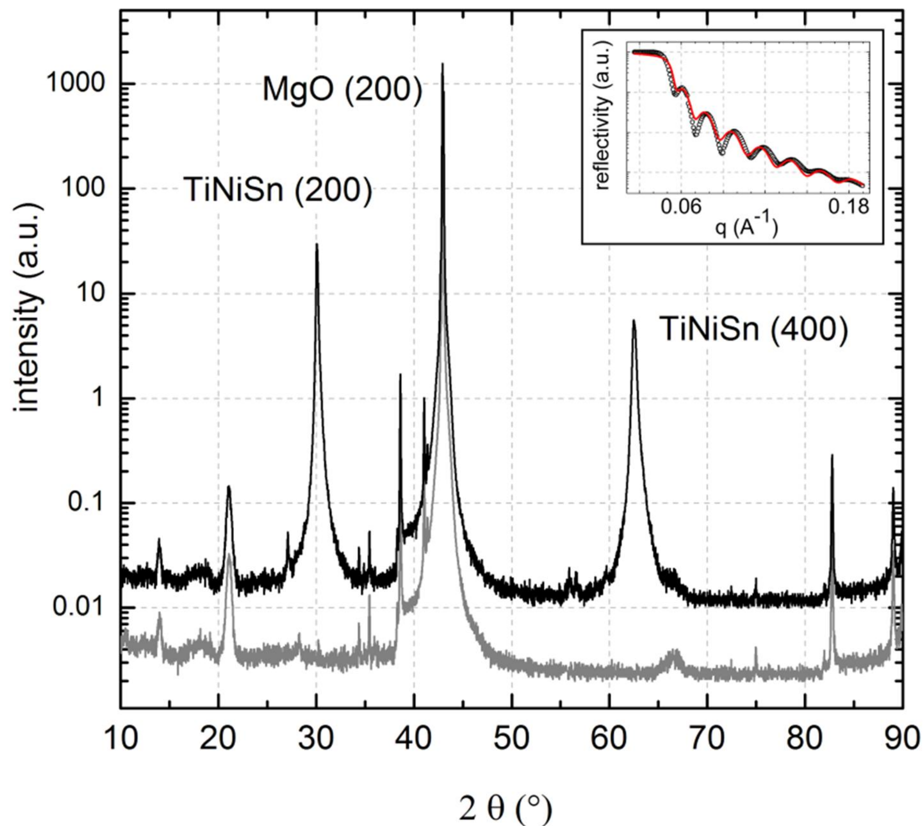

Figure 27 XRD $\theta/2\theta$ and XRR (inset) scans of TiNiSn layers on MgO (100) (black); A XRD $\theta/2\theta$ scan of bare a MgO (100) substrate is shown for comparison (gray).

For comparison, a diffraction pattern of a bare MgO (100) substrate has been shown in Figure 27 (gray). Parasitic radiation (e.g. Cu $\mathbf{K}_\beta$, W $\mathbf{L}_\alpha$) which exists in addition to the main Cu $\mathbf{K}_\alpha$ radiation, leads to additional lines for the intense substrate reflections. Due to the crystal quality and the macroscopic size of the MgO substrates, the diffraction peak

[I] Parratt32 has been used to simulate the XRR scans.

labeled MgO (200) has been the most intensive one. Cu $\mathbf{K}_{\alpha_1}$ and Cu $\mathbf{K}_{\alpha_2}$ radiation with a wave length λ of 1.540598 Å and 1.544426 Å, respectively, and a cubic lattice constant for MgO of 4.21 Å have been used for calculation.[133,I] Identical to the calculation, a double peak structure at 42.93° and 43.03° has been measured in the XRD diffractogram (not resolved in Figure 27).

Additional diffraction peaks can be observed in the XRD $\theta/2\theta$ scan, if thin film TiNiSn with a thickness of 240 nm (black) has been deposited at substrate temperatures of about 500°C. Indicated by the (200) and (400) diffraction peaks, textured polycrystalline TiNiSn films with [100] orientation perpendicular to the film surface have been generated at this sputter conditions. According to Bragg's law

$$\sin\theta = \frac{n\cdot\lambda}{2\cdot d} \qquad 4.2$$

for equal planes of diffraction *n*, peaks generated by crystals with a larger lattice constants *d* occur at smaller angles 2θ. As it is presented in chapter 2, for TiNiSn lattice constants of about 5.94 Å have been reported. Appropriate to the calculation, the (200) and (400) diffraction peaks have been found at 30.06° and 62.48°, respectively. As it has been reported also for bulk samples,[62] beside these diffraction peaks no foreign phases have been observed for TiNiSn.

Using the Scherrer formula[134]

$$L = \frac{0.93\cdot\lambda}{\Delta 2\theta\cdot\cos\theta} \qquad 4.3$$

that includes the full width half maximum (FWHM) $\Delta 2\theta$ and the position θ of the (200) diffraction peak, perpendicular to the film surface a structural coherence length of about 55 nm has been estimated. Due to the film thickness of about 240 nm and the fact that similar structural coherence lengths have been determined for several film thicknesses, TiNiSn films can be seen to consist of several grains with an out-of-plane size of about 55 nm.

For the two-circle diffractometer that was used to measure the diffractogram shown in Figure 27, X-ray source and X-ray detector have been located in the plane perpendicular to the to the film surface. Thus, statements about out-of-plane symmetry can be done by searching diffraction spots in specular alignment. Angles between incident beam and film

[I] Simulations of XRD diffractograms have been performed with Powder Cell

surface θ and incident and diffracted beam 2θ are of importance. If the sample can additionally be tilted perpendicular to plane of incident and diffracted beam, and be rotated perpendicular to the film surface, crystallographic in-plane properties can also be revealed. Due to its possible motions, the instrument is called four-circle diffractometer.

A measurement done by the four-circle diffractometer reveals the origin of the strongly textured polycrystalline growth of the TiNiSn on the MgO (100) substrate. After the orientation of the MgO substrate is known by initial calibration measurements, three diffraction spots have been detected and assigned for determining the orientation of the TiNiSn film on top. Thus, a path called Φ-scan can be set that includes expected in-plane diffraction peaks. In the case of TiNiSn where (200) and (400) diffraction peaks have been observed out of plane, $\langle\mathbf{111}\rangle$ reflections were selected to be measured in-plane. As it is shown in Figure 28, expected fourfold symmetry that is indicated by the four peaks (solid line) has been observed. Because of the absence of diffuse scattering, the high peak to noise ratio indicates that the TiNiSn thin film consists of grains that have a perfect preferential orientation of all principle axes. With respect to the MgO (100) substrate, a rotation about 45° has been measured. Thus, [100] direction of TiNiSn aligns parallel to the [110] of MgO. Considering the periodicity along the [110] direction of about $\sqrt{\mathbf{2}}$ x 4.21 Å = 5.95 Å, leads to a lattice mismatch of less than 1 %.

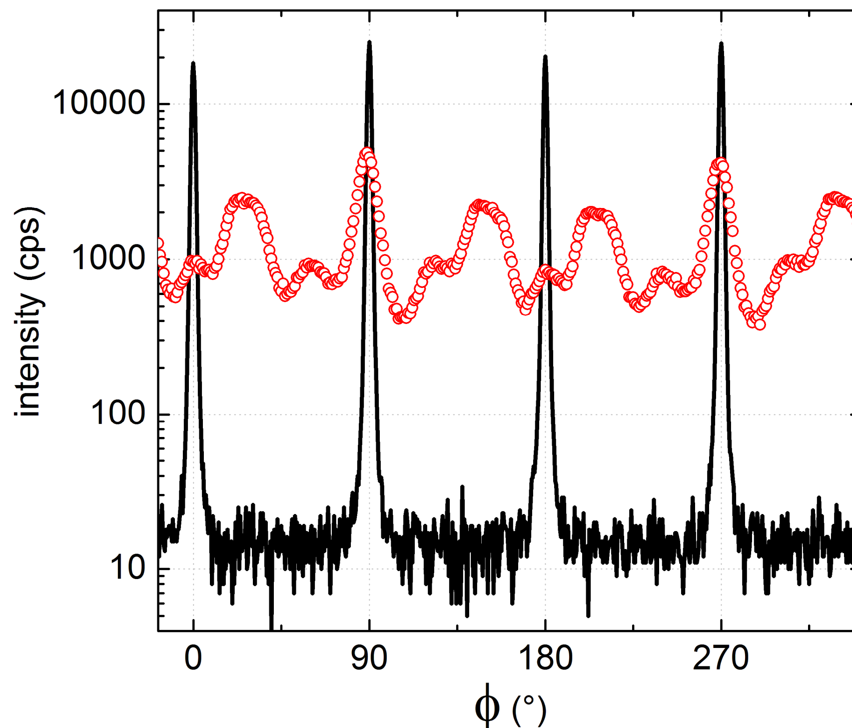

Figure 28 Φ-scan including the <111> reflections of a TiNiSn layers on MgO (solid line) and Al_2O_3 (dotted line) substrates

Besides MgO, Al_2O_3 substrates were used for the deposition of thin film TiNiSn. From the observed low ratio of peak height to background intensity shown in Figure 28 polycrystalline thin film TiNiSn deposited on Al_2O_3 $(11\bar{2}0)$ exhibits only weak crystallographic in-plane order (dotted line). According to the four circle XRD measurements the [001] in-plane direction of the Al_2O_3 $(11\bar{2}0)$ substrate and the [100] axis of most TiNiSn crystallites are perpendicular to each other. For this alignment the lattice mismatch is almost 10 %. However, the ordering perpendicular to the surface is comparable for films deposited on both substrate materials. In contrast to growth on MgO (100), for TiNiSn films deposited on Al_2O_3 $(11\bar{2}0)$ substrates, out-of-plane (110) textured growth has been found. Still, the best results were achieved with growth conditions similar to the ones used for MgO substrates. The FWHM of the (220) diffraction peaks measured with $\theta/2\theta$ have been 0.35°. Thus, textured TiNiSn grains with [110] out-of-plane orientations and diameters of about 26 nm have been grown on Al_2O_3 $(11\bar{2}0)$.

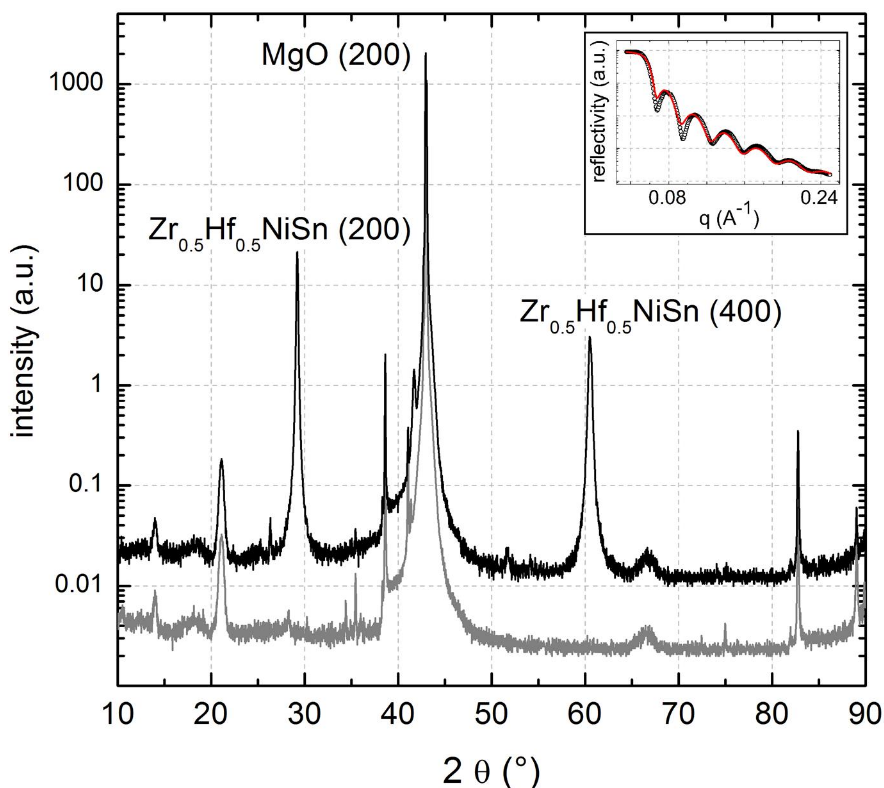

Figure 29 XRD $\theta/2\theta$ and XRR (inset) scans of $Zr_{0.5}Hf_{0.5}NiSn$ layers on MgO (100) (black); An XRD $\theta/2\theta$ scan of a bare MgO (100) substrate is shown for comparison (gray).

Besides TiNiSn films, also $Zr_{0.5}Hf_{0.5}NiSn$ film have been fabricated by dc magnetron sputter deposition. In the same sputter chamber, using an identically constructed sputter

cathode, an additional $Zr_{0.5}Hf_{0.5}NiSn$ target has been installed. Similar to TiNiSn, an argon ambient sputter pressure of 4.0 x 10^{-2} mbar has been found to be appropriate. With an applied sputter power of 23 W, a film thickness of 20 nm has been deposited while the sample stayed above the running cathode for 20 s. Based on the XRR measurement, shown in the inset of Figure 29, the growth rate of 1 nms^{-1} has been calculated. Again, films designated for growth rate determination were grown at RT.

Strongly textured polycrystalline films were obtained if elevated substrate temperature were applied. As the XRD $\theta/2\theta$ scan, shown in Figure 29, reveals, applying a substrate temperature of 500°C enables growth of strongly textured polycrystalline $Zr_{0.5}Hf_{0.5}NiSn$ films. Here, the $Zr_{0.5}Hf_{0.5}NiSn$ (200) film peak is found at 29.21°. According to the 2θ diffraction angle, $Zr_{0.5}Hf_{0.5}NiSn$ films with an out-of-plane lattice constant of 6.11 Å have been fabricated. This is in good agreement with $Zr_{0.5}Hf_{0.5}NiSn$ bulk samples.[57] Using Eq. 4.3, based on the FWHM of the $Zr_{0.5}Hf_{0.5}NiSn$ (200) diffraction peak (0.18°) an out-of-plane crystallite size of 45 nm has been obtained. Thus, compared to TiNiSn deposited on MgO (100), smaller out-of-plane crystallite sizes have been observed for $Zr_{0.5}Hf_{0.5}NiSn$ films.

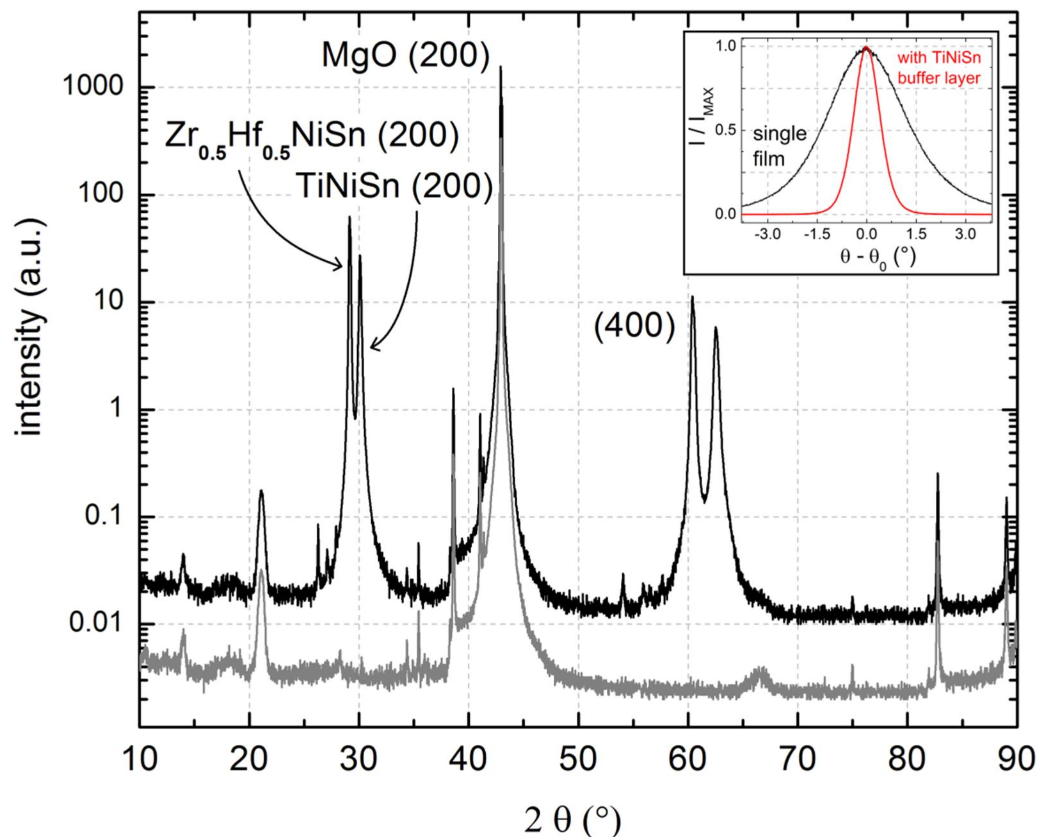

Figure 30 XRD $\theta/2\theta$ scan of a $Zr_{0.5}Hf_{0.5}NiSn$/ TiNiSn bilayer on MgO(100); Normalized rocking curves of $Zr_{0.5}Hf_{0.5}NiSn$ (200) diffraction peaks are illustrate in the inset.

Enhanced crystallographic quality has been received for $Zr_{0.5}Hf_{0.5}NiSn$ films if TiNiSn buffer layers were initially sputtered on the MgO (100) substrate. A corresponding XRD $\theta/2\theta$ scan is shown in Figure 30. At a substrate temperature of 500°C, 144 nm $Zr_{0.5}Hf_{0.5}NiSn$ have been deposited on 234 nm TiNiSn. Due to the differing out-of-plane lattice constants of 6.11 Å and 5.94 Å, respectively, two separate diffraction peaks were observed. Compared to the single $Zr_{0.5}Hf_{0.5}NiSn$ films, here the FWHM of the (200) diffraction peak has decreased from 0.18° to 0.15°. According to Eq. 4.3, out-of-plane crystallite sizes of 55 nm have been formed. Thus, similar crystal dimensions have been obtained for both HH compounds.

An even more important finding than the increased crystallite size is illustrated in the inset of Figure 30. Rocking curves or ω-scans are used to measure the tilt between several crystals. By holding the detector at a fixed 2θ position equal to the observed (200) diffraction peak, the sample is rotated to measure the spreading of crystallites that contribute to the (200) diffraction peak. Therefore the inset in Figure 30 illustrates that the FWHM of the rocking curves for the $Zr_{0.5}Hf_{0.5}NiSn$ films with and without a TiNiSn buffer layer increases from 1.0° to 3.1°. Thus, a TiNiSn buffer layer enhances the quality of the $Zr_{0.5}Hf_{0.5}NiSn$ layer.

By the utilization of a TiNiSn buffer layer, $Zr_{0.5}Hf_{0.5}NiSn$ films have been fabricated with a comparable crystallographic quality to TiNiSn films. Here, $Zr_{0.5}Hf_{0.5}NiSn$ films are composed of crystallites with out-of-plane sizes of about 55 nm. Identical crystallite sizes are obtained for TiNiSn films directly deposited on MgO (100). For both films the FWHMs of rocking curves, measured at the (200) diffraction peak, are about 1.0°.

4.3 Stoichiometric composition of TiNiSn and $Zr_{0.5}Hf_{0.5}NiSn$ films

To determine the elemental composition of the films, Rutherford Backscattering (RBS) measurements were performed. Figure 31 shows the amount of elastically backscattered He^+ ions as a function of retained energy of a bilayer containing TiNiSn (234 nm) and $Zr_{0.5}Hf_{0.5}NiSn$ (190 nm) deposited on MgO.

After ionizing He atoms, they are powerfully accelerated by passing several subsequently arranged capacitor plates. Finally, the He^+ ions have a kinetic energy of 1290 keV and are shot perpendicular on the film surface. By the interaction with electrons, He^+ ions continuously lose energy while passing matter. That goes on until a He^+ ion strikes an atomic core and becomes elastically backscattered. Depending on the

mass of the atomic core, the He^{+} ion retains energy and moves back to the film surface. Here, the amount of He^{+} ions is counted as a function of their energy. As is can be seen in Figure 31, the dotted line has been the spectra obtained by the measurement. The atomic composition is given by comparing a simulated spectrum (solid line) as a sum of different atomic masses distributed with film depth (dashed lines) with the actual measured spectra. By comparing nickel and tin with titanium, zirconium and hafnium, the principle of the measurement can easily be seen. Since nickel and tin are present in TiNiSn and $Zr_{0.5}Hf_{0.5}NiSn$, their single contribution to measurement is about twice in width. Due to varied scatter probabilities for nickel and tin in TiNiSn and $Zr_{0.5}Hf_{0.5}NiSn$, for almost identical atomic concentrations, steps in counts have been simulated for both elements. The broadening of the step arises from an additional interlayer that is characterized below.

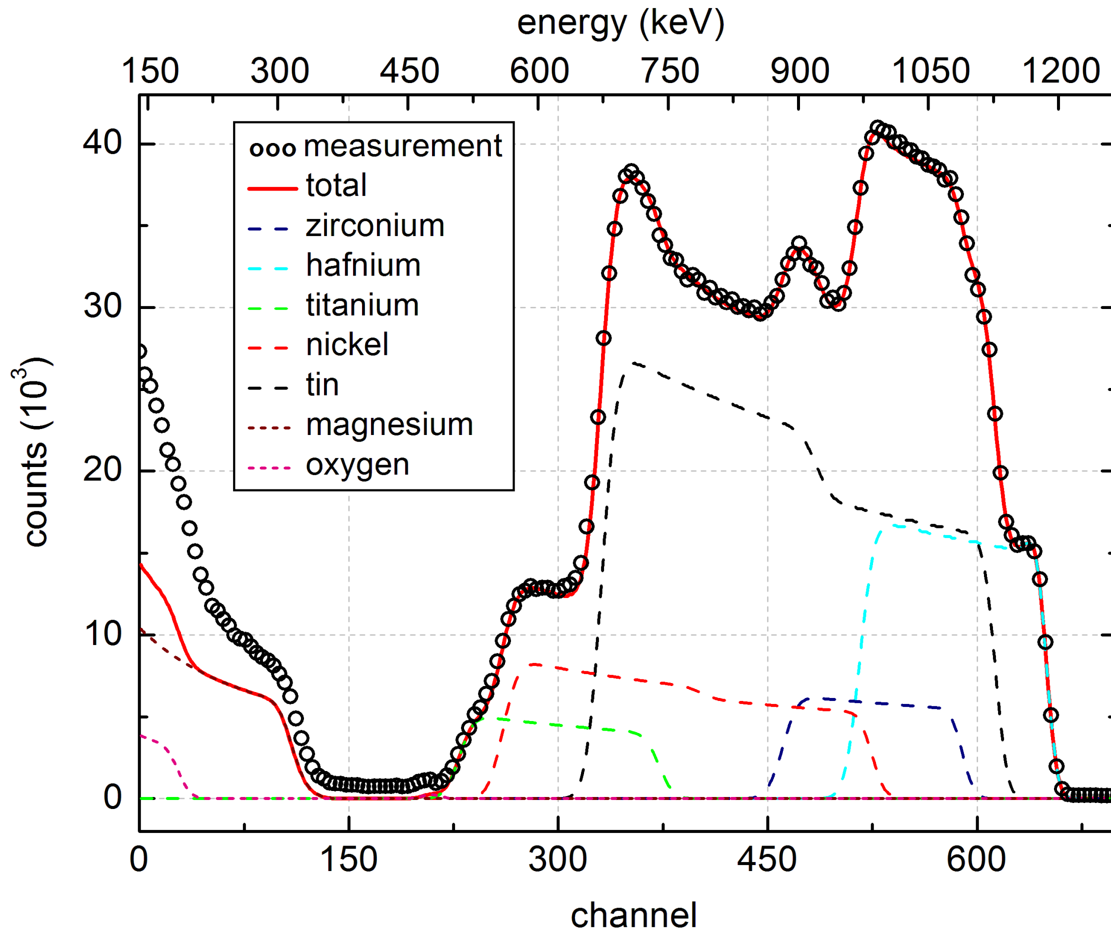

Figure 31 RBS spectra and fit of a $Zr_{0.5}Hf_{0.5}NiSn$/TiNiSn bilayer on MgO(100)[I]

[I] Utilizing a Van de Graaff Accelerator built by High Voltage Engineering (1959) the RBS measurement has been done by Dr. Martin Finsterbusch at the Montana State University.

A last remark concerning the principles of RBS measurements is about hafnium (light blue). Certainly, He^{+} ions with highest kinetic energies are backscattered by the heaviest element. Appropriate to the atomic mass, the onset of He^{+} ions backscattered by tin (black), zirconium (blue) and nickel (orange) follows subsequently. Since multiple scattered ions are not considered in the fit, the deviation between simulation and measurement increases at lower energies.

According to the simulation, a 5 nm oxide layer consisting of $Zr_{0.8}Hf_{1.2}O_4$ is formed at the surface. The interface between TiNiSn and $Zr_{0.5}Hf_{0.5}NiSn$ was fitted with a 12 nm thick layer with atomic percentages of 4 %, 2 %, 28 %, 32 % and 34 % for zirconium, hafnium, titanium, nickel and tin, respectively. According to Atomic Force Microscopy (AFM) measurements, the elemental composition is mainly due to interface roughness rather than interdiffusion. Both cannot be distinguished by the RBS measurement. For the TiNiSn layer, 31.0 %, 33.5 % and 35.5 % have been calculated for titanium, nickel and tin, respectively. 15.5%, 16.5%, 34.0% and 34.0% have been obtained for zirconium, hafnium, nickel and tin concentrations in the $Zr_{0.5}Hf_{0.5}NiSn$ film from the RBS measurement.

Additionally, Energy-Dispersive X-ray (EDX) spectroscopy measurements were performed to measure the elemental composition of the films. Here, with 20 keV an electron beam is accelerated onto the film surface. Within the film, electrons are excited into empty states. Their left states are filled by other electrons. Among others, the energy difference can be released by electromagnetic radiation. Thus for several elements, different X-ray radiation can be observed. By the detection of spectral X-ray intensities, elemental analysis can be done. Due to the probing depth of EDX measurements single films with a thickness of 1 µm have been grown. For TiNiSn, 31.2 %, 33.5 % and 35.3 % have been calculated for titanium, nickel and tin, respectively. For $Zr_{0.5}Hf_{0.5}NiSn$ 16.6 %, 15.5 %, 34.8 % and 33.1 % have been detected for zirconium, hafnium, nickel and tin, respectively.

Cross-plane images have been obtained by High-Angular Annular Dark Field in Scanning Transmission Electron Microscopy (HAADF-STEM) image mode. Therefore samples had to be prepared by Focused Ion Beam (FIB). The outcome can be seen in the inset of Figure 32. While later on, the focus will be set on the images, here an EDX line scan has given answers about the initial film growth of TiNiSn.

About each nanometer, several EDX measurements with a spot size diameter of 0.7 nm have been taken. Starting at the MgO substrate, compositional analyses were

performed along a line within the cross section and finally finished in the TiNiSn film (red line in the inset of Figure 32). In the spectra each dot represents an EDX measurement. Starting at the MgO substrate without any TiNiSn, accumulated titanium has been found at the MgO/TiNiSn interface.

Titanium, but also zirconium and hafnium,[135] are known to be very reactive at interfaces. At SiO_2 surfaces, deposited titanium forms TiO_2 by extracting oxygen atoms from SiO_2.[136] Engaged silicon atoms react also with titanium by the formation of $TiSi_2$. Both reactions take place by heat exposure.

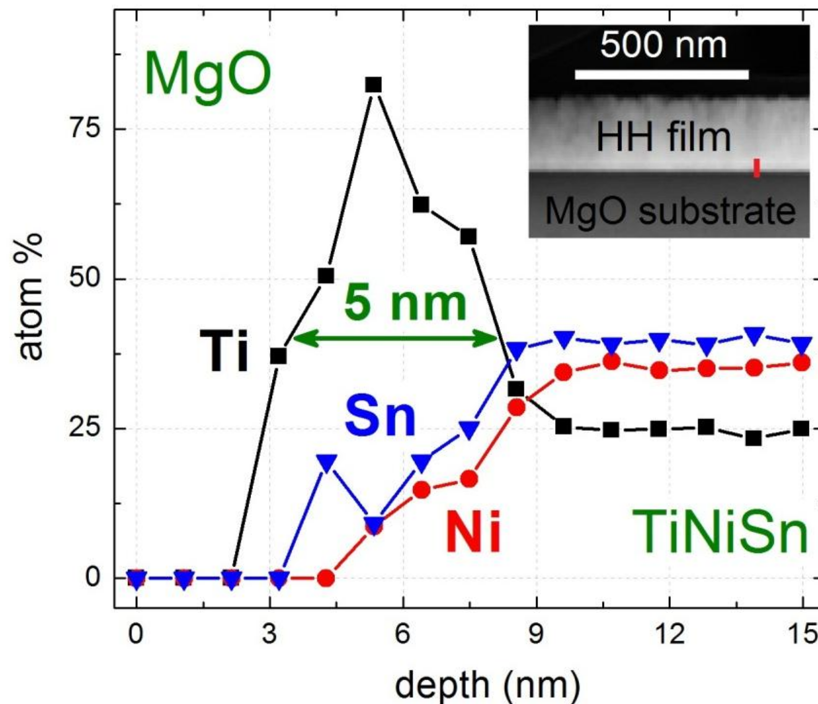

Figure 32 Atomic compositions at the MgO/TiNiSn interface measured by an EDX line scan; The inset shows an image of the cross section taken by an electron microscope (HAADF-STEM)[I].

For titanium on MgO(100) substrates epitaxial growth has been observed.[137] The growth was done at a substrate temperature of about 273 K. Interestingly, no significant amount of TiO_x but a structural transformation has been found for film thicknesses from 4 nm to 6 nm. Here, the titanium layer changes from fcc to hexagonal close-packed (hcp) structure. Two years earlier, in 1997, this structural transformation has been also found by T. Harada et. al. but addressed to very little amounts of desorbed water at a freshly cleaved MgO surface.[138] Thus, initially growing titanium layers contain defects as TiH_x

[I] The measurement was done at the EMPA (Eidgenössische Materialprüfungs- und Forschungsanstalt) by Myriam Haydee Aguirre

and TiO_x. These heal out and finally the hcp structure can be observed. All addressed titanium films have been grown by thermal evaporation under UHV conditions. Similar to titanium deposition on SiO_2, on MgO interdiffusion has been observed by T. Suzuki.[139] Here, 4 ML of magnesium have been exchanged.

Although different results have been found for titanium deposition, remarkable effects have been observed. The EDX line scan shown in Figure 32 indicates inhomogeneous behavior at the TiNiSn/MgO interface. The extraordinary oxygen affinity of titanium seems to play also a key role for strongly textured polycrystalline HH film growth. TiNiSn growths on top of an initially forming titanium seed layer. Although oxygen affinity is also known for hafnium and zirconium,[135] here statements about a seed layer containing zirconium or/and hafnium at the $Zr_{0.5}Hf_{0.5}NiSn$/MgO interface cannot be done. If similar to titanium at the TiNiSn/MgO interface, a seed layer containing zirconium, hafnium or both elements, has formed at the $Zr_{0.5}Hf_{0.5}NiSn$/MgO interface, the presence of non-epitaxial growth could be the difference. On MgO (100), initial titanium layer growth starts with a fcc-structure. According to Kado et. al.,[137] for titanium with a fcc structure, lattice constants from 4.01 Å to 4.42 Å have been reported. Deposited on an aluminum substrate, 4.15 Å has been observed by Kim et. al.[140] Assuming a similar lattice constant for fcc titanium deposited on MgO (100) results in a lattice mismatch of less than 1.5 %. Theoretically, fcc lattice structures have also been considered for zirconium and hafnium. Crystallized in a fcc structure lattice constants of 4.11 Å, 4.52 Å and 4.48 Å have been calculated for titanium, zirconium and hafnium, respectively.[141] Beside others,[142] disclaiming the natural existence of fcc lattice structures for all three elements, importantly, for zirconium and hafnium deposited on MgO (100) lattice mismatches of 7.4 % and 6.4 % would have formed, respectively.

Therefore, about the growth of $Zr_{0.5}Hf_{0.5}NiSn$ directly deposited on MgO (100) substrates only assumptions can be made. Compared to TiNiSn, where an initial titanium growth seems to be the key for further film growth, either a seed layer containing zirconium or hafnium has not been formed at all or worse epitaxial growth has been developed due to the larger lattice mismatch. Due to similarity in the lattice constants of TiNiSn and $Zr_{0.5}Hf_{0.5}NiSn$, the generation of a zirconium and/or hafnium seed layer with worse epitaxial order can be favored.

Due to the formation of the titanium seed layer, the EDX line scan shown Figure 32 demonstrates a depletion of titanium in the ongoing film growth that lasts over at least a range of 5 nm. Here, a stable atomic composition for titanium, nickel and tin of 25.4 %,

35.6 % and 39.04 % has been determined, respectively. But several EDX measurements have shown that the titanium depletion due to the adhesion layer heals out for thicker films. A further EDX measurement was performed at EMPA. The atomic composition in TiNiSn films has been determined to be 31,7 %, 34,3 % and 34,0 % for titanium, nickel and tin, respectively. Similar EDX measurements were performed for $Zr_{0.5}Hf_{0.5}NiSn$. Due to the large probing depth, again films having a thickness of 1 µm have been fabricated. An atomic composition of 18.8 %, 15.1 %, 34.9 % and 33.2 % has been determined for zirconium, hafnium, nickel and tin, respectively.

HH thin film	elements	RBS	EDX (1)	EDX (2)
TiNiSn	*titanium*	31.0 %	31.2 %	31.7 %
	nickel	33.5 %	33.5 %	34.3 %
	tin	35.5 %	35.3 %	34.0 %
$Zr_{0.5}Hf_{0.5}NiSn$	*zirconium*	15.5 %	16.6 %	18.8 %
	hafnium	16.5 %	15.5 %	15.1 %
	nickel	34.0 %	34.8 %	34.9 %
	tin	34.0 %	33.1 %	33.2 %

Table 3 Summarized atomic compositions of TiNiSn and $Zr_{0.5}Hf_{0.5}NiSn$ films measured by RBS and EDX spectroscopy

The chemical compositions of TiNiSn and $Zr_{0.5}Hf_{0.5}NiSn$ thin films determined by RBS and two EDX measurements are summarized in Table 3. Variation from the stoichiometrically aspired composition can be due to target composition, inhomogeneous sputtering or mass dependent MFPs within the plasma. While RBS is not suitable for identification of contaminants with a lower mass than hafnium (heaviest element in the film), such impurities have not been observed by EDX.

4.4 Surface morphology of TiNiSn and $Zr_{0.5}Hf_{0.5}NiSn$ films

Beside the structural quality that has been discussed above, the surface morphology plays an important role in thin film technology. In general, uniformly coated substrates with one specified thickness are preferred. Here, the 3ω method is finally intended to measure cross-plane thermal conductivity using a small heater stripe that is directly deposited onto the film surface. Because for the analysis of the measurement a

homogeneous film thickness as well as one dimensional heat propagation is assumed, uniform films and smooth surfaces are required as well.

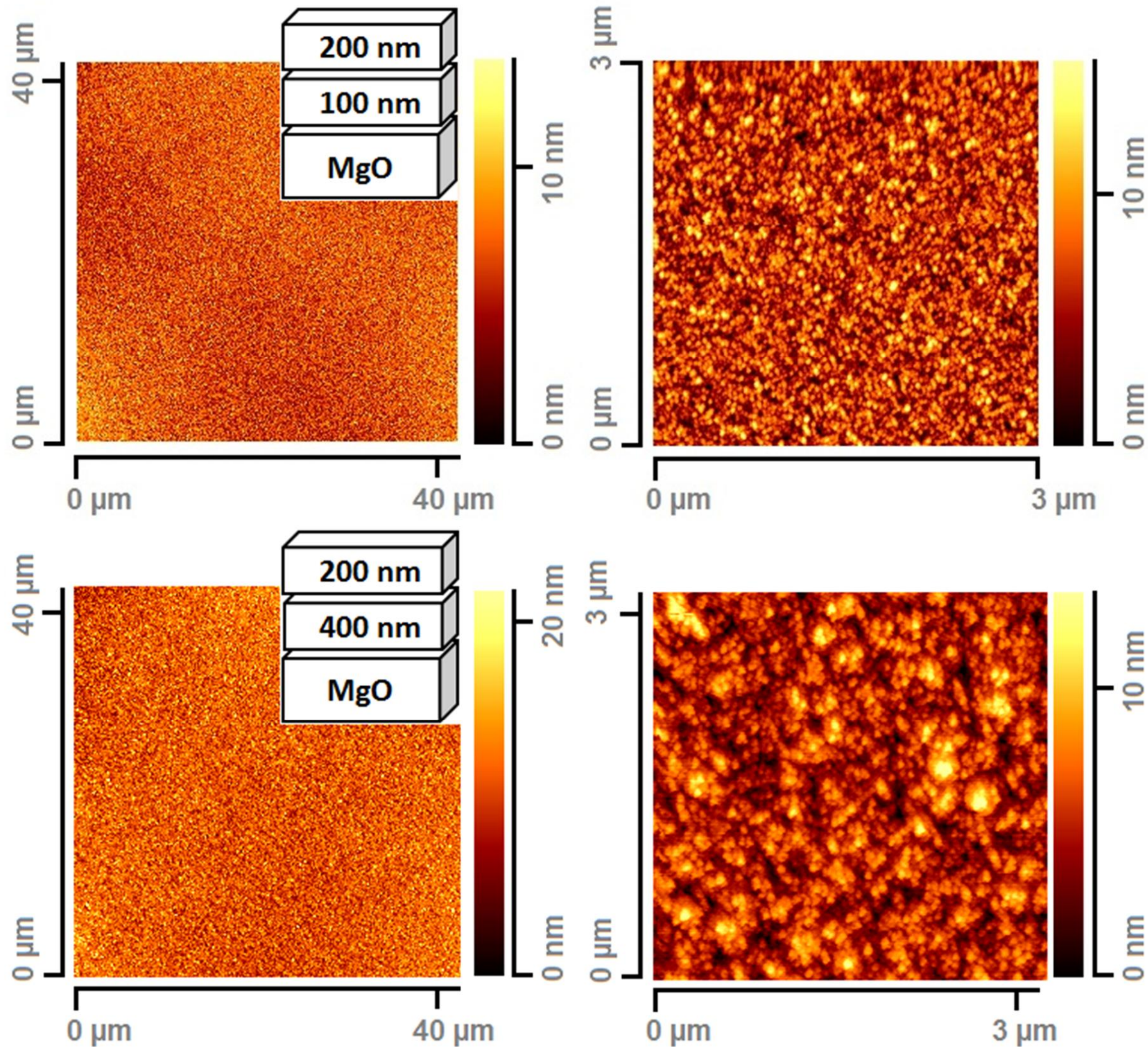

Figure 33 AFM images taken from two bilayers grown at a substrate temperature of 420°C; Giving the individual layer thickness, $Zr_{0.5}Hf_{0.5}NiSn$ has been deposited on TiNiSn. In each row identical samples, but varied magnifications are shown.

AFM measurements (tapping mode) were performed to discover the surface morphology of TiNiSn and $Zr_{0.5}Hf_{0.5}NiSn$ films. For the measurement, a small tip that is connected to a cantilever is oscillated about 80 nm away from the surface. While the tip oscillates, it is moved in two dimensions over the sample surface. Consequently, the distance between sample and tip is changed by surface irregularities. In general, the attraction caused by Van der Waals forces, dipole-dipole interaction and electrostatic forces rises for smaller distances. By applying the resonance frequency of the cantilever even tiny changes in tip-to-surface distance decrease the amplitude of the oscillation. The amplitude is measured by photo diodes detecting LASER light that is reflected on the

backside of the oscillating tip. Using a piezo element the distance between the tip and the surface of the film is adjusted until the cantilever oscillates again with the resonance frequency. Therefore the tip is subsequently moved parallel and perpendicular to the surface. Among others, this motion can be illustrated as two dimensional pictures.

Using the described AFM measurement in combination with XRD analyses, an optimum substrate temperature has been identified to be 420°C. Compared to samples fabricated at substrate temperatures of 500°C, smoother surfaces have been observed while the crystallographic quality remains at a high level. Two examples are shown in Figure 33. The schematic assemblies with corresponding layer thicknesses of the measured bilayers containing $Zr_{0.5}Hf_{0.5}NiSn$ on a TiNiSn buffer layer are given in the left AFM images. Here, a surface area of 40 µm x 40 µm is shown for both samples. At their right hand side, an enlarged area of 3 µm x 3 µm ensures a detailed resolution of the same surface. Being very important for further measurements, at the scale of 40 µm x 40 µm, larger surface irregularities have not been identified. The grain structure of the surface can only suggestively be seen in the AFM image with an area of 40 µm x 40 µm and becomes more dissolved in the image with the higher magnification. Here, the grain structure is much better resolved. The comparison between the thinner (above) and the thicker (below) bilayers exhibits the development of grain sizes with film thickness. In general, larger grains have been observed for thicker films. The influence of individual TiNiSn or $Zr_{0.5}Hf_{0.5}NiSn$ layer thickness on surface roughness has not been investigated. Similar to layer thickness, enhanced surface roughness has been found for higher substrate temperatures applied during the growth process (not shown).

Based on further experimental results, in the following discussions, the observation about surface roughness will be continued showing consistent results. Coincidently, surface roughness is increased with layer thickness and substrate temperature. While layer thickness is partly restricted by the intended measurement, most of the following samples have been fabricated at 420°C.

Chapter 5

Vanadium buffer layer – crystallographic quality enhancement of half-Heusler thin films

5.1 Introduction

Following the discussion about initial film growth of TiNiSn on MgO (100) (see Figure 32) certainly raises the question about a buffer layer to prevent the formation of the titanium seed layer at the TiNiSn/MgO interface. Although it has been proven to be essential for further TiNiSn film growth, the resulting titanium depletion within adjoining grains, prohibits the formation of stoichiometric TiNiSn. By using a buffer layer this titanium depletion could be prevented. Thus the structural quality of the TiNiSn and also of the $Zr_{0.5}Hf_{0.5}NiSn$ layer could be enhanced.

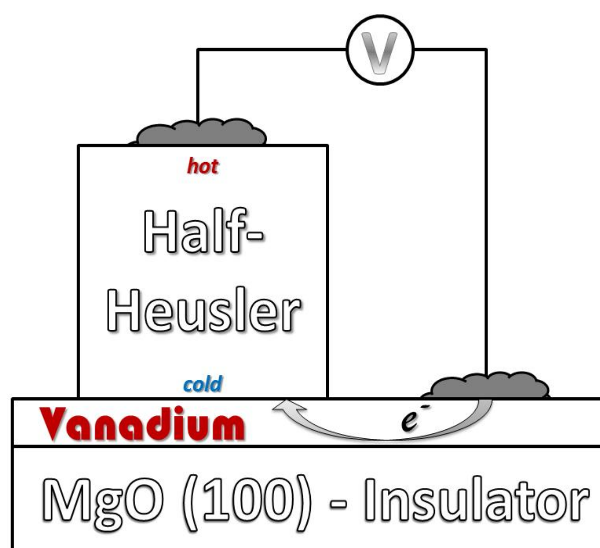

Figure 34 Schematic illustration of a potential cross-plane measurement/application setup

Beside the common quest for buffer layers that enhance the structural quality of the actually investigated thin films, in Figure 6, a further requirement for buffer layers has been already introduced. For a useful application, metallic contacts are brought between TE material and substrate to connect many TE pairs in series. More basic, but in principle identical, in Figure 34, the issue is transferred to the present material system. Since

multilayers with enhanced interface scattering are suitable for cross-plane application, initially TE measurements must be performed for testing electronic properties. Here, a measurement setup is illustrated that would allow to measure cross-plane conductivity. Due to the insulating MgO substrate, only a conducting buffer layer would enable an electrical contact at the backside of the mesa structure. Furthermore, for measuring thin films with the thickness l remarkable resistances R are obtained with mesa structures. By the reduction of the area A, also materials with low specific resistivities ρ can be measured cross-plane (Figure 34 is not correctly scaled):

$$R = \rho \cdot \frac{l}{A} \tag{5.1}$$

By growing additional insulating and conducting structures on top of the mesa structure, also cross-plane Seebeck coefficient measurements become possible.[143,144] For the HH thin films, these measurements have not been performed yet.

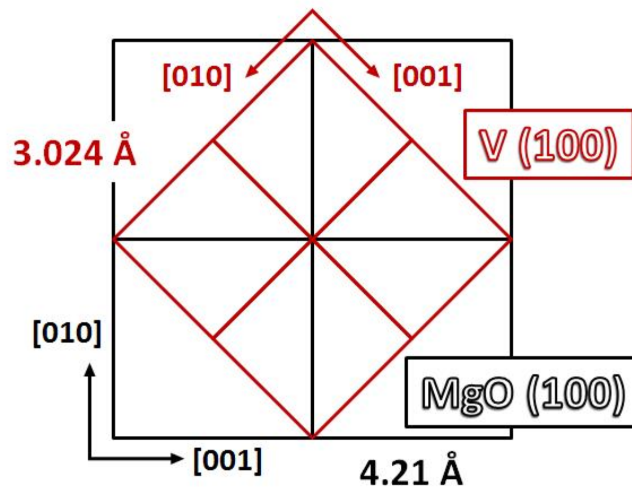

Figure 35 Schematic top view of the alignment of thin film vanadium on a MgO (100) substrate; Lines represent distances between symmetry points of the bcc vanadium (red) and the fcc MgO (black) crystal structures.

The reason, why vanadium has been chosen as a buffer layer is schematically shown in Figure 35. With a lattice constant of 3.024 Å,[145] bulk vanadium shows about half of the lattice constants observed for the HH thin films. Therefore, identical to TiNiSn and $Zr_{0.5}Hf_{0.5}NiSn$ a rotation about 45° that aligns the **[0$\bar{1}$0]** of the vanadium parallel to the **[011]** of the MgO (100) substrate enables heteroepitaxial growth with a lattice mismatch of less than 1.6 %. According to Figure 35, the lattice mismatch x is given by:

$$x = \frac{2 \cdot 3.024\,\text{Å}}{\sqrt{2} \cdot 4.21\,\text{Å}} - 1 = 0.0158 \tag{5.2}$$

To increase the film quality, iron and chromium have been also used as buffer layers in between MgO (100) substrates and Heusler materials.[146,147] Here, Heusler materials with a lattice constant of about 5.7 Å have been deposited. Therefore, iron and chromium with lattice constants (mismatches to MgO (100)) of 2.88 Å (-3.37 %) and 2.87 Å (-3.73 %), respectively, have been chosen.[148] Thus, the in-plane lattice constant of these buffer layers is elongated within the first ML. But with increasing buffer layer thickness the in-plane lattice constant usually relaxes to its natural lattice constant. So, iron and chromium are able to contribute to a better structural growth for Heusler or HH materials with smaller lattice constants than MgO (5.95 Å).

Transferred to TiNiSn and especially $Zr_{0.5}Hf_{0.5}NiSn$, the issue changes into opposite. Without having any experimental evidence, one can assume that a buffer layer with a significantly reduced lattice constant compared to MgO (100) would not increase the structural quality of TiNiSn and $Zr_{0.5}Hf_{0.5}NiSn$. Because a lattice constant of 6.12 Å has been calculated for $Zr_{0.5}Hf_{0.5}NiSn$, the argumentation counts even more. Therefore a buffer layer consisting of vanadium has been chosen.

5.2 Thin film vanadium sputtered on MgO (100)

Before thin film vanadium has been utilized as a buffer layer between the MgO (100) substrates and the HH thin films, single layers have initially been sputtered and analyzed. Identical to previous fabrication processes, under UHV conditions, the MgO substrate was annealed up to 550°C. Beside desorption of residual water, the surface crystallography that has degraded while mounting the sample at atmosphere shall be improved at elevated temperatures. Therefore the substrate temperature was held at 550°C for 60 minutes. To prevent cracks in the sample or at the sample surface that may arise due to inhomogeneous thermal expansion, the temperature ramp was driven with less than 20°C per minute. Due to the absence of any in-situ and surface sensitive measurement technique as Reflected High Energy Electron Diffraction (RHEED), changes in the surface quality of the MgO (100) substrates caused by the utilized pre-growth treatment cannot be shown.

Because, thin film vanadium has been chosen as a buffer layer, growth parameters as substrate temperature and argon ambient pressure have been set by the growth parameters found for TiNiSn and $Zr_{0.5}Hf_{0.5}NiSn$. Using others than utilized for the growth of the actual HH thin films would require an additional adjustment of the growth parameters.

Especially stabilizing a different substrate temperature takes time while the bare vanadium layer could catch up impurities from the argon sputter gas. If one keeps in mind that at a pressure of 10^{-6} mbar, in average, each surface atom is hit by about one gas atom per second, the time of interrupted growth between the vanadium buffer layer and actual HH film growth must be as short as possible. Beside argon atoms that are used as sputter gas and that do not affect the freshly grown surface, impurities arising from background pressure and sputter gas contaminations also exists in the growth chamber. The background pressure of the growth chamber is less than 1 x 10^{-7} mbar. Therefore it takes about half a minute until each surface atom is hit by an impurity atom arising from the background pressure.[149] The background pressure in a growth chamber is usually composed of N_2, O_2 and H_2O. Especially O_2 and H_2O are known to be highly reactive with non-oxidized surfaces. But similar to titanium surfaces, N_2 exhibits also an enhanced sticking probability for vanadium surfaces.[150] Argon 6.0 has been chosen as sputtering gas because of its high purity of at least 99.9999 %. Therefore, the contaminations are about 1 ppm. At a sputter pressure of about 10^{-2} mbar, a surface atom is hit by an argon atom every 0.2 ms. If it takes 1.000.000 argon atoms until a contamination arrives, one ML of impurities needs about 200 s. Similar to the background pressure H_2, N_2, O_2 and H_2O can be assumed to be the most frequent impurities.[I] Although both sources of contaminations are in the same order, this estimation reveals that the majority of impurities in the argon sputter gas come from the background pressure (if highly purified argon is used). Nevertheless, it is shown that when the substrate is rotated from one cathode to the other – it takes about one second in the present growth chamber – some degradation of the vanadium surface quality definitely takes place.

Thus, substrate temperature and argon sputter pressure have been set by the growth parameters also utilized for TiNiSn and $Zr_{0.5}Hf_{0.5}NiSn$ film growth. While 4.0 x 10^{-2} mbar have been used as argon ambient pressure, substrate temperatures between 420°C and 500°C have been found to be suitable for HH film growth (see chapter 4). An XRD diffractogram for a vanadium film (black) with a thickness of 300 nm is shown in Figure 36. Here, the vanadium film was deposited at substrate temperature of about 500°C. Applied dc power and substrate-to-target target distance have been about 60 W and 3 cm, respectively. Similar to previous diffractograms, a measurement of a bare MgO (100) substrate has been also given for comparison (gray). As expected (see Figure 35), cubic

[I] Residual impurities for argon 6.0 given by the gas supplier (Linde)

film growth indicated by the (200) diffraction peak has been observed. The (200) diffraction peak has been detected at $2\theta = 61.27°$. Therefore, a lattice constant of 3.024 Å has been calculated. This value agrees with lattice constants measured for bulk materials.[145] Using the FWHM of the (200) diffraction peak of 0.35° has given an average crystal size perpendicular to the film surface of about 30 nm. The FWHM of the corresponding rocking curve (not shown) has been 0.5°. This value is a measure for the tilt between several crystallites that contribute to the (200) diffraction peak in the $\theta/2\theta$ scan. Therefore, the obtained structural quality has been similar to vanadium films that have been deposited by Gutsche et. al. at substrate temperatures between 50°C and 950°C.[151] Using Φ-scans, the aspired in-plane rotation (see Figure 35) of 45° between thin film vanadium and the MgO (100) substrate to obtain a lattice mismatch of less than 1.6 % has been detected by others.[151,152] Thus, vanadium films with about 300 nm in thickness are strongly textured polycrystalline.

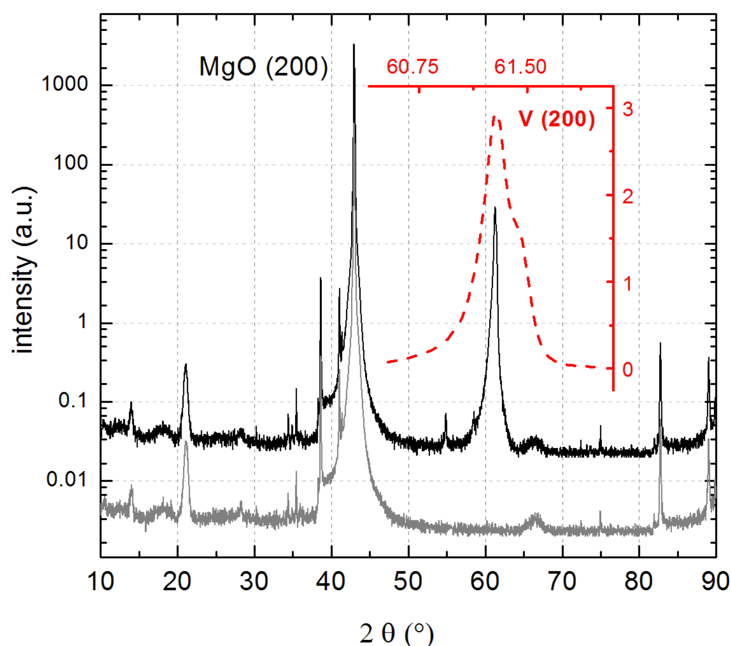

Figure 36 XRD $\theta/2\theta$ scan of 300 nm thin film vanadium sputtered on MgO (100) (black) and a bare MgO (100) substrate (gray); Enlarged, the (200) diffraction peak is shown in the inset (red).

The growth mode of thin films depends on the free surface energy densities of the interfaces between substrate and vacuum, thin film and vacuum and substrate and film. If the sum of the latter ones exceeds the free surface energy of the substrate-vacuum interface, the film starts forming islands or clusters.

As it is written in classical text books dealing with surface science, on MgO most metals are known to nucleate in island growth mode.[153] Especially noble metals as

palladium, platinum and silver exhibit cluster growth.[132,133,154,155] For silver growth on MgO (100) substrates, it has been calculated that island growth starts predominantly at the initial stage of silver deposition.[156] A dependence on substrate temperature has been found for thin film iron that has been deposited on MgO (100) substrates.[131] Here, enhanced island growth has been found at elevated substrate temperatures. For initial nickel growth on MgO (100), the formation of covalent bonding with partial ionic character between desorbed nickel and oxygen surface atoms has been calculated.[157] Therefore, for the first ML a stable 2D structure of nickel ad-atoms on MgO (100) is formed. Furthermore, ongoing nickel growth favors also the formation of 3D metal clusters.

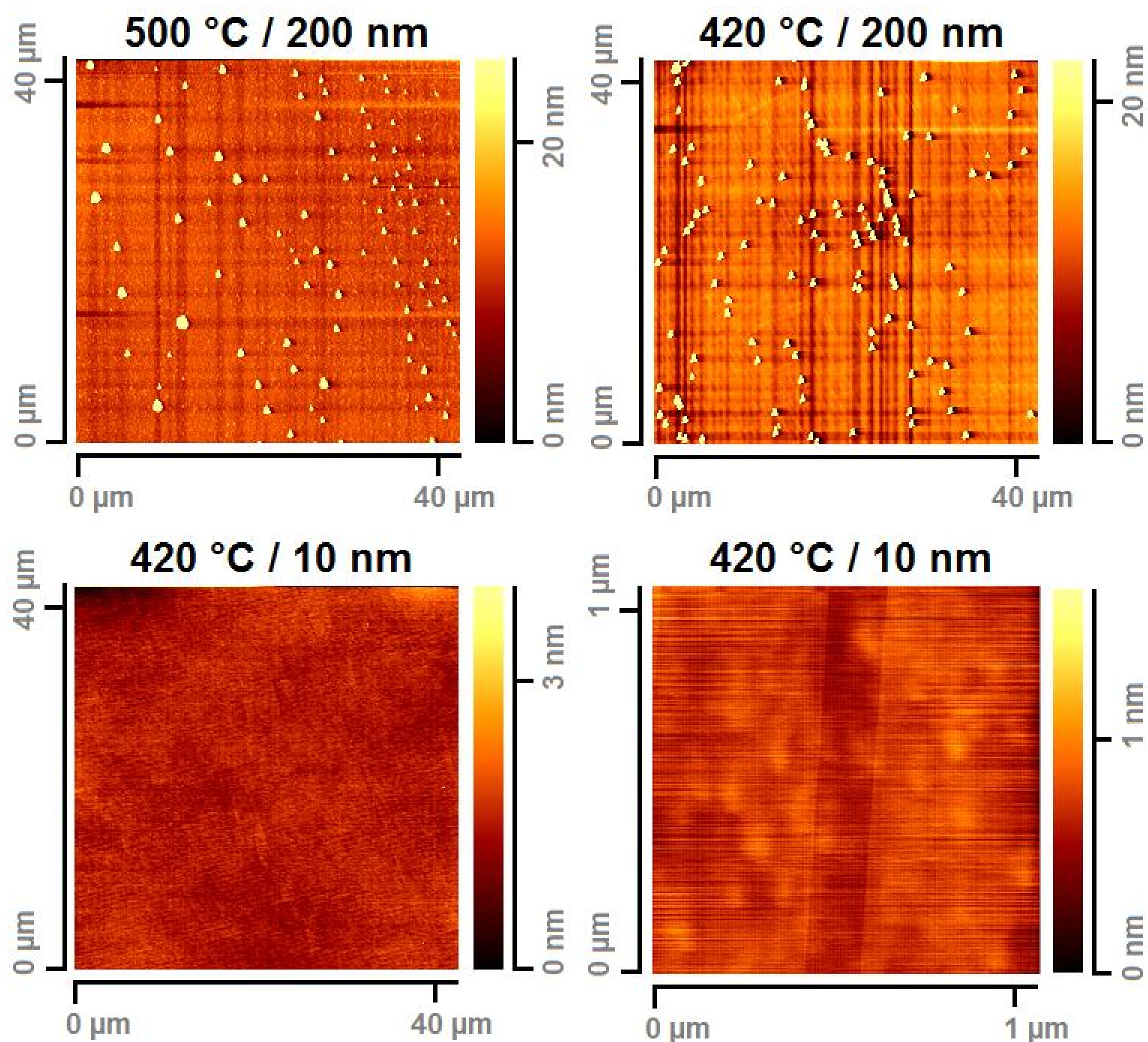

Figure 37 AFM images taken from thin film vanadium deposited on MgO (100); Corresponding substrate temperatures and film thicknesses are given above each AFM image.

So, previously introduced metals seem to be less appropriate for growing smooth buffer layers on MgO (100). Here, one of the major objectives has been the growth of

smooth multilayers with individual layer thicknesses of about 5 nm. Buffer layers that exhibit island growth with humps in the order of layer thickness would prevent the growth of multilayers with a structural coherence length longer than the multilayer periodicity. So, beside its ability of strongly textured polycrystalline growth on MgO (100), vanadium has been chosen as a buffer layer because of low surface roughness. Successfully, thin film Co_2MnSi with a lattice constant about 5.65 Å of has been deposited with a vanadium buffer layer of 42 nm on MgO (100).[158,159] In opposite to the Ni/MgO interface, at the V/MgO interface strongest bonds are formed between the vanadium and the magnesium atom.[133]

To verify, if smooth thin film vanadium has been grown on MgO (100), AFM measurements from a surface area of about 40 x 40 μm^2 have been performed (Figure 37). For vanadium films with a thickness of 200 nm, humps with heights of about 20 nm have been detected. Following the explanation above, the substrate temperatures for the vanadium deposition are set by the substrate temperatures obtained for the deposition of TiNiSn and $Zr_{0.5}Hf_{0.5}NiSn$. Therefore 420°C and 500°C have been applied (see chapter 4). But significant changes in surface composition have not been found for both substrate temperatures. Identical to the film presented in Figure 36, 60 W and 3 cm have been utilized as dc sputtering power and target-to-substrate distance, respectively. But Figure 37 also images that going to a vanadium layer thickness of 10 nm enables the deposition of atomically smooth surfaces. An enhanced AFM measurement showing the surface topology of an area with 1 x 1 μm^2 was also done. Here, it can be seen that other than for silver growth,[156] for vanadium on MgO (100) island growth does not happened from the initial deposition. Because detailed analyses with varied layer thicknesses have not been done and publications about layer-plus-island growth have not been found, statements about the layer thickness of the onset of island nucleation cannot be done.

Remarkably, the crystallographic quality has been also increased while decreasing the vanadium film thickness from 300 nm (Figure 36) to 10 nm. Applying an MgO (100) substrate temperature of 420°C has simultaneously generated smooth and epitaxial films. Therefore, a sample showing the vanadium (200) film peak (Figure 38) could be also utilized for a XRR scan. Performing the $\theta/2\theta$ measurement at grazing angles enabled the calculation of the vanadium film thickness of about 10 nm. The corresponding measurement (black) and its simulation (red) have been shown in the inset of Figure 38. According to the Parrat simulation that has been used for thickness calculation, the root mean square (RMS) surface roughness was decreased from 1.0 nm for the MgO substrate

to 0.6 nm by the deposited vanadium film. Thus, even tiny surface irregularities have been healed out by the thin vanadium layer.

Compared to amorphous vanadium films that have been deposited at RT, for epitaxial vanadium films oxidation seems to happen only in the topmost atomic layer. Otherwise, due to a noticeable reduction of the electron density at the surface, X-rays would penetrate into the film at smaller angles or reciprocal wave vectors if transferred to diffractogram in the inset of Figure 38. In XRR scans taken from amorphous vanadium deposited on MgO (100), such a deviation due to VO_x has clearly been observed.

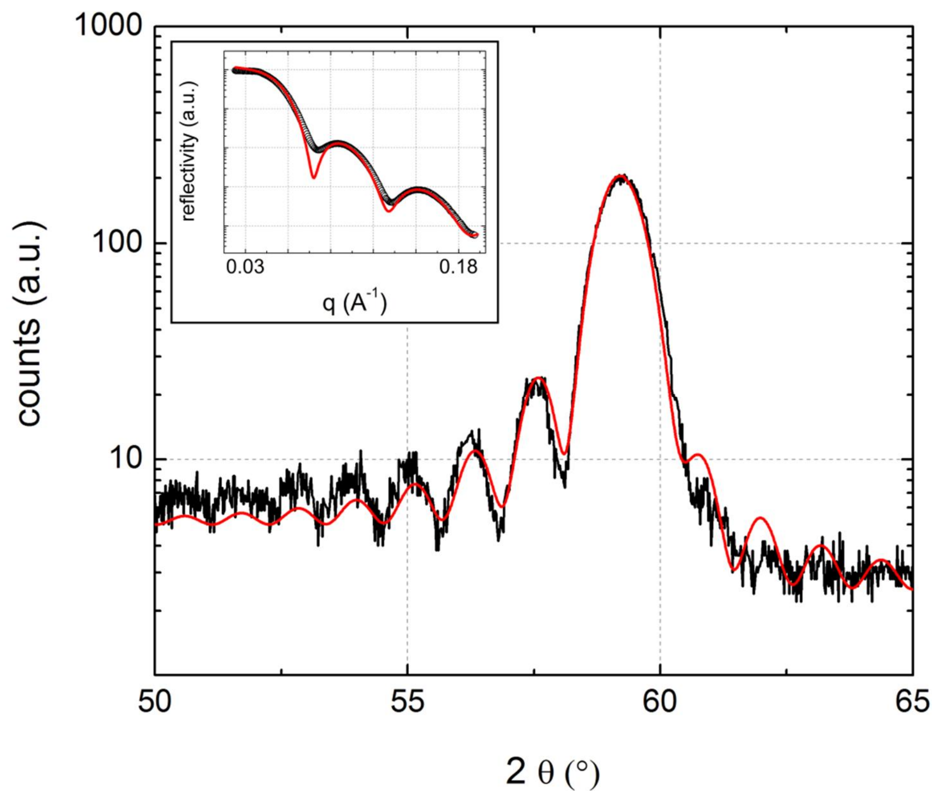

Figure 38 XRD *θ*/2*θ* and XRR scan (inset) of thin film vanadium with a thickness of 10 nm deposited on MgO (100) at substrate temperature of 420°C; For each measurement (black) a corresponding fit is shown (red)

This smooth and epitaxial film growth produced additional peaks beside the vanadium (200) diffraction peak (Figure 38). Due to interference effects, beside the diffracted X-ray beam, so called Laue Oscillations have occurred in addition. Although in textbooks these interference effects are symmetrically described,[160] Huttel et. al. have also observed Laue Oscillations for a (200) vanadium diffraction peak only along smaller diffraction angles.[152] Here, 4 nm of vanadium were epitaxially grown in an MgO/V/MgO structure. Identical to the thickness of the vanadium layer, Huttel et. al. have calculated a structural coherence length perpendicular to the interfaces of 4 nm. Here, the FWHM of the (200)

diffraction peak shown in Figure 38 is about 1.1°. Applying Scherrer formula (Eq. 4.2) leads to structural coherence length of: [134]

$$L = \frac{0.93 \cdot 1.541 \cdot 10^{-10}\,\mathrm{m}}{1.13° \cdot \cos 29.62°} = \mathbf{8.4\ nm} \quad 5.3$$

Within the accuracy of the Scherrer formula, structural coherence length and film thicknesses have been identical. The highest uncertainty is given by the shape factor (0.93) that is given for the spherical crystallites.[161] But the crystallite of the actual film has to be treated as cuboid that is only limited perpendicular to the film surface.

In comparison to the vanadium film with a thickness of 300 nm, the (200) diffraction peak has shifted from 61.27° (Figure 36) to 59.25° (Figure 38). This corresponds to out-of-plane lattice constants of 3.024 Å and 3.117 Å, respectively. Thus, there has been an increased out-of-plane lattice constant for the vanadium layer with a thickness of 10 nm. An elongated lattice constant can be explained by isochoric behavior of a lattice that can occur for very thin films. If the in-plane lattice constant of the vanadium layer has adapted to the MgO lattice constant, the in-plane lattice constant is compressed by:

$$z = \frac{2 \cdot 3.024\ \text{Å}}{\sqrt{2} \cdot 4.21\ \text{Å}} = \mathbf{1.0158} \quad 5.4$$

Because in the plane the layer is compressed in two directions (cubic system), the isochoric adaption appears for the out-of-plane lattice constant as:

$$z^2 = \mathbf{1.0319} = \frac{1}{3.024\ \text{Å}} \cdot \mathbf{3.120}\ \text{Å} \quad 5.5$$

With 3.117 Å, the lattice constant that has been calculated from the (200) diffraction peak is slightly smaller than estimated from the isochoric adaption of the vanadium layer to the MgO (100) (3.120 Å). As it has been shown for the vanadium film with a thickness of 300 nm, a relaxation finally takes place because the internal stress within the lattice of the film becomes too big. Therefore it can be assumed that it is the same ambition that drives the vanadium film with a thickness of 10 nm towards larger and smaller in-plane and out-of-plane lattice constants, respectively.

In the last section, a simple isochoric adaption of a very thin vanadium film to the MgO (100) surface has been utilized to interpret the shift of the (200) diffraction peak to lower angles of diffraction. But by applying only one discrete out-of-plane lattice constant the asymmetric behavior of the Laue Oscillations (Figure 38) cannot be

explained. Here, a more sophisticated simulation was performed that has included not only one but several out-of-plane lattice plane distances. To obtain the simulated $\theta/2\theta$ diffraction pattern (red) varied distanced a_N for neighboring lattice planes N and N–1 were considered. For the initial lattice plane ($N = 0$) that started growing at the MgO (100) surface, an out-of-plane lattice constant of 1.6005 Å has been simulated. Furthermore, 56 lattice planes ($N = 55$) and their single distances have been calculated as the following:

$$a_N = \mathbf{1.6005}\ \text{Å} - \left[\left(1 - e^{-\frac{N}{5}}\right) \cdot \mathbf{0.0475}\ \text{Å}\right] \qquad 5.6$$

Due to the decay length of 5 lattice planes, an approximately constant lattice plane distance of 1.553 Å has already been obtained at $N = 35$. Thus, unit cell lengths from N=0 to $N = 55$ have varied from 3.201 Å to 3.106 Å, respectively. Thus, the simulation of diffracting Cu K_α radiation on these 55 vanadium lattice planes has been almost identical to the measured diffraction pattern (Figure 38). Appropriate to the unit cell length of 3.116 Å, determined by the most intense diffraction peak in Figure 38, a linear weighting of the 56 net plane distances has given a similar mean distance of 3.115 Å.

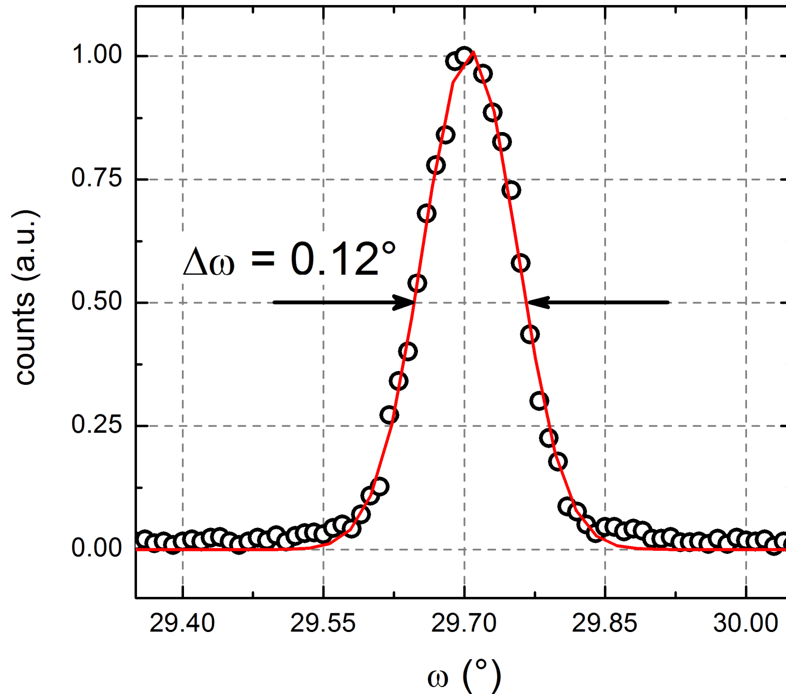

Figure 39 Rocking curve of the (200) diffraction peak taken from thin film vanadium that has already been shown in Figure 38

Beside the $\theta/2\theta$ diffractogram (Figure 38) that has included Laue Oscillations a further extraordinary feature can be addressed to the vanadium film with a thickness of 10 nm.

Thicker vanadium films as it has been presented in the diffractogram of Figure 38 or in the AFM image in Figure 37 have already exhibited rocking curves with FWHMs of about 0.5°. This value is less than half of the rocking curve widths that have been obtained for TiNiSn or $Zr_{0.5}Hf_{0.5}NiSn$ and indicates only a small tilt between several vanadium crystallites. As bigger the tilt as wider is the spreading of the alignment of several crystallites that contribute to a single diffraction peak. In Figure 39, the rocking curve (black circles) of the (200) diffraction peak that has already been shown in the $\theta/2\theta$ diffractogram of Figure 38 has been fitted (red line). In this measurement setup a FWHM of 0.12° is identical to the FWHM ($\Delta\omega$) of the rocking curve taken from the perfectly aligned MgO (100) substrate. Therefore, the width has been defined by the resolution of the diffractometer. Naturally, by the absence of several crystallites (in a single crystalline film) the diffraction of a monochromatic X-ray beam on perfectly aligned atomic planes only scatters into one specified direction.

AFM, $\theta/2\theta$ scan and rocking curve of a vanadium layer that has been deposited with a thickness of about 10 nm at a substrate temperature of 420°C suggest that a single crystalline vanadium film has been heteroepitaxially grown on the MgO (100) substrate.

5.3 Half-Heusler film growth on a vanadium buffer layer

A final decision about the suitability of a buffer layer can only be made if also the actual films have been deposited on top. The excellent structural quality and the smooth surface roughness of the vanadium buffer layer would not be valuable if further film growth of the HH films does not succeed. Thus, TiNiSn and $Zr_{0.5}Hf_{0.5}NiSn$ had to be deposited on the vanadium buffer layer that was previously optimized and introduced above.

As it has been previously explained, for the deposition of the vanadium buffer layer, substrate temperature and argon ambient pressure have been adapted from TiNiSn and $Zr_{0.5}Hf_{0.5}NiSn$ film growth. Thus, similar to single HH or vanadium films 420-500°C and 4.0×10^{-2} mbar have been also applied for growing multilayers, respectively. Equivalent, remaining sputter parameters as target-to-substrate distance and sputtering power that can be set differently for each sputter cathode have been also transferred from single film to multilayer growth.

Therefore, for TiNiSn and vanadium film growth sputtering powers of 26.5 W and 60 W have been applied, respectively. XRD scans that have been taken from a TiNiSn

film sputtered on a thin vanadium buffer layer are illustrated in Figure 40. Here, a diffractogram has been measured from a TiNiSn film grown on a vanadium buffer with thicknesses of 200 nm and 15 nm, respectively. Compared to Figure 38 that has shown an XRD pattern of a single vanadium layer with a thickness of 10 nm, a shift of the vanadium (200) diffraction peak from 59.25° to 60.27° has been observed. This shift corresponds to a change in out-of-plane lattice constants from 3.117 Å to 3.068 Å. Thus, a relaxation to its intrinsic lattice constant of 3.024 Å (Figure 36) has been observed. For TiNiSn, the (200) diffraction spots have shifted from 30.06° (5.94 Å) to 29.86° (5.98 Å) for films deposited without or with vanadium buffer layer. Since the TiNiSn film, grown on the vanadium buffer layer, has been deposited at a substrate temperature of 450°C this change can be addressed to enhanced disorder of atoms at their positions in the HH lattice. This effect (substrate temperature dependent lattice constants) has also been observed if single TiNiSn layers have been grown at lower substrate temperature on MgO (100) substrate. As it has already been introduced in Chapter 2, nickel and titanium are suitable to swap into the vacant site.[47,84]

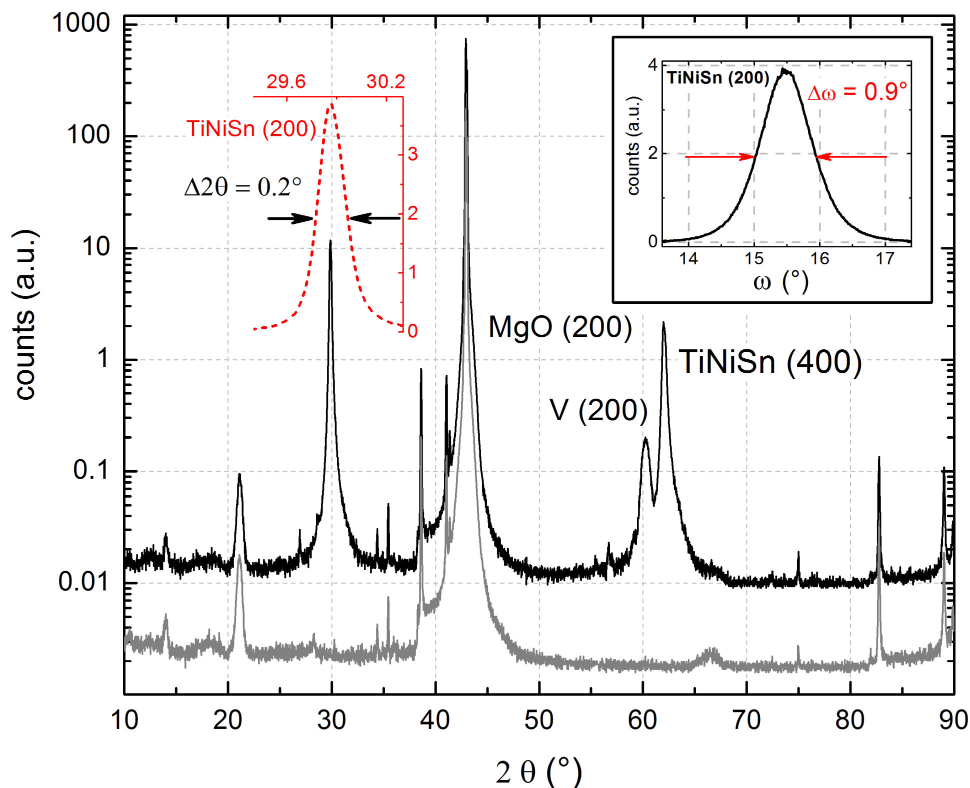

Figure 40 XRD $\theta/2\theta$ scan and rocking curve taken from the (200) diffraction peak (inset) of a TiNiSn layer deposited on a thin vanadium buffer layer

Figure 41 proves two different but important aspects. One is the capability of growing a strongly textured polycrystalline $Zr_{0.5}Hf_{0.5}NiSn$ film on a vanadium buffer layer

indicated by the FWHM of the (200) diffraction peak in the XRD $\theta/2\theta$ scan of 0.18°. Furthermore, a FWHM of the corresponding rocking curve of 1.1° has been observed. Compared to the utilization of a TiNiSn buffer layer (compare Figure 30), the quality of thin film $Zr_{0.5}Hf_{0.5}NiSn$ has been further enhanced by using a vanadium instead of a TiNiSn buffer layer. Simultaneously, a shift in the XRD $\theta/2\theta$ scan for the (200) diffraction peak from 29.15° to 29.23° has been measured. The shift indicates a negligible reduction of the out-of-plane lattice constant of 0.017 Å. It has not been established if the reduction was caused by the TiNiSn/$Zr_{0.5}Hf_{0.5}NiSn$ interface or a variation in target composition.

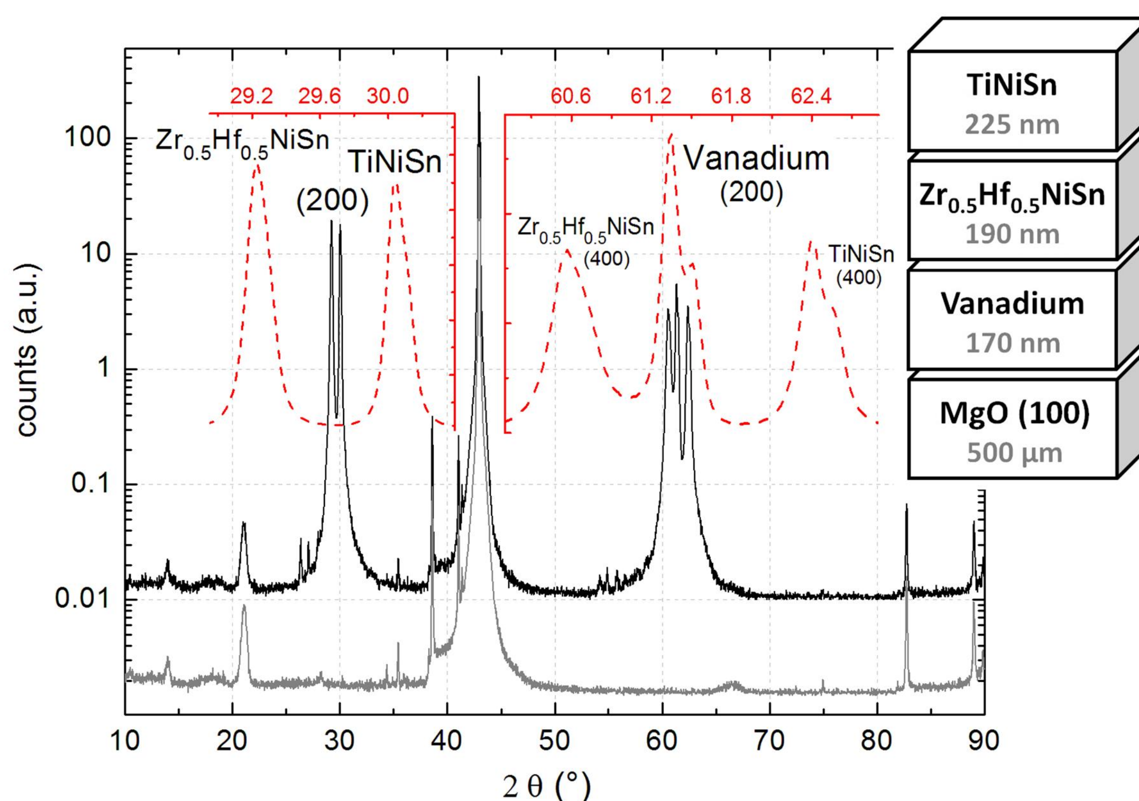

Figure 41 XRD $\theta/2\theta$ scan of the illustrated layer stack that has been grown at a substrate temperature of 500°C. Important diffraction peaks are enlarged (red).

Secondly, the diffractogram (Figure 41) shows that strongly textured polycrystalline TiNiSn has been deposited on $Zr_{0.5}Hf_{0.5}NiSn$ as well. For growing SLs where both have to grow with a structural coherence length alternately on top of each other, this finding is substantial. The FWHM of the $\theta/2\theta$ scan and the rocking curve of the TiNiSn (200) film peak can be determined to be 0.15° and 0.8°, respectively. Similar to TiNiSn that has been deposited on a vanadium buffer layer with a thickness of 170 nm or directly on

MgO (100), the (200) diffraction peak has been found at 30.06°.[I] Concerning thin film TiNiSn on MgO (100), this is an outstanding result. Within the framework of this thesis, no better XRD result has been obtained for a TiNiSn film. The fundament has been formed by an excellent vanadium buffer layer. As it can be seen by eye, in Figure 41 the vanadium film peak starts splitting into both excitation energies Cu K_α one and Cu K_α two. Similar to the single vanadium film with a thickness of 300 nm (Figure 36), a FWHM of the rocking curve of 0.5° proves the strongly textured polycrystalline growth of the vanadium buffer layer that enables improvements for both HH films.

Thus this chapter already shows that vanadium is a suitable buffer layer for TiNiSn and $Zr_{0.5}Hf_{0.5}NiSn$ grown on MgO (100). Beside additional opportunities as cross-plane measurement and application, by the vanadium buffer layer, similar crystallographic quality has been measured for single TiNiSn and $Zr_{0.5}Hf_{0.5}NiSn$ layers.

[I] The (200) diffraction peak differed for TiNiSn that has been deposited on a vanadium buffer layer with a thickness of 15 nm (Figure 40).

5.4 Half-Heusler film growth on native SiO_x

For industry, silicon wafers are still substrates of choice. But also for matching to other potential devices, the behavior of $Zr_{0.5}Hf_{0.5}NiSn$ growth on Si (100) substrates has been tested. Motivated by a few publications claiming not only epitaxial growth of vanadium on sapphire with a lattice match of about 10 %,[151] but also (110) textured growth on native SiO_x the attempt has been done to deposit crystallographic structured $Zr_{0.5}Hf_{0.5}NiSn$ on a vanadium buffer layer.[158] Similar to the current project, Kämmerer et. al. have used a vanadium buffer layer for growing the full Heusler Co_2MnSi with a bulk lattice constant of 5.65 Å on Si (100) that was not previously cleaned. [158,162]

If a silicon wafer is brought from atmosphere into vacuum, its dangling bonds that are uncompensated bonds from surface atoms have picked up contaminations as carbon, water and primarily oxygen.[163,164] To obtain perfect homo- or heteroepitaxial film growth on silicon substrates complex cleaning procedures have to be performed. In doing so, cleaning procedures range from complex etching processes with HNO_3 (65 %), H_2O:NH_4F:HF (12:7:1) and HF (5 %),[165] over H_2SO_4:H_2O (4:1) and HF:H_2O (1:100),[166] to NH_4F:HF (7:1) and also a single HF (5 %) solution.[167,168] Performed on atmosphere, all these cleaning procedures base on generating a hydrogen passivation layer that is stable for a few minutes. During that time, treated silicon substrates have been transferred

into UHV. At elevated temperatures (600-900°C), the hydrogen passivation layer can be removed. Simultaneously, arising dangling bonds compensate each other by forming reconstructed surfaces.[169]

But as it has been already introduced, vanadium buffer layers have been deposited on Si (100) substrates that were not chemically cleaned. Only macroscopic dust particles and grease were removed by acetone. Thus, at RT naturally oxidized Si (100) substrates exhibit a native SiO_x layer of about 10 Å.[170]

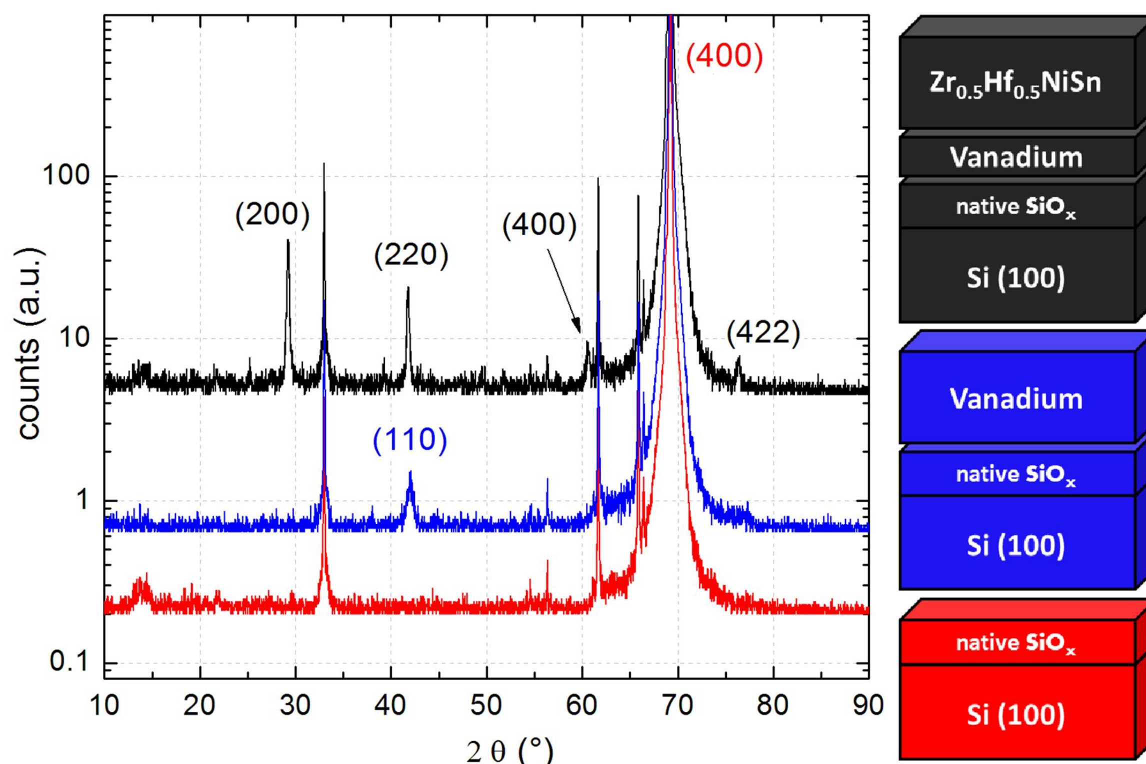

Figure 42 XRD $\theta/2\theta$ scan of polycrystalline $Zr_{0.5}Hf_{0.5}NiSn$ grown on Si (100) by using a 10 nm vanadium buffer layer (black); For comparison, XRD scans of single vanadium layer with a thickness of 180 nm (blue) and of a pure Si (100) substrate (red) are shown.

Despite the amorphous SiO_x surfaces layer, (110) textured growth has been obtained for a vanadium layer with a thickness of 180 nm. As it is illustrated in Figure 42, the comparison between the XRD pattern taken from the pure Si (100) substrate (red) and the vanadium buffer layer (blue) reveals only a weak preferred orientation of growth. Here, the vanadium layer has been deposited at a substrate temperature of 500°C. A vanadium layer that has previously grown at 200°C has not shown any XRD film peak. Due to the XRD finding, the vanadium film quality does obviously not increase with film thickness. Thus only a thin vanadium buffer layer (10 nm) has been utilized for depositing $Zr_{0.5}Hf_{0.5}NiSn$. The XRD pattern of $Zr_{0.5}Hf_{0.5}NiSn$ layer with a thickness of 200 nm has

also been shown in Figure 42 (black). According to the simulation a polycrystalline $Zr_{0.5}Hf_{0.5}NiSn$ film has been generated. Therefore, several film peaks have occurred that can be addressed to different planes of diffraction. (110) and (220) XRD diffraction peaks of vanadium (blue) and $Zr_{0.5}Hf_{0.5}NiSn$ (black), respectively, are located at similar 2θ values. Indeed, the (220) diffraction pattern taken from $Zr_{0.5}Hf_{0.5}NiSn$ (black), can clearly be identified because of the small thickness of the vanadium layer underneath.

Although only a little effort has been applied, initial success has been achieved. The vanadium buffer layer has provided a surface that allows the growth of polycrystalline $Zr_{0.5}Hf_{0.5}NiSn$ films.

Chapter 6

Superlattices –TiNiSn and $Zr_{0.5}Hf_{0.5}NiSn$ subsequently deposited at elevated substrate temperatures

6.1 Introduction

For a long period of time, SLs were understood as lattices containing several atoms in neighboring planes.[171,172] But in the seventies emerging with novel deposition techniques as MBE and electron beam evaporation, SLs composed of two different materials with a certain thickness were fabricated.[173,174] Special interest was already given on artificial band structures in SC physics.[175,176] Up to now, similar interest has been given in the field of optoelectronics. Here, SLs have created enhanced interest because of their ability of band gap engineering. Thus, for a single material system, different band gaps can be obtained by varied SL periods.[177,178]

For magnetic structures, SLs have attracted further interest. Next to exchange bias that can be generated by ferromagnetic layers that are anti-ferromagnetically coupled by diamagnetic spacing layers,[179] also vanishing net magnetization can be obtained by a SL with two half-metallic Heusler compounds. Based on theoretical calculations,[180] Mn_2TiGe (Mn_2VGa) and Co_2TiGe (Co_2VGa) with 22 and 26 valence electrons, respectively, keep their magnetic properties within single layers but exhibit a zero net magnetization along <100> if the interfaces are parallel to {100}. Furthermore in a SL structure magnetoresistance effects can be obtained.[181]

For SLs consisting of $La_{0.7}Sr_{0.3}MnO_3$ and $Nd_{0.6}Ca_{0.4}MnO_3$ layers that are ferromagnetic and antiferromagnetic,[182] respectively, at RT a magnetoresistance of 16 % has been observed which is three times higher than for single $La_{0.7}Sr_{0.3}MnO_3$ films.

In addition, using SLs enables to shift the magnetic anisotropy of a thin film. Thus, magnetic easy axes perpendicular to film surfaces become possible.[183] If soft and hard magnetic layers are combined, different magnetization directions and so-called magnetic exchange spring states can be obtained.[184,185]

Further thin films in terms of SLs have been grown to obtain scientific findings about the complex mechanisms in superconductivity. Besides less complex structures,[186,187] often $YBa_2Cu_3O_7/PrBa_2CuO_7$ SLs,[188,189] and related structures,[190,191] have been fabricated to measure the effects of anisotropy, interfaces, doping, strain, thickness and coupling on superconductivity.

As it has been already demonstrated in former chapters, SLs have also played an essential role in the field of TE. Here, their ability to reduce the thermal conductivity perpendicular to the interfaces is of importance. Similar as it has been done for the single TiNiSn and $Zr_{0.5}Hf_{0.5}NiSn$ films in chapter 4, in the following the structural qualities of the SLs will be discussed. Starting with single films, finally results from Photoelectron Spectroscopy (PES) complete the demonstration of the high quality HH SLs.

6.2 Interface roughness affected by substrate temperatures

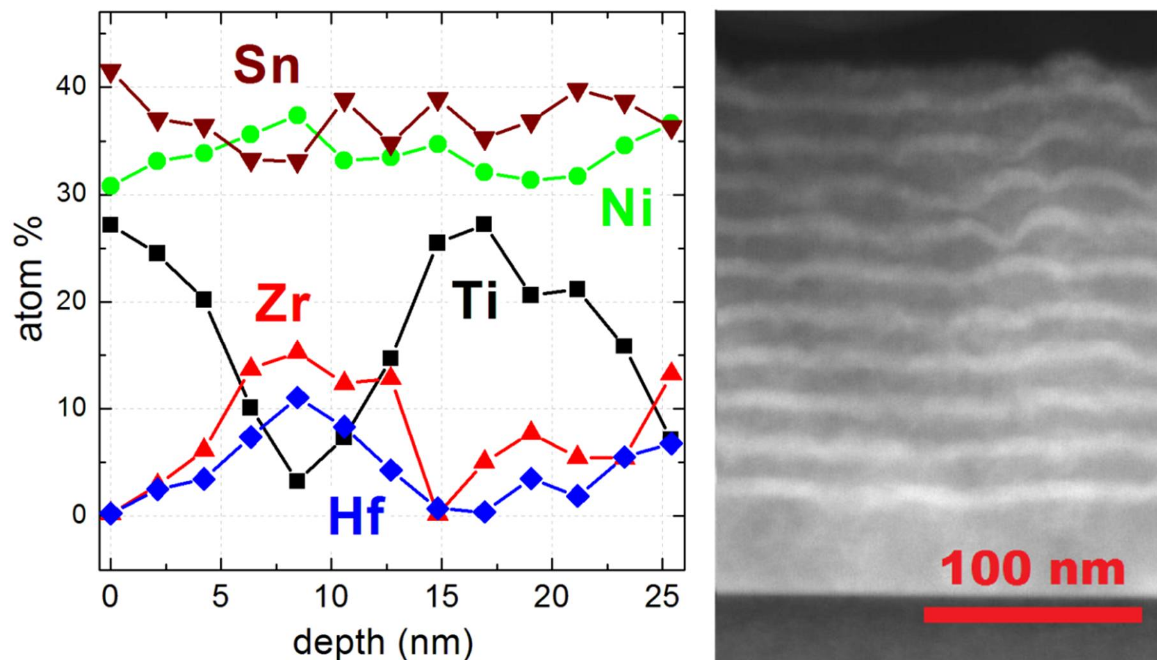

Figure 43 EDX line scan (left) and HAADF-STEM image (right) taken from a SL with a period of 21 nm deposited on a 40 nm TiNiSn buffer layer[I]

The SLs, mentioned above, have been prepared as thin films that were fabricated on varied substrates. If two or more differing materials/layers that are amorphous or polycrystalline are subsequently deposited, multilayers are generated. Exists a structural

[I] The measurement was done at the EMPA by Myriam Haydee Aguirre

coherence length that is much longer than the periodicity, the multilayers can be defined as SLs. Therefore, across several multilayer periods the crystal structure of two neighboring layers consisting of the same material have to be identical aligned. To fulfill this specification, single layers have to be either strongly textured polycrystalline or epitaxial. To transfer the ability the of epitaxial or oriented polycrystalline growth from one to the following layer of the same material, usually the material(s) in-between has (have) to have oriented crystal growth as well. Only a few methods have been developed to overcome this issue.[192,193]

Here, SLs containing TiNiSn and $Zr_{0.5}Hf_{0.5}NiSn$ have been fabricated by sputter deposition. Thus, XRD $\theta/2\theta$ scans shown in Figure 30 and Figure 41 have already affirmed the growth of strongly textured polycrystalline $Zr_{0.5}Hf_{0.5}NiSn$ on TiNiSn and the other way around. This provides the basis to generate not only multilayers but SLs.

SLs have been made by moving MgO (100) substrates back and forth between TiNiSn and $Zr_{0.5}Hf_{0.5}NiSn$ cathodes that are continuously running during the growth. In Figure 43, an element specific line scan and a real space image along the interfaces, performed by EDX and HAAF-STEM, respectively, already confirm the fabrication process of subsequently deposited TiNiSn and $Zr_{0.5}Hf_{0.5}NiSn$ layers. For the demonstration of the titanium accumulation at the MgO/TiNiSn interface shown in Figure 32, an identical measurement configuration was already applied. Utilizing a measurement density of 1 nm^{-1} with a spot size of 0.7 nm for the EDX line scan, perpendicular to the interfaces, variations in the chemical composition have been resolved. One period of the SL has been composed of 13 nm and 8 nm of TiNiSn and $Zr_{0.5}Hf_{0.5}NiSn$, respectively. Similar to the EDX measurements performed at single $Zr_{0.5}Hf_{0.5}NiSn$ films, more zirconium than hafnium has been measured (Table 3). For EDX and HAADF-STEM measurements, a complex sample preparation affords slices with thicknesses perpendicular to the image plane (Figure 43) of about 50 nm. Thus, the information depth is limited by the thickness of a slice. Nevertheless, assuming a similar wavy behavior of the interfaces that is visible in the HAADF-STEM image also perpendicular to the image plane, it becomes obvious, why a blurred characteristic has been obtained for titanium, zirconium and hafnium. To what extend intermixing plays an additional role cannot be clarified. An already shown RBS measurement performed at a TiNiSn/$Zr_{0.5}Hf_{0.5}NiSn$ bilayer (Figure 31), has not given any evidence for a significant intermixing.

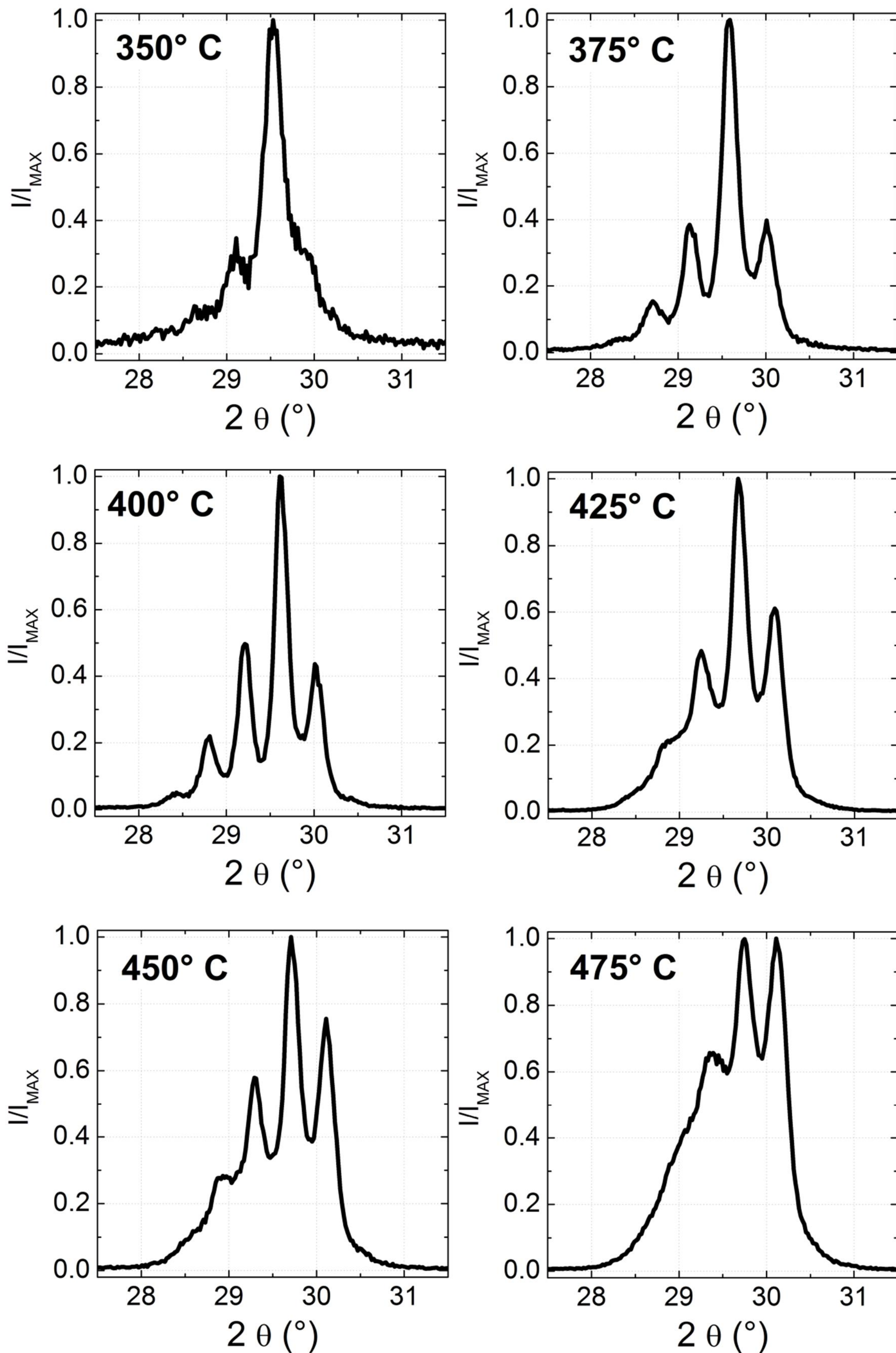

Figure 44 XRD $\theta/2\theta$ scans showing satellite peaks caused by TiNiSn/$Zr_{0.5}Hf_{0.5}NiSn$ SLs with a period of 21 nm grown at given substrate temperatures

In the HAADF-STEM image (Figure 43) three different kinds of material are shown. Because the brightness in the image scales with the atomic number, MgO, TiNiSn and $Zr_{0.5}Hf_{0.5}NiSn$ are noticed to be dark, gray and bright, respectively. Clearly, the smooth initial MgO/TiNiSn interface can be assigned. Going upwards in the image, a TiNiSn buffer layer is followed by ten periods of the HH SL.

For balancing the titanium aggregation at this interface (Figure 32), a TiNiSn buffer layer with a thickness of 40 nm was grown. But, the image already exhibits a variation in the buffer layer thickness from 38.5 nm to 42.7 nm. Beside AFM and XRD measurements this HAADF-STEM image gives further evidence about grain growth that prohibits the formation of very smooth surfaces and interfaces. With proceeding film growth, existing irregularities have been worse. In this case, the SL was fabricated at a substrate temperature of about 450°C.

The discussion, done in the last chapter about impurities captured while moving the substrate from the vanadium to the HH cathode, can easily be transferred to the current issue (see section 5.2.). Thus, both HH layers have been deposited at identical substrate temperatures and ambient argon pressures. Since it has been found suitable for both HH films, an argon ambient pressure of 4.0×10^{-2} mbar was applied for SL growths. Similarly, sputtering powers of 26.5 W and 23 W were also transferred from single TiNiSn and $Zr_{0.5}Hf_{0.5}NiSn$ film growth, respectively. Because it influences the kinetic energy of the ad-atoms and therefore the grain formation at the surfaces, the substrate temperature was varied. While buffer layer thickness, periodicity and amount of SL periods were kept constant to be 40 nm, 21 nm and 10 nm, with increments of 25°C, the substrate temperatures were changed from 375°C to 475°C. Its impact has been revealed by XRD $\theta/2\theta$ scans that are shown in Figure 44. As it was previously discussed, SLs are separated from multilayers by the structural coherence of many neighboring layers. The additional periodicity that occurs next the crystal structure is responsible for the formation of extra diffraction peaks that are known as satellite peaks.[194] In the case of TiNiSn and $Zr_{0.5}Hf_{0.5}NiSn$ SLs where both individual materials have similar lattice constants, the formation of one central diffraction peak can be observed. In addition, the interface roughness must be small compared to the SL periodicity. Under these circumstances, the length of the SL periodicity Λ and the amount of unit cells of the participating materials N_A and N_B result in an average lattice constant $\bar{d}$:

$$\bar{d} = \frac{\Lambda}{N_A + N_B} \qquad 6.1$$

Considering the order of diffraction m, the central diffraction peak can be associated with $\bar{d}$ as:

$$2\bar{d}\sin\theta_n = m\lambda \qquad 6.2$$

Beside the central diffraction peak θ_0, in the XRD $\theta/2\theta$ scan different orders of satellite peaks n can be found at different angles of diffraction θ_n. Using these peak positions, the SL periodicity Λ has been calculated:

$$2\frac{\sin\theta_n}{\lambda} = \frac{m}{\bar{d}} \pm \frac{n}{\Lambda} \qquad 6.3$$

Beside the satellite peak positions, their shapes give information about interface roughness or interlayer disorder.[194] In general it can be assumed that the sharper the interfaces, the more pronounced shape of the satellite peaks. Considering this, in Figure 44 it can be seen that a substrate temperature of about 400°C has been the most appropriate. As it has also been observed for single TiNiSn and $Zr_{0.5}Hf_{0.5}NiSn$ films, a substrate temperature of 350°C is not high enough for sufficient crystal growth. Because oriented crystal growth is required for obtaining a structural coherence length longer than periodicity of the SLs, satellite peaks only barely emerge. But with increasing substrate temperatures the satellite peaks have become more pronounced. But for substrate temperatures higher than 425°C enhanced interface roughness reduces the structural coherence length. Thus, the satellite peaks become less pronounced. Based on the position of the peaks in the diffractogram that was measured from a sample, fabricated at a substrate temperature of 475°C, the highest peaks can still be addressed to the formation of a SL. The intensity of the highest diffraction peaks remain at a high level (not shown) and their gap stays constant. Although the formation of secondary phases cannot be excluded by the XRD measurement, changes of the satellite peaks can be mainly addressed to the formation of imperfections in the symmetry of the SL.

As expected, changes have been also obtained in the HAADF-STEM (Figure 45) images. While for a SL that was fabricated at a substrate temperature of about 450°C (left) dark (TiNiSn) and bright ($Zr_{0.5}Hf_{0.5}NiSn$) stripes partially smear over, for a SL that was fabricated at a substrate temperature of about 400°C (right) rather sharp interfaces can be observed. Thus, resolving a SL with 3 nm in periodicity has become possible.

At a substrate temperature of about 400°C, a SL with ten periods of TiNiSn and $Zr_{0.5}Hf_{0.5}NiSn$ each with layer thickness of 8 nm has been fabricated (on a TiNiSn buffer

layer with a thickness of about 30 nm). A reduced section of the XRD $\theta/2\theta$ scan is logarithmically (left) and linearly (right) scaled and shown in Figure 46. In addition to the measurement (dotted lines), a simulation has been generated (red lines). Therefore, appropriate to the HH lattice structure (Figure 10), the diffraction of an incoming X-ray beam on sequently stacked atomic planes was simulated. According to the type of atoms and their scattering factor, for all different lattice positions the scattering power as a function of scattering angle has been calculated. Remarkably, neither atomic disorder (atoms on wrong lattice positions) nor interface roughness (different periodicities) were embedded for obtaining the simulated diffraction pattern as it is illustrated in Figure 46. Despite, only small deviations have been observed for the intensities of higher orders of reflections. Compared to Figure 44, due to the higher fraction of $Zr_{0.5}Hf_{0.5}NiSn$ with a larger lattice constant than TiNiSn, the most intense satellite peak has shifted to a smaller angle of diffraction.

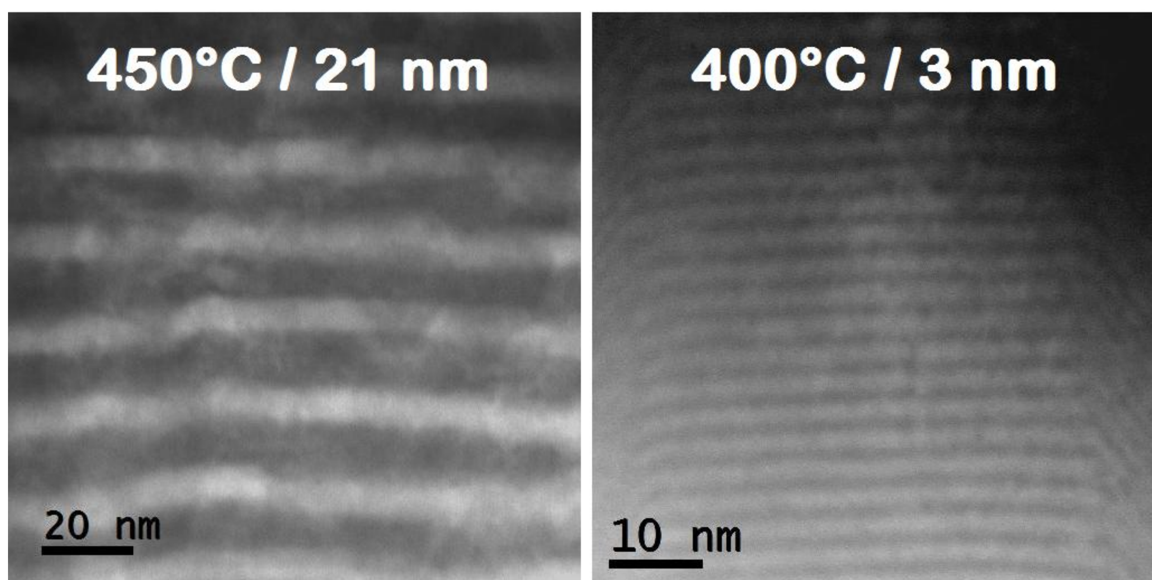

Figure 45 HAADF-STEM images of two SLs grown at substrate temperature of 450°C and 400°C; Simultaneously, the SL period has been decreased from 21 nm to 3 nm[I]

Cho et. al. have investigated the interface properties of sputtered FeCo/Si multilayers.[195] Here, the interfaces have been influenced by sputter parameters as argon pressure and applied target voltage. Among other techniques, XRR measurements in connection with 'Parrat' simulations were applied for interface characterization. For the FeCo/Si multilayers,[195] a minimum in interface layer thickness of about 3 nm has been found. Following the explanation by Cho et. al.,[195] the interface thickness has been

[I] The measurement was done at the EMPA by Myriam Haydee Aguirre

generated by interface roughness, rather than interdiffusion. Each finished layer and its residual roughness, caused by surface diffusion of the atoms, has been assumed to be the crucial factor. A similar behavior can be assumed for HH SLs that were fabricated at a substrate temperature of 400°C. Taking into account the granular structure of single films (Figure 33), the RBS measurement of the bilayer (Figure 31), the STEM image of a SL with a periodicity of 3 nm (Figure 45) and the simulation of the XRD $\theta/2\theta$ scan of a perfect ordered SL (Figure 46), a significant interdiffusion at the interlayers can be excluded.

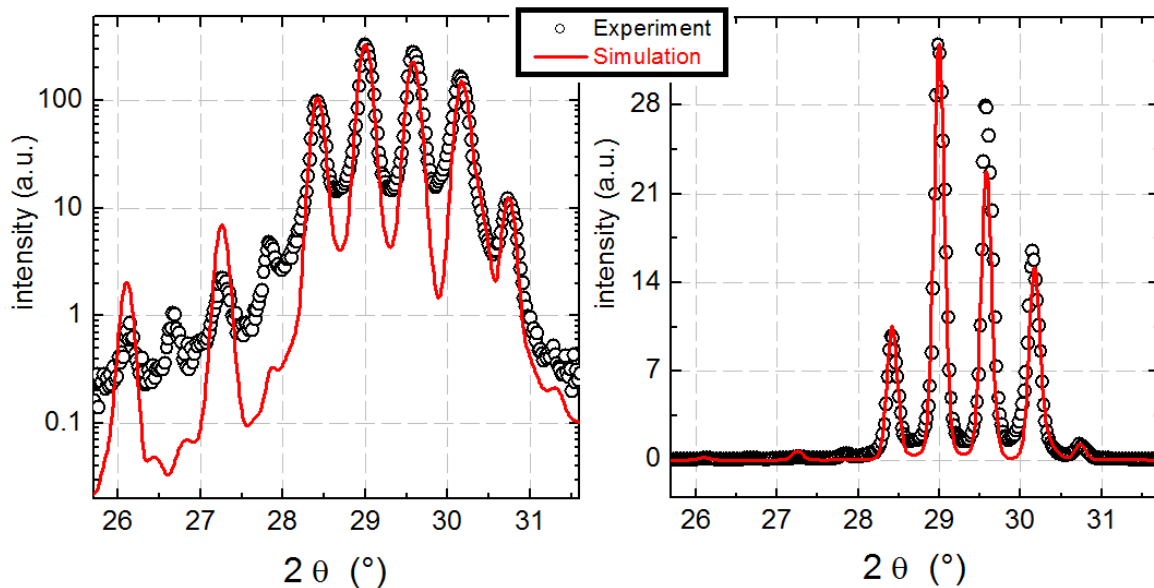

Figure 46 XRD $\theta/2\theta$ scan (dotted lines) and corresponding simulation (red lines) of a SL with a periodicity of 16 nm logarithmically (left) and linearly plotted (right)

6.3 Further enhancement in interface roughness

Because beneficial results have been gained for single HH thin films (see chapter 5), also SLs have been deposited on vanadium buffer layers. In Figure 47, AFM image and XRD $\theta/2\theta$ scan of a SL grown at a substrate temperature of 400°C are shown. For the sample, 55 periods with a thickness of 6.9 nm have been deposited on a vanadium buffer layer with a thickness of 5 nm. Within the SL, TiNiSn and $Zr_{0.5}Hf_{0.5}NiSn$ have had the same layer thickness.

Unlike previous results (STEM images; satellite peaks) have supposed, a granular structure has been also measured for thin films containing SL structures. As it is shown in Figure 47, the AFM image reveals height differences of about 20 nm. Thus, not only the

TiNiSn buffer layer and its initial roughness (Figure 43) accounts for blurry SL structures (Figure 45).

But enhanced structural qualities have been obtained by XRD $\theta/2\theta$ scans. Figure 47 illustrates an example. Due to additional diffraction at the (400) plane, satellite peaks are also located at about twice the angle of diffraction. Thus, next to $2\theta = 30°$ also at about $2\theta = 60°$ satellite peaks can be observed. Beside an naturally increased resolution at higher angles of diffraction, the increased structural coherence length of SLs deposited on a thin vanadium buffer layer afford the visibility of the satellite peak splitting into both excitation energies Cu $K_{\alpha 1}$ and Cu $K_{\alpha 2}$. If the FWHM of a diffraction peak caused by only one excitation energy is taking into account, a structural coherence length of about 68 nm can be calculated.[134] For the current SL periodicity, this distance ranges over about 10 SL periods.

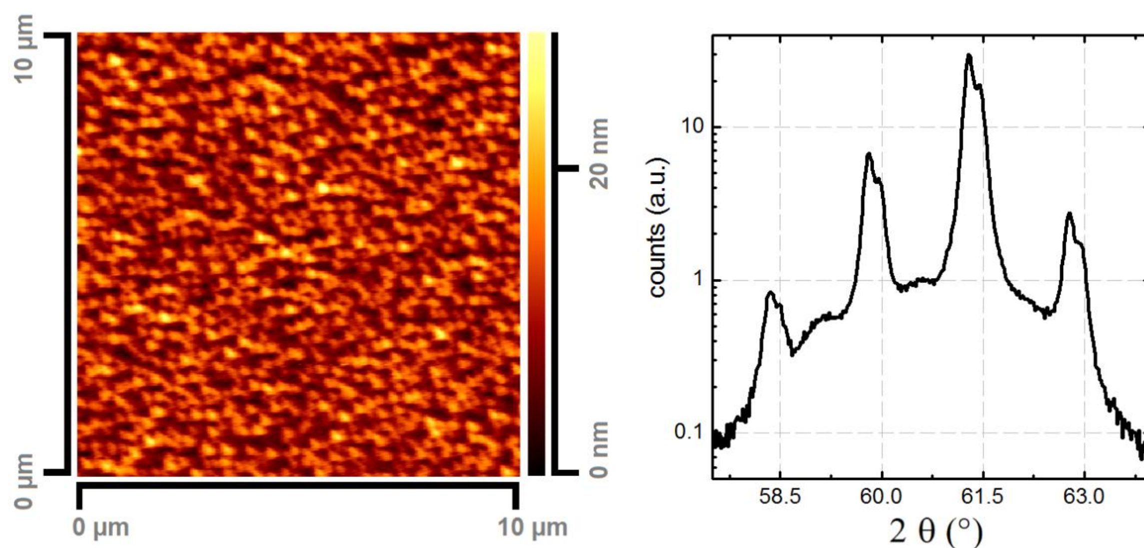

Figure 47 AFM image (left) and XRD $\theta/2\theta$ scan (right) of a SL containing 55 periods of TiNiSn and $Zr_{0.5}Hf_{0.5}NiSn$ with a periodicity of about 6.9 nm

Furthermore, Figure 48 illustrates the difference for identically grown SLs that have been deposited with (red) and without (black) a vanadium buffer layer having a thickness of 10 nm. All illustrated SLs were grown at a substrate temperature of about 400°C. Aspired periodicities, estimated by growth rate and exposition time of the substrate ahead of each cathode, and amount of periods are given for both types of SLs (blue). Using Eq. 6.2 and the satellite peak positions, 22.2 ± 0.5 nm and 50.8 ± 2.8 nm can consistently be calculated. Indicating a higher crystal quality and smother interfaces, for the SL with an aspired periodicity of 21 nm, more pronounced satellite peaks have been observed for the sample with the vanadium buffer layer (red). To overcome the issue about the

titanium segregation at the TiNiSn/MgO interface (see Figure 32), instead of vanadium, a TiNiSn buffer layer (black) with a thickness of 40 nm has been used. Due to the additional TiNiSn film, the XRD $\theta/2\theta$ scan has been influenced at about 30° (Figure 48). Compared to the SL with a vanadium buffer layer (black), a shift of the highest satellite peak has been caused by a changed average cross-plane lattice constant (Eq. 6.1) to a smaller value. In addition to strain affected by interface roughness, this can be addressed to a decreased ratio of TiNiSn to $Zr_{0.5}Hf_{0.5}NiSn$.

For the SLs with the aspired periodicity of 51 nm the satellite peaks can only be observed for the sample with the vanadium buffer layer. Since for SLs with larger periodicities the satellite peak positions move closer together, resolving single peaks becomes less probable. Accordingly, the structural coherence length that still has to exceed the SL period prohibits the formation of satellite peaks. Thus, for the SL grown on a vanadium buffer layer (red) the structural coherence length is increased compared to one without the vanadium buffer layer (black).

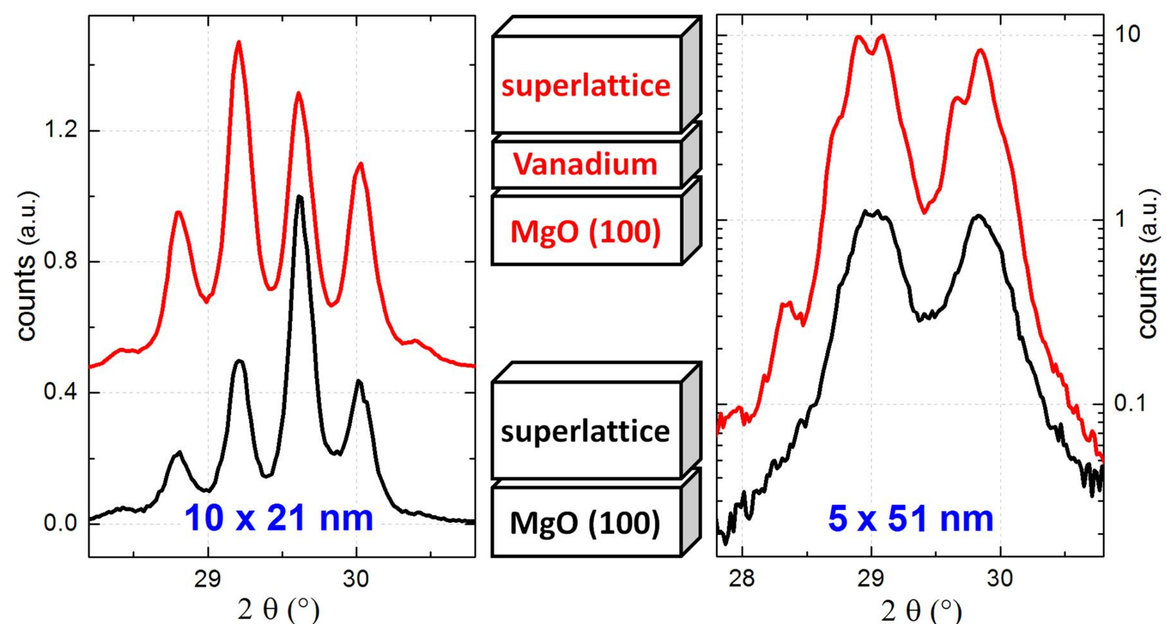

Figure 48 SLs with periodicities of 21 nm (left) and 51 nm (right) deposited with (red) and without a vanadium (black) buffer layer

Different to single TiNiSn and $Zr_{0.5}Hf_{0.5}NiSn$ thin films (see chapter 5), on MgO (100) substrates, for HH SLs the crystallographic quality can be even enhanced by using a vanadium buffer layer.

6.4 Thin films and superlattices investigated by photoelectron spectroscopy

6.4.1 Introduction

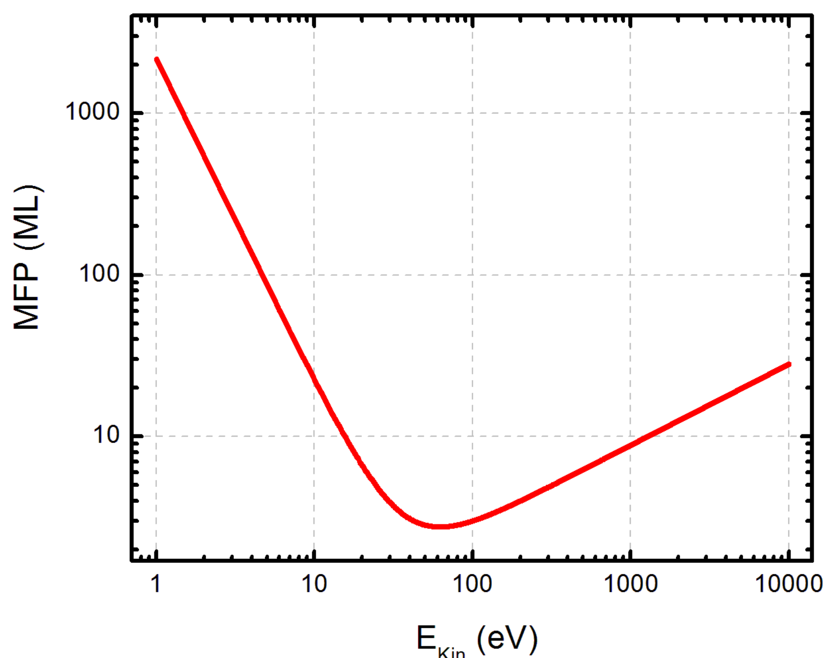

Figure 49 Calculated MFP (Eq. 6.5) for electrons in inorganic compounds with an atomic layer distance of 0.15 nm

Photoelectron Spectroscopy (PES) was used to obtain information about binding energies E_B of electrons in single HH films and in SLs. For the first time, in 1960 K. Siegbahn, who thus obtained the Nobel Prize of Physics in 1981, utilized the Photo effect that had been described by A. Einstein. [196] If an electron that is located close to the surface is hit by a photon with the energy E_{Ph}, there is a probability that this electron leaves the solid. Following energy conservation, its kinetic energy E_{Kin} is given by:

$$E_{Kin} = E_{Ph} - E_B - \Phi \qquad 6.4$$

Because E_B is considered to be the energy difference between the initial energy level of the electron and the Fermi energy E_F, the energy difference between the Fermi energy and the vacuum level is incorporated by the work function Φ. Practically, Φ vanishes by short circuiting sample and analyzer. Therefore, with a known incoming E_{Ph}, E_B can easily be calculated by measuring E_{Kin} of the electrons in the vacuum. Since, each element has a distinct excitation spectrum, formed by E_B and cross sections for varied energy levels, the

chemical compositions can be identified by measuring the amount of electrons as a function of their E_{Kin}.

Douglas et. al. have calculated a work function for TiNiSn of 4.30 eV. It was done by assuming the Fermi energy to be in the middle of the gap between VB and CB that were found at 4.54 eV and 4.09 eV, respectively.[83]

The fact that in PES the E_{Kin} of electrons is measured limits the region of their origin in a solid. Due to inelastic electron scattering, the initial excitation energy changes and Eq. 6.3 loses validity. Similar as it has been frequently discussed above for phonons, MPFs for electrons have to be taken into account. Thus, in PES the location of the electron excitation needs to be less than the MFP away from the surface to account for the measurement. Because electron interactions change from material to material, no universal distances can be given. An attempt to sum up MFPs of electrons *MFP* in several inorganic materials was done by Seah et. al..[197] Taken into account the distance between adjoining atomic layers a, the following equation has been empirically achieved:

$$MFP = \frac{2170}{{E_{Kin}}^2} + 0.72 \cdot \sqrt{a \cdot E_{Kin}} \qquad 6.5$$

For obtaining correct numbers for MFP, E_{Kin} and a the dimensions monolayer ML, eV and nm have to be inserted, respectively.

Using an atomic layer distance of 0.15 nm that is appropriate for HH materials, calculated MFPs are shown in Figure 49. At 63.5 eV a minimum of 2.8 ML (0.42 nm) has been calculated. For 10 eV, 1000 eV and 10.000 eV electron MFPs of 23 ML (3.5 nm) and 8 ML (1.2 nm) 28 ML (4.2 nm) can be calculated. Although enhanced MFPs can be observed along smaller as well as larger E_{Kin}, the information depth in PES remains rather small. Only if one further decreases E_{Kin} MFPs larger than 1000 ML can be obtained.

Depending on the irradiated electromagnetic radiation PES is classified. Widely used, X-ray Photoelectron Spectroscopy (XPS) is performed with aluminum or magnesium anodes utilizing K_α radiation generating a photon energy E_{Ph} of about 1486 eV and 1253 eV, respectively. Consequently the kinetic energy E_{Kin} of the excited electrons is smaller than the energy of the absorbed X-rays. Therefore, the MFP for electrons is in the order of the thickness of native aluminum oxide (1-3 nm) that is formed when pure aluminum is released to atmosphere at RT.[198] For illustration, an example irradiated by aluminum K_α is shown in Figure 50. Here, 10 nm aluminum have been deposited by MBE, brought to atmosphere and subsequently measured by XPS. Obtained by double

peak structure and peak position (inset in Figure 50), metallic aluminum and aluminum in Al_2O_3 have been clearly identified.[199] Surprisingly, the natively formed Al_2O_3 layer is even thinner than the MFP of electrons with a kinetic energy of about 1400 eV.

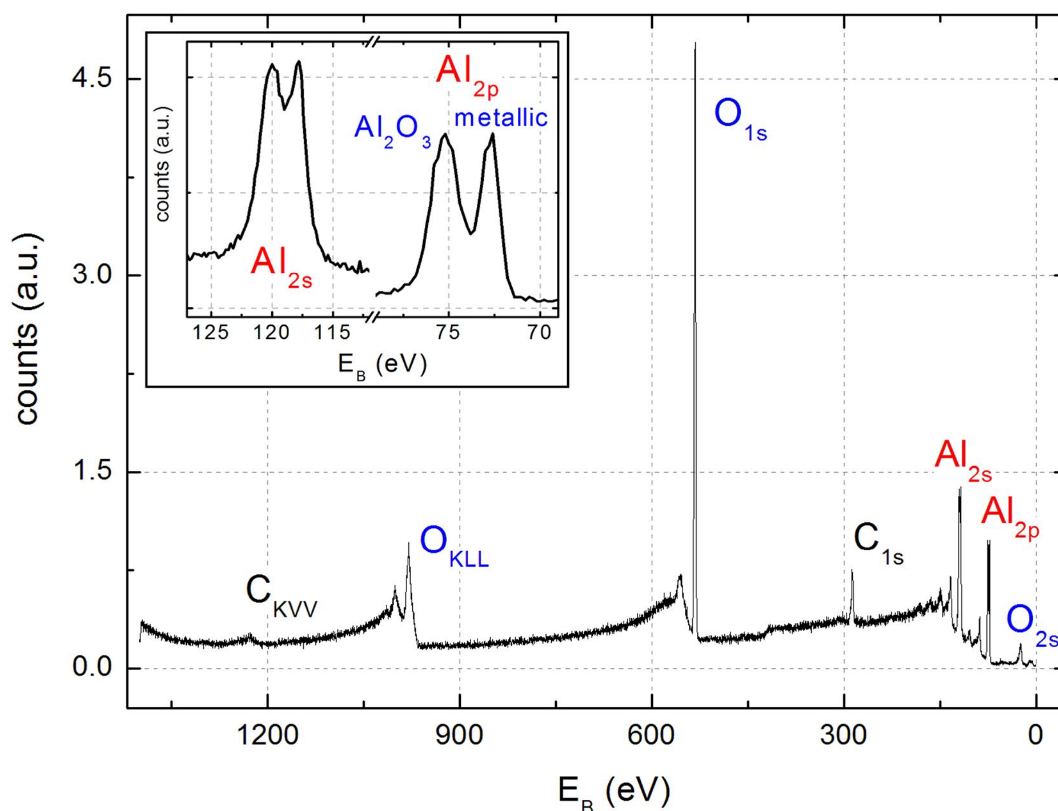

Figure 50 XPS spectrum taken of a natively oxidized aluminum capping layer[I]

To enhance information depth as well as resolution, the following PES measurements were performed at L47XU of Spring-8 (Japan).[II] There, an electron accelerator provides a photon energy up to about 6 keV and the experiment can be performed with resolution of 240 meV. Due to the high photon energy the measurement is named as hard X-ray Photoelectron Spectroscopy (HAXPES).

6.4.2 Core level analysis performed with HAXPES

Initially, HAXPES measurements with a photon energy of 6 keV were done to measure the elements embedded in the films. Therefore the focus was set on core levels that are element specific.

[I] Spectrum was measured within the Galfenol project at ICAL (Montana State University)
[II] Following HAXPES measurements were made by Xeniya Kozina, Institute of inorganic and analytical chemistry, Johannes Gutenberg University of Mainz, the group of Prof. Dr. Claudia Felser

To prevent films from oxidation, an AlO_x capping layer with a thickness of 3.5 nm has been deposited on all films. Thus, in following spectra aluminum, oxygen and also carbon can be found that are not related to the layers of interest. In contrast to the film measured in Figure 50, the AlO_x capping layer was sputtered directly from an AlO_x target. Hence, only single Al_{2s} and Al_{2p} peaks have been measured that implies the absence of any metallic aluminum. Additional assigning can be done by the position of electron binding energies due to chemical bonding. Instead of 73 eV, the Al_{2p} has been found at about 75 eV. In contrast to aluminum, the higher electronegativity of oxygen causes a stronger electron bonding.

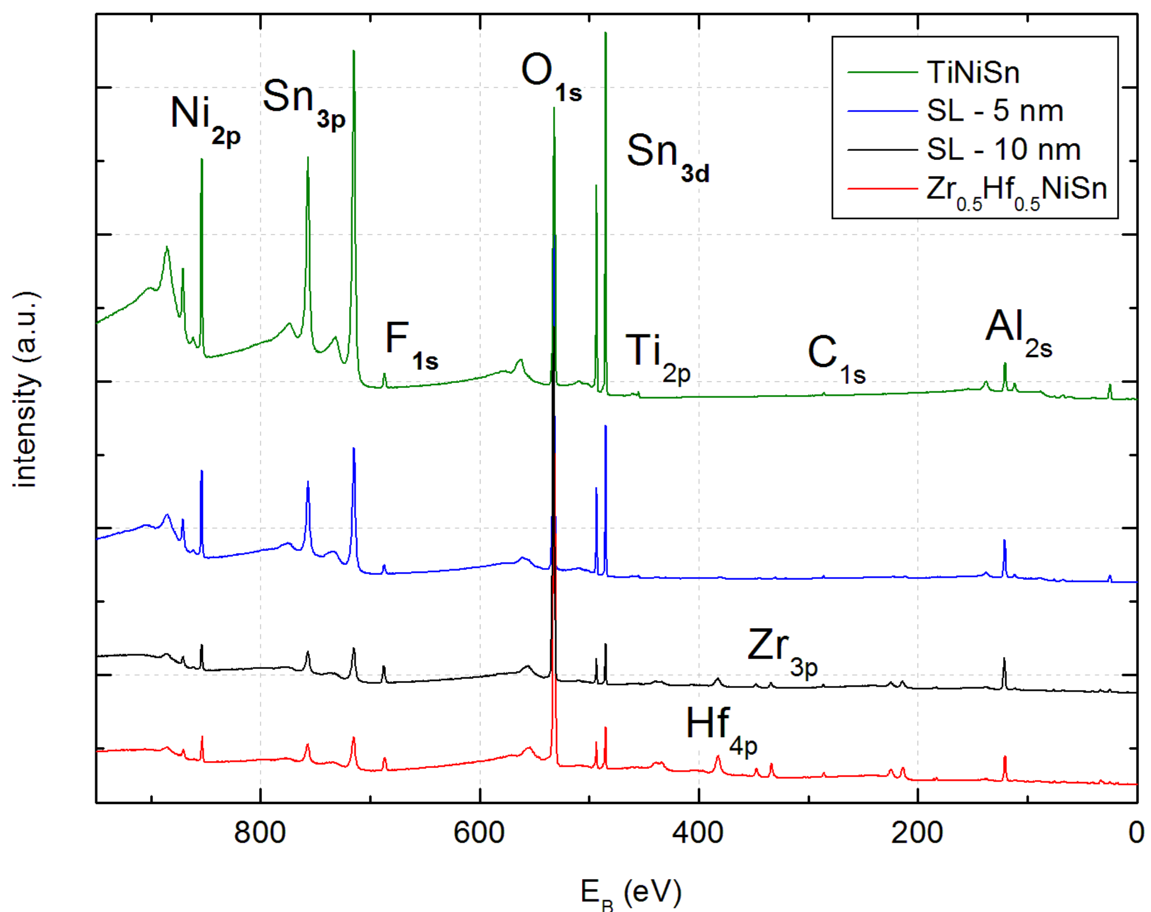

Figure 51 HAXPES survey spectra taken with a photon energy of 6 keV

Survey spectra of single TiNiSn (green) and $Zr_{0.5}Hf_{0.5}NiSn$ (red) films and two SLs with periods of 5 nm (blue) and 10 nm (black) are shown in Figure 51. Each film has thickness of 66 nm. For a better comparison, SLs have been grown on a TiNiSn buffer layer with a thickness of 36 nm. Differently, TiNiSn and $Zr_{0.5}Hf_{0.5}NiSn$ have been the final layers for the SLs with periodicities of 5 nm and 10 nm, respectively. After film

growth with sputtering parameters as described above and a substrate temperature of 425°C, the quality was checked by XRD measurements.

For single films and SLs, E_B has been measured from 0 to 950 eV. Taken into account the applied E_{Ph} of 6 keV, excited core electrons had E_{Kin} of at least 5 keV. As it can be seen in Figure 51, the excitation energy is sufficient that many core electrons of the HH films can penetrate the AlO_x capping layer without having any inelastic interaction. For the TiNiSn film (green), Ni_{2p}, Sn_{3p}, Sn_{3d} and Ti_{2p} have been identified. Due to varied cross sections within one element for different electron levels but also for identical electron levels for varied elements, measured intensity cannot be easily compared. Compared with normal emission, excited with Al K_α, Ni_{2p}, Sn_{3d} and Ti_{2p} have atomic sensitivity factors (peak area) of about 3.7, 4.1 and 1.8.[200] Even though a very weak signal has been measured for Ti_{2p}, this only qualitatively agrees with the measurement. Whether titanium depletion or a change of the atomic sensitivity factors due to increased E_{Ph} has been responsible cannot be specified. Although the topmost layer has also been TiNiSn (apart from AlO_x) reduced intensities have been observed for the SL with a periodicity 5 nm (blue). While the reduction of Ni_{2p} and Sn_{3p} can be seen in Figure 51, the change of the Ti_{2p} becomes only visible in Figure 52. Here an enlarged section of Figure 51 is illustrated. Similar to nickel and tin peaks, the Ti_{2p} is reduced by one half compared to the single TiNiSn layer. The increased height of the Al_{2s} peak, implies a thicker AlO_x capping layer. Beside a varied AlO_x capping layer thickness also its closeness may have influenced the result. Since SLs have been grown more even than single TiNiSn films, a better AlO_x capping layer can be assumed for the SL with a periodicity of 5 nm (blue).

For the single $Zr_{0.5}Hf_{0.5}NiSn$ film (red), instead of Ti_{2p}, Hf_{4p}, Hf_{4d} and Zr_{3p} can be observed. Due to enhanced atomic sensitivity factors,[200] Zr_{3p} and Hf_{4p} are more pronounced and also visible in Figure 51. In Figure 52, it can be seen that all peaks addressed to the $Zr_{0.5}Hf_{0.5}NiSn$ film (red) can also be found in spectrum from the SL with $Zr_{0.5}Hf_{0.5}NiSn$ as the final layer (black). Surprisingly, the topmost layer $Zr_{0.5}Hf_{0.5}NiSn$ (apart from AlO_x) with a thickness of 10 nm has not prohibited the detection of the Ti_{2p} peak. Due to the MFP of the electrons it is unlikely to detect titanium in the TiNiSn layer. Either diffused titanium atoms or titanium atoms that have remained on the surface while the growth of $Zr_{0.5}Hf_{0.5}NiSn$ are detected. In addition, tiny Hf_{4p}, Hf_{4d} and Zr_{3p} peaks have been also observed for the SL having TiNiSn with a thickness of 5 nm as the topmost layer. Here, the penetration of the electrons becomes more likely. But it is still less convincible that electrons excited more than 8 nm away from the sample surface can

escape without having any inelastic interaction. Nevertheless, zirconium and hafnium have been detected.

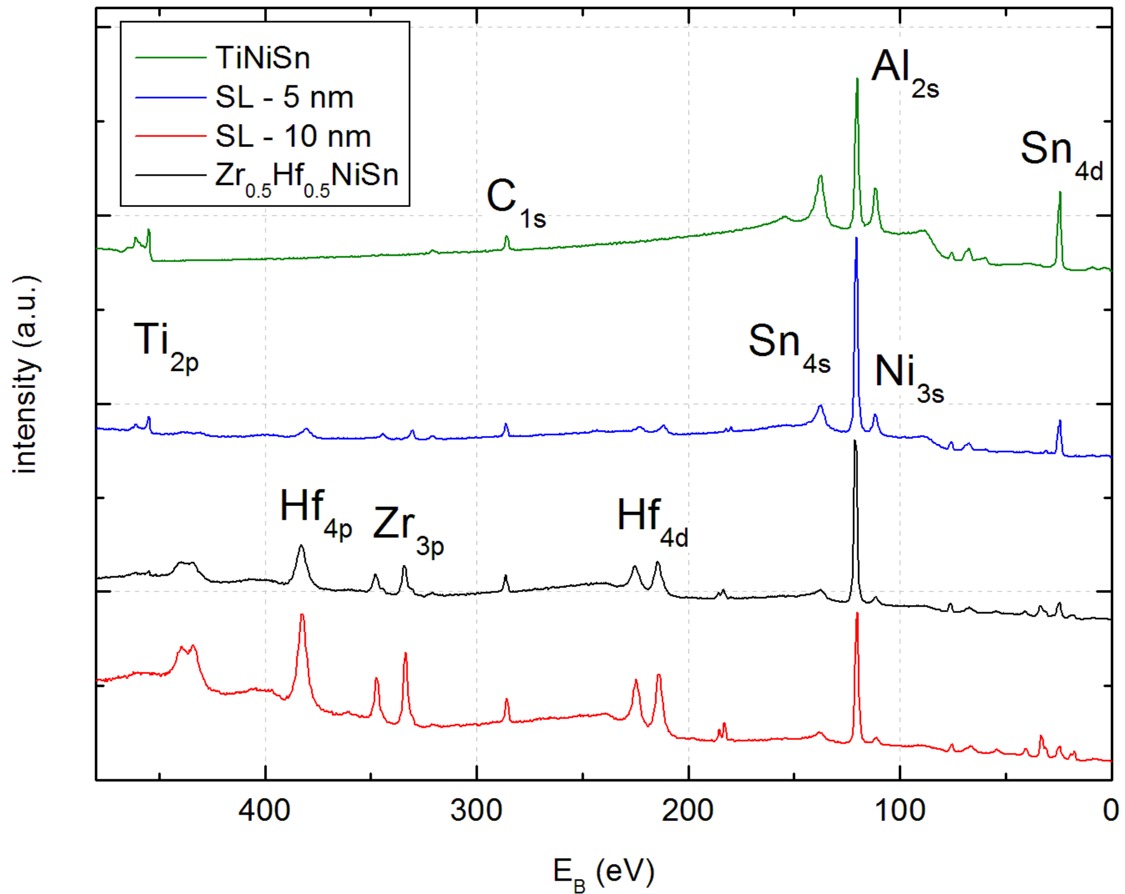

Figure 52 Enlarged HAXPES spectra focused on E_B up to 480 eV

Despite some inconsistencies about titanium, zirconium and hafnium, the layered structure of the SLs has been also proven by HAXPES. Although no chemical composition has been calculated, single films have been composed of the aspired elements.

Unfortunately, fluorine (F_{1s}) has been detected in all films (Figure 51). Therefore it seems that the fluorine contamination does belong to the growth chamber rather than to the sputter targets. Although the TiNiSn and $Zr_{0.5}Hf_{0.5}NiSn$ sputter target cannot be excluded, sources as sputter gas or the greasing of rubber gaskets can be suspected.

6.4.2 Valence band spectra measured with HAXPES[I]

As it has been illustrated in chapter 3, for TE properties of a material, the shape of the VB is of importance. Similar to the electrons located in core levels, electrons from the VB can be excited by photon-electron interaction. Because count rates of the spectra in Figure 51 range from a few hundreds at the Fermi edge to over one million at highest core level peaks, corresponding cross sections of electron-photon interaction for electrons located in core levels are much higher than from those in the VB. Furthermore, the issue about the escape depth of electrons also exists so that high photon energies have to be applied as well for obtaining a sufficient information depth. Assuming excitation energies of 8 keV,[201] as it has been the case for the following HAXPES measurements performed at BL47XU of Spring-8, one has to distinguish if an excited electron has a kinetic energy of 7995.0 eV or 7994.9 eV, which corresponds to a difference of 0.001 %. Nevertheless, applying state-of-the-art electron analyzers do resolve VB structures.

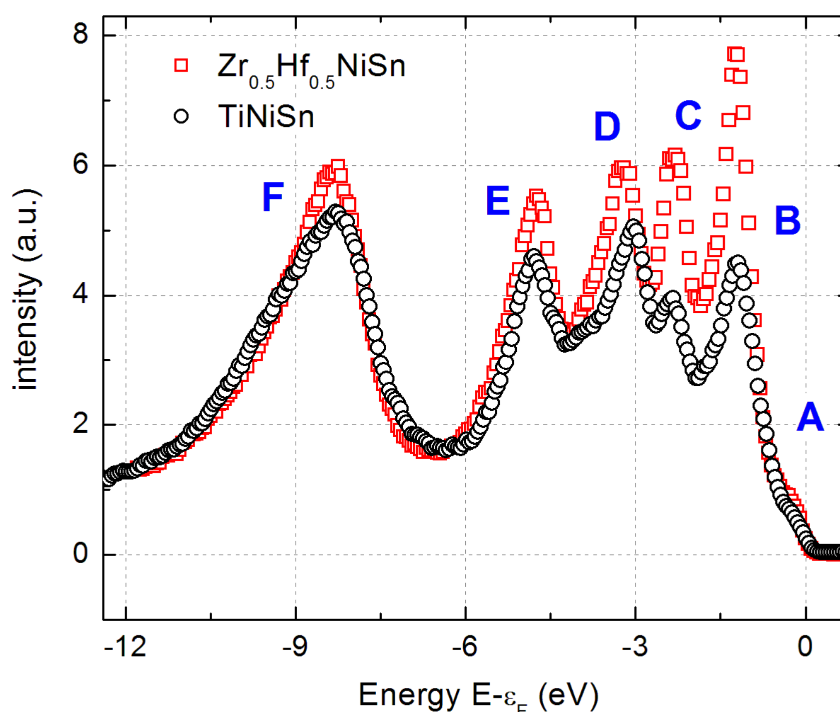

Figure 53 VB spectra for TiNiSn and $Zr_{0.5}Hf_{0.5}NiSn$ prepared as bulk materials

VB spectra taken from TiNiSn and $Zr_{0.5}Hf_{0.5}NiSn$ as bulk samples and thin films are shown in Figure 53 and Figure 54, respectively. At first glance, in particular for TiNiSn, no significant differences can be identified between bulk samples and thin films. Here, polycrystalline bulk samples are compared to strongly textured HH films. Only an

[I] Presented results and most of the conclusions have been published by Kozina et. al..(Ref. 201)

amorphous $Zr_{0.5}Hf_{0.5}NiSn$ film (blue) is characterized by the absence of the peak like shaped VB. Naturally, at the Fermi edge the most states have been measured for the metallic sample. Indicated by feature A, compared to bulk samples more “in-gap” states have been also found for the strongly textured thin films. This can be addressed to enhanced disorder and potential impurities due to sample preparation or missing post annealing.

The most significant change has been measured for two peaks at the VB edge (feature B and C) that correspond to the electrons levels with the least binding energy. Because these energy levels are formed by the covalent sublattice with hybrid orbitals t_2 and e of nickel and tin and their interaction with the X-atom in XNiSn, the most difference has been observed for the features B and C.[84] Due to a larger cross section for Zr_{4d} and Hf_{5d} than for Ti_{3d}, for $Zr_{0.5}Hf_{0.5}NiSn$ stronger peaks have been obtained in the spectra. Possibly the hafnium to zirconium ratio has been larger for the bulk sample. Other than feature E, feature D can be also addressed to the hybridized states involving Ni_{3d} and Sn_{5p} orbitals. In both spectra, for TiNiSn, feature B, C and D are slightly shifted (0.21 eV) to the Fermi edge that perhaps originates from the smaller difference in electronegativities of titanium to nickel and tin. In $Zr_{0.5}Hf_{0.5}NiSn$, the difference in electronegativities is enlarged for zirconium and hafnium compared to nickel and tin.

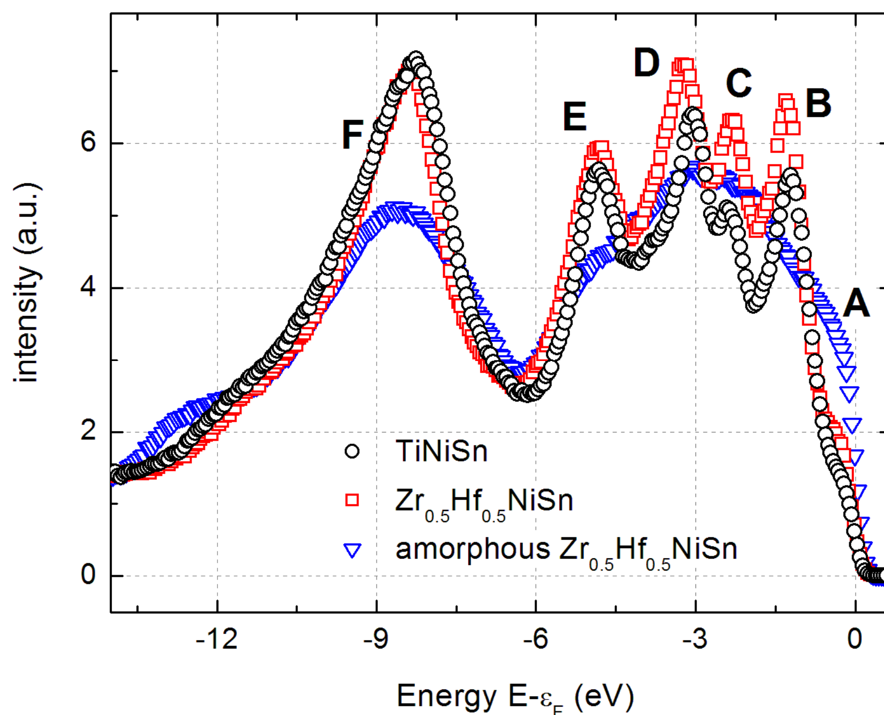

Figure 54 VB spectra of thin film TiNiSn and $Zr_{0.5}Hf_{0.5}NiSn$

At the same energy and at similar heights features E and F have been measured for both materials independently from the type of the sample. In the literature these have been addressed to Sn_{5p} bands and s states that are localized at the tin atom, respectively.[7,202] In-between, the characteristic Heusler hybridization gap can be found.[7,84] Obviously, these are less affected by titanium, zirconium or hafnium.

Similar to the XRD *θ*/2*θ* scan shown in Figure 41, Figure 55 illustrates the growth of TiNiSn on $Zr_{0.5}Hf_{0.5}NiSn$. Therefore, a tri-layer containing TiNiSn, $Zr_{0.5}Hf_{0.5}NiSn$ and TiNiSn, each with a layer thickness of about 30 nm, has been fabricated. The limited information depth of PES secures that only the VB of the upper TiNiSn layer is measured. For comparison a single TiNiSn layer (60 nm) is also plotted. While the peak positions are identical, the peak heights differ. Next to a little deviation for feature C, the biggest difference has been obtained for features F and E. Since these peaks have been mostly addressed to tin, it can be generated to an enhanced tin concentration at the film surface for the pure TiNiSn film. Importantly, the part right below the VB edge seems to be identical for both samples. Thus, no degradation of the TE properties has been found by HAXPES measurements. In order to enhance *ZT* of the system by reducing the cross-plane thermal conductivity, it is of importance to keep the electronic properties of the individual layers. Next to XRD measurements also HAXPES measurements have suggested that both HH compounds can be strongly textured grown on top of each other. As it has been already mentioned, this behavior is required by the growth of SLs.

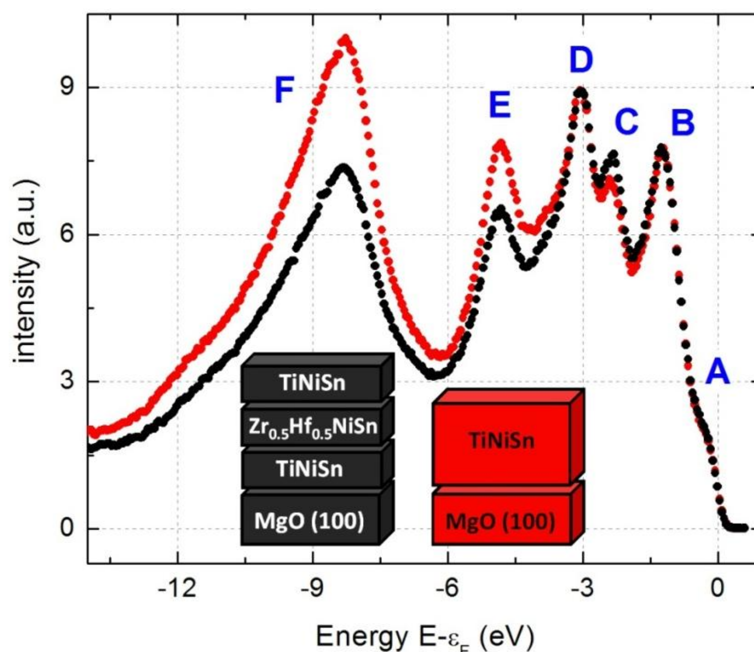

Figure 55 Comparison between VB spectra of 60 nm TiNiSn and a multilayer system containing 30 nm TiNiSn / 30 nm $Zr_{0.5}Hf_{0.5}NiSn$ / 30 nm TiNiSn

Finally, s and p polarized electromagnetic radiation has been used to measure the VB of a SL with a periodicity of 3 nm. Ten times, TiNiSn and $Zr_{0.5}Hf_{0.5}NiSn$ have been subsequently deposited on a TiNiSn buffer layer. Under grazing incidence, the polarization vector has been either aligned parallel (p) or perpendicular (s) to the surface normal. Capped by 2 nm of AlO_x, the VB has been also measured with a photon energy of about 8 keV. Apparently, both peaks assigned to the s and p states from tin are enhanced for p-polarized X-rays. Simultaneously, the intensity of the peaks originating mainly from the d orbitals of nickel, titanium, zirconium and hafnium (B, C and D) are lowered. Essentially, polarization dependent cross sections for different state are responsible for the variation in the VB spectra. Further conclusions can be found elsewhere.[203]

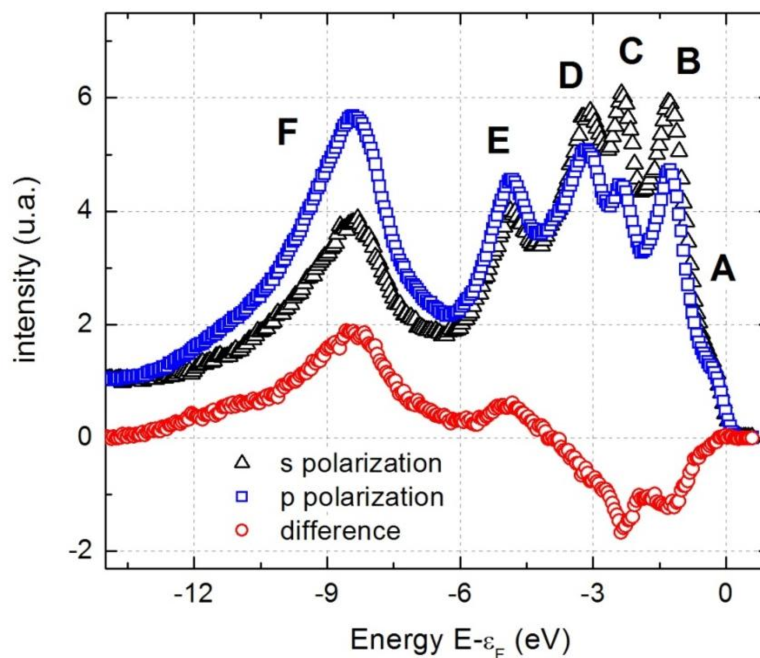

Figure 56 VB spectra of a SL with a periodicity of 3 nm measured with s- and p-polarized x-rays

After successful growths of single TiNiSn and $Zr_{0.5}Hf_{0.5}NiSn$ films, in this chapter the fabrication of SLs containing both HH compounds has been shown. Next to XRD scans that have confirmed a long structural coherence length also HAXPES measurement have given convenient VB spectra. Impressively, applying intermediate substrate temperatures while growth of SLs, periodicities of 3 nm have been resolved by HAADF-STEM images.

Chapter 7

Seebeck coefficients and conductivity measured at varied temperatures

7.1 Introduction

Up to now analyses about structure and composition of single films and SLs have been presented. These analyses were needed to find proper sputter conditions for intended film fabrication. After completing film growth optimization, essential TE properties had to be measured. According to Eq. 2.1, the TE figure of merit *ZT* that expresses the suitability of a material for TE applications also includes electric transport properties namely Seebeck coefficient α and conductivity σ. The latter was measured by four-point-technique. Here electric outer and inner contacts are responsible for a current flow and measuring the voltage drop, respectively. Because no current is flowing through the inner contacts, cable and contact resistances are not noticed. Thus, specific conductivity or specific resistance can precisely be determined by knowing applied current, sample geometry and measured voltage drop. Furthermore, the measurement has been performed at varied ambient temperatures in a cryostat.

Measuring Seebeck coefficients is by far more complex. Here, a well-known temperature gradient needs to be applied along a sample. For measuring the Seebeck coefficient at different ambient temperatures two different measurement devices were used. The physical property measurement system (PPMS) from Quantum Design (San Diego, USA) was utilized for the temperature range between 50 K and RT. Here, perpendicular to their longest dimension (10 mm), the samples (substrate plus thin film) were surrounded by four metal stripes. While two were glued right at the upper and lower ends of the sample, the others were connected without short-circuiting themselves in-between. A little part of the metal stripe (about 2 mm) stuck out from the sample to connect heater, thermometer and electric contacts. Of course, next to stiffness, the glue ensured best thermal and electric contact between sample and metal stripes. By introducing and dissipating thermal energy, using the outer stripes, a thermal gradient was

generated. To prevent incalculable energy losses, the measurement took place in vacuum. Thermal gradient as well as voltage caused by the Seebeck effect were measured at the inner metal stripes. During a temperature sweep, the Seebeck coefficients were assigned to the average temperature measured at both inner metal stripes. At each temperature, the four metal stripes were also used for measuring the specific resistivity.

As long as the thin film is connected to an isolating substrate that gives no contribution for Seebeck voltage and conductivity, in-plane measurements can be performed like that.

For measuring the Seebeck coefficient at elevated temperatures a measurement device (Model RZ2001i; with thin film option) from Ozawa Science (Tokyo, Japan) was used. Instead of measuring at low temperatures, other challenges have to be considered. Beside sample specific issues as decomposition or oxidation, energy losses due to radiation instead of heat conduction had to be taken into account. Because thermal radiation scales with temperature by the power of four, heat losses cannot be compensated if the sample is measured in vacuum. Thus, an ambient temperature is generated by heated argon gas that surrounds the sample. Due to the high surface to bulk ratio, there is an enhanced risk that even small amounts of oxygen significantly change properties of thin films. So, inserted argon 6.0 gas has been passed through further purification stages to ensure highest purity. Additional heating at one site of the sample produces a temperature gradient. Identical to the measurement at low temperatures, the temperature gradient is applied in the film plane. But instead of disposable metal stripes surrounding the sample, four re-usable platinum tips are pressed on the films surface. Arranged in one line, the four point measurement can be performed similar to ones at low temperatures. Within the platinum tips thermocouples are fabricated that permit to measure open circuit voltages (Seebeck voltage) and temperature differences simultaneously. To improve the accuracy of the measurement, at each temperature, several temperature differences up to 5 K are generated. That way, for varied samples Seebeck coefficients and conductivities were measured up to 850 K.

For a better understanding of the results, Hall and XRD measurements were performed. While former experiments have given mobilities and electron densities of the HH compounds, the latter have been used for sample classification. Despite all measured films have been previously characterized by XRD, after HT treatment in argon atmosphere, for comparison, some films have been additionally measured.

7.2 TE properties measured at low temperatures

For several thin films containing TiNiSn and $Zr_{0.5}Hf_{0.5}NiSn$, electric TE properties between 50 K and RT have been measured (Figure 57). Varied growth conditions have generated thin film TiNiSn (black symbols) and $Zr_{0.5}Hf_{0.5}NiSn$ (colored symbols) with different crystallographic qualities. Beside the composition of the HH alloys, also the FWHM of XRD ω scans (rocking curves) are given in the caption. In general, the smaller the FWHM of a XRD ω scan the better the alignment of crystallites within a film. Similar to Mikami et. al. and its observation for Fe_2VAl (full Heusler), [204] semiconducting behavior and absolute value of the Seebeck coefficient increase with increasing film quality (Figure 57a). Thus, at RT for TiNiSn films, the absolute value of the Seebeck coefficient is increased from 12 μVK^{-1} to 29 μVK^{-1} while the FWHM of the ω scans has been reduced from 2.1° to 1.2°. At the same time specific resistivity is enhanced from 4.7 μΩm to 6.9 μΩm (Figure 57b). Because the specific resistivity decreases with temperature, for all samples semiconducting behavior is observed.

Already in 1989,[212] Aliev et. al. have shown that for XNiSn (X = Ti, Zr and Hf) enhanced crystallographic order favors semiconducting behavior and increased specific resistivities.

A similar behavior has been observed for arc-melted TiNiSn bulk samples that were measured before and after an additional annealing. The absolute Seebeck coefficient, measured at RT, has increased from 20 μVK^{-1} to 318 μVK^{-1} by post-annealing at 1073 K for two weeks. Simultaneously, the electrical resistivity has increased about two orders in magnitude.[54]

Recently, Birkel et. al. have fabricated two different TiNiSn bulk samples.[205] As the initial fabrication process, arc-melting has been used for obtaining a homogeneous TiNiSn alloy. Instead of arc-melting, a second sample was initially molten in a microwave oven. Further fabrication of the samples was done identically. Interestingly, similar to thin film TiNiSn (Figure 57), based on the fabrication process, Birkel et. al. have observed a variation in TE properties. While at RT the Seebeck coefficient has changed from -140μVK^{-1} (arc-melted) to -255 μVK^{-1} (rf-melted), simultaneously the specific resistivity has been increased from 67 μΩm to 97 μΩm. This exhibits the sensitivity of the TE properties on the fabrication process and the sample quality of TiNiSn.

Noticeably, specific conductivities measured for thin film TiNiSn have been obtained for doped TiNiSn bulk samples. Analyses with $Ti_{1-x}V_xNiSn$ bulk samples have shown that even small amounts of vanadium can change the electric properties tremendously. Doping of 5 % vanadium generated similar results for Seebeck coefficients and specific resistivity as it has been observed for presented thin films.[60] Remarkable has been the similar linear trend of the specific resistivity at low temperatures. Also for niobium doped $Ti_{1-x}Nb_xNiSn$ samples, about the same specific conductivities have been obtained.[58]

For thin film $Zr_{0.5}Hf_{0.5}NiSn$ two different samples have been sputtered. Without any buffer layer an amorphous film (blue circles) and a strongly textured film with a 15 nm TiNiSn buffer layer (red squares) were measured. In agreement with VB measurements obtained by HAXPES (Figure 54), the amorphous $Zr_{0.5}Hf_{0.5}NiSn$ film with its multiple metallic states at the Fermi energy exhibits a low absolute Seebeck coefficient. Instead of 9 μVK^{-1} for the amorphous film, for strongly textured polycrystalline $Zr_{0.5}Hf_{0.5}NiSn$ an increased absolute value of 63 μVK^{-1} has been obtained for the Seebeck coefficient if a TiNiSn buffer layer with a thickness of 15 nm is deposited underneath. For the latter sample the FWHM of the (200) ω scan has been 1.0°.

Compared to thin film TiNiSn, the higher absolute Seebeck coefficient for the $Zr_{0.5}Hf_{0.5}NiSn$ film originates from a better crystallinity as well as the different material properties of $Zr_{0.5}Hf_{0.5}NiSn$.[63] In comparison to other HH compounds (XNiSn), the highest absolute Seebeck coefficients have been also obtained for $Zr_{0.5}Hf_{0.5}NiSn$.[52] Based on the fabrication process for $Zr_{0.5}Hf_{0.5}NiSn$ bulk samples, at RT Seebeck coefficients from -160 μVK^{-1} to -350 μVK^{-1} have been observed.[76]

Similar to TiNiSn, specific resistivities for thin film $Zr_{0.5}Hf_{0.5}NiSn$ (Figure 57b) are an order of magnitude lower than observed for $Zr_{0.5}Hf_{0.5}NiSn$ bulk material.[63] At RT, for thin film $Zr_{0.5}Hf_{0.5}NiSn$, 14.2 µΩm and 12.3 µΩm have been measured for the strongly textured and the amorphous sample, respectively. Again, these values are comparable with doped $(Zr_{0.5}Hf_{0.5})_{0.99}X_{0.01}NiSn$ bulk samples. For X = tantalum and niobium, specific resistivities of 10 µΩm and 14 µΩm have been observed by Hohl et. al..[63]

The sensitivity about the electric properties of $Zr_{0.5}Hf_{0.5}NiSn$ on fabrication process and therefore on crystal structure has been shown by Uhler et. al..[76] Utilizing post-annealing, the correlation between increased crystallographic quality and enhanced semiconducting behavior has been shown. Thus, there has been a decreased electron density, but an enhanced absolute Seebeck coefficient (from 136 μVK^{-1} to 203 μVK^{-1}).

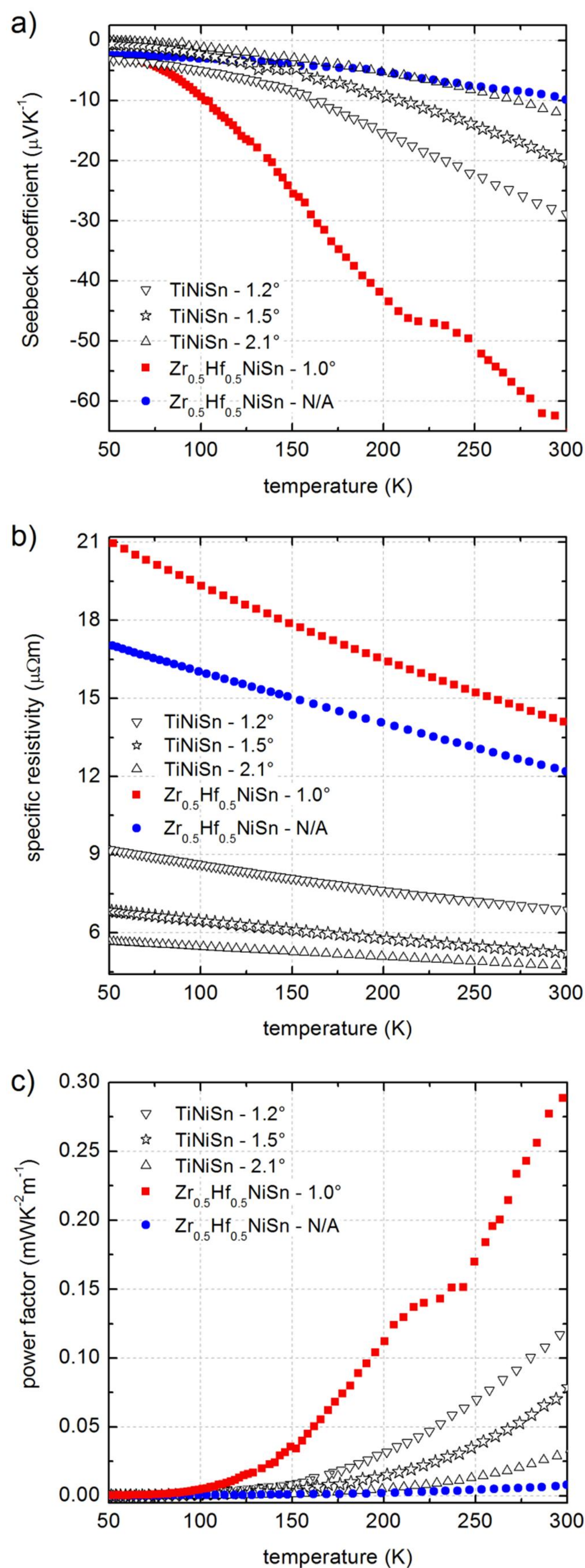

Figure 57 Seebeck coefficient a), specific resistivity b) and power factor c) of TiNiSn (black/open symbols) and $Zr_{0.5}Hf_{0.5}NiSn$ (colored/solid symbols) thin films

As it has been proven by bulk analysis for TiNiSn and $Zr_{0.5}Hf_{0.5}NiSn$, enhanced conductivities as well as decreased absolute Seebeck coefficients can be explained by stoichiometry, crystallographic order and contaminations within the films. Stoichiometry and crystallographic order are mostly affected by growth rate, sputtering pressure and substrate temperature. Contaminations could have originated from target production, sputter gas and residual gas in the chamber. A detectable amount of fluorine has been already identified by HAXPES measurements (Figure 51). Since the specific resistivity decreases with increasing temperature, all samples exhibit semiconducting behavior which was improved by enhancing epitaxial quality.

The power factor $\alpha^2\sigma$ is used to combine the electric coefficients that are essential for TE application. For the low temperature range, in Figure 57c calculated power factors are illustrated for TiNiSn and $Zr_{0.5}Hf_{0.5}NiSn$ films. For thin film HfNiSn, Wang et al. have obtained similar values.[206] Since TiNiSn and $Zr_{0.5}Hf_{0.5}NiSn$ exhibit highest *ZT* values at elevated temperatures, power factors are still increasing at RT.

Finally it should be noted that the electric transport properties were measured in-plane while the HH SL structure has been designed for cross-plane application. For isotropic films with thicknesses above 150 nm, in-plane and cross-plane electric properties are identical.[1] Also for Si/Ge SLs with a periodicity of 10 nm, cross- and in-plane power factors were shown to be comparable.[207]

7.3 Origin of enhanced conductivity

Having the majority of the conduction to be done by electrons, specific resistivity ρ and specific conductivity σ depend on carrier concentration n, elemental charge e and electron mobility μ_e. Those are linked as the following:

$$\sigma = \frac{1}{\rho} = e \cdot n \cdot \mu_e \qquad 7.1$$

By applying an electric and a magnetic field, as it is illustrated in the inset from Figure 58 (down left), it can be determined whether electron mobility or carrier concentration is mostly responsible for the electrical conductivity in a solid. Plotting arising Hall voltage U_H divided by (applied) current I as a function of magnetic induction B, this information can be obtained by the slope of the plotted function in Figure 58:

$$\frac{U_H}{I} = \frac{R_H}{d} \cdot B \qquad 7.2$$

In the present case with isolating MgO as substrate material, the HH film thickness d is taken into account. Finally, the slope that includes the Hall constant R_H gives information about the carrier concentration:

$$R_H = \frac{1}{n \cdot e} \tag{7.3}$$

In combination with Eq. 7.1 and measured specific conductivity, afterwards the electron mobility can be calculated.

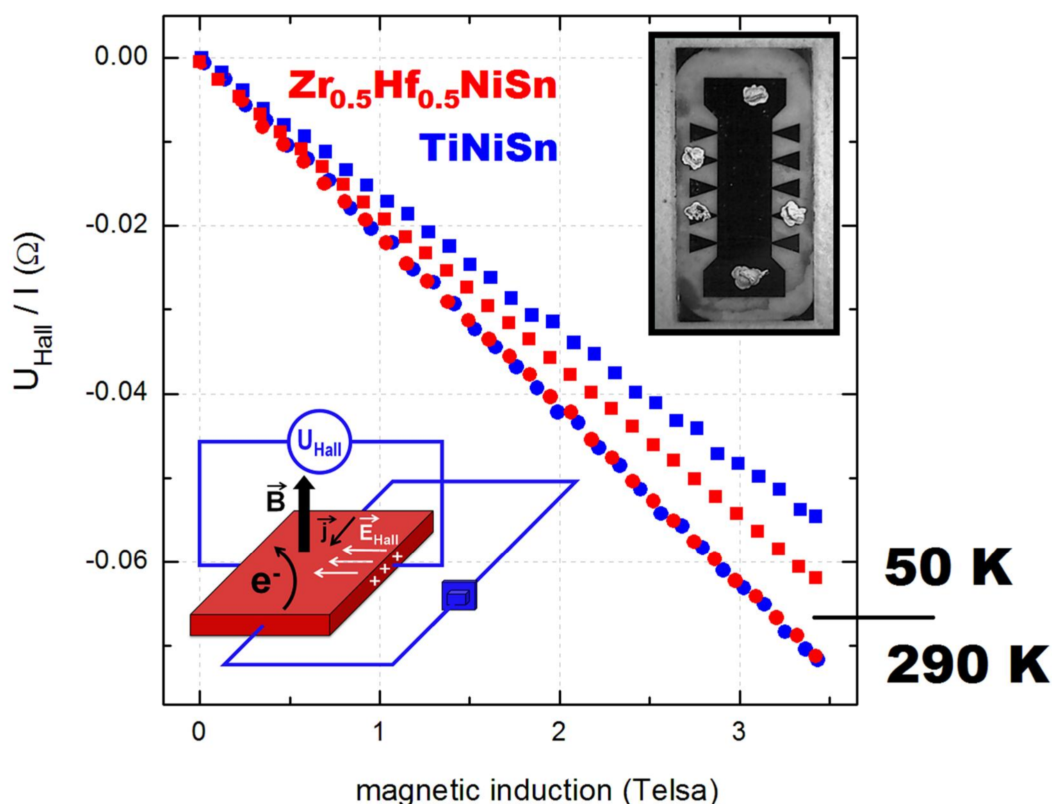

Figure 58 Hall measurements taken from TiNiSn (blue) and $Zr_{0.5}Hf_{0.5}NiSn$ (red) performed at 290 K (circles) and 50 K (squares)

Beside the schematic illustration of the measurement also a picture of a measured film is shown in the inset from Figure 58. Here, the picture has been taken from a top view of the MgO substrate with the following dimensions: 10 x 5 mm^2. To obtain defined dimensions for the calculation of material dependent transport properties, the HH thin films have been wet-chemically etched. With a positive photo resist and optical photolithography, the aspired structure was brought on the film surface. For etching TiNiSn as well as $Zr_{0.5}Hf_{0.5}NiSn$ at the accessible film surface, aqua regia (Kings's water) was used. Thus, an etching rate in the order 5 nms^{-1}, was obtained by using HCl and HNO_3 in the wt. ratio of 3 : 1.

The bright spots (conductive silver) located at the residual HH film structure (dark) indicate the electrical connections. While the two located at the wide stripe ensure the electron flow perpendicular to the applied magnetic field, the three spots located at the triangles are responsible for measuring Hall voltage and specific conductivity. These are measured perpendicular and parallel to the applied current, respectively.

To determine carrier concentrations and electron mobilities, using a cryostat, magnetic field strengths up to 3.5 T were applied at ambient temperature of 50 K and 290 K. Thus, for TiNiSn and $Zr_{0.5}Hf_{0.5}NiSn$ films with thicknesses of 150 nm, Hall constants (Eq. 7.2) have been obtained by plotting Hall resistance $U_H I^{-1}$ as a function of B (Figure 58). At 290 K carrier concentrations of 2.0 x 10^{21} cm^{-3} and 1.6 x 10^{21} cm^{-3} were determined for strongly textured polycrystalline TiNiSn (blue circles) and $Zr_{0.5}Hf_{0.5}NiSn$ (red circles). Thus, there are about 0.1 electrons per formula unit. Considering specific conductivities and Eq. 7.1, electron mobilities of 1.7 $cm^2V^{-1}s^{-1}$ and 2.1 $cm^2V^{-1}s^{-1}$ have been determined, respectively. Again, for bulk materials, similar carrier concentrations were measured for doped HH bulk materials.[214,215] Simultaneously, present electron mobilities for thin films are an order of magnitude lower.

	TiNiSn		$Zr_{0.5}Hf_{0.5}NiSn$	
	290 K	**50 K**	**290 K**	**50 K**
electron mobility $\left(\frac{cm^2}{Vs}\right)$	**1.7**	**1.0**	**2.1**	**1.2**
electron density $\left(\times 10^{21} \frac{1}{cm^3}\right)$	**2.0**	**2.6**	**1.6**	**1.9**

Table 4 Electron mobilities and electron densities (carrier concentrations) for TiNiSn and $Zr_{0.5}Hf_{0.5}NiSn$ measured at 50 K and 290 K

Using the same TiNiSn (blue squares) and $Zr_{0.5}Hf_{0.5}NiSn$ (red squares) samples, Hall measurements were also performed at 50 K (Figure 58). At this temperature, carrier concentrations of 2.6 x 10^{21} cm^{-3} and 1.9 x 10^{21} cm^{-3} and electron mobilities of 1.0 $cm^2V^{-1}s^{-1}$ and 1.2 $cm^2V^{-1}s^{-1}$ have been obtained, respectively. Carrier concentrations and electron mobilities that were measured at 50 K and 290 K are summarized in Table 4.

Initially, it should be noted that in SCs carrier concentrations as well as electron mobilities can vary over decades at different temperatures. Thus only small variations have been observed for both HH thin films. Temperature dependent electron mobility can be explained by electron-phonon interaction and impurity scattering. Starting from 0 K, donators or impurities that have electron levels right below the CB edge are ionized. Thus additional charged scattering centers occur with temperature and therefore depress electron mobility. But the effect ends when all donators are ionized. Due to electron-phonon interaction, at elevated temperatures an increasing number of phonons basically causes a further reduction in electron mobility. Because the electron mobility does not change a lot from 50 K to 290 K (Table 4), it can be assumed that some donator or impurity states are already ionized at 50 K.

Similar to $Zr_{0.25}Hf_{0.25}Ti_{0.5}NiSn$ bulk samples,[208] at 50 K higher carrier concentrations than at 290 K have been observed for HH thin films. Performing Hall measurements also at intermediate temperatures, Tang et. al. have obtained a minimum at about 150 K.[208] A similar observation has been done by Uher et. al. for ZrNiSn and of $Zr_{0.5}Hf_{0.5}NiSn$ bulk samlples.[76] Deviating from a single parabolic band structure, the present band structures for HH materials (Figure 11) have been more complex. Beside in-gap states (see Figure 54) that contribute to the conduction starting from hopping mechanisms up to the generation of impurity bands, the chemical potential of electrons can vary with temperature. Therefore, the number of carriers does not necessarily increase with temperature. Enhanced electron-hole excitations can decrease the effective amount of carrier concentration by different mobilities in different bands. Thus, several mechanisms that contribute to the electrical conductivity have caused a little depressed carrier concentration at enhanced temperatures.

Nevertheless, very high carrier concentrations have been measured for TiNiSn and $Zr_{0.5}Hf_{0.5}NiSn$ thin films. Apart from predicted semiconducting behavior, this deviating behavior can be explained by atomic disorder.[37] A theoretical analysis using several models for DOS calculation showed that up to 0.5 % nickel interstitials at the titanium side cause the heavily doped intrinsic behavior of TiNiSn.[209]

Although for HH thin films foreign phases have not been identified by XRD or EDX mapping, J. P. A. Makongo et al. have shown for $Zr_{0.25}Hf_{0.75}NiSn$ bulk samples that additional metallic phases can enhance the carrier concentration and even more importantly depress the electron mobility tremendously.[210] Because similar behavior has been also detected for HH thin films, present metallic secondary phases should not be

excluded. For HH bulk samples, electron mobilities of about 10 $cm^2V^{-1}s^{-1}$ have been obtained.[59,76] Simultaneously, the HH bulk samples have exhibited a higher absolute Seebeck coefficienst.

Despite the depressed Seebeck coefficients, for TiNiSn and $Zr_{0.5}Hf_{0.5}NiSn$ thin films reasonable power factors (Figure 57c) have been obtained by conductivities that are two magnitudes higher than observed for most HH bulk samples.[76]

Schwall et. al. have obtained similar power factors for $(Zr_{0.5}Hf_{0.5})_{1-x}Nb_xNiSn$ bulk samples.[57] Although the absolute Seebeck coefficients have been decreased for all niobium doping concentrations, the power factor has been increased due to an enhancement in conductivity about two orders of magnitude.

For heavily doped SCs, where the donator states and their energy gap to the CB E_d are essentially responsible for the electrical conductivity, the temperature dependence can be fitted by:[130,211]

$$\rho \propto \exp \frac{E_d}{2k_BT}. \tag{7.4}$$

According to the specific resistivities illustrated in Figure 57, for TiNiSn (1.2°) and $Zr_{0.5}Hf_{0.5}NiSn$ (1.0°) films with highest structural quality (FWHM of the corresponding rocking curves), E_d of 2.9 meV and 4.2 meV have been calculated, respectively. Therefore the conductivity of the HH films strongly depends on the impurity states in the energy gap. The energy gap is in the order of about 0.1 eV if it is optically measured.[212] Additionally the effective mass of electrons in TiNiSn can be estimated to be 3-4 m_0.[213]

Results that have been presented in the last sections exhibit HH compounds with partial metallic and semiconducting behavior. Both have effects on TE properties. In his content thin films fabricated by sputter depositing match with published results obtained by HH bulk samples. Atomic disorder, secondary phases and/or impurities have shifted TiNiSn and $Zr_{0.5}Hf_{0.5}NiSn$ thin films to be more metallic than comparable bulk samples. These have led to depressed absolute Seebeck coefficients and decreased electron mobilities. Beside these properties also enhanced carrier concentrations have been obtained which have increased the powerfactor.

Compared to the presented thin film results, $Zr_{0.4}Hf_{0.6}NiSn$ bulk samples doped with 2 % antimony at the tin side exhibited similar carrier concentrations.[214] Here, Yu et. al. have achieved that the electron mobility has not been reduced by the doping. But a depressed absolute Seebeck coefficient has not been prevented. As a following step Zhu

et. al. have fabricated $(Zr_{0.6}H_{0.4})_{1-y}Y_yNiSn_{0.98}Sb_{0.02}$ bulk samples with only a small reduction in carrier concentration.[215] While electron mobility remained high, importantly, the absolute Seebeck coefficient has been enhanced. Thus, a *ZT* value of about 0.65 has been achieved for $(Zr_{0.6}Hf_{0.4})_{0.99}Y_{0.01}NiSn_{0.98}Sb_{0.02}$. Without considering thermal conductivity that is also influenced by electrical conductivity and plays a role in TE efficiency, it can be seen how single material parameters can be optimized by the composition of HH compounds. While for bulk materials, plenty of work has already been done for optimized TE properties, for HH thin films this research is still at the beginning.

7.4 Thermoelectric measurements and thin film stability at elevated temperatures

7.4.1 TiNiSn

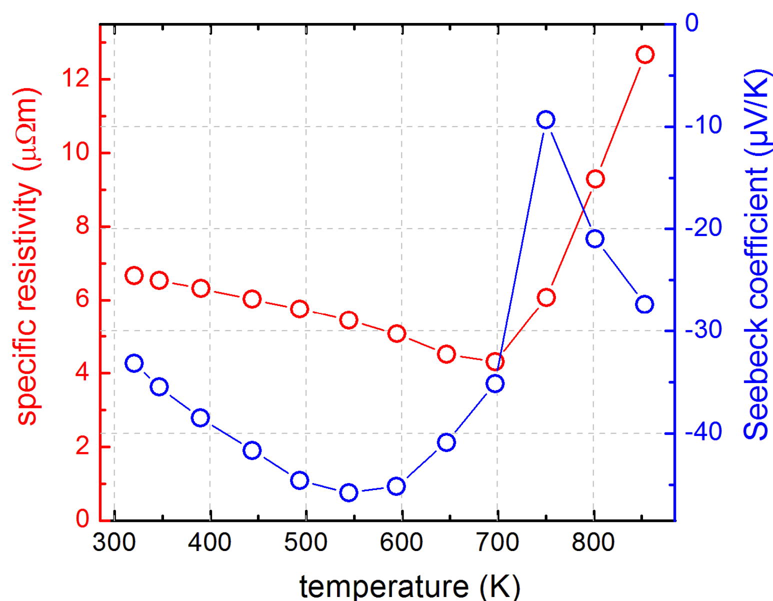

Figure 59 Specific resistivities and Seebeck coefficients for a TiNiSn thin film measured up to an average ambient temperature of 850 K

As it has been described in the introduction of this section, a device from Ozawa Science has been used for measuring TE properties at elevated temperatures.[I] Although, transport properties obtained at low temperatures have already given revealing

[I] The following HT TE measurements were performed at the EMPA (Eidgenössische Materialprüfungs- und Forschungsanstalt) by Dr. Sascha Populoh

information, above RT, higher absolute Seebeck coefficients and higher conductivities were expected. For TiNiSn bulk samples, highest *ZT* values are measured above 700 K (see Table 1).

As it is illustrated in Figure 59, specific resistivity (red) and Seebeck coefficient (blue) measurements were performed for thin film TiNiSn. A previously applied XRD ω scan revealed a FWHM of the (200) TiNiSn diffraction peak of 2.4°. At about 550 K, a maximum power factor of about 0.4 $mWK^{-2}m^{-1}$ has been measured. Compared to TiNiSn bulk samples (see Figure 61), the maximum power factor is about one fifth. Furthermore, for TiNiSn bulk samples the maximum has been obtained at an average temperature that is about 150 K higher.

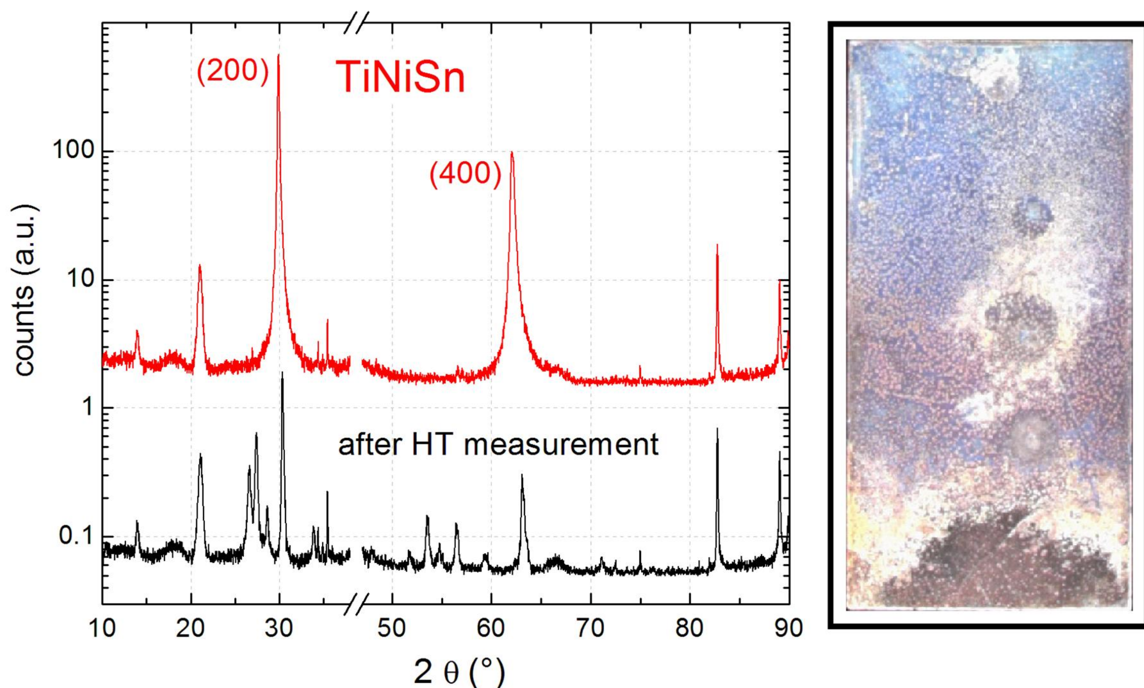

Figure 60 XRD $\theta/2\theta$ scans (left) and a picture taken from the TiNiSn sample surface (right) after HT Seebeck treatment (the intense MgO (200) reflection is omitted)

Importantly, the measurement for Seebeck coefficient and specific resistivity (Figure 59) at an average temperature of about 700 K has been the final reliable data point that can be addressed to the TiNiSn film. Above this temperature, the measurement condition change tremendously. In the previous section, the characteristic behavior for the specific resistivity between 500 K and 1000 K has been described by Eq.7.4. Thus, the specific resistivity is supposed to decrease monotonically with temperature. Beside the irregularity in specific resistivity, between 700 K and 725 K, also an unexceptional big step for the Seebeck coefficient has been observed.

An additional XRD $\theta/2\theta$ scan, illustrated in Figure 60, was performed after the HT TE measurement (Figure 59). While the intensities of diffraction peaks that can be assigned to the TiNiSn film have decreased by a factor of more than 10, several other diffraction peaks are observed. These can be addressed to additional phases that are obviously formed at ambient temperatures of about 700 K. Jung et. al. analyzed thermal expansion and the melting points of TiNiSn, ZrNiSn and HfNiSn.[61] In contrast to ZrNiSn and HfNiSn that could be annealed right up to the melting point without measuring any significant change in the XRD diffractogram, TiNiSn decomposed at 1453 K into additional $TiNi_2Sn$, Ti_2Sn and Sn phases. If composition, grain structure or measurement setup made the difference for the thin films has not been clarified.

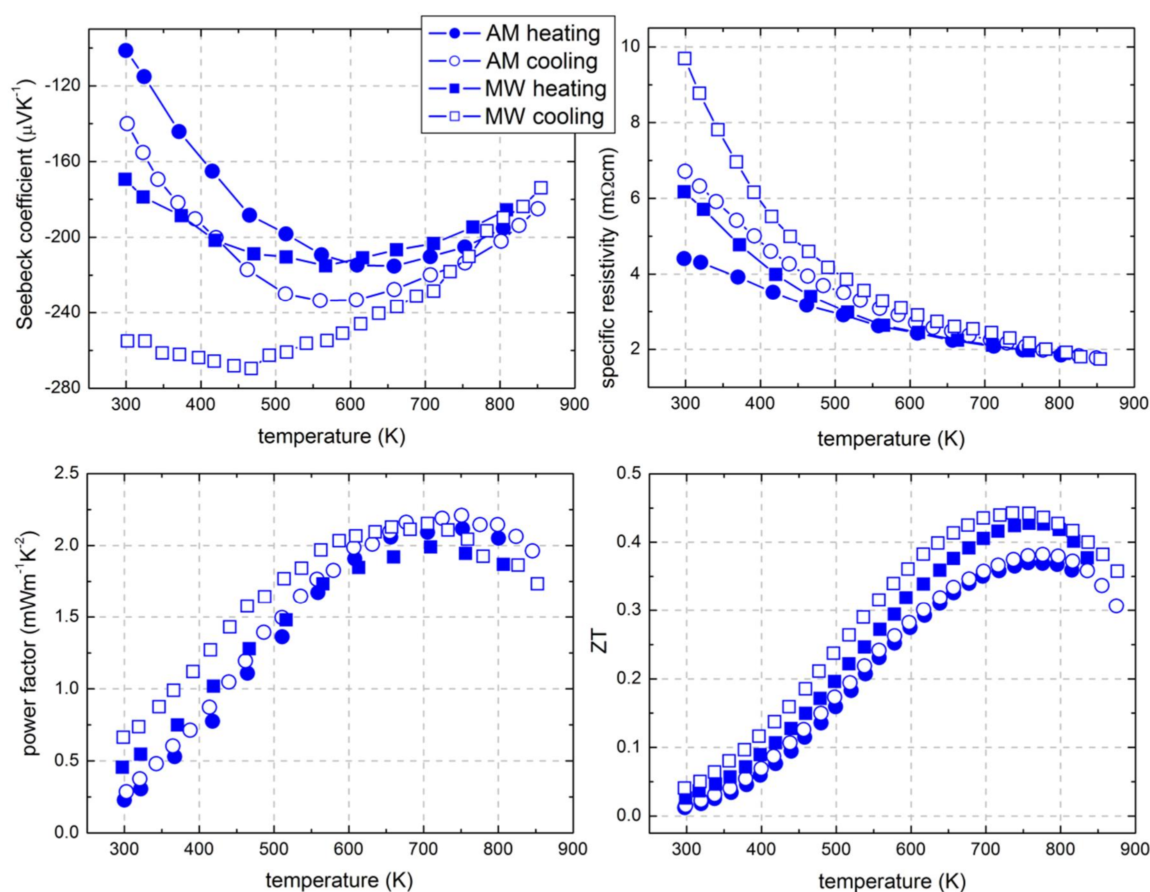

Figure 61 Seebeck coefficient, specific resistivity, power factor and figure of merit of TiNiSn bulk samples generated by arc-melting (AM) and microwave (MW) techniques; Open and close symbols were taken while heating and cooling, respectively. (Adapted from Ref. 205)

An image of the surface from TiNiSn thin film after HT TE measurement is also shown in Figure 60 (right). Beside clearly visible discoloration, also a countless number of bright spots have occurred.

Although it is seldom in the field of TE, Birkel et. al. have published TE properties of bulk TiNiSn (Figure 61) not just while heating up (open symbols) to 880 K but also while cooling down (solid symbols) to RT.[205] AM and MW correspond to different fabrication processes that have already been discussed above. Surprisingly, power factor $\alpha^2\rho^{-1}$ and TE figure-of-merit *ZT* showed almost identical values, while specific resistivity and the absolute Seebeck coefficient decrease significantly. Importantly, a compositional change, as it did happen for thin films at about 550 K, has not appeared for TiNiSn bulk samples.

If the change that has been responsible for the difference in TE parameters, obtained while heating and cooling, not only depends on a certain temperature, but also on the duration of the TE measurement at elevated temperatures, thin films would be even more affected. Because for thin film samples all TE material is close to the surface, it completely rearranges or/and reacts with surrounding atoms much faster than bulk samples having macroscopic dimensions. Additionally, smaller grain sizes obtained in the thin films enhance the density of grain boundaries that are possibly the starting point of chemical reactions.

7.4.2 $Zr_{0.5}Hf_{0.5}$NiSn/TiNiSn bilayer

At HT, TE measurements were performed using a bilayer consisting of $Zr_{0.5}Hf_{0.5}$NiSn and TiNiSn (buffer layer) with thicknesses of about 300 nm and 200 nm, respectively. As it can be seen in Figure 62, several heating cycles were subsequently driven. In first heating cycle, the sample was heated up to an average temperature of 550 K. Back to RT, the cooling curve has been approximately identical. Afterwards, the sample was annealed up to 700 K. Again, Seebeck coefficient and specific resistivity have been similar to the previous heating cycle. While heating, at 680 K the maximum powerfactor of about 0.32 $mWK^{-2}m^{-1}$ has been obtained. Still, at the same temperatures similar values are obtained while decreasing the temperature back to RT. For the bilayer, the maximum power factor has been found at a higher temperature than for the single TiNiSn layer. Because a XRD ω scan had not been done before the HT TE measurement was performed, a statement about the crystallographic quality has not been implemented.

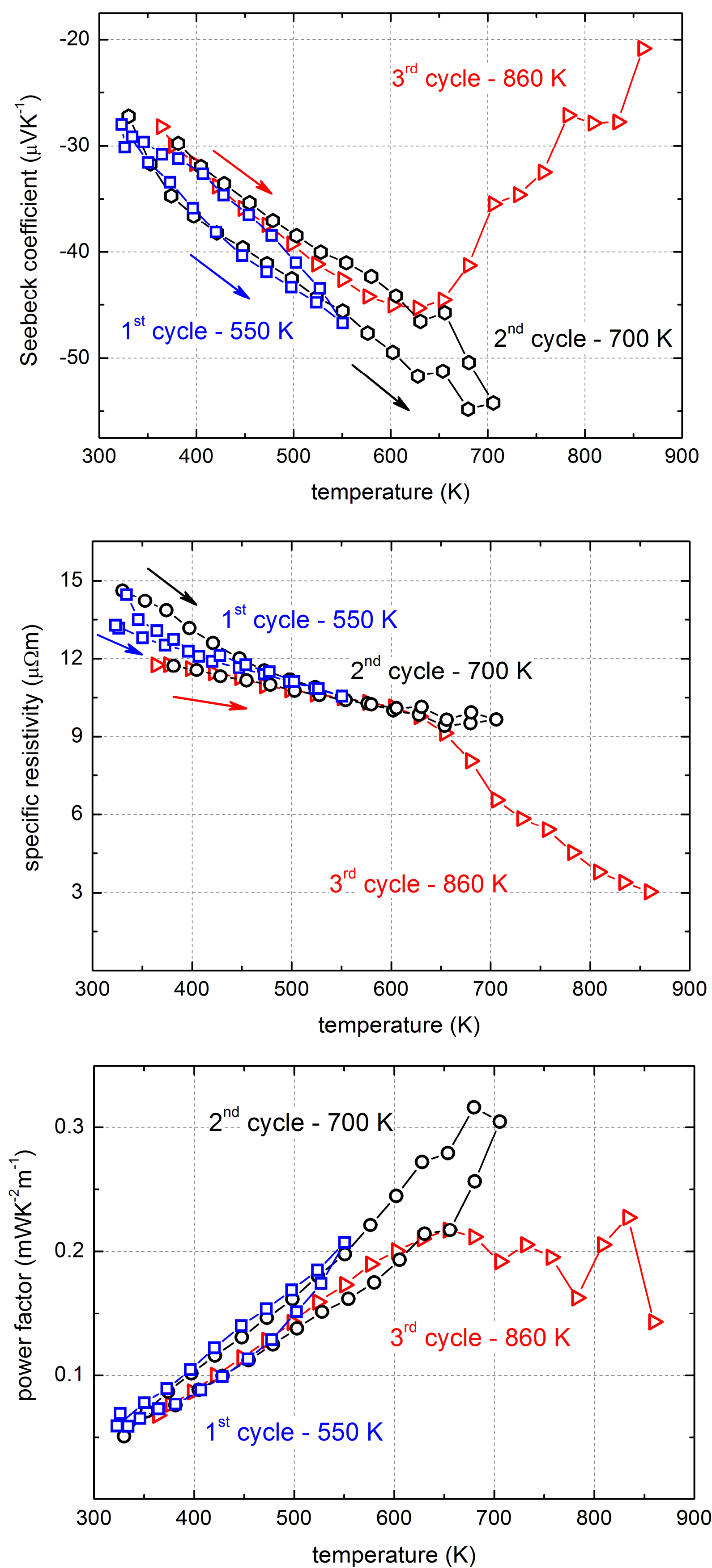

Figure 62 Up to different temperatures, three cycles of HT TE measurements conducted with a $Zr_{0.5}Hf_{0.5}NiSn$/TiNiSn bilayer

Surprisingly, during the third heating cycle, absolute Seebeck coefficient and specific resistivity diverged the previously measured path at about 650 K. At 700 K, a lower power factor of ~ 0.2 $mWK^{-2}m^{-1}$ has been calculated. For higher temperatures, decreased absolute Seebeck coefficients have prohibited higher power factors although further decreased specific resistivities have been simultaneously found. For the final cooling, no data points have been recorded. Similar to the single TiNiSn layer (Figure 59), the decomposition also for the bilayer has started at about 650 K. Due to the variation between second and third heating cycle, also the duration the thin film is at elevated temperatures, and not only a certain temperature have obviously played a key role in the decomposition of the films.

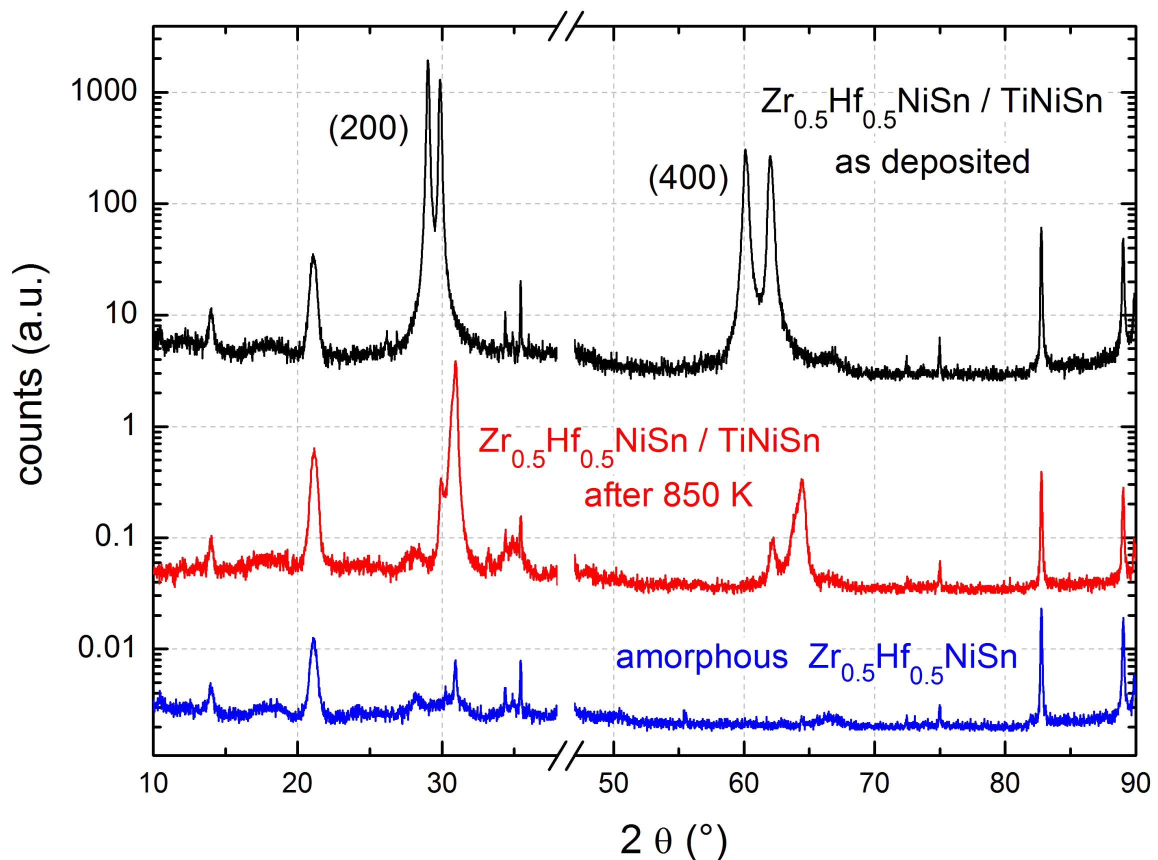

Figure 63 XRD $\theta/2\theta$ scans of a $Zr_{0.5}Hf_{0.5}NiSn/TiNiSn$ bilayer measured before (black) and after (red) HT TE measurements; After HT TE measurement, a XRD $\theta/2\theta$ scan of a single amorphous $Zr_{0.5}Hf_{0.5}NiSn$ layer is additionally shown in blue (intense MgO (200) reflection is omitted).

For a $Zr_{0.5}Hf_{0.5}NiSn/TiNiSn$ bilayer, similar to the previously discussed one (Figure 62), FWHMs of the XRD ω scans of 2.4° and 2.5° have been measured, respectively. Afterwards, a HT TE measurement with one heating cycle up to 850 K was performed. Based on the TE properties, the decomposition occurred at about 700 K. A comparison

between XRD $\theta/2\theta$ scans performed before (black) and after (red) the HT TE measurement is shown in Figure 63.

Appropriate to the $Zr_{0.5}Hf_{0.5}NiSn$/TiNiSn bilayer, introduced in chapter 4, before the HT TE measurement (black/as deposited), Figure 63 shows a similar diffraction pattern (see Figure 30). Identically, a double peak structure has been measured. The diffraction peaks located a lower and higher angles of diffraction can be addressed to $Zr_{0.5}Hf_{0.5}NiSn$ and TiNiSn, respectively. Different to the measurement shown in Figure 62, for now, only one heating cycle up to 850 K was applied at the HT TE measurement. After the bilayer has been at elevated temperatures, again a XRD $\theta/2\theta$ scans was performed (red/after 850 K). By comparing the diffractograms ‘as deposited’ and ‘after 850 K’ it can be noticed that the bilayer has not composed into several phases as it has been previously presented for the single TiNiSn film (see Figure 60). Essentially, a reduction in film peaks has been observed (red). While a small TiNiSn film peak has remained, the $Zr_{0.5}Hf_{0.5}NiSn$ film peaks have completely vanished. Instead, a new film peak has occurred at a higher diffraction angle. The occurrence of a diffraction peak at higher angles corresponds to a smaller lattice constant and is rather unusual because within the HH compounds TiNiSn exhibits the smallest one.

Importantly, the decomposition of TiNiSn happens differently for single films and for bilayers with $Zr_{0.5}Hf_{0.5}NiSn$ as a capping layer. While the single film has decomposed into several phases (Figure 60), a similar decomposition has not been observed for the TiNiSn/$Zr_{0.5}Hf_{0.5}NiSn$ bilayer (Figure 63).

For comparison, also a $Zr_{0.5}Hf_{0.5}NiSn$ film that was fabricated under non-ideal sputter conditions was measured in the HT TE measurement device. Although it does not necessarily mean that the film have had an amorphous structure, ‘amorphous’ expresses the absence of any film peak in the XRD $\theta/2\theta$ scan after fabrication process (in contrast to Figure 42). But after the sample was heated in only cycle up to 850 K, no difference has been obtained in the XRD $\theta/2\theta$ scan. As it is illustrated in Figure 63, no significant film peaks have been observed (blue). Because the HT TE measurement is similar to an additional heat treatment, the attempt with a non- or only weakly structured sample was performed. Barely visible peaks at about 30° were also previously detected. Remaining diffraction peaks can be assigned to the intense MgO (200) substrate reflection that is omitted in Figure 63. By heating an amorphous $Zr_{0.5}Hf_{0.5}NiSn$ layer up to 850 K, the formation of any phases has not been observed either.

7.4.3 Superlattices

Beside single TiNiSn layers and $Zr_{0.5}Hf_{0.5}NiSn$/TiNiSn bilayers, also SLs have been analyzed. Although the SLs were fabricated for cross-plane application, TE in-plane measurements have given information about thermal stability. But one has to keep in mind that the contribution of electron scattering at the interfaces for the HH SLs remains unknown. Therefore, using TE in-plane properties to draw conclusions about suitability for cross-plane application becomes difficult.

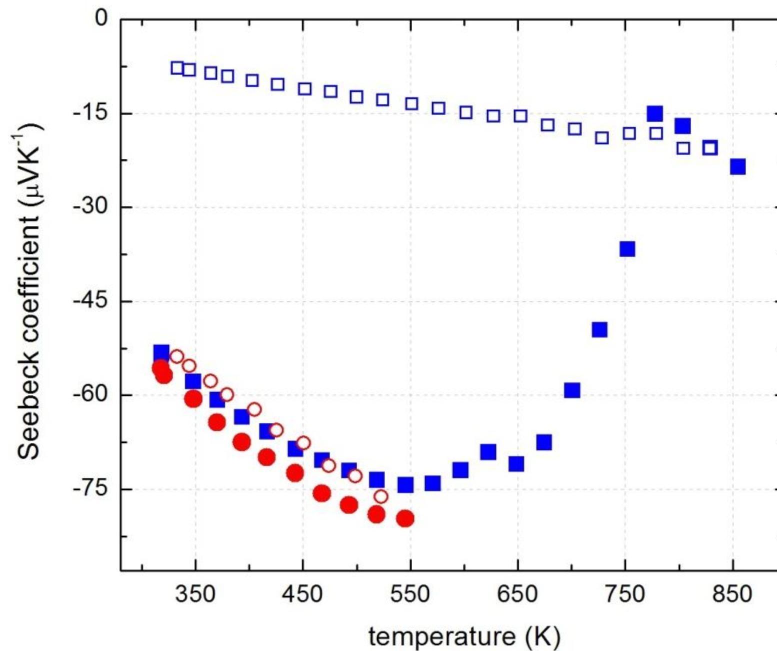

Figure 64 HT Seebeck measurement of two identical SLs measured up to 550 K (red) and 850 K (blue)

In the following, results from SLs having ten periods each with a periodicity of 21 nm are presented. Within a total thickness of 210 nm, there have been 19 regularly contributed interfaces.

For the HT TE measurement two identically grown SLs were measured up to two different maximum temperatures. While recorded Seebeck coefficients are illustrated in Figure 64, one was heated to 550 K (red) and the other up to 850 K (blue). Increasing and decreasing temperatures are labeled with closed and open symbols, respectively. Identical to the bilayer, shown in Figure 62, similar values have been obtained for heating and cooling curves if the sample was heated only up to 550 K. Besides, the unchanged sample composition is illustrated in Figure 65. Here, XRD $\theta/2\theta$ scans, before (red) and after (blue) the HT TE measurement, have shown an identical satellite peak structure. Both identical diffractograms imply that there has been no significant intermixing at the

interfaces. Because the maximum temperature of 550 K is about 150 K lower than the substrate temperature during growth, intermixing cannot be expected.

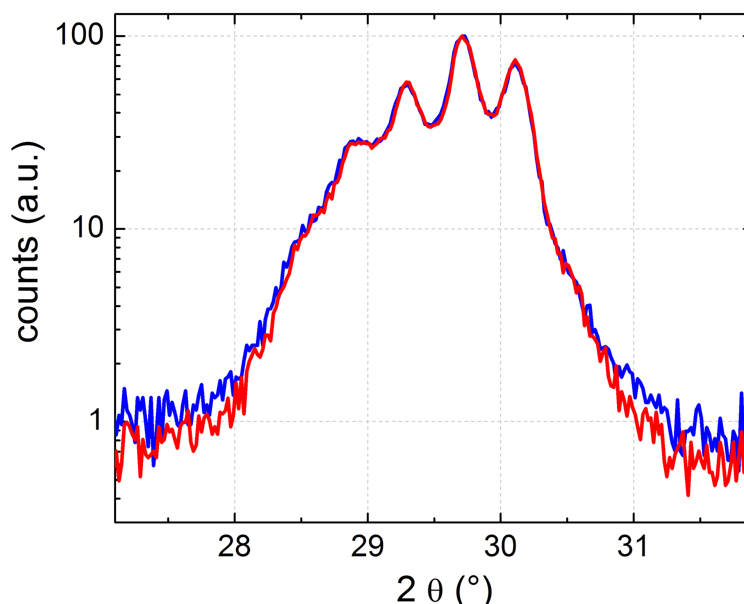

Figure 65 XRD $\theta/2\theta$ scan of a SL measured before (red) and after (blue) a HT TE measurement with a maximum temperature of 550 K.

As it has been the case for a single TiNiSn layer and a $Zr_{0.5}Hf_{0.5}NiSn$/TiNiSn bilayer, also for a SL an irreversible change has been observed if the HT TE measurement was performed up to 850 K (blue). In Figure 64, heating and cooling path of the Seebeck coefficients are not similar anymore. A similar behavior has already been found for a TiNiSn film (Figure 59) and for a TiNiSn/$Zr_{0.5}Hf_{0.5}NiSn$ bilayer (Figure 62). In the same temperature range at about 700 K, again an irreversible change has happened to the SL. Therefore, during cooling down the sample, the absolute Seebeck coefficients monotonically decrease and do not follow the heating path.

The decomposition of the SL has been also obtained by XRD $\theta/2\theta$ scans, shown in Figure 66. Before (blue) and after (red) the HT TE measurement with a maximum temperature of 850 K, the diffractograms were taken. Similar to the $Zr_{0.5}Hf_{0.5}NiSn$/ TiNiSn bilayer (Figure 63), no decomposition into many phases has been detected by the latter XRD $\theta/2\theta$ scan. While the film peak intensities have shrunk, the satellite peaks have completely vanished (inset of Figure 66). The decomposition into few phases with similar lattice constants can be seen.

Interestingly, for a $Ti_{0.5}Zr_{0.25}Hf_{0.25}NiSn_{0.998}Sb_{0.002}$ bulk sample, a diffraction peak structure, similar to one obtained for the SL after decomposition, has been obtained by Schwall et. al..[216] Here, the (220) diffraction peaks at a scattering angle 2θ of about 42°

have been shown. For the $Ti_{0.5}Zr_{0.25}Hf_{0.25}NiSn_{0.998}Sb_{0.002}$ bulk sample, the high *ZT* value of 1.2 at 830 K is ascribed to phase separation. For sample preparation, the ingots were annealed to 1273 K. According to their calculation, lattice constants of 6.075 Å, 6.029 Å and 5.989 Å have been obtained in a single sample. Titanium and hafnium rich phases have been assigned to the smallest and the biggest lattice constants, respectively. Transferred to the diffraction peaks that are shown in the inset of Figure 66, lattice constants of 5.94 Å and 5.81 Å have been calculated for the decomposed SL. Even though the lattice constants differ for the SL and the phase separated $Ti_{0.5}Zr_{0.25}Hf_{0.25}NiSn_{0.998}Sb_{0.002}$ bulk sample, a similarity in diffraction peak structure exists. Possibly, the difference in lattice constants has been caused by the variation in maximum annealing temperatures, the attached MgO substrate or impurities in the SL.

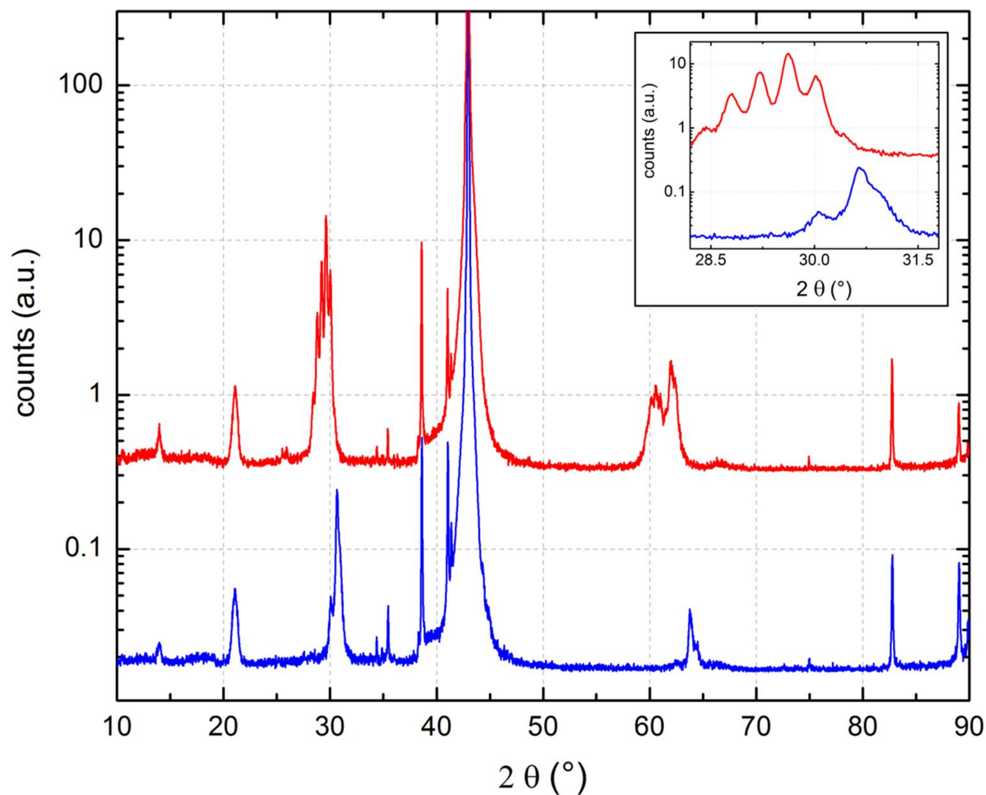

Figure 66 XRD $\theta/2\theta$ scans of a SL measured before (red) and after (blue) a HT TE measurement with a maximum temperature of 850 K; The essential range is shown with a higher resolution (inset).

For a better comparison between the single TiNiSn, the $Zr_{0.5}Hf_{0.5}NiSn$/TiNiSn bilayer and the SL, their XRD $\theta/2\theta$ scans have been summarized in Figure 67. During the HT TE measurement all samples were heated up to 850 K. While a similarity between SL and $Zr_{0.5}Hf_{0.5}NiSn$/ TiNiSn bilayer exists, significant differences have been obtained for the single TiNiSn layer.

Importantly, for the SL that has been heated up to just 550 K (see Figure 64), the highest power factor has been obtained at the maximum temperature. Seebeck coefficient and specific resistivity were determined to be -79.7 μVK^{-1} and 8.23 $\mu\Omega m$. Thus, a power factor of 0.772 $mWK^{-2}m^{-1}$ has been calculated for the SL.

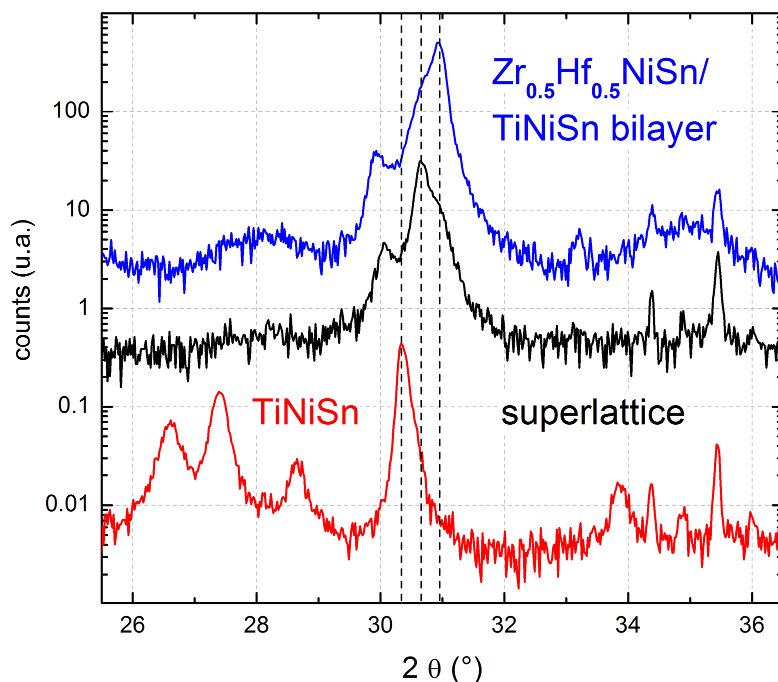

Figure 67 XRD *θ/2θ* scan of a TiNiSn layer (red), a SL (black) and a $Zr_{0.5}Hf_{0.5}NiSn$/TiNiSn bilayer (blue) done after the HT TE measurements

Beginning with TE measurements that were performed at low temperatures, the dependency between SC behavior and crystal quality has been observed. The better the several crystallites have been aligned while growth, the higher power factors have become.

Compared to XNiSn (X = Ti, Zr and Hf) bulk samples, for thin films enhanced carrier concentrations and depressed electron mobilities have been addressed to atomic disorder as well as impurities. For bulk samples, highest *ZT* values were measured for selectively doped HH compounds having identical carrier concentrations. But in contrast to the thin films, electron mobilities and Seebeck coefficients remained at the level of un-doped bulk samples.

At elevated temperatures further increased power factors have been obtained. Due to the fabrication of strongly textured polycrystalline growth, also for SLs highest power factors were measured. Reversible measurements were performed up to 550 K. Unfortunately, the reason why similar bulk samples were measured up to much higher temperatures without a similar degradation remains unsolved.

Chapter 8

Reduced thermal conductivity for superlattices measured by 3ω method

8.1. Introduction

As it has been discussed in Chapter 3, there are ongoing discussions about the thermal conductivity in SLs. While a minimum in thermal conductivity for Bi_2Te_3/Sb_2Te_3 SLs has been measured by some,[101] it has not by others.[217] That the thermal conductivity has been measured by differential 3ω method and by thermoreflectance, respectively, might be one reason. In principle, the differential 3ω method determines a thermal resistance. So, it exhibits advantages if films with a sufficient thickness and a low thermal conductivity have to be measured.

But also in theory, the thermal conductivity of SLs is still under discussion. Recently, Jiang et. al. applied a non-equilibrium Green's function approach to calculate the minimum in thermal conductivity for graphene and BN SLs.[218] By assuming the total SLs thicknesses L between 60 and 120 unit cells, thermal conductivities for varied SL period thicknesses d_S have been calculated. It has been revealed that at a fixed ratio of

$$\frac{d_S}{L} = 0.05 \qquad 8.1$$

a minimum in thermal conductivity occurs for several total SL thicknesses. It has been attributed to an interplay between number of confined modes and their localization. Theories, exhibiting a minimum as a function SL period thickness have been intensively discussed in Chapter 3. Here, a minimum in thermal conductivity that depends on film thickness has been calculated.

But an increasing number of samples are measured by ultrafast LASER flash methods that are developed to measure diffusivity in thin films.[219] Either pulsed heating and temperature detection are performed at one side of the film (temperature decay gives information) or on opposite sides of the film. In the latter case, the delayed temperature rise can be used to determine the diffusivity.[110,220] In both cases, specific heat capacity

and density of the material have to be known to calculate its thermal conductivity. This gives one of the biggest advantages: the thermal conductivity can directly be obtained by the differential 3*ω* method.

Compared to SLs, the effect of mass fluctuation on the thermal conductivity is less controversially discussed. At RT a thermal conductivity for TiNiSn bulk samples of 4.3 W/mK has been measured. By tuning the nickel content additional scattering centers could be included. Therefore the thermal conductivity was lowered to 3 $Wm^{-1}K^{-1}$.[53] Compared to single HfNiSn and ZrNiSn bulk samples with thermal conductivities of 5.4 $Wm^{-1}K^{-1}$ and 5.7 $Wm^{-1}K^{-1}$, respectively, for $Zr_{0.4}Hf_{0.6}NiSn_{0.98}Sb_{0.02}$ 3.9 $Wm^{-1}K^{-1}$ have been observed.[214] Both examples are already showing the reduction of thermal conductivity by of mass fluctuation.

Kurosaki et. al. have utilized SPS at different sintering temperatures for generating bulk samples containing $(Zr_{0.6}Hf_{0.4})_{0.7}Ti_{0.3}NiSn$.[221] At higher sintering temperatures the formation of pure ZrNiSn has been observed by XRD. Due to the reduced mass fluctuation within the sample an increasing thermal conductivity from 3.2 to 3.9 $Wm^{-1}K^{-1}$ has been measured if the sintering temperature is changed from 1173 to 1373 K.

Since thermal conductivity is formed by an electric and a lattice contribution, there is not only a reduction in thermal conductivity observed if additional phases or scattering centers are present in a material system. Although the lattice contribution in $Zr_{0.25}Hf_{0.75}NiSn$ bulk samples is depressed, the overall thermal conductivity rises in the presence of metallic $Zr_{0.25}Hf_{0.75}Ni_2Sn$.[210]

But if titanium in TiNiSn is exchanged by 10 % of zirconium or hafnium without essentially changing the electronic properties, the thermal conductivity can be depressed from 7 $Wm^{-1}K^{-1}$ to about 4 $Wm^{-1}K^{-1}$.[54] So, there is only a reduction in the contribution of the thermal conductivity that belongs to the phonons.

For the material system $ZrNi_{1-y}Cu_ySn$ the thermal conductivity increases up to a copper concentration of 4 % (highest measured compositions).[222] Since in the periodic table copper and nickel are direct neighbors, they exhibit a negligible difference in mass. Therefore, the additional electronic contribution in the thermal conductivity counts more.

A similar effect has been measured for a p-type HH. In contrast to n-type SCs where one has to increase the number of valence electrons to increase the conductivity, for a p-type HH as HfPtSn one has to decrease the number of valence electrons to enhance the number of holes in the VB. So, instead of platinum (subgroup VIII) Kimura et. al. have doped HfPtSn with iridium and cobalt (subgroup VII).[223] Therefore, the specific

resistivity decreased from 191 μΩm to 7.6 μΩm and 7.1 μΩm, respectively. But even more important for now is the observed shift in thermal conductivity. By exchanging iridium as a nearest neighbor of platinum in the periodic table, the thermal conductivity increased from 14.9 $Wm^{-1}K^{-1}$ to 16.4 $Wm^{-1}K^{-1}$. As it was previously discussed for $ZrNi_{1-y}Cu_ySn$, the enhancement of the electronic part to the thermal conductivity dominates the reduction due mass fluctuation in the system. If copper is used instead of iridium, atomic mass and thermal conductivity change from 195 u to 63.5 u and 14.9 $Wm^{-1}K^{-1}$ to 12.8 $Wm^{-1}K^{-1}$, respectively. However, the number of electrons and their mobility has been affected almost identically for both types of doping, again the thermal conductivity has been decreased by artificially embedded scattering centers. It is worth pointing out that Kimura et. al. were able to obtain a *ZT* value of 0.25 at 1100 K for a p-type HH compound.

While in chapter 3 the focus was set on the effect of SLs on thermal conductivity, here the mass fluctuation in HH bulk samples and their impact on thermal conductivity has been extensively presented. So, combining both approaches has been the task of the thesis. While the electronic properties shall remain rather unchanged, the phonons shall highly scatter at the interfaces of a SL. Here, as an initial model system TiNiSn and $Zr_{0.5}Hf_{0.5}NiSn$ have been chosen. By using titanium, zirconium and hafnium that are located above each other in the periodic table, different atomic masses (47.88 u, 91.22 u and 178.49 u)[10] are successively contributed perpendicular in a thin film surface (beside nickel and tin).

To measure low thermal conductivities in thin films, the differential 3ω method that has been invented by David G. Cahill in 1960,[224,225] can be applied. But before the thermal conductivity of the conducting thin films could be measured, several issues had to be overcome. So, before the thermal conductivity of several HH SLs is presented, the principle of the measurement and related difficulties are given in the following.

8.2 Thermal conductivity measured by the differential 3ω method

8.2.1 Temperature oscillations obtained by 3ω voltage

Using dc magnetron sputter deposition, optical lithography and wet-chemical etching, a heater structure that is the essential part of the 3ω method has been fabricated on the sample surface. Before the heater structure has been electrically contacted for further

processing, an image of a sample was taken (Figure 68). Initially, a gold layer with a thickness of 50 nm has been sputtered on the sample. During the sputtering process 5.6 x 10^{-2} mbar and 15 mW have been applied as argon ambient pressure and sputter power, respectively. While the substrate was at RT, growth rates of 0.6 nms^{-1} have been obtained. After transferring the sample to atmosphere, further processing takes place in a clean room. Using optical lithography, the heater structure has been copied from a mask to the sample surface. Afterwards, diluted potassium iodine (2.5 wt.%) has been used to etch the accessible gold surface with an etching rate of about 10 nms^{-1}. Finally, remaining photo resist that protected the gold layer at the desired area has been removed by acetone.

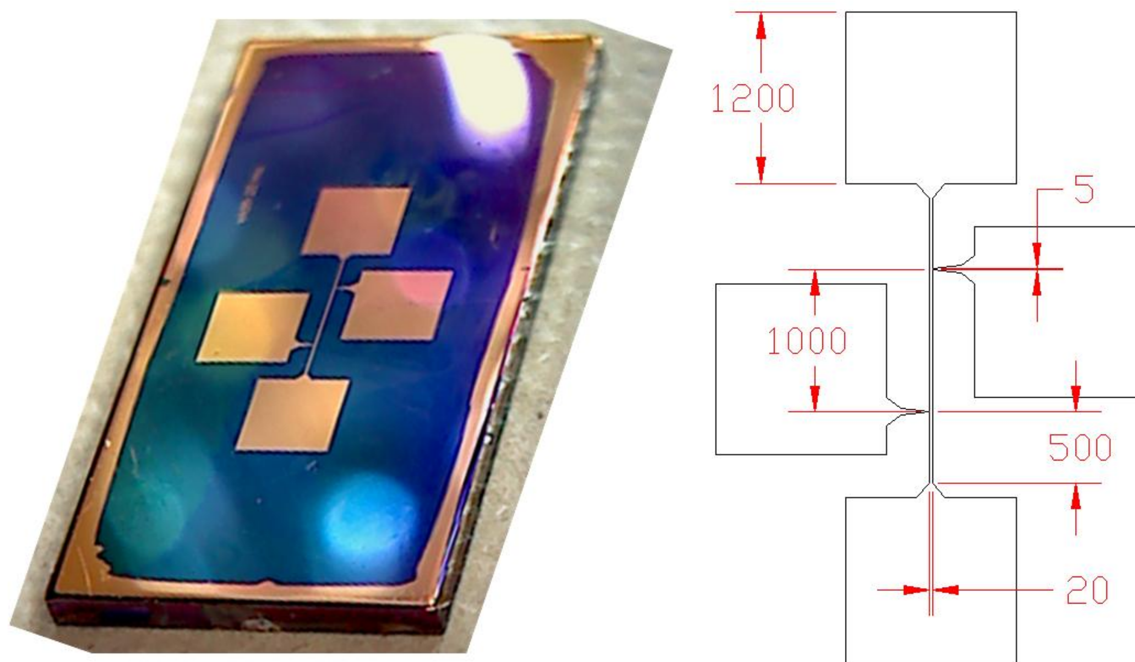

Figure 68 Heater structure for measuring thermal conductivity with 3ω method (left: sample size: 10 x 5 mm^2 / right: given dimensions in µm)

In Figure 68, also a technical drawing of the 3ω heater structure is illustrated. Importantly, using four-point probe technique, a heater stripe with 1 mm in length l and 20 µm in width $2b$ is connected. While the upper and lower pads are used to apply a certain current, the pads on the right and left side of the heater are for measuring the voltage drop without any current flow. Due the applied semi-infinite model that assumes a line symmetric heat distribution into the sample, the heater is extended at both sides of the voltage pads. To keep possible heat losses as low as possible, the connection of the voltage pads goes down to 5 µm. While heater length and heater width can be varied in principle, the described heater structured has been fabricated on the samples designated for 3ω measurements.

This heater structure is chosen to perform an electrical measurement that is described in the following. An ac current I with the frequency ω is applied at the current pads:

$$I = \hat{I}\cos(\omega t) \tag{8.2}$$

Due to the applied current there is a mean temperature rise that expands from the heater structure to the whole sample. Besides, an additional temperature oscillation $\Delta\tilde{T}$ can be observed in the heater structure. The temperature oscillates at 2ω with a phase shift φ.

$$\Delta\tilde{T} = \Delta T(\cos(2\omega t + \varphi)) \tag{8.3}$$

Regarding to the temperature dependent resistance coefficient β, the resistance of the heater stripe oscillates likewise. Here, the resistance of the heater stripe R_0 already includes an increased resistance due to the mean temperature rise:

$$R = R_0\left(1 + \beta\Delta\tilde{T}\right) = R_0\left(1 + \alpha\Delta T(\cos(2\omega t + \varphi))\right) \tag{8.4}$$

According to Ohms law $(U_\omega = RI)$, this also affects the voltage drop U_ω at the inner pads. No additional shift between voltage and current is assumed at low frequencies:

$$U_\omega = R_0(1 + \beta\Delta T\cos(2\omega t + \varphi)) \cdot \hat{I}\cos(\omega t) \tag{8.5}$$

Applying trigonometric functions leads to:

$$U_\omega = R_0 I + \frac{1}{2}\hat{I}R_0\beta\Delta T(\cos(3\omega t + \varphi) + \cos(\omega t + \varphi)) \tag{8.6}$$

Finally, the voltage $U_{3\omega}$ that oscillates with the frequency of 3ω, can be used to calculate the temperature oscillation in the heater stripe. By exchanging $\beta = \mathrm{d}R_0\mathrm{d}T^{-1}R_0^{-1}$ and $\hat{I} = \hat{U}_\omega R_0^{-1}$, the summand $U_{3\omega}$ of Eq. 8.6 that oscillates 3ω can be written:

$$U_{3\omega} = \frac{1}{2}\frac{\hat{U}_\omega}{R_0}\frac{\mathrm{d}R_0}{\mathrm{d}T}\Delta T\cos(3\omega t + \varphi) \tag{8.7}$$

Eq. 8.7 can be resolved to the amplitude (Eq. 8.3) of temperature oscillations ΔT:

$$\Delta T = 2\frac{1}{\frac{\mathrm{d}R_0}{\mathrm{d}T}}R_0\frac{U_{3\omega}}{\hat{U}_\omega}\frac{1}{\cos(3\omega t+\varphi)} \tag{8.8}$$

$$\Delta T = 2\frac{1}{\frac{\mathrm{d}R_0}{\mathrm{d}T}}R_0\frac{\hat{U}_{3\omega}}{\hat{U}_\omega} \tag{8.9}$$

According to the derivation (Eq. 8.9), the maximum values $\hat{U}_{\omega}$ and $\hat{U}_{3\omega}$ have to be taken for the calculation of ΔT. Because voltmeter and lock-in amplifier are giving effective values U^{eff} for both voltages, the conversion with $\sqrt{2}$ cancels out. Thus, ΔT can be calculated using:[226]

$$\Delta T = 2 \frac{1}{\frac{\mathrm{d}R_0}{\mathrm{d}T}} R_0 \frac{U_{3\omega}^{eff}}{U_{\omega}^{eff}} \tag{8.10}$$

Utilizing I (Eq. 8.2) as a reference signal for the lock-in amplifier, $U_{3\omega}^{eff}$ is measured at 3ω using $\varphi = 0$. Therefore, real and imaginary parts of $U_{3\omega}^{eff}$ are obtained. Applying Eq. 8.10, both can be converted into temperature oscillations. Thus, the retardation of the temperature oscillation is considered.

Furthermore, for each heater stripe, $\mathrm{d}R\mathrm{d}T^{-1}$ is determined. Here, a Pt100 reference resistance that has a well-known and precise $\mathrm{d}R\mathrm{d}T^{-1}$ behavior of 0.390802 ΩK^{-1} has been thermally connected to the sample with the heater structure. At about RT, 25°C 30°C and 35°C, a comparison between the both resistances (heater stripe and Pt100), gives the $\mathrm{d}R\mathrm{d}T^{-1}$ behavior of the unknown heater stripe (see inset of upcoming Figure 71).

According to the change in the resistance of the 3ω heater stipe between $\mathrm{d}R\mathrm{d}T^{-1}$ measurement that is initially performed with 100 µA at RT and the actual 3ω measurement that is performed with 18 mW (about 10 mA), the 3ω measurement is done at an increased temperature of about 10 K above RT. Thus, about 30 minutes are needed for the sample to be in equilibrium. Due to the warming of the surrounding, a change in the resistance of the 3ω heater can still be recognized.

8.2.2 Measurement setup

Because $U_{3\omega}$ is about 1000 times smaller than U_{ω} some effort needs to be done to measure the $U_{3\omega}$ with high accuracy. Among others,[227] passive circuits have been used to subtract the voltage components that oscillate with ω from the signal that has to be analyzed (see Eq. 8.6).

In Figure 69, a schematic assembly of the passive bridge circuit that has been used for 3ω measurements is shown.[228] Here, $U_{applied}$ generates a current flow. R_1,..,R_4 are about 4 kΩ and ensure to keep the electron flow in the upper mesh. Following the 3ω heater (red), with its voltage and current pads according to Figure 68, a well-known resistance R_I of 10 Ω enables to determine the applied current I. Afterwards, a resistance decade R_{RD}

has been inserted to generate a reference signal. By the utilization of an adjustable resistance decade with negligible temperature dependence, at the frequency ω, an identical reference signal is generated. For R_1=R_2=R_3=R_4 and $R_{3\omega}$ equal to R_{RD}, U_ω vanishes if both signals are subtracted as it is illustrated in Figure 69. By eliminating U_ω that is about 1 V, $U_{3\omega}$ that is about 500 µV can be measured by a lock-in-amplifier. According to the connection scheme, 0.5 $U_{3\omega}$ is measured by the lock-in-amplifier if $U_\omega - U_{RD} = \mathbf{0}$. Using Eq. 8.10 the temperature oscillations can be calculated using effective voltages.

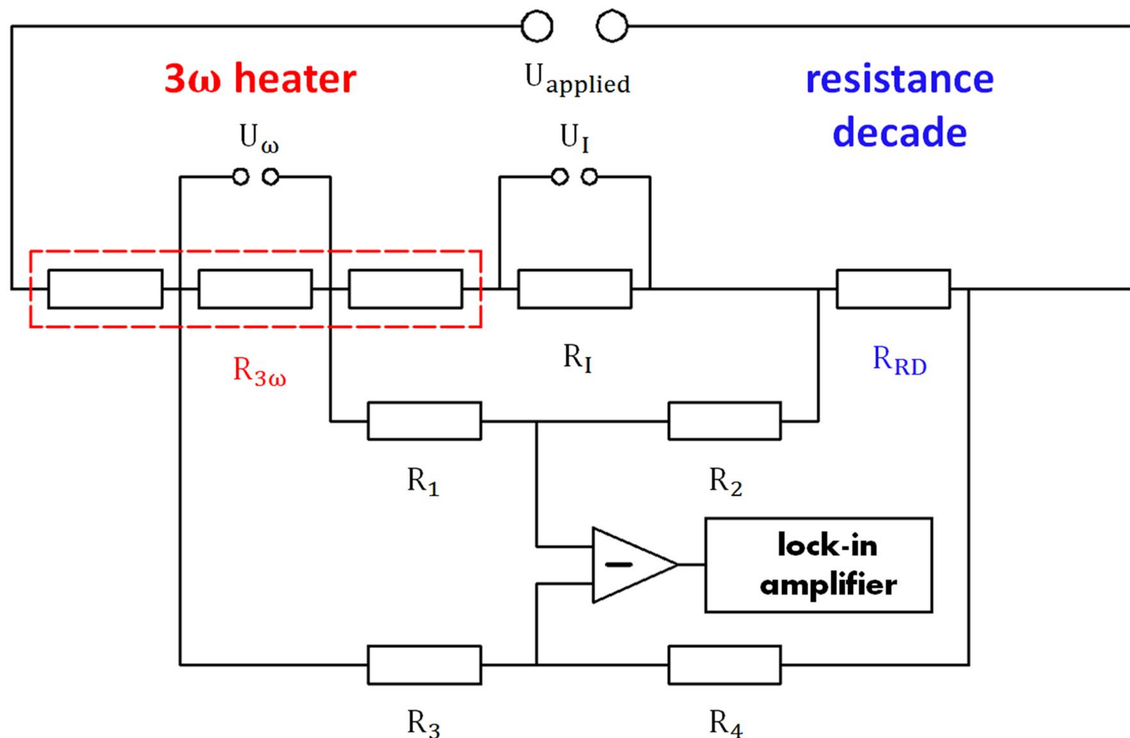

Figure 69 Schematic assembly of the 3ω measurement setup using a passive bridge circuit (passive bridge circuit similar to Ref. 228)

In the following, calculations about thermal conductivities for substrates and thin films are only considering heat losses from the 3ω heater into the subjacent material. To prevent heat losses to the atmosphere above, the measurement can be performed in vacuum. But due to the thermal conductivity of air of about 25 x 10^{-3} $Wm^{-1}K^{-1}$, the effect of heat losses to the atmosphere can be neglected. Furthermore, the thermal conductivity of thin films is determined by the differential method that compares the difference of two films. Since appearing effects are almost equal for both samples, the effect cancels out.

The thermal conductivity of gases is directly proportional to particle density as well as the MFP of single particles.[229] Thus, from RT to about 10^{-3} mbar the thermal conductivity

does not change with ambient pressure. Here, the MFP exceeds 10 cm and becomes the order of distance between 3*ω* heater and bordering walls. Thus, below a pressure of about 10^{-3} mbar the dependence of the thermal conductivity does not depend on MFP anymore and decreases linearly with pressure.

In terms of technical equipment, the differential 3*ω* method can be performed with a lock-in amplifier (also providing a reference signal: $U_{applied}$), two voltmeters, a resistance decade and a bridge circuit containing several resistances. For sample preparation, a clean room with optical lithography is advantageous. In addition, the determination of $\mathrm{d}R\mathrm{d}T^{-1}$ for each 3*ω* heater must be performed.

8.2.3 The calculation of thermal conductivities

Above, one result of the interaction between applied current and affected resistance that oscillate with *ω* and 2*ω*, respectively, has been shown to be $U_{3\omega}$. Furthermore, by applying $U_{3\omega}$ to Eq. 8.10, temperature oscillations $\Delta\tilde{T}$ in the heater stripe can be calculated.

Here, a model is briefly presented that allows calculating thermal conductivities of materials underneath. By using a semi-infinite model, temperature oscillations of an infinite heater stripe (thickness *2b*) that is in direct contact to a solid surface can be described by semi-cylindrical heat waves leaving the heater stripe and propagating into the solid.

Based on the equation of heat propagation (diffusion equation) that includes thermal conductivity *κ*, density *ρ* and specific heat capacity c_s

$$\kappa_x \frac{\partial^2 \Delta\tilde{T}}{\partial x^2} + \kappa_y \frac{\partial^2 \Delta\tilde{T}}{\partial y^2} + \kappa_z \frac{\partial^2 \Delta\tilde{T}}{\partial z^2} = \rho c_s \frac{\partial \Delta\tilde{T}}{\partial t} \qquad 8.11$$

for an infinite narrow line (2*b*≪length *l*), the propagation of temperature oscillations is described by the utilization of the zero order modified Bessel function $K_0(rq)$ that includes the distance $r = \sqrt{x^2 + y^2}$ to the narrow line (heater) and the thermal penetration depth *q*:

$$\Delta\tilde{T}(r,t) = \frac{P}{l\pi\kappa} K_0(rq) \exp(i2\omega t) = \Delta T(r) \exp(i2\omega t) \qquad 8.12$$

The amplitude of the power per unit length at the frequency 2*ω* is considered by Pl^{-1}. To omit confusion about the exact meaning of *P*, the oscillating power $\tilde{P}$ is shown in Figure

70. Here, $U = \hat{U}\,\mathbf{sin(\omega t)}$ (top left) and instantly corresponding current I (top right) are multiplied. Importantly, P can be obtained by multiplying the effective voltage U_{ω}^{eff} and effective current I_{ω}^{eff}. The latter one is obtained at R_I (10 Ω) by measuring U_I^{eff} (see Figure 69).[I]

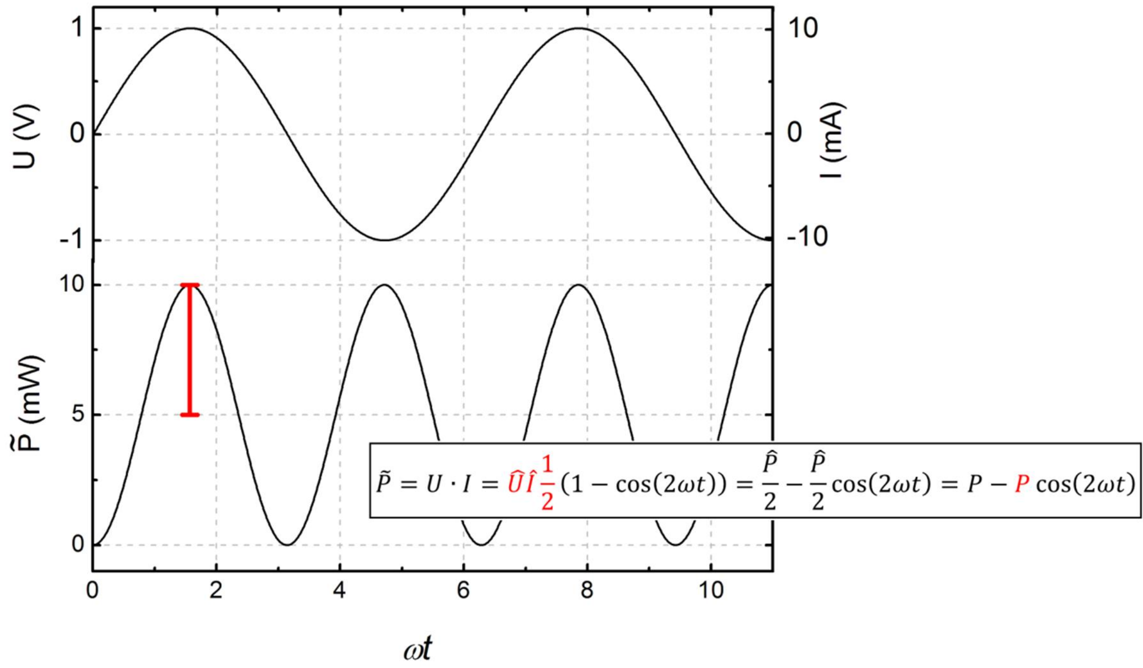

Figure 70 Applied power (below) calculated by voltage and current oscillations (above)

$K_0(rq)$ has been used to solve the diffusion equation (Eq.8.11). In the solution, the wavelength of the diffusive thermal wave q^{-1} ($[q^{-1}]$ = m), or thermal penetration depth,[227] depends on thermal diffusivity $D = \lambda\rho^{-1}c_s^{-1}$ and 2ω:

$$\frac{1}{q} = \sqrt{\frac{D}{i2\omega}} = \sqrt{\frac{\kappa}{\rho c_S i2\omega}} \qquad 8.13$$

For silicon, with a diffusivity of 8.8 x 10^{-5} m^2s^{-1}, at 2ω of 500 s^{-1}, $|q^{-1}|$ is of about 0.42 mm. Thus, for materials with high diffusivities, samples with sufficient dimensions have to be measured. Otherwise, interference with reflected waves occurs and temperature oscillations are not only generated by the applied power oscillation.[230]

[I] To resolve uncertainties about the amplitude of power linked to effective voltages that are actually obtained from the experiment at this point a detailed explanation is given. Similar to the oscillating power $\tilde{P}$ with its amplitude P, the temperature oscillation $\Delta\tilde{T}$ oscillates with amplitude ΔT with a frequency of 2ω around a fixed temperature above ambient temperature.

For $|qr| \ll 1$, meaning that r is much smaller than $|q^{-1}|$, for ΔT inserted in Eq. 8.12 can be written:[I]

$$\Delta T(r) = \frac{P}{l\pi\kappa}\left(\frac{1}{2}\ln\frac{D}{r^2} + \ln 2 - 0.58 - \frac{1}{2}\ln(2\omega) - i\frac{\pi}{4}\right) \quad 8.14$$

According to Eq. 8.14, the amplitude ΔT of the temperature oscillation $\Delta\tilde{T}$ is a complex number with its absolute value proportional to Pl^{-1} and κ^{-1}. Zero phases correspond to an oscillation in phase with the applied power. Beside an existing imaginary part, the real part of the temperature oscillations is affected by the frequency of the applied power. Ignoring all the constant summands in Eq. 8.14 (e.g. $r = 0$ is not defined), a dependency of $\Delta T = -0.5 \ln(2\omega)$ can be found.

With increasing applied frequency 2ω heating cycles become shorter in time. Although the maximum amplitude of the heater power stays the same, the energy inserted into the heater stripe in a single heating cycle decreases. Thus, the temperature oscillations become smaller with higher applied frequencies. Basically, in the 3ω method the thermal conductivity is obtained by the variation of energy per pulse and its consequences on temperature oscillations measured by $U_{3\omega}$.

For a $Ti_{0.5}Zr_{0.25}Hf_{0.25}NiSn$ bulk sample, the real part and the imaginary part of $U_{3\omega}^{eff}$ have been measured. According to Eq 8.10, ΔT has been calculated. As a function of 2ω, both contributions are illustrated in Figure 71. In comparison with Eq. 8.14, the negative linear slope of Re($U_{3\omega}$) and related ΔT as a function of ln(2ω) can be seen. The deviation of Im($U_{3\omega}$) from a constant value has been also observed by others,[224] and can be caused by extraordinary high ΔT. In further investigations of thin films only negligible differences have been obtained using highly conducting substrates.

Importantly, by comparing the imaginary parts of Eq. 8.10 and Eq. 8.14, an equation for the thermal conductivity can be determined:

$$\kappa = \frac{\frac{\mathrm{d}R}{\mathrm{d}T}}{8lR_0^2}\frac{\left(U_{\omega}^{eff}\right)^3}{\mathrm{Im}U_{3\omega}^{eff}} \quad 8.15$$

According to highest effective imaginary part of $U_{3\omega}$, shown in Figure 71, for the $Ti_{0.5}Zr_{0.25}Hf_{0.25}NiSn$ bulk sample a thermal conductivity of 3.31 $Wm^{-1}K^{-1}$ has been calculated.

[I] Among others, a detailed calculation can be found at the Diploma theses of C. Mix.

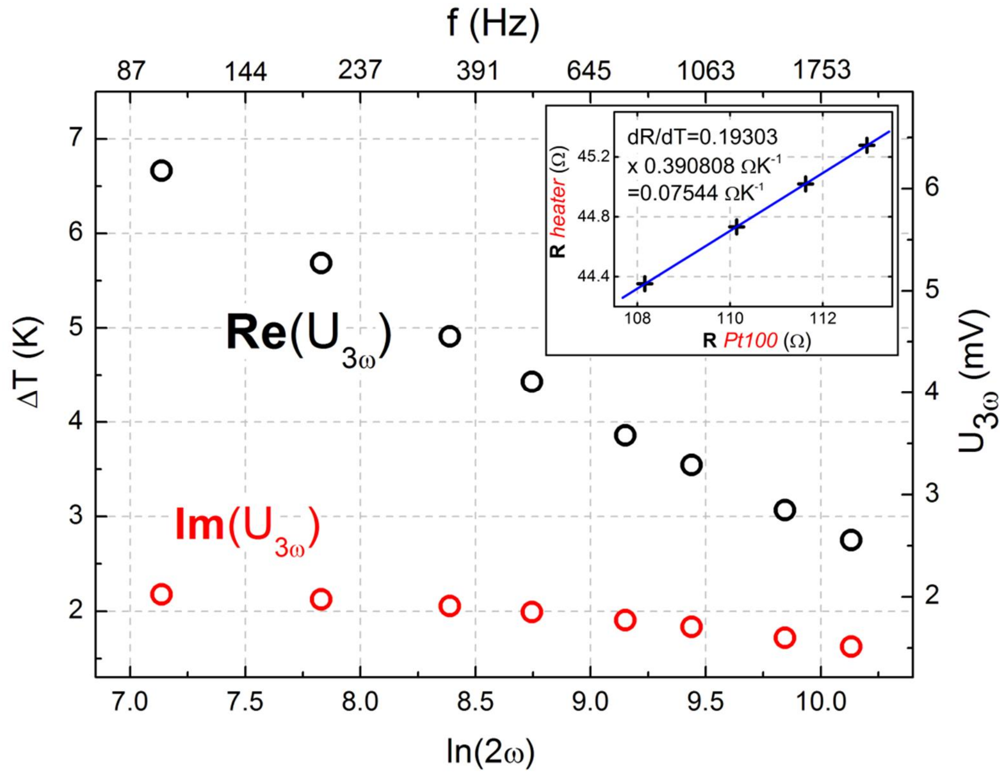

Figure 71 Real (black) and imaginary part (red) of the $U_{3\omega}$ voltage (right) and corresponding temperature oscillation (left) as a function of applied frequency; The calculation of $\mathrm{d}R\mathrm{d}T^{-1}$ for the 3ω heater is shown in the inset.

Applying two different effective real parts of $U_{3\omega}$ and corresponding differences in frequency to Eq. 8.10 and Eq. 8.14,[224] the thermal conductivity can be also obtained by subtracting both individually. Due to the linear dependency between $Re\left(U_{3\omega}^{eff}\right)$ and $\ln(2\omega)$, it can also be calculated as following:

$$\kappa = -\frac{\frac{\mathrm{d}R}{\mathrm{d}T}}{4\pi l R_0^2}\frac{\left(U_{\omega}^{eff}\right)^3}{\frac{\mathrm{d}\left(\mathrm{Re}U_{3\omega}^{eff}\right)}{\mathrm{d}(\ln(2\omega))}} \quad 8.16$$

By fitting the slope of $Re\left(U_{3\omega}^{eff}\right)$ in Figure 71 to be -0.00123 V, a thermal conductivity of 3.49 $\mathrm{Wm^{-1}K^{-1}}$ has been calculated.

Because reliable thermal conductivities have been calculated for many substrates by using Eq. 8.16 and only one value for $\mathrm{Im}U_{3\omega}^{eff}$ has not been obtained, for the $Ti_{0.5}Zr_{0.25}Hf_{0.25}NiSn$ bulk sample a thermal conductivity of 3.5 $\mathrm{Wm^{-1}K^{-1}}$ is more probable.

Beside numerical simulations,[231] the differential 3ω method can be applied to determine the thermal conductivity of thin films.[225] Thin films, deposited on substrates that have been previously discussed as bulk materials, act as thermal resistances between

heater stripes and the substrates. Thus, immediately it becomes obvious that only films with low thermal conductivities can be measured. Furthermore, substrates with a high thermal conductivity are advantageously.

In the differential 3ω method,[230] the thermal conductivity of a thin film can be extracted by the difference in ΔT ($\Delta(\Delta T) = \Delta T_{TF}$) generated in heater structures on top of two different samples. The set of samples then consists of two coated substrates that differ only in the thickness of the thin film with its thermal conductivity to be measured. In an extreme case, the material system is simply grown with and without the thin film. Because interfaces can have a significant influence on the thermal conductivity,[232,233] here sets of samples that only differ in layer thickness are used for the differential 3ω method. In the case of SLs, different thicknesses with identical SL periodicities have been fabricated.

The one dimensional model, applied for the calculation of the thermal conductivity for thin films, can analogously be considered to Ohm's law. Here, an electric voltage U is causing an electric current I in a wire with the cross section A, the length L and the specific conductivity σ:[234]

$$I = \sigma \frac{A}{L} U \tag{8.17}$$

For the differential 3ω method, applying a one dimensional heat flow model, L has to be exchanged by the difference in film thicknesses d_{TF} of the thicker and the thinner layer. Instead of the cross section A, the area below both identical heaters structures is considered. The heat flow $\dot{Q}$ that needs to be equal for both film thicknesses is analogous to an electric current I. Essentially, the thermal conductivity κ_{TF} of the material with different film thicknesses generates the difference in temperature oscillations ΔT_{TF}. Compared to Eq. 8.17, ΔT_{TF} corresponds to the electric voltage U. Thus for Eq. 8.17 it can be written:

$$\dot{Q} = \kappa_{TF} \frac{A}{d_{TF}} \Delta T_{TF} \tag{8.18}$$

According to Figure 70, the heat flow $\dot{Q}$ is generated by power oscillations with amplitudes P. Additionally, the area below the heater is given by its width $2b$ and its length l. Thus, Eq. 8.18 can be written as:

$$\kappa_{TF} = \frac{P \cdot d_{TF}}{2b \cdot l \cdot \Delta T_{TF}} \tag{8.19}$$

For the differential 3ω method, Eq. 8.19 can be utilized to determine the thermal conductivity of the thin films.

8.2.4 Layer stack for differential 3ω method

In the introducing chapters as well as in chapters presenting results, TE materials in general and HH thin films in particular are introduced as conducting materials. Thus, by only fabricating a heater structure on top of thin films an unknown part of the applied current would not flow through the heater structure but through the film to be measured. As Figure 68 already suggestively reveals by the colored surface (apart the heater structure), the thin films are covered by an insulating layer. Here, alumina has been used as a barrier between TE films and gold layer. Because alumina is transparent for visible light, interference effects have been observed. Using an average electron density of HH compounds, the interference color as a function of alumina thickness has been generated and is illustrated in Figure 72.[I] Appropriate to the aspired alumina film thickness of about 250 nm, interference of purple and blue light has been observed (Figure 68).

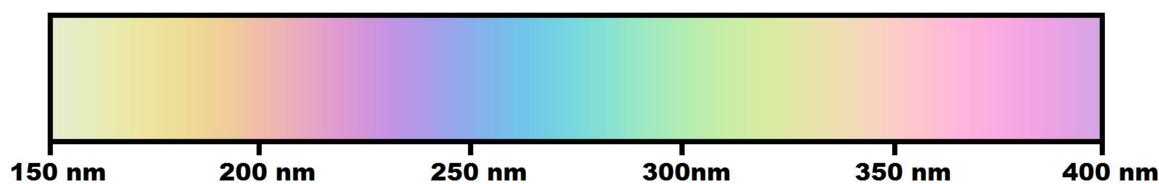

Figure 72 The color of alumina as a function of layer thickness[I]

Assuming a break through field of 10 kVmm^{-1} leads to a thickness for a proper isolation layer of about 100 nm if 1 V is applied.[235] Because at the outer contact pads (current pads) even higher voltages are applied and to have a sufficient safeness for rough interfaces and oxygen vacancies, 250 nm of alumina are intend to be grown between a conducting material and the gold layer on top.

Finally, a layer stack as it is illustrated in Figure 73 has to be grown. Therefore, HH compounds have been sputtered as previously described. After the system cooled down (usually overnight), at RT alumina has been sputtered by reactive rf-magnetron sputtering. Using a pure aluminum target and an argon sputter gas containing 8 % of oxygen,[236,237] at 1.5 x 10^{-2} mbar and 30 W applied power, growth rates of about 35 nm per hour have been obtained. After seven hours of growth, the substrate temperature rose well

[I] Interference spectrum has been generated at http://www.raacke.de/index.html?airy.html

above 50°C. Although the influence of following gold growth and its diffusion into the insulation layer has not been analyzed, the substrate was cooled down once again. Afterwards, 15 W and 5.6 x 10^{-2} mbar have been applied as sputter power and argon ambient pressure, respectively. With a growth rate of about 0.6 nms^{-1}, thin gold layers with a thickness of 35 nm to 50 nm have been deposited by dc magnetron sputtering.

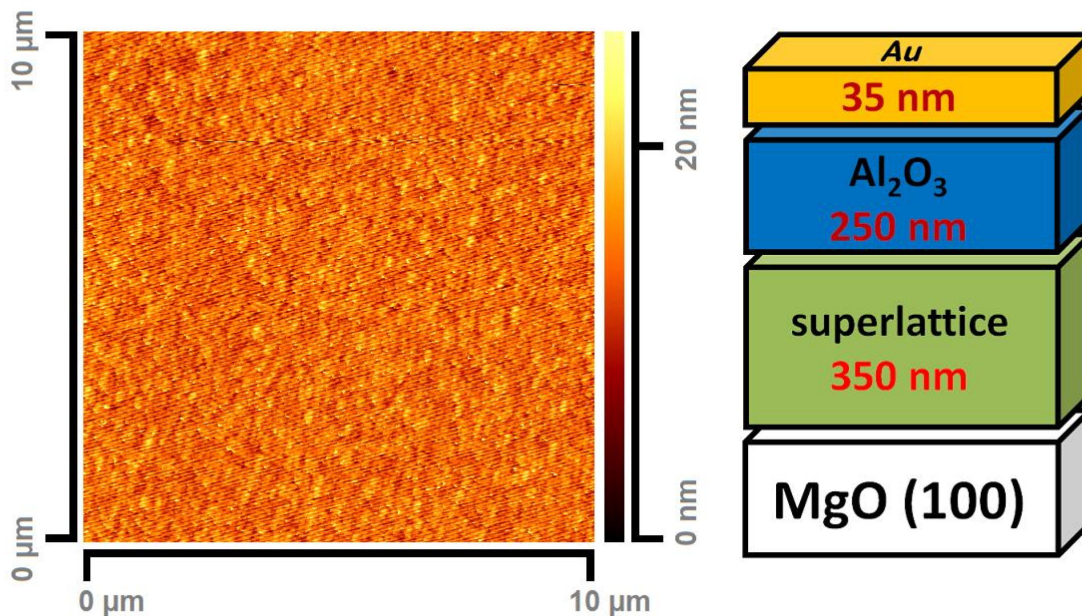

Figure 73 AFM image of a layer stack intended for 3ω measurement

Importantly, after the deposition of all different kinds of layers and a total thickness of more than 600 nm, a flat and homogeneously contributed surface has been still obtained. Considering the heater width of 20 µm that is twice the AFM image section of Figure 73 (left) and the heater height of less than 50 nm that is about twice surface roughness obtained in the AFM, the surface quality is essential for a precise 3ω measurement. As it has been already shown with AFM images in Figure 33, the surface roughness of $TiNiSn/Zr_{0.5}Hf_{0.5}NiSn$ bilayers are enhanced with film thickness. Therefore, heater stripes with identically intended geometries have shown larger resistances if the HH layers underneath became thicker.

The effect of the granular heater structure on the 3ω measurement has been calculated by M. Feuchter from the Karlsruhe Institute of Technology. Applying a finite element method, heat flow from the heater into a MgO substrate has been calculated. Shown in Figure 74, temperature oscillations of two different 3ω heater stripes have been calculated. In the calculation, the 3ω heater consisted of platinum with a width of $2b$ = 10 µm and a height of a = 100 nm. Starting with an ideally flat heater (Figure 1), a

second heater fits with the adapted morphology containing grains at the interface with a height of 20 nm and a diameter of 200 nm (Figure 2). While in the general graph, showing $\Delta T = f(f)$, no difference can be seen for varied 3ω heater stripes, in the enlarged inset of Figure 74, a negligible deviation of less than 0.05 % can be identified. Other than assumed in the simplified model above, here a true heater width and not only an infinite narrow line has been considered. So, heat waves leaving the granular heater structure can interfere again with the heater structure at a different position. If an identical power per heater length is applied for both heater structures only a negligible difference has been obtained. Thus, the leaving heat waves are not considerably influenced by the granular structure of the films.

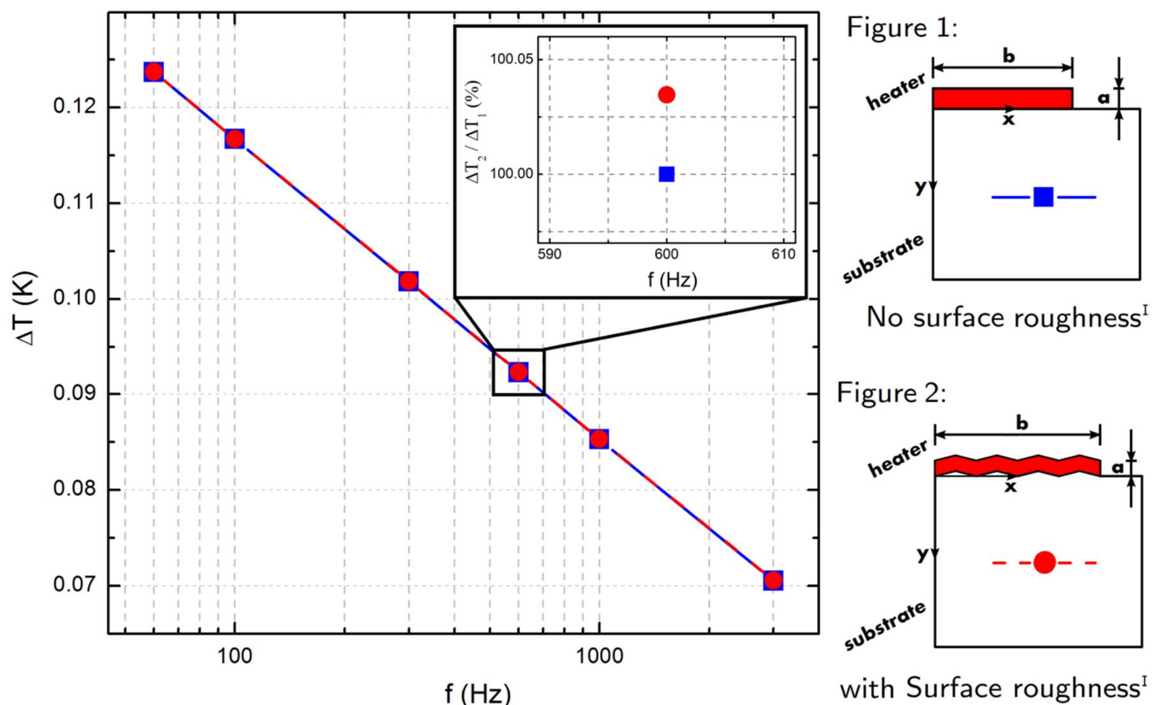

Figure 74 Temperature oscillations simulated for different heater structures[I]

For the differential 3ω method two films with varied HH or SL thicknesses have been grown. Due to the fabrication process, two samples of the same kind have been fabricated in each run. Therefore, four samples have been used to determine the thermal conductivity. Ideally, both thicker and both thinner samples have shown the same temperature oscillations as a function of 2ω. By comparing the results of all four samples, the thermal conductivity has been calculated by Eq. 8.19.

[I] After extensive discussions, the simulation of different heater geometries and their influence on the 3ω measurement was performed by Manuel Feuchter at the Karlsruhe Institute of Technology.

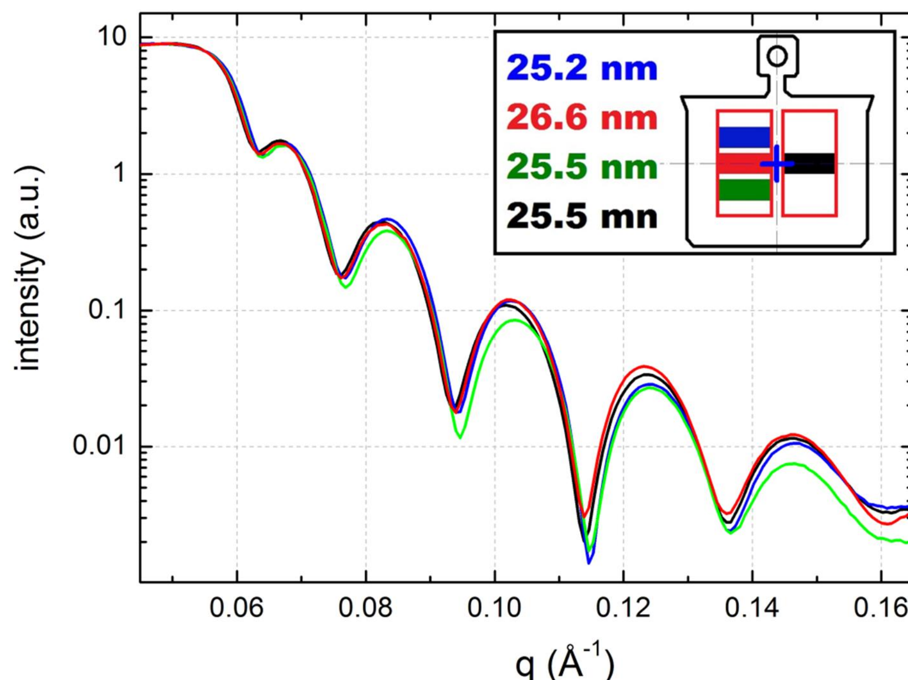

Figure 75 By XRR, thicknesses of two $Zr_{0.5}Hf_{0.5}NiSn$ films are determined at different positions on the sample surface.

Since the calculation of thermal conductivity is directly related to the difference in film thickness it is of importance to fabricate layers without a thickness gradient. So, Figure 75 shows XRR diffractograms for two simultaneously grown $Zr_{0.5}Hf_{0.5}NiSn$ films. In the inlet, the utilized Omicon sample holder is drawn. The blue cross in the middle shows the intended sputter center given by cathodes (magnet behind the sputter target) and sample positions. Both red rectangles, right and left from the blue cross, represent the fixed positions of the substrates (5 x 10 mm^2) while deposition. So, XRR measurements were performed on different film positions to determine the homogeneity of the fabrication process. Differently colored thicknesses in the inset of Figure 75 correspond to equally colored positions on the sample holder. One can calculate that the deviation in the case of $Zr_{0.5}Hf_{0.5}NiSn$ has been about 3.1 % (see Table 5).

	1	*2*	*3*	*4*	Δd
$Zr_{0.5}Hf_{0.5}NiSn$	25.2 nm	26.0nm	25.5 nm	25.5 nm	3.1 %
TiNiSn	31.4 nm	31.0 nm	30.8 nm	31.4 nm	1.9 %
Vanadium	27.9 nm	28.0nm	27.5 nm	28.2 nm	2.5 %
Gold	20.6 nm	20.6nm	20.2 nm	21.1 nm	4.4 %
Al_2O_3	49.7 nm	49.2 nm	49.0 nm	49.5 nm	1.4 %

Table 5 Calculated thicknesses of various deposited films measured at different positions; The colors of the numbers are representing the position shown in Figure 75.

Similar to $Zr_{0.5}Hf_{0.5}NiSn$, analyses about the thickness gradients have been done for TiNiSn, vanadium, gold and alumina. Summarized in Table 5, thicknesses measured at different positions and relative deviations Δd are given.

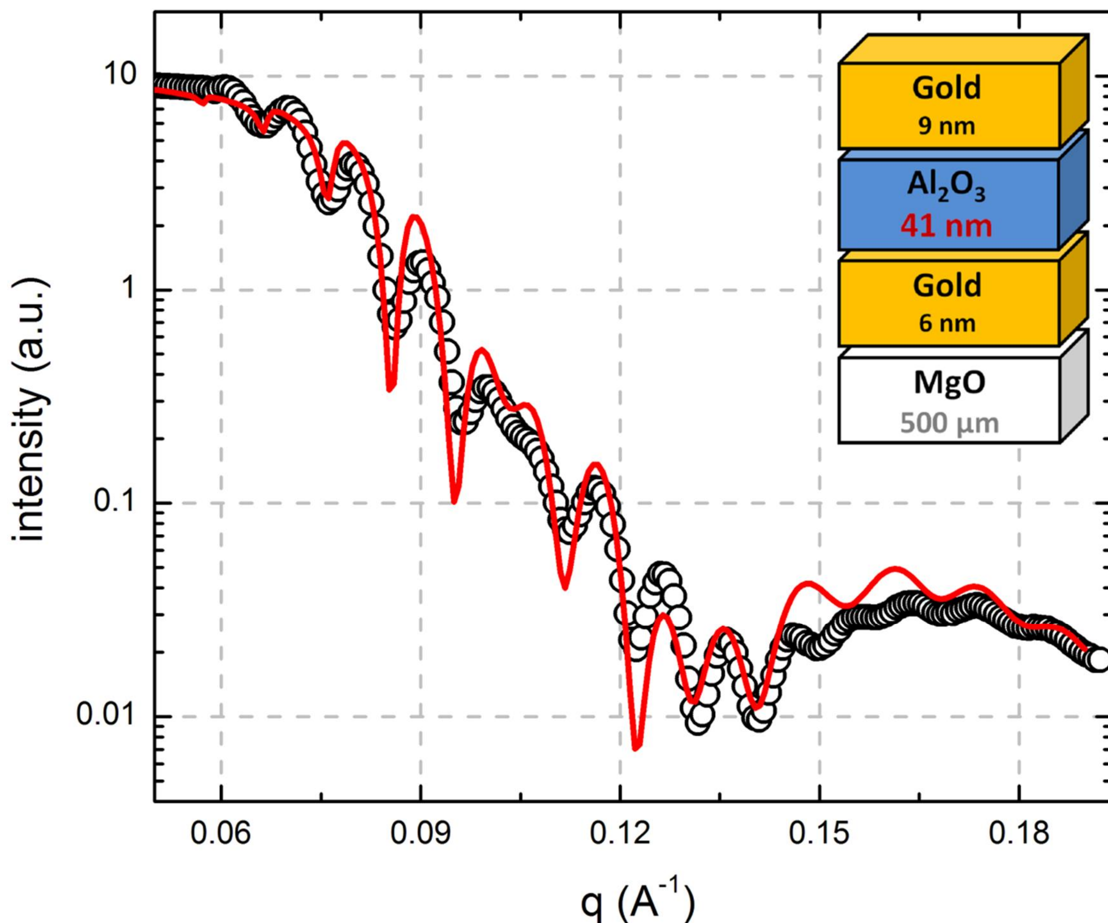

Figure 76 XRR scan of the shown layer stack to determine the layer thickness of alumina

Because of the similar electron densities, XRR is not the method of choice for measuring the thickness of alumina on MgO substrates. To overcome this issue, the alumina layers have to be enclosed by two thin layers with differing electron densities as gold (inset of Figure 76). Thus, penetrating X-ray beams are reflected at both adjacent alumina interfaces. Because several other interfaces that also generate interference effects are present as well, the simulation of the XRR measurement becomes more sophisticated. But if alumina is much thicker than the gold layers, the narrow oscillations are mainly formed by the alumina layer.

After the 3ω method has been implemented and measurements were conducted to enhance the accuracy and reliability, finally thermal conductivities of HH thin films and SLs have been determined.

8.3 Thermal conductivities of TiNiSn, $Zr_{0.5}Hf_{0.5}NiSn$ and superlattices

Using Eq. 8.19 (one dimensional heat flux), the thermal conductivities of TiNiSn, $Zr_{0.5}Hf_{0.5}NiSn$ and a variety of SLs with several periodicities have been determined by the differential 3ω method. Initially, the calculated temperature oscillations ΔT that base on the measured real part of $U_{3\omega}$ are extensively discussed, to demonstrate the reliability of the obtained results. Finally, thermal conductivities obtained for SLs and single HH thin films are discussed. For the SLs the periodicity has been formed single TiNiSn and $Zr_{0.5}Hf_{0.5}NiSn$ layers that have been equal in thickness.

Using a lock-in-amplifier, half of $U_{3\omega}^{eff}$ (see Figure 69) was measured as a function of frequency. For each sample, several frequencies f (100 Hz, 200 Hz, 350 Hz, 500 Hz, 1000 Hz, 1500 and 2000 Hz) were applied. With one exception ($Zr_{0.5}Hf_{0.5}NiSn$), $U_{applied}$ was set that 18 mW dissipated at R_0 (R_ω). Therefore, the generated heat was identical for almost all samples. Having R_0 of around 100 Ω, U_ω^{eff} and I_ω^{eff} were about 1 V and 10 mA, respectively. Beside measuring $U_{3\omega}^{eff} = \mathrm{f}(f)$, dR_0/dT has been determined to calculate ΔT by using Eq. 8.10. $\Delta T = \mathrm{f}(f)$ for different sets of samples is shown in Figure 77. Beside single TiNiSn and $Zr_{0.5}Hf_{0.5}NiSn$ films, also SLs have been measured. In Figure 77, corresponding periodicities are given in the graphs. For each sample, heater widths that have been generated by photolithography and chemical etching are given in addition. Due to the fabrication process most heater widths have been smaller than the width of 20 µm given by the exposer mask (Figure 68).

In general, two identical samples were fabricated and processed as explained above. So, the measurements of both identical samples that were fabricated in the same sputtering process are supposed to be similar. But as it is illustrated in Figure 77, differences in ΔT have been obtained. The biggest uncertainties, causing differing ΔT for identical samples, have been identified to be surface roughness and heater width.

ΔT has been very sensitive to variations in heater widths $2b$. Because the heat that is flowing from the heater into the substrate depends on the contact area of the heater, ΔT is also proportional to $(2b)^{-1}$. For the differential method that uses ΔT_{TF} ($\Delta(\Delta T)$) for the calculation of the thermal conductivity, even small deviations cause extreme errors. Therefore, measured variations in heater widths, using an optical microscope, from

16.8 µm to 21.2 µm have been taken into account. Here, the initially obtained temperature oscillations $\Delta T'$ (illustrated in Figure 77) have been calibrated by:

$$\Delta T = \frac{2b}{20\ \mu\text{m}} \Delta T' \quad 8.20$$

Thus, for heater widths smaller (larger) than 20 µm, ΔT is lower (higher) than $\Delta T'$. An affirmation about the accuracy of the calibration can be obtained by comparing Figure 77 ($\Delta T' = f\ (\ln(2\omega))$) with Figure 78 ($\Delta T = f\ (\ln(2\omega))$). Among others, TiNiSn reference samples (thinner samples) with only a TiNiSn thickness of 96 nm are well suited for explanation. According to the small difference in temperature oscillations ΔT_{TF} (compared to the other set of samples with similar thickness differences) between the thicker samples and the reference samples, it can be easily seen that TiNiSn exhibits the highest thermal conductivity (Eq. 8.19) of the measured material systems. But only the small heater width of the reference samples (16.8 µm) causes that $\Delta T'$ cannot be distinguished from ΔT´ of other reference samples. But after calibration, ΔT of the TiNiSn reference samples that have the lowest thermal resistance between the heater and the substrate have become the lowest of all ΔT. The isolation layer has had an identical thickness for all samples.

Furthermore, thinner heater widths of identical samples (Figure 77) have caused higher $\Delta T'$. Beside the reference samples for $Zr_{0.5}Hf_{0.5}NiSn$ (insignificant), only one example, out of 16 pairs, can be found where Eq. 8.20 increases the difference of ΔT compared to $\Delta T'$ significantly. But next to this conspicuous behavior for SLs with a periodicity of 27.34 nm, the thicker sample with the heater width of 20.3 µm exhibits also an increased slope of $\Delta T = f\ (\ln(2\omega))$. Thus, the decreased thermal conductivity of the MgO substrate (Eq. 8.16) has also shifted ΔT to higher values. Therefore the sample was not considered for determining the thermal conductivity of the SL with a periodicity of 27.34 nm.

Taken into account the thermal conductivities that can be calculated for one set of samples, in average, the maximum deviation has been decreased from 0.34 $Wm^{-1}K^{-1}$ to 0.21 $Wm^{-1}K^{-1}$. If the sample with the deviating slope (27.34 nm; 20.3 µm) is not taken into account, in average, the maximum deviation changes from 0.33 $Wm^{-1}K^{-1}$ to 0.17 $Wm^{-1}K^{-1}$.

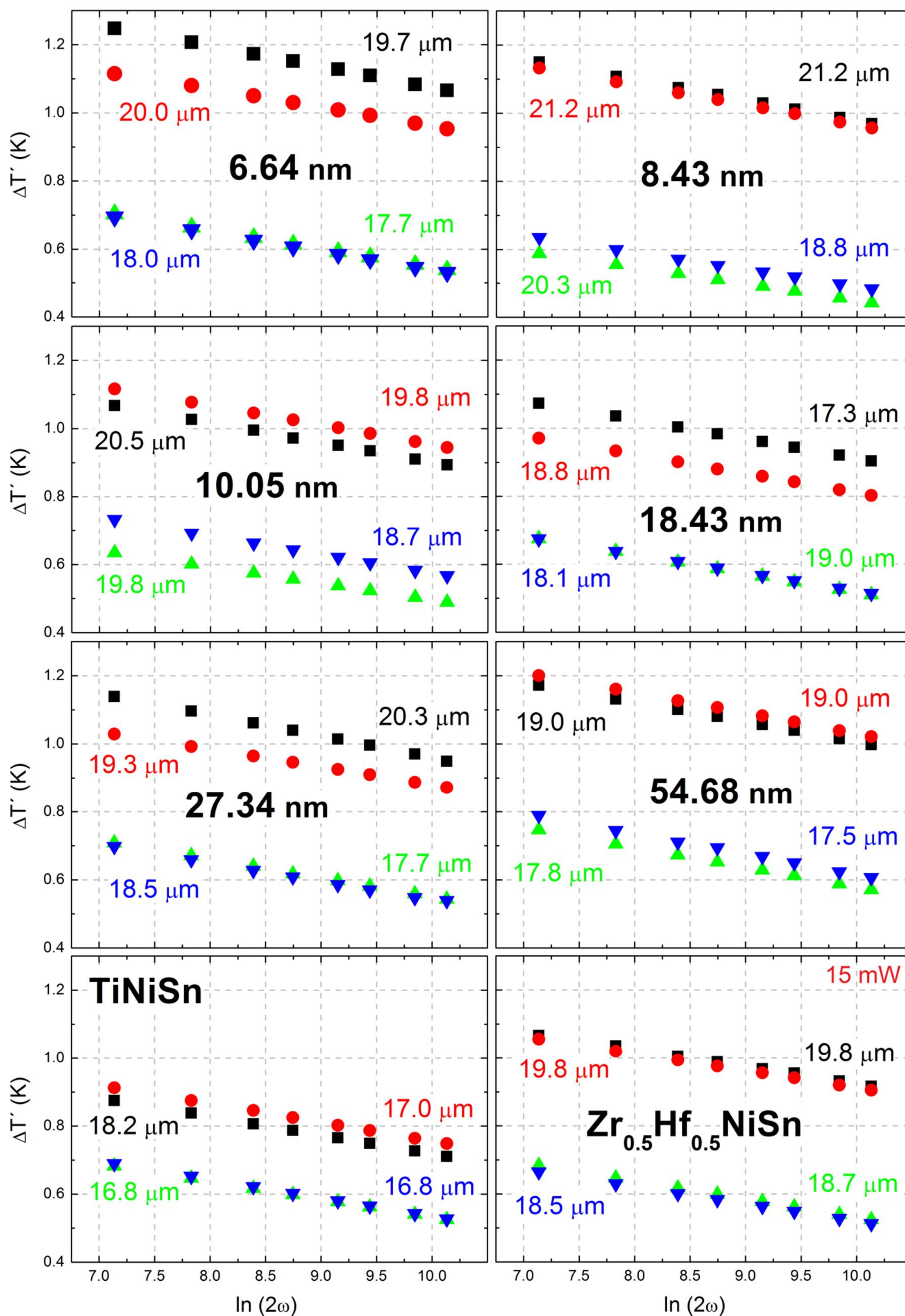

Figure 77 As measured, $\Delta T' = f(\ln(2\omega))$ are shown for TiNiSn, $Zr_{0.5}Hf_{0.5}NiSn$ and SLs (periodicities are labeled). For each set of samples two thicker (red, black) and two thinner samples (green, blue) were measured. Heater widths for each sample are given.

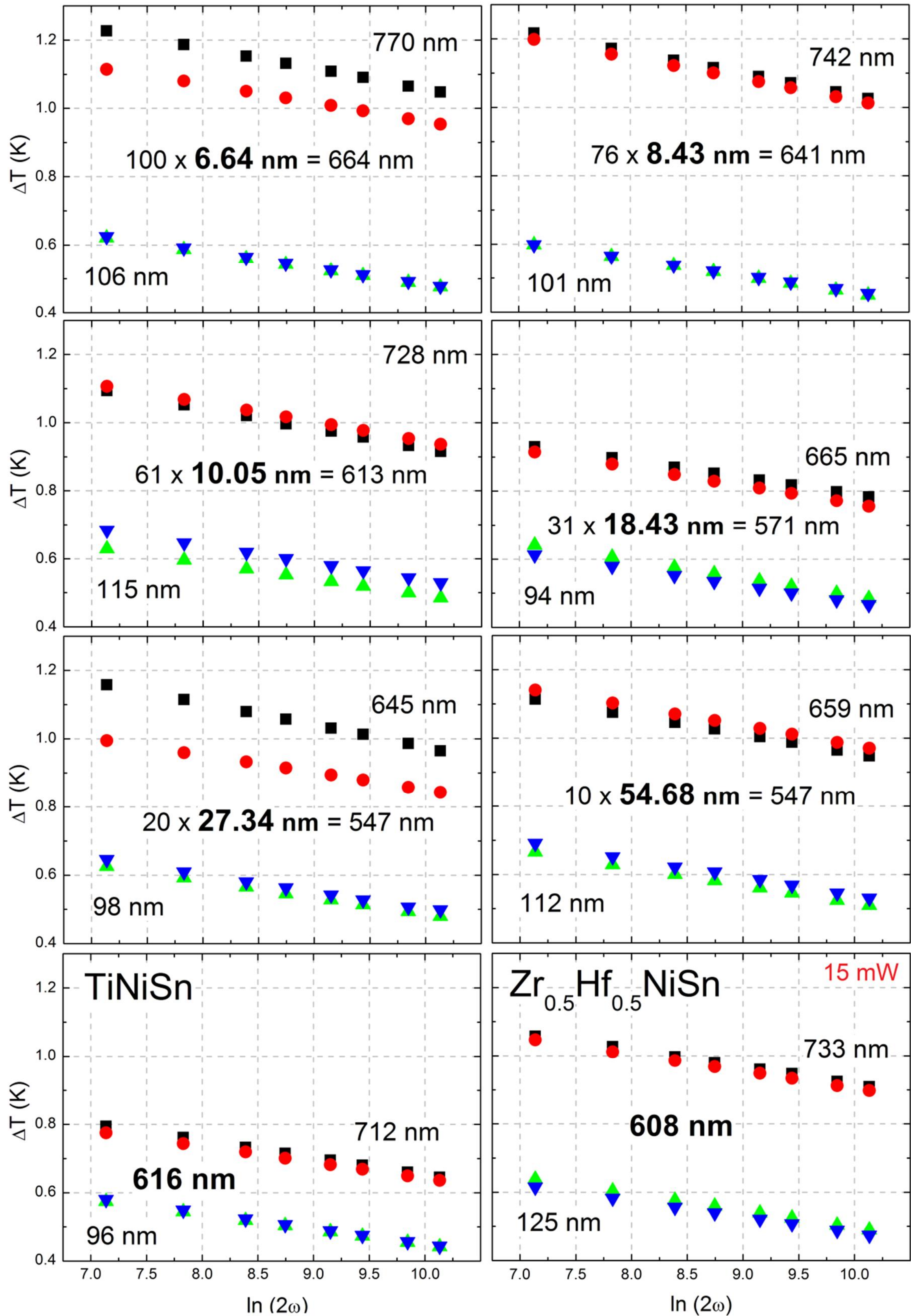

Figure 78 Calibrated with Eq. 8.20, $\Delta T = f(\ln(2\omega))$ are shown for TiNiSn, $Zr_{0.5}Hf_{0.5}NiSn$ and SLs (periodicities are labeled). For each set of samples two thicker (red, black) and two thinner (green, blue) samples were measured. Thicknesses and thickness differences (bold) or periodicities (bold) and amount of periods are given.

For the SL with a periodicity of 8.4 nm, the highest relative change in maximum error from 0.15 $Wm^{-1}K^{-1}$ to 0.03 $Wm^{-1}K^{-1}$ has been observed. A decreased absolute maximum error for the thermal conductivity from 0.56 $Wm^{-1}K^{-1}$ to 0.28 $Wm^{-1}K^{-1}$ and from 0.50 $Wm^{-1}K^{-1}$ to 0.22 $Wm^{-1}K^{-1}$ have been found for the TiNiSn and for the SL with a periodicity of 10.05 nm, respectively.

As it has been already mentioned, surface roughness cannot be excluded to influence the ΔT´ (ΔT). Here, surface roughness changes with SL periodicity, material and film thickness. Enhanced surface roughness has caused higher heater resistances. Although, there have been similar gold thickness (50 nm) and a comparable heater width (20 µm) for all samples, R_0 varied from 44 Ω to 118 Ω. To what extend the characteristics of the gold layer and/or also the alumina layer underneath has been influenced by the surface roughness of the HH thin film has not been analyzed.

In general, higher R_0 have been obtained for the thicker samples (up to 118 Ω). For reference samples, R_0 of 44 Ω to 65 Ω have been obtained. The highest difference for one set of samples has been measured for $Zr_{0.5}Hf_{0.5}NiSn$. Next to 118 Ω and 112 Ω, 58.3 Ω and 58.4 Ω have been calculated for the reference samples. If the similarity of all heater resistivities (55 Ω, 59 Ω and 52 Ω, 47 Ω) has been responsible for the high thermal conductivity obtained for TiNiSn, cannot be clarified. A contrary indication has been found for the ticker samples of the SL with the periodicity of 10 nm. Here, the wider heater (Figure 77) has a resistance of 84.3 Ω. Nevertheless, after calibration no significant difference in ΔT can be found compared to the thinner heater with resistance of only 67.2 Ω (Figure 78).

To solve the origin of the difference in heater resistivities will be necessary for determining the thermal conductivity with even higher accuracy. As it has been shown by a simulation (Figure 74), surface roughness in general does not strongly influence ΔT.

Finally, based on temperature differences ΔT_{TF} obtained by ΔT illustrated in Figure 78, thermal conductivities of thin films have been calculated. Therefore, for each set of samples (in one plot) ΔT measured for reference samples have been subtracted from ΔT obtained by thicker samples. The calculation was performed for all applied frequencies (Figure 78). Because in the measured frequency range, the slope of $\Delta T = f(\ln(2\omega))$ is determined by the thermal conductivity of the MgO substrate, the maximum difference in ΔT_{TF} obtained from one thicker sample minus one reference sample is less than 0.02 K and insignificant compared to the deviation given by $\Delta T = f(\ln(2\omega))$ of identical samples.

For SLs with periodicities from 6.6 nm to 54.7 nm, thermal conductivities are plotted in Figure 79. Additionally, the thermal conductivities of single TiNiSn and $Zr_{0.5}Hf_{0.5}NiSn$ thin films are shown by the shaded area. Given uncertainties have been calculated by the highest and lowest possible thermal conductivities. The lower thermal conductivity has been obtained by the higher and lower ΔT that has been obtained by one thicker sample and one reference sample, respectively. Accordingly, the higher thermal conductivity has been calculated vice versa. As an averaged value, the red cross is plotted for several SLs. For single films, only minimum and maximum thermal conductivities are illustrated by the blue rectangles that do not belong to the modulation length (abscissa).

For the different SLs, the film thicknesses have been calculated by the satellite peak positions in combination with Eq. 6.3. Importantly, the thickness differences d_{TF} have been determined by multiplying the periodicity times the amount of periods (noticed while fabrication) grown for the thicker sample minus the reference samples. The amount of periods has been adapted to film thicknesses of about 100 nm and 700 nm for reference samples and thicker samples, respectively. Therefore, d_{TF} that caused ΔT_{TF} have been about 600 nm. Specified thicknesses have been already given in Figure 78. For single films, film thicknesses have been controlled by known growth rates and deposition time. Because κ_{TF} is proportional to d_{TF} , its correct specification is of importance.

Furthermore, as a measure for crystallographic quality, the FWHM of rocking curves are given in Figure 79. The most intense satellite peaks and the (200) diffraction peaks have been used for measuring SLs and single HH films, respectively. For the XRD measurements, the thicker samples have been utilized. For each pair of samples, about the same FWHM of the rocking curves have been received.

For TiNiSn films, a thermal conductivity of 2.8 $Wm^{-1}K^{-1}$ has been measured. Given in Figure 79, with 0.77° the smallest FWHM of all rocking curves has been observed. This small tilt, indicating a well-ordered film, and the enhanced thermal conductivity for TiNiSn compared to $Zr_{0.5}Hf_{0.5}NiSn$ (see Figure 17), explains the highest of all measured thermal conductivities. In contrast to bulk TiNiSn with a thermal conductivity at RT of about 8 $Wm^{-1}K^{-1}$,[75] the decreased thermal conductivity can be addressed to the reduced grain size. Instead of a grain size perpendicular to the film surface of about 65 nm, Bhattacharya et. al. have fabricated bulk samples with a grain size diameter of 8 µm.[75] 3.7 $Wm^{-1}K^{-1}$ have been obtained for a $TiNiSn_{0.95}Sb_{0.05}$ bulk sample with a grain size diameter less than 50 nm. In the present case, enhanced atomic disorder could have caused a further reduction in thermal conductivity.

Basically, one of the lowest thermal conductivities has been observed for $Zr_{0.5}Hf_{0.5}NiSn$ films. Although $Zr_{0.5}Hf_{0.5}NiSn$ bulk samples already exhibit a reduced thermal conductivity of about 5 $Wm^{-1}K^{-1}$, for thin films a tremendous reduction to 1.1 $Wm^{-1}K^{-1}$ has been measured. Beside the intrinsic behavior of a reduced thermal conductivity due to the variation in atomic mass (ZrNiSn: ~5.7 $Wm^{-1}K^{-1}$; HfNiSn: ~5.4 $Wm^{-1}K^{-1}$),[214] again the reduced grain size (similar to TiNiSn) has caused the depressed thermal conductivity. Furthermore, $Zr_{0.5}Hf_{0.5}NiSn$ films exhibited the worst crystallographic quality of the analyzed samples. The FWHM of the rocking curves has been 1.8°.

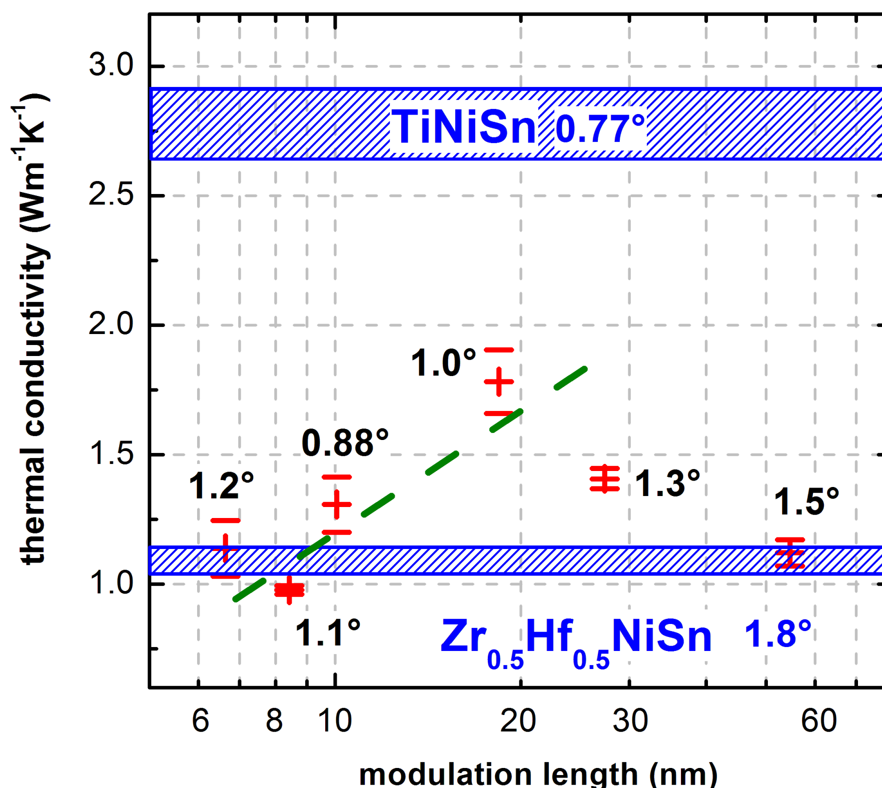

Figure 79 Based on ΔT_{TF} (obtained by ΔT), for TiNiSn, $Zr_{0.5}Hf_{0.5}NiSn$ and a variety of SLs with periodicity from 6.6 nm to 55 nm, the thermal conductivity has been calculated. Additionally, FWHMs of measured rocking curves are given.

Marked by the green dashed line, in Figure 79 attention is drawn to thermal conductivities of SLs with intermediate periodicities. According to the FWHMs determined by rocking curves of 1.1°, 0.88° and 1.0°, similar crystallographic qualities have been obtained for SLs with periodicities of 8.4 nm, 10 nm and 18.4 nm. Starting at the highest periodicity, with 1.8 $Wm^{-1}K^{-1}$ also the highest thermal conductivity has been measured. Assuming, a homogenous contribution of TiNiSn and $Zr_{0.5}Hf_{0.5}NiSn$ layers with their single thermal conductivities of 2.8 $Wm^{-1}K^{-1}$ and 1.1 $Wm^{-1}K^{-1}$, here an average

thermal conductivity of 1.95 $Wm^{-1}K^{-1}$ can be obtained. Because in this layered structure (1.0°), $Zr_{0.5}Hf_{0.5}NiSn$ probably appears with a higher thermal conductivity than observed for the single film (1.8°), already an effect of interface scattering can be suspected.

Going to SLs with lower periodicities strengthened the assumption of interface scattering. Although the crystallographic quality has been the best, for the SL with a periodicity of 10 nm, a reduced thermal conductivity of 1.3 $Wm^{-1}K^{-1}$ has been observed. Therefore, increasing the interface density from 0.11 nm^{-1} to 0.20 nm^{-1} has caused a reduction in the thermal conductivity from 1.8 $Wm^{-1}K^{-1}$ to 1.3 $Wm^{-1}K^{-1}$. Notably, the thermal conductivity is still higher than observed for single $Zr_{0.5}Hf_{0.5}NiSn$ films.

Unfortunately, a FWHM of 1.1° has been obtained by the SL with a periodicity of 8.4 nm. Thus, the lowest measured thermal conductivity of about 0.97 $Wm^{-1}K^{-1}$ cannot only be addressed to the increased interface density to 0.24 nm^{-1}. Here, a single HH layer exhibits only a thickness of 4.2 nm.

Increasing the interface density to 0.3 nm^{-1} have led to an enhanced FWHM of about 1.2°. Thus, again the crystallographic quality has been decreased by reducing the periodicity from 8.4 nm to 6.6 nm. However, with about 1.1 $Wm^{-1}K^{-1}$, the thermal conductivity has not been decreased further.

As it has been shown in chapter 3, for Bi_2Te_3/Sb_2Te_3 SLs a minimum in thermal conductivity has been found at periodicities of 5 nm.[101] In a similar range, a minimum has been also found for ZrN/ScN SLs.[105] For $TiNiSn/Zr_{0.5}Hf_{0.5}NiSn$ SLs a minimum in thermal conductivity between 6.6 nm and 10 nm has been observed. But according to only a single measurement point that has been taken from the differential 3ω method it cannot be stated for sure. Certainly, a trend has been shown that an increased interfaces density also lowers the thermal conductivity.

To complete the results about thermal conductivity, the SLs with a periodicity of 27.3 nm and 54.7 nm have to be discussed. With 1.1 $Wm^{-1}K^{-1}$ and 1.3 $Wm^{-1}K^{-1}$, respectively, the effect of crystal growth on thermal conductivity can be seen. Due to the little interface densities of 0.7 nm^{-1} and 0.4 nm^{-1}, the observed FWHMs of 1.3° and 1.5° are mainly responsible for the reduced thermal conductivities. Interestingly, the thermal conductivity of the SL with the periodicity of 54.7 nm is barely distinguishable from the single $Zr_{0.5}Hf_{0.5}NiSn$ films, suggesting that TiNiSn with a comparable poor crystallographic quality exhibits a similar low thermal conductivity. Vice versa, it can be assumed that $Zr_{0.5}Hf_{0.5}NiSn$ films with a better crystallographic quality also exhibits a higher thermal conductivity.

Importantly, the *ZT* is not only given by the thermal conductivity. In the last chapter, the dependence between FWHMs of the rocking curves and the electric properties have been shown. Here, enhanced Seebeck coefficients have been found for samples with smallest FWHMs. Therefore, not only the depressed thermal conductivity of the single $Zr_{0.5}Hf_{0.5}NiSn$ films but also the low FWHM of the SL with a periodicity of 10 nm has to be taken into account. Here, enhanced electric properties can be assumed, while a reduced thermal conductivity of 1.3 $Wm^{-1}K^{-1}$ has been proven.

The differential 3ω method has been implemented by the optimization of the passive bridge circuit (Figure 69), the insulation layer (Figure 76) and the heater structure (Figure 68). Finally, a set of samples (Figure 78) enabled to measure the thermal conductivity of single TiNiSn and $Zr_{0.5}Hf_{0.5}NiSn$ layers. Besides the dependency to thermal conductivity on SL periodicity has been measured (Figure 79). Actually, in a certain range of SLs periodicities having similar crystallographic qualities, the dependency of interface density on thermal conductivity has been verified. The thermal conductivity has been decreased with decreased periodicity. At a periodicity of 8.4 nm a minimum thermal conductivity of about 1 $Wm^{-1}K^{-1}$ has been measured.

However, based on only one data point, an increased thermal conductivity at very low periodicities cannot be stated for sure. Therefore, further measurements of thermal conductivities, in particular of thin film $Zr_{0.5}Hf_{0.5}NiSn$ with higher crystallographic quality and SLs with periodicities less than 8 nm, will be performed to answer open questions. Notably, further questions are appearing due to promising results for the thermal conductivities that can be depressed by increasing the interface density in half-Heusler superlattices.

Chapter 9

Summary and Outlook

The aim of this thesis was to demonstrate the tailoring of thermoelectric (TE) properties using nanostructured half-Heusler (HH) superlattices (SLs). As TE materials, the suitability of n-type TiNiSn and n-type $Zr_{0.5}Hf_{0.5}NiSn$ bulk samples has been successfully proven. Besides doping to increase the power factor, mixing of atoms with similar electronic properties, but with varied atomic masses for a reduced thermal conductivity has been achieved. For thin films, perpendicular to the film surface, mass fluctuations can artificially be integrated by superlattices (SLs). Therefore, TiNiSn and $Zr_{0.5}Hf_{0.5}NiSn$ were alternatingly deposited by dc magnetron sputtering. In the field of TE, only a few semiconducting Heusler materials (Fe_2VAl, HfNiSn, YNiBi) have been analyzed so far as thin films. But for none of it, the thermal conductivity has been published.[204,206, 238] Using hot-pressed compound targets, thin film TiNiSn and $Zr_{0.5}Hf_{0.5}NiSn$ were fabricated for the first time.

After single film growth conditions were optimized, SLs were fabricated that showed additional satellite peaks in the XRD $\theta/2\theta$ scan. By lowering the substrate temperature from 500°C to 420°C, smooth interfaces were achieved. Utilizing a HAADF-STEM a SL with a periodicity of 3 nm was resolved. Furthermore, a comparison between simulated and measured XRD $\theta/2\theta$ scan revealed the absence of any significant atomic intermixing at the TiNiSn and $Zr_{0.5}Hf_{0.5}NiSn$ interface. The excellent structural quality of single films as well as SLs was achieved on insulating MgO (100) substrates. On MgO (100), having a cubic lattice constant of 4.21 Å, strongly textured polycrystalline growth of TiNiSn and $Zr_{0.5}Hf_{0.5}NiSn$ films with rocking widths of about 1.0° was obtained. For $Zr_{0.5}Hf_{0.5}NiSn$, a TiNiSn buffer layer had to be used for achieving high quality films. For both HH materials, perpendicular to the surface, grain sizes were about 55 nm.

As a suitable metallic buffer layer, vanadium was established. For $Zr_{0.5}Hf_{0.5}NiSn$ layers, comparable crystallographic results were obtained on both buffer layers. At the TiNiSn/MgO interface, the formation of a titanium seed layer was previously found. By omitting the resulting titanium depletion in adjacent atomic layers, with a vanadium buffer layer, an enhanced structural quality was obtained for TiNiSn films.

For a thickness of 10 nm, a single crystalline vanadium buffer layer has been hetero-epitaxially grown on MgO (100). The atomically flat surface as well as the FWHM of the rocking curve (0.12°) completed the outstanding result of this thin metal layer grown on an insulating substrate.

In-plane, TE measurements were performed at low ambient temperatures. Here, the correlation between crystallographic quality, semiconducting behavior and power factor was identified for TiNiSn and $Zr_{0.5}Hf_{0.5}NiSn$ films. To get suitable TE properties, the growth of high quality films was indispensable.

Similar measurements were performed at high temperatures (HT). At about 550 K, for TiNiSn the highest power factor of 0.4 $mWK^{-2}m^{-1}$ was observed. For a SL with a periodicity of 21 nm, an in-plane power factor of 0.77 $mWK^{-2}m^{-1}$ was measured at the same temperature. Compared to bulk samples, the power factor has been generated by depressed Seebeck coefficients (-80 μVK^{-1}), but enhanced conductivities (8.2 μΩm). Furthermore, decomposition occurred for the thin films at about 600 K. A reduced grain size and the closeness of the TE material to the surface were suspected as an essential difference to bulk samples that sustain much higher ambient temperatures.

Assuming a single band model, the origin of enhanced conductivities was investigated by Hall measurements. At RT, for TiNiSn and $Zr_{0.5}Hf_{0.5}NiSn$ carrier concentrations of 2.0×10^{21} cm^{-3} and 1.6×10^{21} cm^{-3} were measured. It corresponds to about 0.1 electrons per formula unit. According to the conductivity, electron mobilities of 1.7 $cm^2V^{-1}s^{-1}$ and 2.1 $cm^2V^{-1}s^{-1}$ were calculated, respectively. Besides potential impurities, in particular atomic disorder caused the observed TE behavior.

Determining the thermal conductivity of thin films was the major challenge of this work. Initially, for a HH bulk sample, fabricated at the Institute of Chemistry, a thermal conductivity of 3.5 $Wm^{-1}K^{-1}$was measured at RT. Therefore, a single $Ti_{0.5}Zr_{0.25}Hf_{0.25}NiSn$ sample was capped by alumina and gold. Compared to thermal conductivities of TiNiSn, ZrNiSn and HfNiSn of 8 $Wm^{-1}K^{-1}$, 5.7 $Wm^{-1}K^{-1}$ and 5.4 $Wm^{-1}K^{-1}$ given in literature already a reduction was obtained by enhanced mass fluctuation.[75,214] By the differential 3ω method, the thermal conductivity for thin film TiNiSn was determined to be 2.8 $Wm^{-1}K^{-1}$. Due to a grain size of about 55 nm, the depressed thermal conductivity was observed.

By the utilization of SLs containing $Zr_{0.5}Hf_{0.5}NiSn$ and TiNiSn, artificial mass fluctuation was inserted into the direction of thermal transport. The variation of single layer thicknesses allowed fabricating thin films with different periodicities (interface

densities). In a range from 18.4 nm (0.11 nm^{-1}) to 8.4 nm (0.24 nm^{-1}) a reduction of cross-plane thermal conductivity from 1.8 $Wm^{-1}K^{-1}$ to 1.0 $Wm^{-1}K^{-1}$ was measured for SLs with a similar structural quality. For a periodicity (interface density) of 6.6 nm (0.30 nm^{-1}), a thermal conductivity of 1.1 $Wm^{-1}K^{-1}$ was obtained. Furthermore, the correlation between crystal qualities and thermal conductivities was observed. Independently, depressed conductivities (1.1 $Wm^{-1}K^{-1}$) were exhibited by single films and SLs with reduced epitaxial growth. Structural qualities were determined by XRD rocking curves that exhibited FWHMs between 0.77° and 1.8°.

For measuring the cross-plane thermal conductivity of the thin films, the differential 3ω method has been implemented. Next to the optimization of the passive bridge circuit and the 3ω heater structure, the identification of growth parameters for insulating alumina was the most time consuming task. Here, the optimization of growth parameters as rf-power, oxygen content in argon sputtering gas and target-to-substrate distance played a challenging role. Finally, alumina with a thickness of 250 nm was sufficiently for insulating the 3ω heater structure with applied voltages of about 2 V from conducting HH films underneath.

A new growth chamber was constructed and assembled to fabricate the layer stack containing buffer layer, TiNiSn, $Zr_{0.5}Hf_{0.5}NiSn$, alumina and gold in situ. Due to its transfer system, later on Photoelectron Spectroscopy (PES) will be performed at freshly grown surfaces. For the installation of an expected Low-Energy Electron Diffraction (LEED) system, the sample holder was pivot-mounted.

Although some questions have been answered, crucial questions are still open for discussion. So far the thermal conductivity has been measured on SLs with periodicities that were homogeneously contributed with TiNiSn and $Zr_{0.5}Hf_{0.5}NiSn$. Here, analyses about asymmetric SLs (one layer is thicker than the other) can give detailed information about scattering mechanisms at the interface.

Furthermore, the behavior of the thermal conductivity of SLs with very short periodicities has not been sufficiently done. The confirmation about a significant trend to higher or lower thermal conductivities with decreasing SL periodicities still needs to be conducted. Therefore the fabrication of SLs, having only a few atomic layers in one layer, with suitable crystallographic quality will be the challenging task.

To evaluate the effect of the interface scattering for the present SLs, the thermal conductivity of $Zr_{0.5}Hf_{0.5}NiSn$ films with a higher crystallographic quality has to be measured. Based on thermal conductivities of single films, the TiNiSn/$Zr_{0.5}Hf_{0.5}NiSn$

interface resistance can be calculated. Here, performing additional four-point conductivity measurements, the electronic part of the thermal conductivity must be considered by using the Wiedemann-Franz law.

Besides thermal conductivity measurements, the power factor of thin films has to be enhanced in order to increase *ZT* above values that are already obtained for bulk values. Though, the reduced electron mobilities that are most likely caused by atomic disorder have to be improved. Seebeck coefficients that are linked to the electron mobility are increased therewith. Although this would presumably involve a decreased conductivity due to lower electron densities, the power factor still goes up.

The growth of vanadium on natively oxidized Si (100) has already given promising results. Polycrystalline $Zr_{0.5}Hf_{0.5}NiSn$ was deposited on a thin vanadium buffer layer. If enhanced structural properties can be obtained on a cleaned silicon surface, the application of HH SLs in real devices would move closer.

Finally, a brief estimation of *ZT* for thin film SLs is done. At 550 K, the highest power factor of 0.77 $mWK^{-2}m^{-1}$ was obtained by a SL with a periodicity of 21 nm. Concerning the FWHM of the rocking curve (4.2°), rather higher power factors can be obtained for better SLs. SL periodicities, applied for measuring thermal conductivities, are assumed to have an insignificant influence on the electric behavior and thus on the cross-plane power factor. Therefore, using a thermal conductivity of 1.0 $Wm^{-1}K^{-1}$ appears to be possible. With increasing temperature, the thermal conductivity is additionally decreased by phonon-phonon interaction. Thus, at a temperature of 550 K, a *ZT* value of 0.4 seems plausible (thermal conductivity: 1.0 $Wm^{-1}K^{-1}$; power factor: 0.77 $mWK^{-2}m^{-1}$). To prove the argumentation, conductivity measurements that are performed in cross-plane direction with MESA structures would give answers about the anisotropic behavior of the power factor in HH SLs.

Based on TiNiSn and $Zr_{0.5}Hf_{0.5}NiSn$, thin films and SLs were fabricated for the first time. Already, the high potential of HH SLs has been revealed by a depressed thermal conductivity that has been obtained by the differential 3ω method. Therefore, half-Heusler superlattices will play an essential role in field of TE research. Concerning thin films, TE research is still at the beginning.

Bibliography

[1] L. D. Hicks and M. S. Dresselhaus; Phys. Rev. B 47; 12727; **1993**

[2] A. Weidenkaff, R. Robert, M. H. Aguirre, L. Bocher and L. Schlapbach; Phys. Stat. Sol. 1; 247; **2007**

[3] H. Hohl, A. Ramirez, C. Goldmanny, G. Ernst, B. Wölfing and E. Buchery; J. Phys.: Condens. Matter 10; 7843; **1998**

[4] S. J. Poon, D. Wu, S. Zhu, W. Xie, T. M. Tritt, P. Thomas and R. Venkatasubramanian; J. Mater. Res. 26; 2795; **2011**

[5] W.J. Xie, J. He, S. Zhu, X.L. Su, S.Y. Wang, T. Holgate, J.W. Graff, V. Ponnambalam, S.J. Poon, X.F. Tang, Q.J. Zhang, T.M. Tritt; Acta Mater. 58; 4705; **2010**

[6] T. Wu, W. Jiang, X. Li, Y. Zhou and L. Chen; J. Appl. Phys. 102; 103705; **2007**

[7] S. Ouardi, G. H. Fecher, B. Balke, M. Schwall, X. Kozina, G. Stryganyuk, C. Felser, E. Ikenaga, Y. Yamashita, S. Ueda and K. Kobayashi; Appl. Phys. Let. 97; 252113; **2010**

[8] R. Venkatasubramanian, E. Siivola, T. Colpitts and B. O'Quinn; Nature 413; 597; **2001**

[9] G. E. Bulman, E. Siivola, R. Wiitala, R Venkatasubramanian, M. Acree and N. Ritz; J. Electr. Mat. 38; 1510; **2009**

[10] Das große Tafelwerk; Volk und Wissen Verlag GmbH & Co.; 1. Auflage, **1999**

[11] J. Sommerlatte, K. Nielsch and H. Böttner; Physik Jounal 6 (5); **2007**

[12] T. J. Seebeck and A. Koenigl; Akad. Wiss. Berlin 265; **1822**

[13] A. Shakouri; Annu. Rev. Mater. Res. 41; 399; **2011**

[14] M.-J. Huang, R.-H. Yen and A.-B. Wang; Int. J. Heat Mass Transfer 48; 413; **2005**

[15] M.-J. Huanga, P.-K. Choua and M.-C. Lin; Sens. Actuators A 126; 122; **2006**

[16] G. J. Snyder and E. S. Toberer; Nat. Mater. 7; 105; **2008**

[17] J. Nurnus and B. Habbe; Techn. Messen 77; 44; **2010**

[18] A. Shakouri, C. LaBounty, J. Piprek, P. Abraham and J. E. Bowers; Appl. Phys. Let. 74; 88; **1999**

[19] S.-D. Kwon, B.-K. Ju, S.-J. Yoon and J.-S. Kim; J. Electron. Mater. 38; 920; **2009**

[20] M.-Y. Kim and T.-S. Oh; J. Electr. Mat. 40; 759; **2011**

[21] M. Takashiri, T. Shirakawa, K. Miyazaki and H. Tsukamoto; Sens. Actuators A 138; 329; **2007**

[22] L. M. Goncalves, J. G. Rocha, C. Couto, P. Alpuim, GaoMin, D. M. Rowe and J. H. Correia; J. Micromech. Microeng. 17; 168; **2007**

[23] I.-H. Kim and K.-W. Jang; Met. Mater. Inter. 12; 269; **2006**

[24] A. Matsumotoa, M. Mikamib, K. Kobayashic, K. Ozakid and T. Nishioe; Mater. Sci. Forum 539; 3285; **2007**

[25] I. Chowdhury, R. Prasher, K. Lofgreen, G. Chrysler, S. Narasimhan, R. Mahajan, D. Koester, R. Alley and R. Venkatasubramanian; Nat. Nanotech. 4; 235; **2009**

[26] R. S. Prasher, J.-Y- Chang, I. Sauciuc, S. Narasimhan, D. Chau, G. Chrysler, A. Myers, A. Prstic and C. Hu; Intel Tech. J. 9; 285; **2005**

[27] A. Bar-Cohen and P. Wang, E. Rahim; Bremen Microgravity Sci. Technol. XIX; 48; **2007**

[28] V. A. Semenyuk1, T. V. Pilipenko, G. C. Albright, L. A. Ioffe and W. H. Rolls; The 14th International Conference on Thermoelectrics; 150; **1995**

[29] V. A. Semenyuk; J. Eng. Phys. 32; 196; **1977**

[30] Edited by D. M. Rowe; Thermoelectrics Handbook: Macro to Nano; section III; chapter 1; **2006**

[31] H. Littman and B. Davidson; J. Appl. Phys. 32; 217; **1961**

[32] A. Weidenkaff, M.H. Aguirre, L. Bocher, M. Trottmann, P. Tomes and R. Robert; J. Korean Chem. Soc. 47; 47; **2010**

[33] H. Böttner; Proceedings MRS April 2009; San Francisco; **2009**

[34] P. Tomes, R. Robert, M. Trottmann, L. Bocher, M.H. Aguirre, A. Bitschi, J. Hejtma Nek and A. Weidenkaff; J. Electr. Mater. 39; 1698; **2010**

[35] W. Jeitschko; Metall. Mater. Trans. B 1; 3159; **1970**

[36] S. Ishida, T. Masaki, S. Fujii and S. Asano; Physica B 237; 363; **1997**

[37] S. Özgüt and K. M. Rabe; Phys. Rev. B. 51; 10443; **1995**

[38] H. C. Kandpal, C. Felser and R. Seshadri; J. Phys. D: Appl. Phys. 39; 776; **2006**

[39] W. Wunderlich and Y. Motoyama; Mater. Res. Soc. Symp. Proc. Vol. 1128; 1128-U01-10; **2009**

[40] T. Graf, C. Felser and S. S. P. Parkin; Prog. Solid State Chem. 39; 1; **2011**

[41] I. Galanakis, P. Mavropoulos and P. H. Dederichs; J. Phys. D: Appl. Phys. 39; 765; **2006**

[42] L. Chaput, J. Tobola, P. Pécheur and H. Scherrer; Phys. Rev. B 73; 045121; **2006**

[43] J. Yang, H. Li, T. Wu, W. Zhang, L. Chen and J. Yang; Adv. Funct. Mater. 18; 2880; **2008**

[44] T. Stopa, J. Tobola, S. Kaprzyk, E. K. Hlil and D. Fruchart; J. Phys.: Condens. Matter 18; 6379; **2006**

[45] J. Tobola and J. Pierre; J. Alloys Compd. 296; 243; **2000**

[46] L. L. Wang, L. Miao, Z. Y. Wang, W. Wei, R. Xiong, H. J. Liu, J. Shi and X. F. Tang; J. Appl. Phys. 105; 013709; **2009**

[47] S. Ouardi, G. H. Fecher, B. Balke, X. Kozina, G. Stryganyuk, C. Felser, S. Lowitzer, D. Ködderitzsch, H. Ebert and E. Ikenaga; Phys. Rev. B 82; 085108; **2010**

[48] J. Black, E. M. Conwell, L. Seigle and C. W. Spencer; J. Phys. Chem. Solids. 2; 240; **1957**

[49] C. M. Bhandari and D. M. Rowe; Contemp. Phys. 21; 219; **1980**

[50] X. W. Wang, H. Lee, Y. C. Lan, G. H. Zhu, G. Joshi, D. Z. Wang, J. Yang, A. J. Muto, M. Y. Tang, J. Klatsky, S. Song, M. S. Dresselhaus, G. Chen and Z. F. Ren; Appl. Phys. Lett. 93; 193121; **2008**

[51] J. O. Sofo and G. D. Mahan; Phys. Rev. B. 49; 4565; **1994**

[52] Y. Kimura, H. Ueno and Y. Mishima; J. Electron. Mater. 38; 934; **2009**

[53] H. Hazama, M. Matsubara, R. Asahi and T. Takeuchi; J. Appl. Phys. 110; 063710; **2011**

[54] T. Katayama, S. W. Kim, Y. Kimura and Y. Mishima; J. Electron. Mater. 32; 1160; **2003**

[55] Y. Skolozdra, N. Tal, A. Yarmek, Y. Rosenberg, M. P. Dariel, S. Ouardi, B. Balke, C. Felser and M. Köhne; J. Mater. Res. 26; 1919; **2011**

[56] Y. Stadnyk, L. Romaka, A. Horyn, A. Tkachuk, Y. Gorelenko and P. Rogl; J. Alloys Compd. 387; p. 251; **2005**

[57] M. Schwall and B. Balke; Appl. Phys. Let. 98; 042106; **2011**

[58] H. Muta, T. Kanemitsu, K. Kurosaki, S. Yamanaka; J. Alloys Compd. 469; 50; **2009**

[59] V. A. Romaka, Y. V. Stadnyk, D. Fruchart, T. I. Dominuk, L. P. Romaka, P. Rogl and A. M. Goryn; Semiconductors 43; 1124; **2009**

[60] Y. V. Stadnyk, A. M. Goryn, Y. K. Gorelenko, L. P. Romaka and N. A. Mel'nichenko; Inorg. Mater. 46; 939; **2010**

[61] D. Jung, K. Kurosaki, C. Kim, H. Muta and S. Yamanaka; J. Alloys Compd. 489; 328; **2010**

[62] H. Hazama, R. Asahi, M. Matsubara and T. Takeuchi; J. Electron. Mater. 39; 1549; **2010**

[63] H. Hohl, A. Ramirez, C. Goldmann, G. Ernst, B. Wölfing and E. Bucher; J. Phys.: Condens. Matter 11; 1697; **1999**

[64] T. M. Tritt, S. Bhattacharay, Y. Xia, V. Ponnambalam, S. J. Poon and N. Thadhani; 20th International Conference on Thermoelectrics; 7; **2001**

[65] W. Demtröder; Experimentalphysik 3; 2. Auflage; Kapitel 12; **2004**

[66] E. P. Pokatilov, D. L. Nika and A. A. Balandin; J. Appl. Phys. 95; 5626; **2004**

[67] C. Kittel; Einführung in die Festkörperphysik; 4. Kapitel; 13. Auflage; **2002**

[68] J. P. Strivastava; Elements of Solid State Physics; 2nd edition; 113; **2006**

[69] N. M. Ashcroft and N. D. Mermin; Festkörperphysik; 25. Kapitel; 2. Auflage; **2005**

[70] C. Kittel; Einführung in die Festkörperphysik; 5. Kapitel; 13. Auflage; **2002**

[71] C. Kittel; Einführung in die Festkörperphysik; 6. Kapitel; 13. Auflage; **2002**

[72] H. Muta, T. Kanemitsu, K. Kurosaki and S. Yamanaka; Mater. Trans. 47; 1453; **2006**

[73] C. G. S. Pillai and A. M. George; Int. J. Thermophys.12; 207; **1991**

[74] R. Berman, E. L. Foster and J. M. Ziman; Proc. R. Soc. Lond. A 231; 130; **1955**

[75] S. Bhattacharya, M. J. Skove, M. Russell, T. M. Tritt, Y. Xia, V. Ponnambalam, S. J. Poon and N. Thadhani; Phys. Rev. B 77; 184203; **2008**

[76] C. Uher, J. Yang, S. Hu, D. T. Morelli and G. P. Meisner; Phys. Rev. B. 59; 8615; **1999**

[77] B. Abeles; Phys. Rev. 131; 1906; **1963**

[78] P. G. Klemens; Phys. Rev. 119; 507; **1960**

[79] J. Callaway and H. C. von Baeyer; Phys. Rev. 120; 1149;**1960**

[80] J. Yang, G. P. Meisner and L. Chen; Appl. Phys. Let. 85; 114; **2004**

[81] P. G. Klemens; Proc. Phys. Soc. A 68; 1113; **1955**

[82] B. D. Indu and R. P. Gairola; Phys. Stat. Sol. B; 100; K119; **1980**

[83] J. E. Douglas, C. S. Birkel, M.-S. Miao, C. J. Torbet, G. D. Stucky, T. M. Pollock and R. Seshadri; Appl. Phys. Lett. 101; 183902; **2012**

[84] K. Miyamoto, A. Kimura, K. Sakamoto, M. Ye, Y. Cui, K. Shimada, H. Namatame, M. Taniguchi, S. Fujimori, Y. Saitoh, E. Ikenaga, K. Kobayashi, J. Tadano and T. Kanomata; Appl. Phys. Express 1; 081901; **2008**

[85] N. Savvides and H. J. Goldschmid; J. Phys. C 13; 4657; **1980**

[86] S. Bhattacharya, T. M. Tritta, Y. Xia, V. Ponnambalam, S. J. Poon and N. Thadhani; Appl. Phys. Let. 81; 43; **2002**

[87] J. W. Sharp, S. J. Poon, and H. J. Goldsmid; Phys. Stat. Sol. (a) 187; 507; **2001**

[88] H. Beyer, J. Nurnus, H. Böttner, A. Lambrecht, T. Roch and G. Bauer; Appl. Phys. Lett. 80; 1216; **2002**

[89] B. K. Ridley; Phys. Rev. B 49; 17253; **1994**

[90] A. A. Kiselev, K. W. Kim and M. A. Stroscio; Phys Rev B 62; 6896; **2000**

[91] S. Tamura, Y. Tanaka and H. J. Maris; Phys. Rev. B 60; 2627; **1999**

[92] K. Termentzidis, P. Chantrenne, J.-Y. Duquesne and A. Saci; J. Phys.: Condens. Matter 22; 475001; **2010**

[93] J. Garg, N. Bonini and N. Marzari; Nano Let. 11; 5135; **2011**

[94] S. Y. Ren and J. D. Dow; Phys. Rev. B 25; 3750; **1982**

[95] M.V. Simkin and G. D. Mahan; Phys. Rev. Let. 84; 927; **2000**

[96] B. Yang and G. Chen; Phys. Rev. B 67; 195311; **2003**

[97] B. C. Daly, H. J. Maris, K. Imamura and S. Tamura; Phys. Rev. B 66; 024301; **2002**

[98] G. Chena and M. Neagu; Appl. Phys. Lett. 71; 2761; **1997**

[99] X. Y. Yu, G. Chena, A. Verma and J. S. Smith; Appl. Phys. Lett. 67; 3554; **1995**

[100] W. S. Capinski, H. J. Maris, T. Ruf, M. Cardona, K. Ploog and D. S. Katzer; Phys. Rev. B 59; 8105; **1999**

[101] R. Venkatasubramanian; Phys. Rev. B 61; 3091; **2000**

[102] V. Narayanamurti, H. L. Störmer, M. A. Chin, A. C. Gossard and W. Wiegmann; Phys. Rev. Let. 43; 2012; **1979**

[103] S. Tamura, D. C. Hurley and J. P. Wolfe; Phys. Rev. B 38; 1427; **1988**

[104] S. Chakraborty, C. A. Kleint, A. Heinrich, C. M. Schneider, J. Schumann, M. Falke and S. Teichert; Appl. Phys. Let. 82; 4184; **2003**

[105] T. Borca-Tasciuc, W. Liu, J. Liu, T. Zeng, D. W. Song, C. D. Moore, G. Chen, K. L. Wang, M. S. Goorsky, T. Radetic, R. Gronsky, T. Koga and M. S. Dresselhaus; Superlattices Microstruct. 28; 199; **2000**

[106] S. T. Huxtable, A. R. Abramson, C.-L. Tien, Arun Majumdar, C. LaBounty, X. Fan, G. Zeng, J. E. Bowers, A. Shakouri, E. T. Croke; Appl. Phys. Lett. 80; 1737; **2002**

[107] S.-M. Lee, D. G. Cahill and R. Venkatasubramanian; Appl. Phys. Lett. 70; 2957; **1997**

[108] G. Pernot, M. Stoffel, I. Savic, F. Pezzoli, P. Chen, G. Savelli, A. Jacquot, J. Schumann, U. Denker, I. Mönch, C. Deneke, O. G. Schmidt, J. M. Rampnoux, S.Wang, M. Plissonnier, A. Rastelli, S. Dilhaire and N. Mingo; Nature Mat. 9; 491; **2010**

[109] V. Rawat, Y. K. Koh, D. G. Cahill and T. D. Sands; J. Appl. Phys. 105; 024909; **2009**

[110] N. Oka, R. Arisawa, A. Miyamura, Y. Sato, T. Yagi, N. Taketoshi, T. Baba and Y. Shigesato; Thin Solid Films 518; 3119; **2010**

[111] Y. K. Koh, Y. Cao, D. G. Cahill and D. Jena; Adv. Funct. Mater. 19; 610; **2009**

[112] D. G. Miller; Chem. Rev. 60; 15; **1960**

[113] N. M. Ashcroft and N. D. Mermin; Festkörperphysik; 1. Kapitel; 2. Auflage; **2005**

[114] L. Onsager; Phys. Rev. 37; 405; **1931**

[115] H. B. Callen; Phys. Rev. 73; 1349; **1948**

[116] C. Goupil, W. Seifert, K. Zabrocki, E. Müller and G. J. Snyder; Entropy 13; 1481; **2011**

[117] N. M. Ashcroft and N. D. Mermin; Festkörperphysik; 13. Kapitel; 2. Auflage; **2005**

[118] C. Hamaguchi; Basic Semiconductor Physics; chapter 6.2; **2005**

[119] Edited by D. M. Rowe; Handbook of Thermoelectrics; section I;, chapter 4; **1995**

[120] D. R. Penn and M. D. Stiles; Phys. Rev. B 59; 13338; **1999**

[121] N. M. Ashcroft and N. D. Mermin; Festkörperphysik; 16. Kapitel; 2. Auflage; **2005**

[122] Y.-M. Lin, X. Sun and M. S. Dresselhaus; Phys. Rev. B 62; 4610; **2000**

[123] Edited by D. M. Rowe; Thermoelectrics Handbook: Macro to Nano; section III; chapter 30; **2006**

[124] M. Cutler and N. F. Mott; Phys. Rev. 181; 1336; **1969**

[125] C. Kittel; Einführung in die Festkörperphysik; 10. Kapitel; 13. Auflage; **2002**

[126] J. Heremans and O. P. Hansen; Phys. C: Solid State Phys. 12; 3483; **1979**

[127] J.-P. Issi; Aust. J. Phys. 32; 585; **1979**

[128] Edited by D. M. Rowe; Thermoelectrics Handbook: Macro to Nano; section I; chapter 8; **2006**

[129] Y. Pei, X. Shi, A. LaLonde, H. Wang, L. Chen and G. J. Snyder; Nature 473; 66; **2011**

[130] C. Kittel; Einführung in die Festkörperphysik; 8. Kapitel; 13. Auflage; **2002**

[131] G. Fahsold, A. Priebe and A. Pucci; Appl. Phys. A 73; 39; **2001**

[132] J. Goniakowski and C. Mottet; Phys. Rev. B 81; 155443; **2010**

[133] Y. Ikuhara, Y. Sugawara, I. Tanaka and P. Pirouz; Interface Sci. 5; 5; **1997**

[134] P. Scherrrer; Göttinger Nachrichten 2; 98; **1918**

[135] R. Ptetorius, J. M. Harris and M.-A. Nicolet; Solid-State Electron. 21; 667; **1978**

[136] M. A. Taubenblatt and C. R. Helms; J. Appl. Phys. 53; 6308; **1982**

[137] T. Kado; Surf. Sci. 454; 783; **2000**

[138] T. Harada and H. Ohkoshi; J. Cryst. Growth 171; 433; **1997**

[139] T. Suzuki and R. Souda; J. Phys. Chem. B 106; 5747; **1999**

[140] S. K. Kim, F. Jona and P. M. Marcus; J. Phys.: Condens. Matter 8; 25; **1996**

[141] A. Aguayo, G. Murrieta, and R. de Coss; Phys. Rev. B 65; 092106; **2002**

[142] Y.-Q. Xie, K. Peng and X.-X. Yang; J. Cent. South Uni. Technol. 8; 83; **2001**

[143] X. Fan, G. Zeng, C. LaBounty, J. E. Bowers, E. Croke, C. C. Ahn, S. Huxtable, A. Majumdar and A. Shakouri; Appl. Phys. Lett. 78; 1580; **2001**

[144] B. Yang, J. L. Liu, K. L. Wang and G. Chen; Appl. Phys. Lett. 80; 1758; **2002**

[145] R.W.G. Wyckoff; Crystal Structures; vol. 1; Wiley, New York; **1963**

[146] G. Ortiz, M. S. Gabor, T. Petrisor (Jr.), F. Boust, F. Issac, C. Tiusan, M. Hehn and J. F. Bobo; J. Appl. Phys. 109; 07D324; **2011**

[147] M. Kallmayer, A. Conca, M. Jourdan, H. Schneider, G. Jakob, B. Balke, A. Gloskovskii and H.-J. Elmers; J. Phys. D: Appl. Phys. 40; 1539; **2007**

[148] C. Kittel; Einführung in die Festkörperphysik; 1. Kapitel; 13. Auflage; **2002**

[149] K. Oura, V. G. Lifhits, A. A. Saranin, A. V. Zotov and M. Katayama, Surface Science An Introduction; Chapter 3.1; **2003**

[150] E. Fromm and O. Mayer; Surf. Sci. 74; 259; **1978**

[151] M. Gutsche, H. Kraus, J. Jochum, B. Kemmather and G. Gutekunst; Thin Solid Films 248; 18; **1994**

[152] Y. Huttel, E. Navarro and A. Cebollada; J. Cryst. Growth. 275; 474; **2005**

[153] H. Lüth; Solid Surfaces, Interfaces and Thin Films; Chapter 3; 4. Edition; **2001**

[154] P. C. McIntyre, C. J. Maggiore and M. Nastasi; J. Appl. Phys. 77; 6201; **1995**

[155] J. Goniakowski and C. Mottet; Phys. Rev. B 81; 155443; **2010**

[156] D. Fuks, S. Dorfman, Y. F. Zhukovskii, E. A. Kotomin and A. M. Stoneham; Surf. Sci. 499; 24; **2002**

[157] Y.F. Dong, S.J. Wang, Y.Y. Mi, Y.P. Feng and A.C.H. Huan; Surf. Sci. 600; 2154; **2006**

[158] S. Kämmerer, S. Heitmann, D. Meyners, D. Sudfeld, A. Thomas, A. Hütten and G. Reiss; J. Appl. Phys. 93; 7945; **2003**

[159] Y. Miura, K. Abe and M. Shirai; J. Phys: Conf. Ser. 200; 052016; **2010**

[160] U. Pietsch, V. Holy and T. Baumbach; High-Resolution X-Ray Scattering: From Thin Films to Lateral Nanostructures; Chapter 8; 2. Edition; **2004**

[161] A. L. Patterson; Phys. Rev. 56; 978; **1939**

[162] Y. Miura, K. Abe and M. Shirai; J. Phys.: Conf. Ser. 200; 052016; **2010**

[163] J. C. Kim, J.-Y. Ji, J. S. Kline, J. R. Tucker and T.-C. Shen; Appl. Surf. Sci. 220; 293; **2003**

[164] T. Hitosugi, T. Hashizume, S. Heike, H. Kajiyama, Y. Wada, S. Watanabe, T. Hasegawa and K. Kitazawa; Defect Diffus. Forum 162; 43; **1998**

[165] K. Arima, K. Endo, T. Kataoka, Y. Oshikane, H. Inoue and Y. Mori; Appl. Phys. Lett. 76; 463; **2000**

[166] E. Wirthl, H. Sitter and P. Bauer; J. Cryst. Growth 146; 404; **1995**

[167] G. S. Higashi, Y. J. Chabal, G. W. Trucks and K. Raghavachari; Appl. Phys. Lett. 56; 656; **1990**

[168] A. Miyauchi, Y. Inoue, T. Suzuki and M. Akiyama; Appl. Phys. Lett. 57; 676; **1990**

[169] H. Lüth; Solid Surfaces, Interfaces and Thin Films; Chapter 6; 4. Edition; **2001**

[170] M. Morita, T. Ohmi, E. Hasegawa, M. Kawakami and M. Ohwada; J. Appl. Phys. 68; 1272; **1990**

[171] J. F. Nicholas; Proc. Phys. Soc. A 66; 201; **1953**

[172] T. Eguchi, C. Kinoshita, S. Kiyoto and K. Yasutake; Jpn. J. Appl. Phys. 5; 645; **1966**

[173] P. Petroff, A. Gossard and W. Wiegmann; Bull. Am. Phys. Soc. 22; 293; **1977**

[174] L. Esaki; J. Cryst. Growth 52; 227; **1981**

[175] D. Mukherji and B.R. Nag; Phys. Stat. Sol. (b) 3; K35; **1976**

[176] J. N. Schulman and T. C. McGill; Phys. Rev. Lett. 39; 1680; **1977**

[177] J. Hwang and J. D. Phillips; Phys. Rev. B 83; 195327; **2011**

[178] J.-J. Li, X. Liu, S. Liu, S. Wang, D. J. Smith, D. Ding, S. R. Johnson, J. K. Furdyna and Y.-H. Zhang; Appl. Phys. Lett. 100; 121908; **2012**

[179] M. Ziese, F. Bern and I. Vrejoiu; J. Appl. Phys. 113; 063911; **2013**

[180] S. Tırpancı, E. Sasıoglu, and I. Galanakis; J. Appl. Phys. 113; 043912; **2013**

[181] J. Zhu, L. Qian, J. Hua, L. Zhou and Z. Zeng; Physica B 406; 3446; **2011**

[182] M.Y. Song, W.C. Chen, D. Hsu, C.R. Chang and J.G. Lin; Appl. Phys. A 104; 881; **2011**

[183] R. Bručas, H. Hafermann, I. L. Soroka, D. Iuşan, B. Sanyal, M. I. Katsnelson, O. Eriksson and B. Hjörvarsson; Phys. Rev. B 78; 024421; **2008**

[184] G. B. G. Stenning, G. J. Bowden, S. A. Gregory, P. A. J. de Groot, G. van der Laan, L. R. Shelford, P. Bencok, P. Steadman, A. N. Dobrynin and T. Hesjedal; Phys. Rev. B 86; 174420; **2012**

[185] M. J. Bentall, R.A. Cowley, W. J. L. Buyers, Z. Tun, W. Lohstroh, R. C. C. Ward and M. R. Wells; J. Phys.: Condens. Matter 15; 4301; **2003**

[186] M. Jalochowski; Z. Phys. B: Condensed Matter 56; 21; **1984**

[187] G. Balestrino, S. Lavanga, P. G. Medaglia, P. Orgiani and A. Tebano; Phys. Rev. B 64; 020506(R); **2001**

[188] G. Jakob, P. Przyslupski, C. Stölzel, C. Tomé ‐ Rosa, A. Walkenhorst, M. Schmitt and H. Adrian; Appl. Phys. Lett. 59; 1626; **1991**

[189] A. E. Tahan, G. Jakob, D. Miu, I. Ivan, P. Badica and L. Miu; Supercond. Sci. Technol. 24; 045014; **2011**

[190] M. V. Elizarova and V. E. Gasumyants; Phys. Solid State 41; 1248; **1999**

[191] K. Horiuchi, T. Kawai, S. Kawai, Y. Fujiwara and S. Hirotsu; Physica C 209; 531; **1993**

[192] A. Cho; Science 313; 164; **2006**

[193] O. G. Schmidt and K. Eberl; Nature 410; 168; **2001**

[194] E. R. Fullerton, I. K. Schuller, H. Vanderstraeten and Y. Bruynseraede; Phys. Rev. B 45; 9292; **1992**

[195] S.-J. Cho, T. Krist and F. Mezei; Thin Solid Films 444; 158; **2003**

[196] A. Einstein; Annalen der Physik. 322; 132; **1905**

[197] M. P. Seah and W. A. Dench; Surf. Interface Anal. 1; 2; **1979**

[198] F. Ostermann; Anwendungstechnologie Aluminium; 2. Auflage; Tabelle 2.5.1.; p. 233; **2007**

[199] Y. Li, S. Zhang, Y. Liu, T. P. Chen, T. Sritharan, and C. Xu; J. Nanosci. Nanotechnol. 9; 1; **2009**

[200] J. F. Moulder, W. F. Stickle, P. E. Sobol and K. D. Bomben; Handbook of X-ray Photoelectron Spectroscopy; Physical Electronics, Inc.; **1995**

[201] X. Kozina, T. Jaeger, S. Ouardi, A. Gloskowskij, G. Stryganyuk, G. Jakob, T. Sugiyama, E. Ikenaga, G. H. Fecher and C. Felser; Appl. Phys. Lett. 99; 221908; **2011**

[202] L. Chaput, J. Tobola, P. Pécheur and H. Scherrer; Phys. Rev. B 73; 045121; **2006**

[203] S. Ouardi, G. H. Fecher, X. Kozina, G. Stryganyuk, B. Balke, C. Felser, E. Ikenaga, T. Sugiyama, N. Kawamura, M. Suzuki and K. Kobayashi; Phys. Rev. Lett. 107; 036402; **2011**

[204] M. Mikami, T. Kamiya and K. Kobayashi; Thin Solid Films 518; 2796; **2010**

[205] C. S. Birkel, W. G. Zeier, J. E. Douglas, B. R. Lettiere, C. E. Mills, G. Seward, A. Birkel, M. L. Snedaker, Y. Zhang, G. J. Snyder, T M. Pollock, R. Seshadri and G. D. Stucky; Chem.Mater. 24; 2558; **2012**

[206] S.-H. Wang, H.-M. Cheng, R.-J. Wu and W.-H. Chao; Thin solid Films 518; 5901; **2010**

[207] B. Yang, W. L. Liu, J. L. Liu, K. L. Wang and G. Chen; Appl. Phys. Lett. 81; 3588; **2002**

[208] M. B. Tang, J. T. Zhao; J. Alloys Comp. 475; 4; **2008**

[209] V. A. Romaka, P. Rogl, V. V. Romaka, E. K. Hlil, Y. V. Stadnyk and S. M. Budgerak; Semiconductors 45; 850; **2011**

[210] J. P. A. Makongo, D. K.Misra, J. R. Salvador, N. J.Takas, G. Wang, M. R.Shabetai, A. Pant, P. Paudel, C. Uher, K. L.Stokes and P. F. P. Poudeu; J. Solid State Chem. 184; 2948; **2011**

[211] B. K. Tanner; Phys. Educ. 11; 97; **1976**

[212] F. G. Aliev, N. B. Brandt, V. V. Moshchalkov, V.V. Kozyrkov, R. V. Skolozdra and A.I. Belogorokhov; Z. Phys. B: Condens. Matter 75; 167; **1989**

[213] F. G. Aliev; Physica B 171; 199; **1991**

[214] C. YU, T.-J. Zhu, K. Xiao, J.-J. Shen, S.-H. Yang and X.-B. Zhao; J. Electron. Mater. 39; 2008; **2010**

[215] T. J. Zhu, K. Xiao, C. Yu, J. J. Shen, S. H. Yang, A. J. Zhou, X. B. Zhao and J. He; J. Appl. Phys. 108; 044903; **2010**

[216] M. Schwall and B. Balke; Phys. Chem. Chem. Phys. 15; 1868; **2013**

[217] M. N. Touzelbaev, P. Zhou, R. Venkatasubramanian and K. E. Goodson; J. Appl. Phys. 90; 763; **2001**

[218] J.-W. Jiang, J.-S. Wang and B.-S. Wang; Appl. Phys. Lett. 99; 043109; **2011**

[219] T. Yagi, N. Oka, T. Okabe, N. Taketoshi, T. Baba and Y. Shigesato; Jpn. J. Appl. Phys. 50; 11RB01; **2011**

[220] T. Baba, N. Taketoshi and T. Yagi; Jpn. J. Appl. Phys 50; 11RA01; **2011**

[221] K. Kurosaki, T. Maekawa, H. Muta and S. Yamanaka; J. Alloys Compd. 397; 296; **2005**

[222] S. Katsuyama, H. Matsushima and M. Ito; J. Alloys Compd. 385; 232; **2004**

[223] Y. Kimura and A. Zama; Appl. Phys. Lett. 89; 172110; **2006**

[224] D. G. Cahill; Rev. Sci. Instrum. 61; 802; **1990**

[225] S.-M. Lee and D. G. Cahill; J. Appl. Phys. 81; 2590; **1997**

[226] D. G. Cahill; Rev. Sci. Instrum. 73; 3701; **2002**

[227] D. G. Cahill and R. O. Pohl; Phys. Rev. B 35; 4067; **1987**

[228] C. E. Raudzis, F. Schatz and D. Wharam; J. Appl. Phys. 93; 6050; **2003**

[229] W. Demtröder; Experimentalphysik 1; 3. Auflage; Kapitel 7; **2004**

[230] T. Borca-Tasciuc, A. R. Kumar and G. Chen; Rev. Sci. Instrum. 72; 2139; **2001**

[231] A. Jacquot, B. Lenoir and A. Dauscher; J. Appl. Phys.91; 4733; **2002**

[232] E. T. Swartz and R. O. Pohl; Rev. Mod. Phys. 61; 605; **1989**

[233] A. Majumdar and P. Reddy; Appl. Phys. Lett. 84; 4768; **2004**

[234] C. E. Raudzis; Dissertation: Anwendung und Erweiterung der 3ω Methode zur Charakterisierung komplexer Mehrschichtsysteme in der Mikrosystemtechnik. Der Andere Verlag; Eberhard-Karls-Universität Tübingen; **2007**

[235] M. Voigt and M. Sokolowski; Mater. Sci. Eng. B 109; 99; **2004**

[236] Y. Chiba, Y. Abe, M. Kawamura and K. Sasaki; Vacuum 83; 483; **2009**

[237] L. Paven-Thivet, C. Malibert, P. Houdy and P. A. Albouy; Thin Solid Films 336; 373; **1998**

[238] R. Shan, S. Ouardi, G. H. Fecher, L. Gao, A. Kellock, A. Gloskovskii, C. E. ViolBarbosa, E. Ikenaga, C. Felser and S. S. P. Parkin; Appl. Phys. Lett. 101; 212102; **2012**